USCIPI REPORT #316

Real Time Effects in Volume Holographic Materials for Optical Storage, Copying, and Optical Neural Networks

by

Sabino Piazzolla

December 1997

Signal and Image Processing Institute
UNIVERSITY OF SOUTHERN CALIFORNIA
Viterbi School of Engineering
Department of Electrical Engineering-Systems
3740 McClintock Avenue, Suite 400
Los Angeles, CA 90089-2564 U.S.A.

Dedication

This work is dedicated to Cecilia, Giuseppe, Maria Grazia, Antonia, Carlo, Salvatore, Claudia, and (little) Cecilia.

They never understood why I left them to come to play with light beams and mirrors in Southern California.

Acknowledgment

Foremost, I would like to thank my advisor, Dr. B. Keith Jenkins for providing the financial support and the research environment during my graduate work at USC. Dr. Jenkins's teachings about thoroughness, dedication, and science are undoubtedly an invaluable heritage that I will carry during my future professional life. I would like also to thank Dr. A. Protopapadakis, Dr. A. A. Sawchuk, and Dr. W. H. Steier for their help in serving on my defense committee.

During my stay at USC I was very lucky to meet a number of people that made my world a very special one, and I would like to mention and to thank a few of them. My officemates, Giorgio C. C. Huang, Federico S. G. Kong, Nunzio Ramlagan, and Luigi Li, faced the incredible task of putting up with me on (almost) daily basis, and they succeeded brilliantly. My best kudos to them.

I really enjoyed the friendship and the sense of humor of Greg Petrisor, however, I enjoyed much less his continuous cannibalization (usually without a warning) of my optical lab. With Adam Goldstein I shared several technical and not-so-technical interesting debates. Andrew Miller and Charles Kuznia were great friends. I really appreciated their help on technical issues and our common interest for geographic explorations, as the mystery of the total eclipse in Baja (with the first one) and the contemplation of the wild beauties of Niagara (with the second one). Alan Webber was very precious for coming to rescue during my moments of crisis with hostile computers. Gloria Halfacre

provided the best of the administrative help along with a (usually) full cookie jar. Diana Demetras help about bureaucratic matters was not short from being "lyrical". I was very fortunate to meet and become friend with Chris Kyriakakis, Wee Ling Wong, Zahid Karim, and Tina Morris. I am in debt for their sincere friendship which was an enjoyable relief during some of my unavoidable stressful periods of life in graduate school. I tried to pay them back (respectively) with lessons on basketball, Italian food, wine tasting, and white garments. Finally, I would like to thank Raimondo Betti his continuous support, great sense of humor, and unique fraternal friendship.

Table of Contents

Chapter 5

Chapter 6

Chapter 7

List of Figures

Abstract

Holographic memories can be a solution to the continuous demand for high capacity, fast access time, and high data transfer rate storage devices required for storage-intensive data processing systems. In fact the inherent properties of holographic memories and optical elements allow high three dimensional storage capacity with fast parallel access. The widespread use of such holographic memories, however, may be limited in part by the lack of availability of a simple to use, economically advantageous, and reliable medium, and, moreover, by their lack of manufacturability. To alleviate these two problems, in this dissertation we present our investigation on the characterization of holographic photopolymers and on hologram copying. The reasons for the interest in using photopolymers for holography lie in the properties of these media: high sensitivity, high resolution, long shelf life, easy dry processing, and low cost.

The holographic grating formation mechanism in photopolymers can be qualitatively described by the following processes: photoinitiation of free radicals, grating formation by free monomer polymerization due to radical initiation, and free monomer diffusion. By linking together the photopolymerization process, free monomer diffusion, and coupled wave theory, we model the temporal dynamics of holographic grating formation, and its associated diffraction efficiency in photopolymers. Particularly, we characterize the (1) grating formation in photopolymers considering a high diffusion rate of the free mono-

mers, (2) the recording of multiplexed holograms, (3) the effects of self diffraction during recording, and (4) the interaction between free monomer diffusion and grating formation at high recording intensity. The theory is validated with a set of experiments that were carried out using DuPont HR-150-38 photopolymer.

In the second part of this dissertation we present and analyze a technique to copy the index or absorption modulation of a multiplexed volume hologram into a secondary volume holographic material. This technique uses a set of self-coherent but mutually incoherent optical sources (I/C recording) and can perform the copy process in a single exposure. By further extending the analysis of our proposed copying technique we determine the conditions for blind copying of multiplexed holograms. Blind copying refers to a copying technique which does not require *a priori* knowledge of the diffraction efficiency of the individual holograms to create a theoretically exact replica of a master hologram. Furthermore, we define how the recording intensity can influence the different figures of merit of the copy when it is not an exact replica of the master. Fidelity of the copy is one of these parameters, which is functionally dependent on the magnification gain and as well as on the attenuation of the copied diffraction efficiencies of the holograms. Because of the architectural flexibility of the presented system, we extend its application to the case of use of different material for copy and master. Particularly, we studied the compatibility between photorefractive crystals and holographic photopolymers as copy/master materials, because of the attractive possibility of storing in a reliable, permanent and economically convenient material (photopolymers) the information from a train-

able and therefore non permanent holographic material (photorefractive crystals).

As an application of our copying technique, we simulated the case of the training of a two layer feedforward optical neural network whose first layer weights are implemented by holograms which are angularly multiplexed in a photorefractive crystal. First we train the network to solve the XOR problem using the back error propagation algorithm; next we copy the holographic weights of the trained network into a secondary holographic medium; then we asses the copy errors in the network when replacing the original master hologram with its copy.

Chapter 1

Introduction

1.1 Motivation

Since the early theoretical studies, [VanHeerden, 1963] and [Leith *et al.*, 1966], assessed the tremendous advantages of using volume holography for storage applications, the alluring idea of retrieving optical information from holograms which are multiplexed in thick photosensitive media has driven a large interest and investigative effort. Moreover, recent results from experimental demonstrations were able to prove that current volume holographic memories can be competitive with the other current optical based storage systems, as CD-ROM's or DVD's [Bell, 1996], in terms of capacity, data transfer rate, compactness and signal fidelity. For example, [Pu and Psaltis, 1996] using a 100μm thick photopolymer presented an experimental design of a holographic disk with a surface density of 10 bits/μm^2. Such surface density is already comparable with that of the next generation (and therefore not yet commercially available) dual layer and double sided DVD's. In a different architecture, [McMichael *et al.*, 1996] presented an experimental demonstration for the fast random access (39 μs) and high data transfer of $2X10^4$ digital images composed by 320X220 pixels (with 8 gray-levels) stored in twenty 1-mm thick slides of

lithium niobate crystal. Interestingly, while today consumer technology is in demand of storage intensive applications, as in multimedia and video on line, the necessary electronic circuitry and interface hardware for a successful and economically viable implementation of holography based memories can finally available at low cost. In fact, the same technology for the fabrication of high quality and high contrast, flat panel display [Bahadur, 1984] can be used for the production of spatial light modulators which can encode the information to be recorded in a volume media; low cost sources and detector arrays, used for the projection and the readout of the optical information stored in holograms, can be practically available off-shelf [Liu *et al.*, 1997]; acoustical and optoelectronic beam steering systems for the control and the deflection of the recording and/or readout beams are largely available [McMichael *et al.*, 1996]; advances in the growth and preparation of new volume holographic materials are continuously presented. In essence, holography can be a technology almost mature for a large market, however, this same technology still may suffer from its two major historical drawbacks: lack of economically advantageous, reliable, and easy to use real time holographic materials and the lack of manufacturability.

Significantly, three decades ago [Chen *et al.*, 1968] with the discovery of the holographic properties in photorefractive crystals, holography experienced a true revolution, because photorefractive crystals represented the first real time (*i.e.* not requiring a post exposure processing of the holograms) and reconfigurable (*i.e.* write/read/erase capability) volume materials ever available. In fact, the study of photorefractive crystals opened the way to research and applications of holography in the fields of optical storage [Kukhtarev *et al.*, 1979],

optical signal processing [Yeh *et al.*, 1989], and optical neural networks [Psaltis *et al.*, 1988], while, unfortunately, the high cost of these materials makes difficult a future prospected use in a large consumer arena of these materials. The investigations and the development of more economically advantageous holographic materials has more recently proposed a new generation of holographic photopolymers. These real time holographic materials are permanent, durable, and reliable, while having a relatively large thickness (up to 100μm) and modulation index (up to 0.015). The recording mechanism of these materials, however, has not been completely characterized and understood and therefore, in a first investigative effort of this dissertation, we dedicate our attention to this existing problem. Particularly, we are motivated to characterize the interaction between photopolymerization kinetics and grating formation during holographic exposure, the effects and the presence of self diffraction during recording, and the diffraction efficiency scalability in case of hologram multiplexing.

Volume holography, as any new technology, can be successful if its products can be manufactured in a simple and convenient way. Usually, the duplication of a volume hologram or of multiplexed volume holograms largely consisted in repeating the original recording process, which most of the time may involve complex exposure schedules which may be extremely time consuming. Holographic duplication is even more critical for the case of holographic neural networks. In these systems, multiplexed holographic weights are obtained after time consuming and hardware demanding training sessions. However, a simple way to duplicate such holograms and to avoid another training session would be to copy the stored holograms in a single step exposure. In

this thesis, therefore, we present an optical architecture which allows such single step duplication of a master hologram with the simultaneous copy of the stored multiplexed holograms. Along with the design of the copying technique, we present an analysis of the copying errors. In fact, hologram cross-talk gratings, lack of fidelity, and grating phase noise are relevant sources of errors that badly can affect the performances of copied holograms. Therefore, we provide an assessment of these copying errors by analyzing the problem of the generation and duplication of a holographic based neural network.

1.2 Thesis Organization

In the first part of this dissertation, from Chap. 2 to Chap. 5, we present our research about holographic photopolymers. Next, Chap.'s 6 and 7, this dissertation, we present our investigation about hologram copying and holographic implementation of neural networks.

In Chap. 2 we introduce the basics notions of photopolymerization kinetics, and we combine such notions with the results of the coupled wave theory to determine an analytically simple closed form model which describes the grating formation in holographic photopolymers. This model is termed as the HFMD model, an acronym for High Free Monomer Diffusion, because it is based on the assumption that the free monomer diffusion is much faster than grating formation time when recording intensity is relatively low. In Chap. 3 the HFMD model is used to control and predict the grating formation of angularly multiplexed volume holograms which are recorded simultaneously or sequentially.

Moreover, we prove that the HFMD is also able to describe the recording of a single holographic grating in presence of an additional incoherent light. In Chap. 4 the effects of self diffraction on holographic photopolymers are modeled and experimentally demonstrated. Finally, in Chap. 5 the assumption of instantaneous monomer diffusion is abandoned, and therefore we model the grating recording taking into account a limited free monomer diffusion. In this way a number experimental physical observations regarding the recording of holographic grating in photopolymers can be understood, modeled and predicted such as the varying saturation diffraction efficiency with the recording intensity and the dark diffusion transient.

In Chap. 6, we introduce a technique for copying the grating modulations of a master hologram in a secondary holographic medium. The technique utilizes a set of coherent by mutually incoherent optical sources and can perform the copying process in a single exposure step. Moreover, by further extending the analysis of our copying technique, we present a blind copying system which allows a parallel recording of all holograms multiplexed in the master without *a priori* knowledge of the multiplexed holograms in the master. In Chap. 7, we discuss an optical system which uses reconfigurable multiplexed holograms to implement the synaptic weights of an artificial neural networks. Particularly, we simulate the training of the XOR problem in a two layer feedforward network. After the training of the network, we consider the blind copying of the holographic weights and the analysis of the copying errors. Finally, in Chap. 8 we present a summary of our work, while new researches and application avenues related to the investigation of this thesis, are also indicated.

1.3 Contributions

The original research contributions of this thesis can be summarized as it follows.

1. The HFMD Model. We derive the HFMD model which leads to an analytical closed form expression describing the grating formation in holographic photopolymers under the assumption that, during exposure, the recording intensity is relatively low so that the grating formation is much slower than the free monomer diffusion. The HFMD model, which is combining polymerization kinetics with results from the coupled wave theory, indicates that the grating formation time depends sublinearly on the average holographic recording intensity, and the grating index modulation at saturation depends only on the beam intensity ratio. The model is validated by comparing its predictions with results of experiments using DuPont HR-150-38 photopolymer. Moreover, the HFMD model is extended to characterize more complex recording scenarios including the incoherent/coherent recording of angularly multiplexed holograms. This last extension is also experimentally verified.

2. Self Diffraction in photopolymers. Using the results of the HFMD model, we characterize the effects of self diffraction. Comparing the results from a computer simulation with experimental data, we demonstrate that self diffraction effects include the spatial-temporal variation of the phase and of the amplitude of the grating modulation within the holographic region, and the shifting of the optimum readout angle during hologram reconstruction.

Finally, the material limitations due self diffraction in thicker photopolymers are investigated.

3. Diffusion Model. The HFMD model fails to characterize the grating dynamic for holographic exposures with high recording intensities, therefore to describe these recording conditions we develop a diffusion model. This diffusion model is derived by combining basics photopolymerization principles and the free monomer diffusion which is described with Flick's diffusion laws. We experimentally confirm the results and the predictions of the model which indicates that the saturation diffraction efficiency depends in a nonlinear fashion on the recording intensity. Furthermore, we characterize and document, for the first time in literature, the dark diffusion transient which is the increment of the diffraction efficiency of the recorded hologram in photopolymers noticeable right after the interruption of the exposure.

4. Hologram Copying. We introduce a novel technique to copy angularly multiplexed volume holograms using incoherent/coherent illumination. This technique is extended to allow blind copying of angularly multiplexed holograms. We define how the ratio between the intensities of the master reference beams and of the copy reference beams can control the diffraction efficiency and the fidelity of the copy. Because of the architectural flexibility of out copying technique, we also characterize the system performances when different materials are used for copy and/or master. Particularly, we have investigated the compatibility between photorefractive crystals and photopolymers, because of the attractive possibility of storing in a reliable, permanent, and eco-

nomically convenient material (photopolymers) the information from a trainable and therefore volatile material (photorefractive crystals).

3 A neural network application. We present a simple neural architectures which uses a photorefractive crystal to implement holographically the weights of the first layer of a feedforward neural network. As an example, we simulated the training of the XOR problem. During the simulation, cross-talk noise generated by the cross-gratings is characterized and compared for different levels of beam intensity modulations during hologram recording. The holographic weights are duplicated in a secondary holographic material using blind copying. After that, we assess the copying errors due to cross-gratings, lack of fidelity, and phase noise.

1.4 Bibliography

Bell, A. E.,"Next-Generation Compact Discs," Scientific American, 275,42-46,(1996)

Bahadur, B.,"Liquid Crystal Displays," Mol. Cryst. Liq. Cryst.,**109**, 3-98,(1984)

Chen, F. S., J. T. LaMacchia, and D. B. Fraser, "Holographic Storage in Lithium Niobate," Appl. Phys. Lett., **13**(7), 223-225, (1968).

Kukhtarev, N. V., V. B. Markov, S. G. Odulov, M. S. Soskin, and V. L. Vinetskii, "Holographic Storage in Electrooptic Crystals. I. Steady State," Ferroelectrics, **22**, 949-960, (1979).

Leith, E. N., A. Kozma, J. Upatneiks, J. Marks, and N. Massev, "Holographic Data Storage in Three-Dimensional Media," Appl. Opt. **5**, 1303-1311, (1966).

Liu, Y., M. Hibbs-Brenner, B. Morgan, J. Nohava, B. Walterson, T. Marta, S. Bounnak, E. Kalweit, J. Lehman, D. Carlson, and P. Wilson, "Integrated VCSELs, MSM Photodetectors, and GaAs MESFETs for Low Cost Optical Interconnects," Spatial Light Modulators, Incline Village, Nevada, (1997).

McMichael, I., W. Christian, D. Pletcher, and T. Chang, "Compact Holographic Storage Demonstrator with Rapid Access," Appl. Opt., **35**(14), 2375-2379, (1996).

Pu, A., and D. Psaltis, "High-Density Recording in Photopolymer-Based Holographic three Dimension disks," Appl. Opt., **35**(14),(1996).

Psaltis, D., D. Brady, and K. Wagner, "Adaptive Optical Networks Using Photorefractive Crystals," Appl. Opt., **27**(9), 1752-1759, (1988).

VanHeerden, J. P., "Theory of Optical Information Storage in Solids," Appl. Opt., **2**, 393-400, (1963).

Yeh, P., A. E. Chiou, J. Hong, P. Beckwitt, T. Chang, and M. Khoshnevisan, "Photorefractive Nonlinear Optics in Optical Computing," Opt. Eng., **28**(4), 328-343, (1989).

Chapter 2

Photopolymers for Real Time Holography

2.1 Introduction

This chapter gives an introduction to the holographic properties of Du Pont photopolymers. Since their introduction, DuPont holographic photopolymers have capitalized on increasing interest and favor because of their reliability, high sensitivity, easy dry processing, and moreover for their low cost [Smothers *et al.*, 1990]. Because of these properties, holographic photopolymers are suitable materials in applications such as optical storage, optical interconnections, and holographic copying architectures. The proper use of such materials, however, relies upon the knowledge of their physical properties and the accurate understanding of the grating formation process during holographic exposure. Therefore this chapter, and the three following ones, present our results in modeling and characterizing the holographic properties of DuPont photopolymers.

Particularly, in this chapter a brief historical introduction to photoimaging applications of photopolymers proceeds a concise description of the photoinduced polymerization mechanisms. This description introduces the basic concepts of photochemistry and polymerization kinetics which are continuously referred to and used in this thesis. The main purpose of this chapter, however, is to present our new model which describes the real-time grating formation in holographic photopolymers, under the assumption that the diffusion of free monomers is much faster than the grating formation. This model, which combines polymerization kinetics with results from coupled wave theory, indicates that the grating formation time depends sublinearly on the average holographic recording intensity, and the beam intensity ratio controls the grating index modulation at saturation. The model is validated by comparing its predictions with results of experiments using DuPont HRF-150-38 photopolymer.

2.2 Photopolymers for Holography

Photosensitized polymers, or photopolymers, have been used in photoimaging applications for many decades, primarily as photoresist for the development of printed electronic circuits. As early as 1970, different results about holographic applications of photopolymers were presented in the literature

[Wopschall and Pampalone, 1972], with the great expectation that such materials could replace dichromated gelatin and silver halide in refractive index imaging systems, which were the materials then available [Kurtz and Owen, 1975]. Dichromated gelatin [Shankoff, 1968] and silver halide presented, and still present the drawbacks of a cumbersome post-exposure wet processing, high scattering noise (silver halide) [Kozna, 1968] and lack of reliability (dichromated gelatin). The expectations on photopolymers faded away, however, because they had even more disadvantages than the other existing holographic materials. Specifically, the exhibited a short shelf life, smaller refractive index modulation, and more importantly, a lack of reproducibility.

The interest in using photopolymers for holography resurged recently when Du Pont developed a family of photopolymers that present nearly ideal holographic properties including high reliability, large thickness for volume application (up to 100μm for the film DuPont HRF-150-100), high index modulation (0.06 for the film DuPont HRF-700), dry processing, reasonable shelf life [Curtis and Psaltis, 1994], and ultimately, and very importantly in case the of large volume production, low price [Weber *et al.*, 1990].

The commercially available Du Pont photopolymers are dry photosensitive films composed of acrylic monomers, polymeric film binder, initiator, and photosensitizer dye. The material is available as a foil of various sizes and thicknesses enclosed and isolated by two layers of (unfortunately birefringent) Mylar, or in the form of solutions ready to be mixed and spun to create any desired recording geometry and the necessary thickness. Table 1 summarizes

the performance and the holographic characteristics of some of the photopolymer films currently available from Du Pont in terms of index modulation, thickness and wavelength sensitivity.

Table 1: Summary of Du Pont Holographic Recording Films

Film	Recording Geometry	Thickness (μm)	Index Modulation	Wavelength Sensitivity (nm)
HRF-150	Transmission	38	0.008	450-550
HRF-160	Transmission	38	0.008	570-670
HRF-352	Reflection	25	0.03	450-550
HRF-500E	Reflection	15, 20,25,30	0.02	450-550
HRF-600	Transmission	10, 20	0.03	450-525
HRF-600	Reflection	10, 20	0.06	450-525
HRF-610	Transmission	10, 20	0.035	633-647
HRF-610	Reflection	10, 20	0.04	633-647
HRF-700	Reflection	10, 20	0.06	450-550
HRF-705	Reflection	30	0.04-0.06	RGB
HRF-710	Reflection	10, 20	0.06	633-647
HRF-750	Refl/Trans	20	-	RGB

Recording and processing in Du Pont photopolymer is very simple: the photopolymer is deposited onto a high quality glass plate and then exposed. An ultraviolet (UV) illumination fixes the grating and increases the total hologram throughput efficiency by bleaching the dye which is responsible for light absorption. After fixing, the material is transparent, colorless, and ready for use, with unlimited shelf life [Curtis and Psaltis, 1994].

2.3 Polymerization Kinetics

Before introducing the detailed mechanisms of holographic recording in photopolymers, it is necessary to briefly describe some basic principles of polymer kinetics [Odian, 1991]. When a photosensitive polymer is illuminated by a light source, the first step to photopolymerization is the creation of free radicals. The molecular species able to generate these free radicals are called initiators. After their creation, the free radicals (R•) react with monomers to create polymeric molecules, as sketched by the following sequence, and depicted in Fig. 2-1 and Fig.2-2:

(1) $h\nu$ +Initiator -------> R• Photogeneration of free radicals

(2) R• + M --------> RM• Polymeric chain generation

(3) RM_{n-1}• + M -------> RM_n• Chain propagation

(4) RM_n• + R• -------> RM_nR Chain termination

(5) RM_m• + RM_n• -------> RM_{m+n}R Chain termination

Upon illumination, the initiator system generates free radicals (R•) in step **(1)**. The radicals react with monomers (M) to create a reaction chain of polymers (RM•), step **(2)**. While other reaction chains are generated (the indices *n* and *m* refer to the number of monomers linked to the polymer chain), the already existing polymeric chains propagate by linking to other monomers, step **(3)**. The propagating chain is terminated when it is combined with another radical, or another propagating chain, steps **(4)** and **(5)**. Fig. 2-2 illustrates the important fact that while photoinduced polymerization is localized where illu-

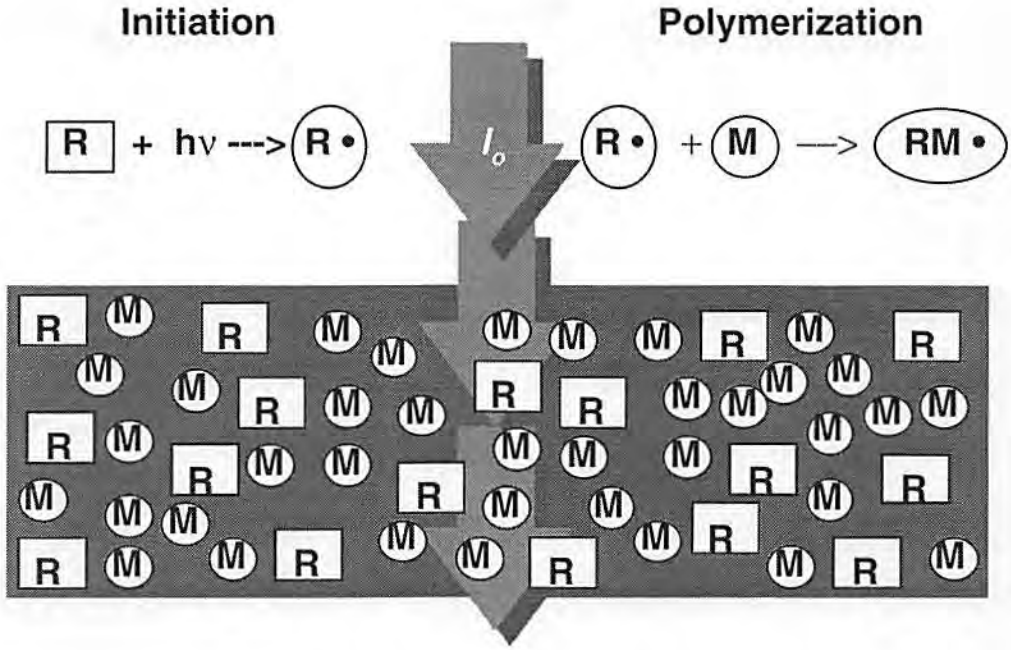

Figure 2-1. Photoinitiated polymerization. **R** stands for the initiator system. **M** is a free monomer molecule. Upon illumination, light of intensity I_o excites the initiator system and free radicals, **R•**, are generated. The free radicals bond the free monomers, and a polymeric chain is created. The process continues until the illumination is interrupted, or the free monomer concentration is depleted.

mination takes place, free monomers tend to diffuse in the medium, and replace those polymerized.

The kinetics of the above process is described by the rates of radical initiation (R_i), chain propagation (R_p), and chain termination (R_t), as [Reiser, 1989]

$$R_i = 2\phi I_o \ , \tag{2-1}$$

$$R_p = k_p [M] \ [M\bullet \ ] \ , \text{and} \tag{2-2}$$

$$R_t = 2k_t [M\bullet \ ]^2 , \tag{2-3}$$

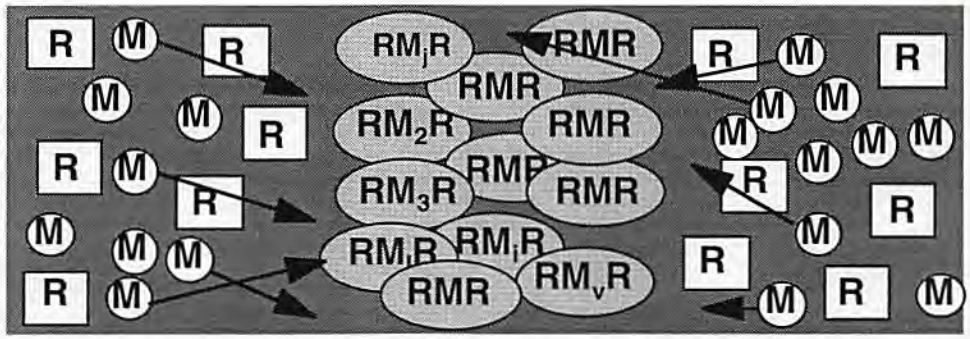

Figure 2-2. Results of photopolymerization. After illumination, there is a concentration of large polymeric molecules localized in the illuminated area. During the process, free monomers diffuse into the monomer depleted area. Thus the free monomer concentration is kept spatially uniform in the medium. $\mathbf{RM_jR}$ is a polymeric molecule linking a number **j** of monomer molecules.

in which ϕ is the overall initiation efficiency of the process (*i.e.* the ratio between the number of separated free radical pairs per number of absorbed photon) which is linked to the process quantum efficiency, I_o is the illumination intensity, $[M]$ is the monomer density (in concentration), $[M\bullet]$ is the total concentration of chain radicals. The coefficients k_p and k_t are the rate constants of chain propagation and termination, respectively. At steady state, the rate of termination must be equal to the rate of initiation; in these conditions ($R_i = R_t$) we can express the above rate equations for the concentration of chain radical and free monomers as [Reiser, 1989]

$$[M\bullet\ ] = \left(\frac{\phi I_o}{k_t}\right)^{\delta}, \text{ and} \qquad (2\text{-}4)$$

$$R_p = \frac{k_p}{2\sqrt{k_t}} (\phi I_o)^{\delta} [M] . \qquad (2\text{-}5)$$

The expression $k_p/2\sqrt{k_t}$ is commonly called the characteristic ratio of the polymeric reaction, and δ is the reaction order, which for the case described here is $\delta = 0.5$. It must be pointed out that the characteristic ratio is not always a constant. Actually in a viscous solution of free monomers with a film binder, such as a DuPont photopolymer, it may increase in time during polymerization. This variation of the characteristic ratio is related to the changing conditions of the material, such as viscosity and temperature, which slow down the termination of polymeric chains (step **(5)**, **(6)** and Eq. 2-3). Therefore with k_t that tends to zero, the characteristic ratio increases in time, originating an autoacceleration of the polymerization rate of the free monomers, [Wei *et al.*, 1989] and [Odian, 1991]. Finally, one must notice that Eq. 2-5, which expresses the rate of polymerization or the rate in which polymers are created, equivalently can be used to define the rate of free monomer disappearance as

$$\frac{d}{dt}[M] = \frac{-k_p}{2\sqrt{k_t}} (\phi I_o)^{\delta} [M] . \qquad (2\text{-}6)$$

2.4 Photpolymerization in DuPont Holographic Photopolymers and Choice of the Experimental Material

The initiator systems are mostly sensitive to light in th UV portion of the spectrum. Differently, for a large number of practical applications, polymer based holographic materials must be sensitive to light in the visible range. To

make photopolymerization happen in the visible range, photopolymers relay on dye sensitized initiation. During this process, the dye is photoexcited in the visible range and then reacts with the initiator system to create free radicals. In the specific case of DuPont photopolymers [Smothers *et al.*, 1990], the photoinitiator system is composed of the light absorbing dye, termed DEAW, a light initiator, hexaarylbiimidazole or more briefly HABI, and a chain transfer agent, 2-mercaptobenzoxazole or more familiarly termed MBO. In this contest, the photopolymerization can be sketched as:

(1) $h\nu$ +DEAW -------> DEAW* Dye excitation

(2) DEAW*+HABI -------> R• Free radical formation

(3) R• + MBO+M -------> RM• Polymeric chain generation

In step **(1)**, the dye is photoexcited, and reacts in step **(2)** with the HABI to generate free radicals. Free radicals, via the chain transfer agent, initiate the polymer chain, step **(3)**.

In dye induced polymerization, the wavelength sensitivity range is related to the dye absorption peak. By doping the polymer with the appropriate dye, it is possible to create a holographic photopolymer sensitive to different wavelength ranges. Fig. 2-3 indicates the transmittance of two kinds of photopolymers, HRF-150-38 and HRF-750-20, that we measured using a spectrophotometer. The HRF-150-38 is an orange colored 38 μm thick film, sensitive in the wavelength range of 450-550 nm. The photospeed of such material, according to the manufacturer data sheet, is approximately 150 mJ/ cm^2 at 514 nm. As depicted in Fig. 2-3 (a), the transmittance spectrum of this

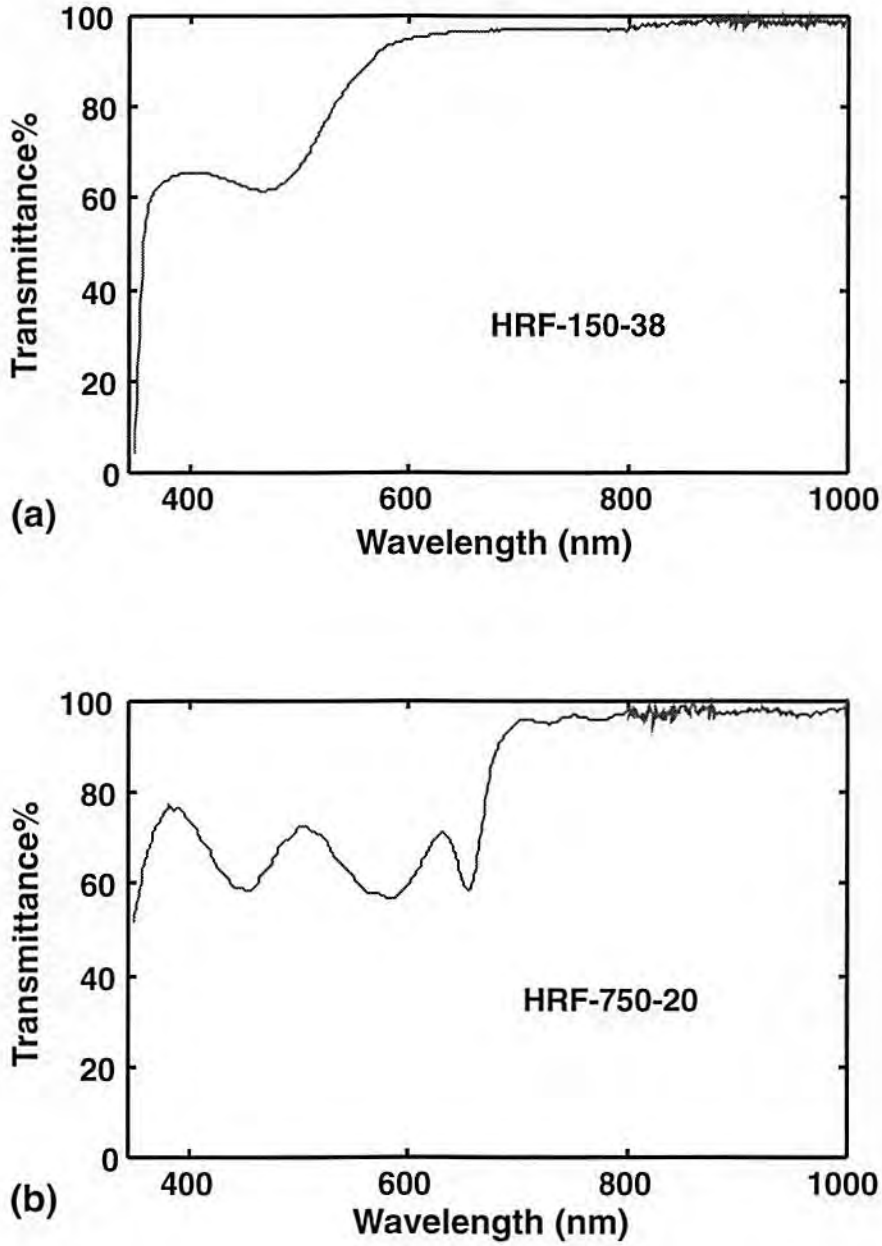

Figure 2-3. Transmittance of HRF-150-38 and HRF-750-20 DuPont holographic photopolymers. **a)** The HRF-150-38 is sensitive in a wavelength range of 450-550 nm and is 38 μm thick. The dye causes an absorption peak with a 61% transmittance at 470 nm. **b)** The HRF-750-20 film is 20 μm thick and suitable for broad wavelength spectrum applications. In this material, the dye-related absorption peaks are located at 476, 532, and 656 nm, with associated transmittance of 56%, 58%, and 56%.

material resembles a high pass filter with a related cut-off wavelength of 350 nm. The dye related absorption peak manifests itself, however, with a local minimum of 61% of transmittance at 470 nm. The film is practically absorption-free from the red wavelength range (600 nm) upward, with a transmittance of nearly 100%.

In contrast to the HRF-150-38, the DuPont HRF-750-20 photopolymer is a gray-colored 20 μm thick material. The reason for the gray color is related to the absorption peaks of the material, shown in Fig. 2-3 (b), which are around the red, green, blue wavelengths, with the consequence that this material is suitable for recording holograms in a broad range of the visible spectrum. The transmittance at the absorption peaks is 58% at 456 nm, 56% at 585 nm, and 58% at 656 nm. According to DuPont indications, the photospeed of the HRF-750-20 is 13, 9, and 17 mJ/cm^2, respectively at 476, 532, and 647 nm, which are considerably less than that of the HRF-150-38. The transmittance of both materials is 0% and 100% respectively in the UV and infrared ranges. In both materials, upon exposure to UV light, the dye is bleached and all the monomers are polymerized. Thereafter, the transmittance spectra of the materials appear exactly as a high pass filters in wavelength, as depicted in Fig. 2-4 which presents the measured spectrum of a sample of HRF-150-38 after UV curing.

We selected the HRF-150-38 as the material to use exclusively during our investigation, and hereafter all the experiments and measurements on photopolymers presented in this thesis we performed using, and are solely relevant to, the HRF-150-38 film. This preference of HRF-150-38 was motivated by to two

main advantages which this material possesses, film thickness and its sensitivity spectrum. The HRF-150-38 film is almost twice as thick as the HRF-750-20, and this makes the HRF-150-38 more suitable for volume hologram applications, such as multiplexed volume holograms, which are among the main interests of this work. Moreover, the fact that the film is not sensitive to red light facilitates monitoring the material characteristics. In fact we may use a readout light source, such a He-Ne laser, to probe the grating formation time during exposure, without altering the grating formation process itself.

Before presenting further experimental results, we would like to emphasize for the reader that there are a variety of possible fluctuations in the photopolymer figures of merit, such as the material thickness, the maximum

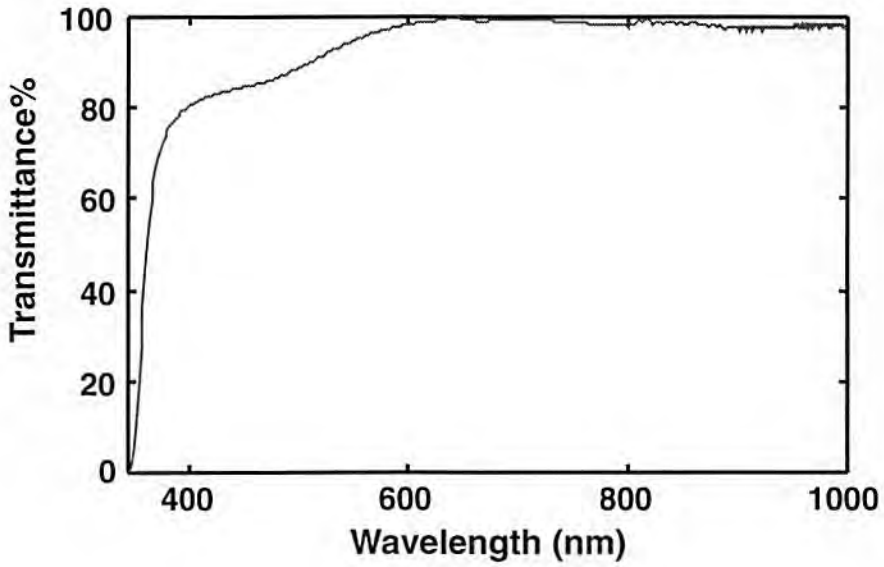

Figure 2-4. Transmittance of HRF-150-38 after UV exposure. After bleaching all the dye and polymerizing all the free monomers, the transmittance spectrum looks like a high pass filter with associated cut-off wavelength of 350 nm.

modulation of the refractive index, and the film photospeed. Moreover aging may affect the material sensitivity. The fluctuations of these values may be reflected as scatter in the experimental data. To reduce the variance of caused by these factor, great care was taken in using material samples belonging to the same foil during experiments of the same nature. In this way, it was possible to reduce fluctuation of the measured data during experiments. Our experiments were not exempt from errors due to the exposure environment. Air fluctuations and vibrations are always present, and they can affect holographic exposures. It is our belief that these two factors are mostly responsible for the spreading of the measured data.

2.5 Grating Formation in Du Pont Photopolymers: The High Free Monomer Diffusion (HFMD) Model

During hologram recording, the material is exposed to a spatially varying interference intensity pattern. As such, a holographic photopolymer material has to be capable of polymerizing according to the geometry of the intensity pattern. As an example, in Fig. 2-5 is depicted the scenario during an exposure of two plane waves. According to the mechanism and concepts introduced in the previous paragraphs, we can describe the holographic grating formation mechanism in photopolymers by the following sequence of processes [Colburn and Haines, 1971], [Smothers *et al.*, 1990]: **(1)** during holographic exposure, the excited dye photoinitiates the formation of free radicals having spatial distribution that follows the illumination pattern; **(2)** the free radicals initiate mono-

mer polymerization (*i.e.*, free monomers are linked to stable polymeric chains), mapping the interference pattern; **(3)** free monomers keep diffusing in the material, until their eventual depletion by polymerization. All the above steps happen simultaneously, and the combination of nonuniform polymerization and free monomer diffusion creates a spatial modulation of the refractive index. Based on these processes, we next introduce our model of the dynamics of single grating formation in photopolymers, which is directly derived from kinetics of the free radical polymerization and variation of the monomer density.

When two coherent plane waves of constant intensity I_1 and I_2, each polarized normal to the plane of incidence, interfere in the material, photopolymerization is initiated and the rate of free monomer consumption is described by [Shultz and Joshi, 1984]

$$\frac{\partial}{\partial t}[M]\,(x,t) = -k_R(t)\,[M]\,(x,t)\,I(x)^{\delta}, \tag{2-7}$$

in which $[M](x,t)$ is the free monomer density, $I(x)$ is the interference intensity pattern, δ is the order of the photochemical reaction, and $k_R(t)$ is a polymerization function, which, equivalently to the characteristic rate coefficient of Eq. 2-5, depends on the ratio of the coefficients k_p and k_t, which are the rate constants of chain propagation and termination. For purposes of modeling the spatially varying component of the refractive index $n(x,t)$, we assume that the combination of all the above described processes (this section steps **(1)** to **(3)**) induce a temporal change in $n(x,t)$ that is proportional to the local rate of creation of the polymers (which is the negative of the rate in Eq. 2-7, as also indicated in Eq. 2-6), as

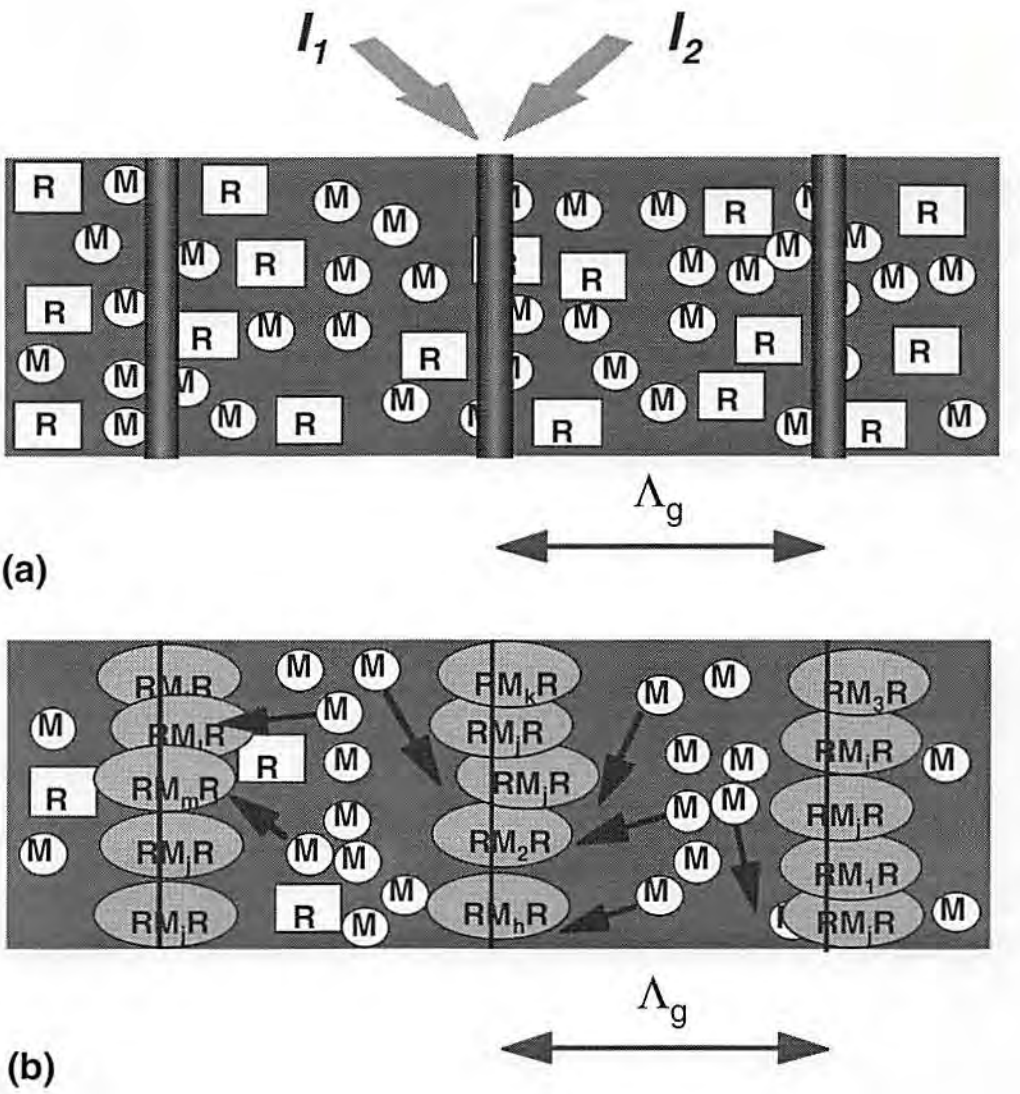

Figure 2-5. Recording of a hologram in photopolymers. **(a)** When two plane wave of intensity I_1 and I_2 interfere in a holographic photopolymer, a sinusoidal interference pattern is created inside the medium. Therefore because of such nonuniform illumination, the photopolymerization itself is not spatially uniform, and is more prominent along the bright fringe peaks. **(b)** After the exposure. The grating modulation is created by the presence of polymeric chains which have been formed along th bright spots. At the same time, free monomer diffusion tends to replace those monomers that have been polymerized in the bright spots. Nonuniform polymerization and monomer diffusion give rise to the holographic grating modulation. **M** stands for free monomer; **R** stands for intitiator system; $\mathbf{RM_jR}$ stands for a polymeric chain composed of a number **j** of monomers; Λ_g is the grating period.

$$\frac{\partial}{\partial t} n(x,t) = c_n k_R(t) [M](x,t) I(x)^{\delta}, \tag{2-8}$$

where c_n is a constant. Solution of Eq. 2-8 through Eq. 2-7 gives the dynamics of the grating formation. To solve these two differential equations, we use certain approximations. We assume that the recording intensity is sufficiently low for the grating formation process to be much slower than the diffusion of the free monomers. We refer to this assumption as the high free monomer diffusion (HFMD) assumption, and the corresponding grating formation model will be termed the HFMD model. Due to this high diffusion rate assumption, $[M](x,t)$ in Eq. 2-8 can be considered uniform in space, because any gradient of the monomer concentration created by polymerization is eliminated by the fast monomer diffusion. The monomer concentration, therefore, can be simplified to its spatial average $[M](t)$. The intensity pattern of the two interfering plane waves can be expressed as

$$I(x) = I_o [1 + m\cos(K_g x)], \tag{2-9}$$

in which $I_o = I_1 + I_2$ is the average recording intensity, $K_g = 2\pi/\Lambda_g$ is the grating wavenumber with the grating period Λ_g, and the term

$$m = \frac{2\sqrt{I_1 I_2}}{I_o} \leq 1 \tag{2-10}$$

is the beam intensity modulation.

Once the spatial intensity pattern is expressed as a sinusoid, we can write the intensity term $I(x)^{\delta}$ of Eq. 2-8 in term of a binomial expansion:

$$I(x)^{\delta} = I_o^{\delta}\left(1 + m\delta\cos(K_g x) + m^2\frac{\delta(\delta-1)}{2!}\cos^2(K_g x) + HOT\right) \qquad (2\text{-}11)$$

where *HOT* is the acronym for higher order terms. For $m < 1$ and $\delta m < 1$ (which, we experimentally will demonstrate, as shown later in the chapter, that is always true), we can approximate the above with the only two terms of such expansion:

$$I(x)^{\delta} \approx I_o^{\delta}\,[1 + m\delta\cos(K_g x)]\,. \qquad (2\text{-}12)$$

Substituting Eq. 2-12 in Eq. 2-8, we can approximate the refractive index modulation (or grating modulation) as a sinusoid whose amplitude evolves in time as

$$\frac{d}{dt}\Delta n(t) = m\delta c_n k_R(t)\,[M](t)\,I_o^{\delta}\,. \qquad (2\text{-}13)$$

The time derivative of $[M](t)$ can be obtained by retaining the D.C. term of the spatial Fourier series expansion of Eq. 2-7, thus

$$\frac{d}{dt}[M](t) = -k_R(t)\,[M](t)\,I_o^{\delta}\,. \qquad (2\text{-}14)$$

The equations 2-13 and 2-14 are fundamental to the description of the single grating formation under the high free monomer diffusion hypothesis. Given the initial condition $[M](0) = [M]_o$ and $\Delta n(0) = 0$, the problem of the grating formation can be now solved, yielding

$$[M](t) = [M]_o \exp\left(-I_o^{\delta}\int_0^t k_R(\tau)\,d\tau\right), \qquad (2\text{-}15)$$

$$\Delta n\,(t) \;=\; m\Delta n_M\Big[\,1-\exp\Big(-I_o^{\delta}\textstyle\int_0^t k_R\,(\tau)\,d\tau\Big)\Big]\,, \qquad (2\text{-}16)$$

in which $\Delta n_M = c_n\delta[M]_o$ is the maximum available modulation index. Because $k_R(t) > 0$, at saturation $(t = \infty)$ $[M](\infty) = 0$.

Even if still general in their writing, a careful reading of the above two equations can lead to a number of significant physical insights. At saturation, the index modulation, Δn_{sat}, is independent of I_o,

$$\Delta n_{sat} \;=\; m\Delta n_M\,, \qquad (2\text{-}17)$$

where for saturation we indicate the point in the process in which there is no increase of refractive index modulation, because all the free monomers have been polymerized, and consequently the exponential term in the Eq. 2-15 and 2-16 is equal to zero. Interestingly, the HFMD model solution of the Eq.2-16 indicates that at saturation the beam intensity modulation m is the only external variable that can affect and control the value Δn_{sat}. In contrast, I_o controls the temporal evolution of the grating formation. For example, when recording with the same m but different I_o, the grating modulations will exhibit different time dependencies but equal saturation value of grating modulations. These basic reasonings suggest a number of experiments whose results confirm and enrich our theoretical findings. These experiments are therefore presented in the next section.

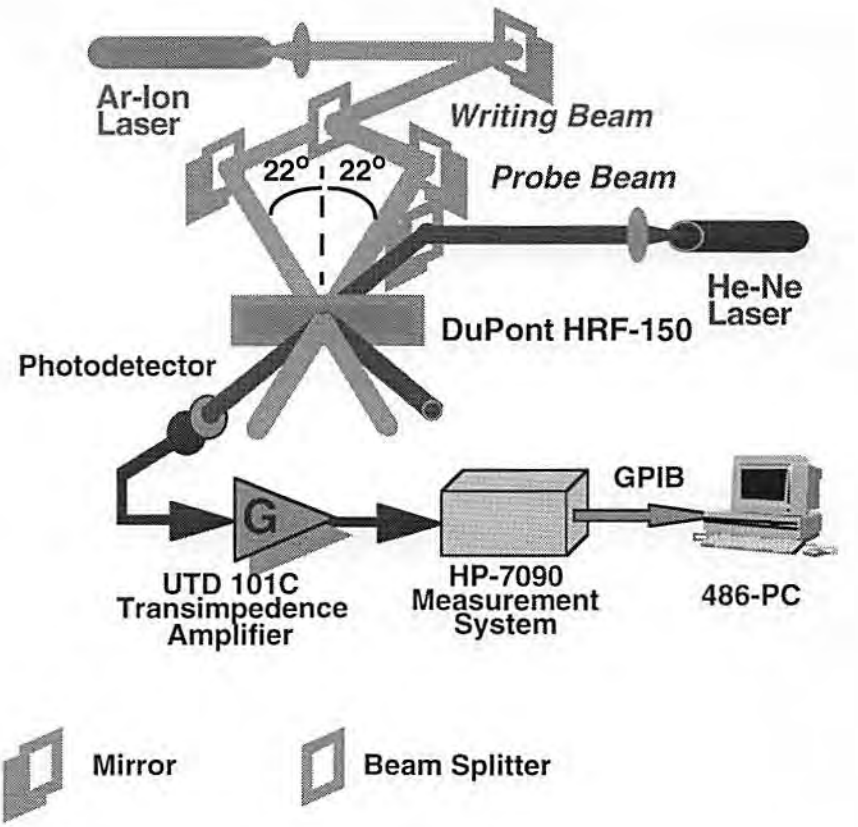

Figure 2-6. Schematic representation of the experimental set-up used during the measurements of the grating formation HRF-150-38 photopolymers. Two beams, with a wavelength $\lambda = 514$ nm, generated by an argon-ion laser write a diffractive grating. A He-Ne laser generates a red probe beam ($\lambda_p = 633$ nm), which reads out the diffractive grating in real time. The probe beam does not interfere with the writing process because the photopolymer initiator system is not sensitive to the red light. The probe zero order variations are read by a photodetector, amplified, and stored in a computer, which automatically converts the reading to diffraction efficiency values.

2.6 Experimental Set-Up Description

To validate experimentally our theoretical findings a number of transmission holograms in DuPont HRF-150-38 photopolymer were exposed and monitored, as sketched in Fig. 2-6. An argon-ion laser (wavelength $\lambda = 514$ nm)

supplied the two recording beams, which were polarized normal to the incidence plane. The recording beams were symmetrically interfering with a Bragg angle from the normal to the of holographic plate of 22° in air. The Bragg angle is the angle required to a readout beam to maximize the diffraction efficiency during readout, which is (usually) the same when beams with the same wavelength are used for recording and readout. As previously shown in Fig. 2-3 (a), the initiator system of the material is not sensitive to the red light. Therefore a Bragg-matched beam from a HeNe laser (λ_p = 633 nm) was used to monitor the diffraction efficiency, by reading the evolution of the diffraction efficiency of the light diffracted by the forming transmission grating. According to the results of the coupled wave theory, the temporal evolution of the measured diffraction efficiency $\eta(t)$, (where $\eta(t)$ indicates the ratio of the intensity of the first diffracted order to the total output intensity, which is the sum of the intensity of the zero and the first diffracted order) is

$$\eta(t) = \sin^2[\pi \Delta n(t) T / (\lambda_p \cos(\theta_p))], \qquad (2\text{-}18)$$

in which T is the material thickness (38 μm) and θ_p is the Bragg angle of the He-Ne probe beam.

2.7 Recording with Beam Intensity Modulation as a Variable: Theoretical and Experimental Results

A first set of exposures was carried out to verify the relation between the beam intensity modulation m and the diffraction efficiency, as described in Eq.

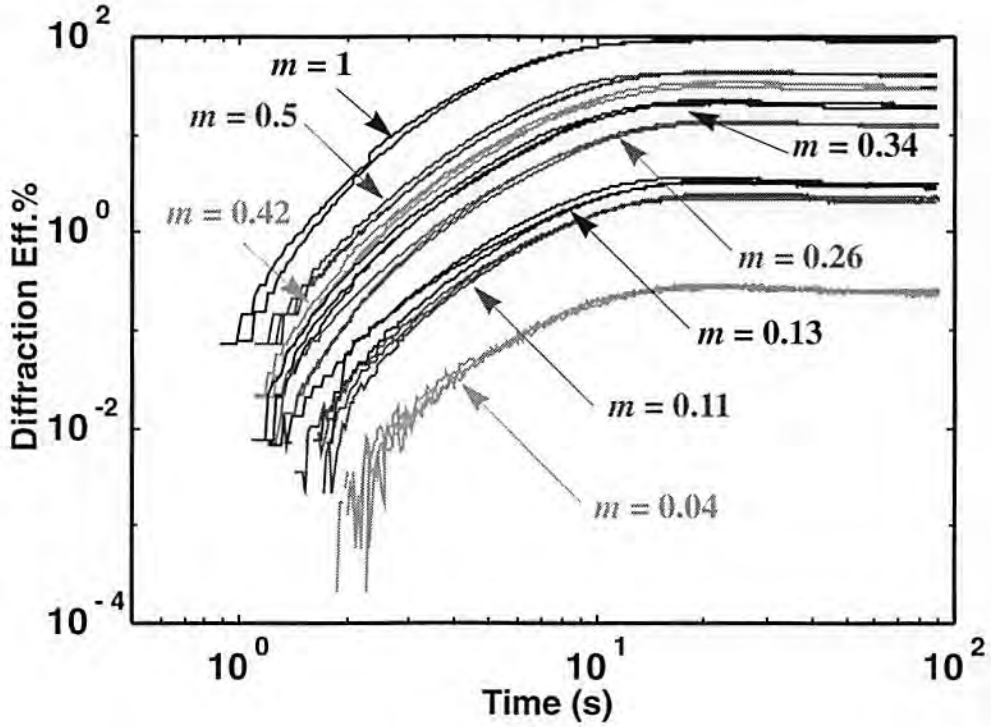

Figure 2-7. Experimental grating formation in holograms recorded with I_o = 81 mW / cm^2, and beam modulation intensity varying as: m = 0.04, 0.11, 0.13, 0.26, 0.34, 0.42, 0.5, and 1. Three curves for each value of m are plotted in the figure.

2-15, Eq. 2-16, and Eq. 2-17. During each exposure, the average recording intensity was kept constant as I_o = 81 mW/cm^2, and the beam intensity modulation was varied according to values m = 0.04, 0.11, 0.13, 0.26, 0.34, 0.42, 0.5, and 1. Three exposures were monitored and recorded for each value of m, and the relative data are plotted in Fig. 2-7. Each of the curves in the figure exhibits how the material experiences first an inhibition period of the duration of almost a second. The nature of the inhibition period will be analyzed later in the next section. Then there is the temporal response to the recording exposure with the grating formation, as demonstrated by the increasing diffraction efficiency.

To confirm and compare the HFMD model derivations with the above experimental measurements, we consider two aspects of the grating formation: the time evolution and the saturation. All the curves have the same average recording intensity $I_o = 81$ mW/cm^2. Therefore, according to Eq. 2-15 and Eq. 2-16, the time evolution of the modulation term of refractive index, once normalized by multiplicative term $m\Delta n_M$ must have the same exponential dependency $f(t)$ as:

$$f(t) = 1 - \exp\left(-I_o^{\delta}\int_0^t k_R(\tau)\,d\tau\right). \tag{2-19}$$

Such time evolution dependency is depicted in Fig. 2-8, where the function $f(t)$ is plotted by extraction from four different curves of Fig. 2-7. Each curve in Fig. 2-8 corresponds respectively to a different value of the modulation term as $m = 1$, 0.43, 0.11, and 0.04. For the sake of clarity in the graph, we show only one curve for each m. All the curves appear formally identical and share the same inhibition time, same saturation time (approximately 20 s) and same exponential evolution. This temporal behavior of the exponential term that governs the time evolution of the grating formation is therefore solely dependent on the average recording intensity and does not depend on m, which is a confirm of what is theoretically indicated in Eq. 2-16.

The diffraction efficiency at saturation is determined by the beam intensity modulation. According to Eq. 2-17 and 2-18, the diffraction efficiency at saturation must be solely a function of the beam intensity modulation as

$$\eta_{sat} = \sin^2(m\beta)\,, \tag{2-20}$$

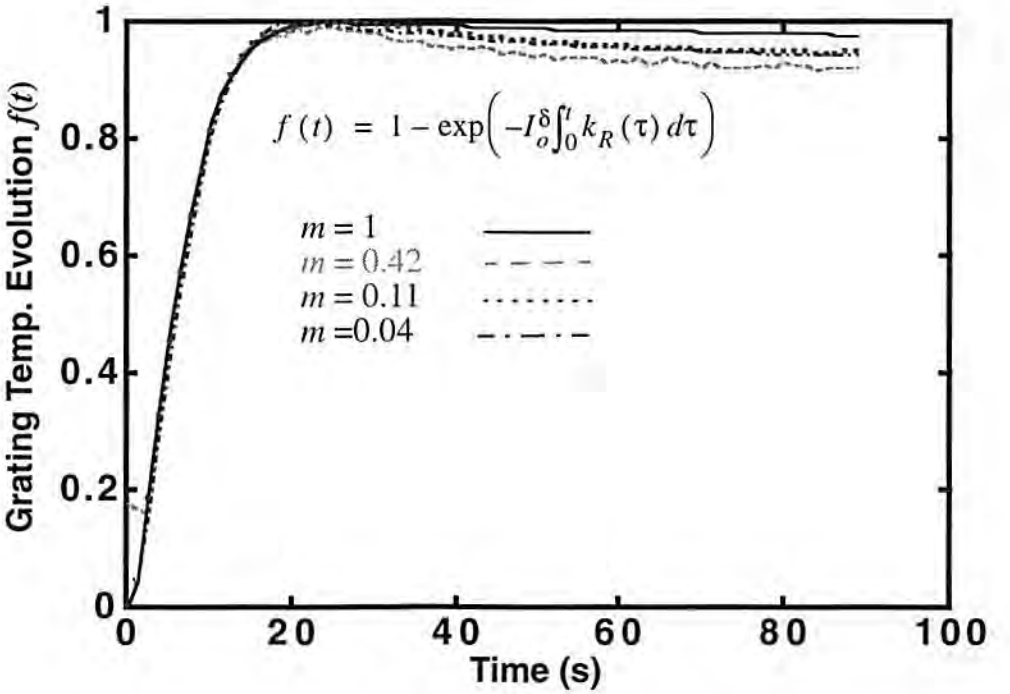

Figure 2-8. Grating temporal evolution. After normalization by $m\Delta n_M$, the exponential term governing the index modulation temporal evolution, $f(t)$, has to be independent of the beam intensity modulation m, as indicated in Eq. 2-16. In the picture are plotted four curves describing the function $f(t)$, which are extracted from four corresponding curves in Fig. 2-7. These curves have distinct values of m = 1, 0.42, 0.11,and 0.04.

in which $\beta = \pi\Delta n_M T/\lambda_p \cos(\theta_p)$ is a constant describing the recording condition and the material. After calculating β from the measurements for $m = 1$ (β = 1.34), the theoretically predicted and experimentally measured values of the saturation diffraction efficiency (with m as a variable) are plotted in Fig. 2-9, indicating agreement over two orders of magnitude of m. This last result is an important one, because it allows us to map at the system level the relation between an input signal, intended as beam intensity modulation, and an output

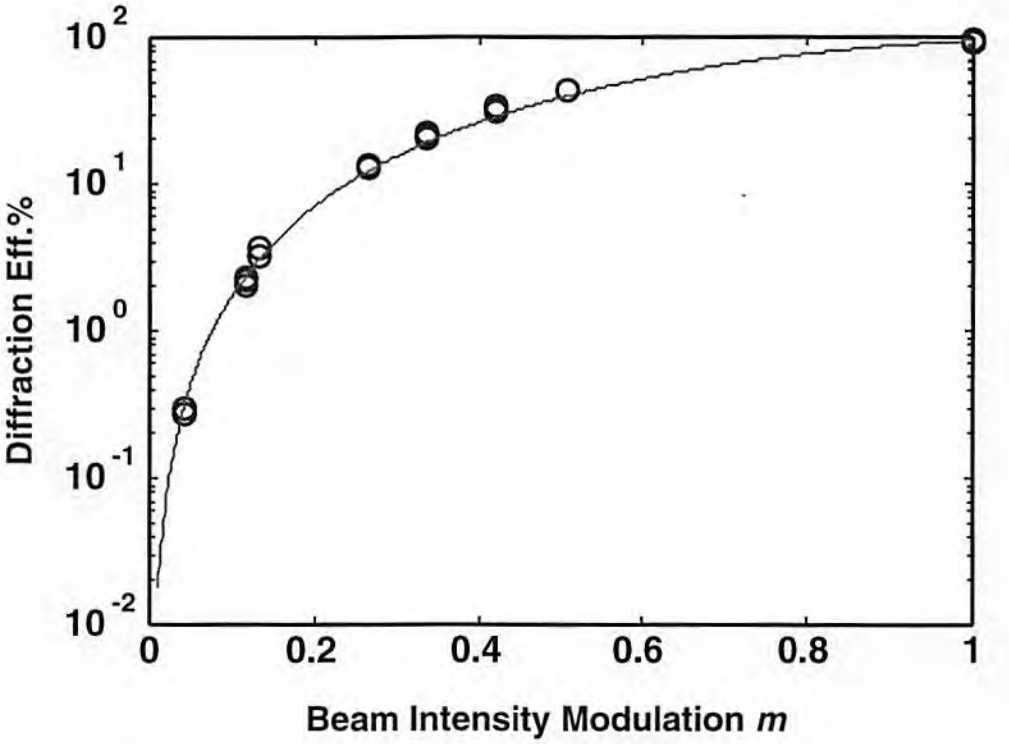

Figure 2-9. Comparison of experimental (open circles) and theoretical (solid curve) saturation diffraction efficiencies. The exposures have the same average recording intensity, $I_o = 81$ mW/cm^2, and beam intensity modulation m as a parameter. Such relationship between m and the saturation diffraction efficiency can be used at system level to map an input signal (m) to an output signal (saturation diffraction efficiency), in architectures using holographic interconnections or holographic memories.

signal intended as saturation diffraction efficiency. This input/output mapping can be thought of as the building block for a signal representation scheme using holographic photopolymers, and it will be used extensively in our copying architecture as described later.

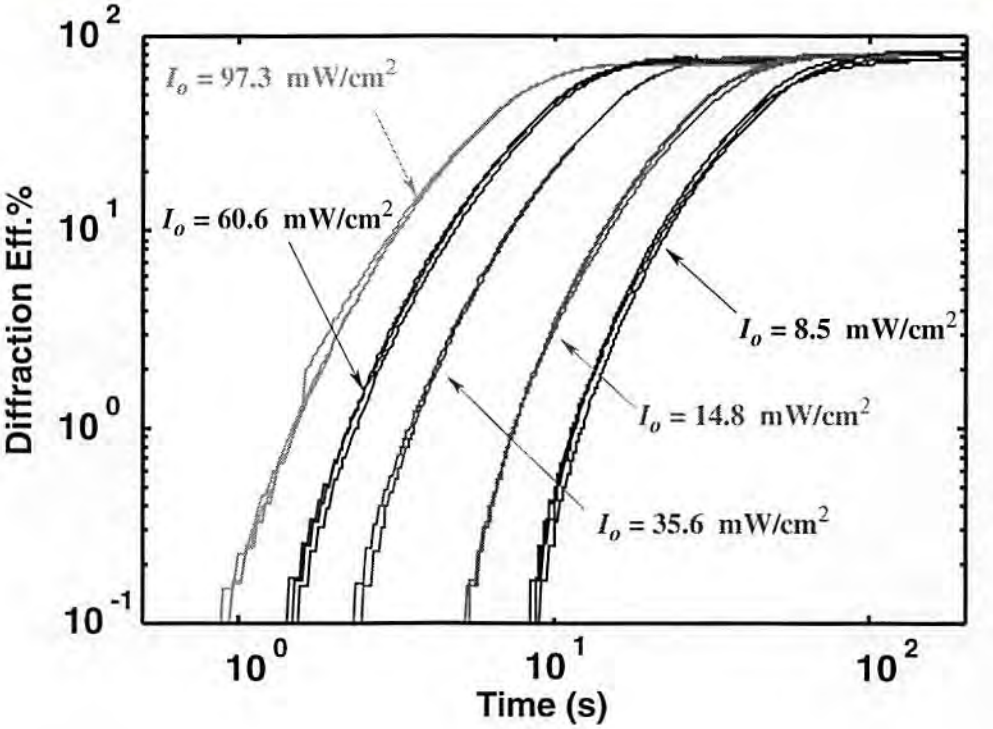

Figure 2-10. Experimental grating recording in HRF-150-38. The exposures where recorded with $m = 0.8$ and the average recording intensity I_o as a parameter, I_o = 8.5, 14.6, 35.6, 60.6, 97.3 mW/cm^2 (from right to left). Three recordings are reported for each value of average recording intensity. While each curve has a different temporal evolution, their saturation diffraction efficiencies have approximately the same value. This last result confirms that under the high monomer diffusion hypothesis, saturation diffraction efficiency is independent of the average recording intensities I_o, once the intensity beam ratio is fixed.

2.8 Recording with Average Recording Intensity as a Variable: Theoretical and Experimental Results

As stated by the result of the HFMD model solutions of Eq. 2-15 and Eq. 2-16, the average recording intensity is responsible for the time evolution of the grating modulation. A different set of experiments was carried out to characterize the time dependence of the grating formation during holographic exposure. This set of exposures consisted of writing a number of holograms at constant

beam intensity modulation $m = 0.8$, with the average recording intensity I_o as parameter. Three separate recordings were made for each value of I_o, as plotted in Fig. 2-10. In basic agreement with the predictions of Eq. 2-17, and Eq. 2-20, we measured $\eta_{sat} = 71.9 \pm 0.5$, 75.3 ± 2, 75 ± 3, 80 ± 3, 79 ± 4 (the values are in%, and the variations refer to the variance around the measured average value of η_{sat}), for $I_o = 97.3$, 60.6, 35.6, 14.8, 8.5 (mW/cm^2), respectively, indicating that η_{sat} is approximately independent of I_o, even if there is a detectable trend of a decreasing η_{sat} with an increasing I_o. This trend is due to the fact that a higher average recording intensity implies that the HFMD assumption is weaker, and a variation of results from the theory may be noticeable. Another interesting observation is that at lower recording intensity there is higher variation in saturation diffraction efficiency. Such a variation of the measured data may be caused by the recording noise. In fact, a longer exposure time corresponds to a lower recording intensity, which may integrate a larger amount of recording noise due to the environment. The result is a larger fluctuation of the measured data.

Upon holographic exposure, the material exhibits three phases. First, there is an induction time period (not included so far in our model), in which the material does not respond to the recording energy (diffraction efficiency is zero), as shown by Fig. 2-10. Next, grating formation occurs, in which the diffraction efficiency grows until a saturation value is reached. Finally, after saturation, all the monomers are all polymerized, and the diffraction efficiency value (almost) no longer changes from the saturation value. Significantly, an analysis of the data from this set of experiments allows us to characterize the

first two phases and determine the physical parameters that affect the temporal evolution of the grating formation process such as the reaction order δ and the grating formation time constant. This analysis is therefore presented in the next section.

2.9 Characterization of the Grating Formation Process Phases

The aim of this section is to analyze the data of Fig. 2-10, and to find the all the necessary information which allow us to characterize the grating formation process under the HFMD hypothesis. In order to have a (possible) closed form expression for the model, it is required to determine the reaction order δ, and the polymerization function $k_R(t)$. Consequently, the following subsections are mainly dedicated to such determination of $k_R(t)$ and δ. The first topic to be treated in the subsection, however, is the characterization of the inhibition time, which is not part of the HFMD model per se, but is inherent to the photopolymerization process itself.

2.9.1 Determination of the Inhibition Period

It is typical to observe an inhibition period preceding polymerization in almost every polymerization process. The origin of such phenomenon is related to the presence of free radical scavengers (S) in the material. Radical scavengers can be thought as impurities of varied nature (stabilizers, antioxidants, and mainly oxygen [Reiser, 1988]) which, upon illumination and in competition

with free monomers, react with free radicals forming other nonreactive molecular specimens. These nonreactive molecular specimens do not contribute to the initiation of the polymerization, and the rate of their creation is approximately proportional to the rate of creation of free radicals, as indicated by the following the reaction

$$R\bullet + S \text{ --------> } \text{nonreactive products.}$$

As result of the action of these radical scavengers, photopolymerization is inhibited because of the lack of free radicals which tend to react with the free monomers. Because the rate of production of nonreactive products is much larger that rate of reaction between free monomers and free radical [Reiser, 1988], photopolymerization can begin only after an inhibition time period, which is the time necessary to eliminate, by reaction with free radicals, the radical scavengers existing in the material. For a given initiator concentration, the rate of formation of free radicals, Eq. 2-1, is proportional to the intensity of the illumination. Therefore, if we suppose a constant rate of production of nonreactive products due to the reaction between free radicals and scavengers, the duration of the inhibition period, Δt_i, is inversely proportional to the average recording intensity as

$$\Delta t_i = \frac{A_o}{I_o}, \tag{2-21}$$

in which A_o is a material dependent constant.

Fig. 2-11 indicates the measured inhibition periods (o) related to average recording intensity, as extracted by the experimental curves of Fig. 2-10. In this

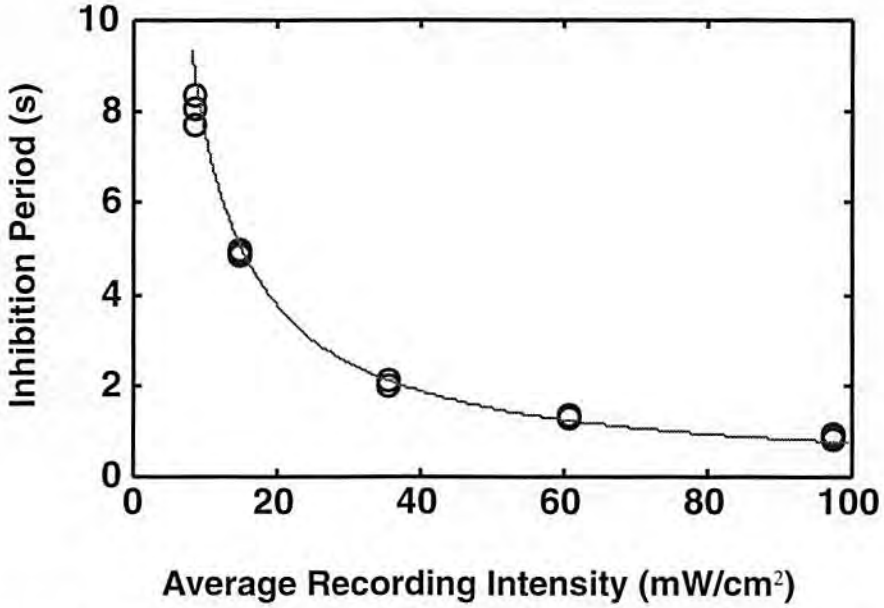

Figure 2-11. Functional dependence of the inhibition period. The inhibition time is inversely proportional to the average recording intensity. Above are plotted the inhibition time measured during the set of recordings of Fig. 2-10.

figure the solid line expresses the relation in Eq. 2-21, with an associated average value $A_o = 75.1$ mW•s/cm^2, which has been estimated over all the exposures of Fig. 2-11. Because of this precise relationship, the grating formation time delay, caused by the inhibition period, is not a concern during hologram recording. It can be either easily estimated, once A_o and the average recording intensity associated with the writing beams are known, by taking into account during the exposure time, or it can be eliminated by pre-exposing the material with the required amount of radiation energy (not necessarily of coherent nature), so as to generate the initiation, the reaction, and the elimination of the radical scavengers as nonreactive final products.

2.9.2 Grating Formation Phase, and the Determination of the Reaction Order δ

After the inhibition period, the material starts responding to the holographic exposure, and the refractive index modulation starts increasing. If we consider the initial grating formation period, for small initial growths of $\Delta n(t)$, the free monomer concentration and the characteristic coefficient can be considered constant, $[M](x,t) \approx [M]_0$, and $k_R(t) \approx k_R(0)$, which corresponds to the hypothesis of small depletion of free monomers and unchanged physical condition of the material [Bjorklund *et al.*, 1980], [Torodov *et al.*, 1984]. Therefore we can rewrite, after the Eq. 2-13, the initial growth rate of the modulation of the refraction index as

$$\frac{d}{dt}\Delta n(t) = C_1 I_o^{\delta} , \qquad (2\text{-}22)$$

in which $C_1 = c_n m \delta [M]_0 k(0)$ is a constant depending on the material characteristics and the beam intensity modulation. By solving the above equation, describing the initial small increments of refractive index modulation, it shows that the temporal evolution of $\Delta n(t)$ has to be linearly dependent on time as

$$\Delta n(t) = C_1 I_o^{\delta} t , \qquad (2\text{-}23)$$

in which the value $C_1 I_o^{\delta}$ is the slope of the line or the grating growth rate. For a given m, the grating growth rate is solely dependent on the external variable I_o.

This finding is experimentally confirmed by Fig. 3-12, where in (a) the

temporal evolution of the refractive index modulation is plotted for five different recordings of Fig. 2-10, one for each value of average recording intensity I_o. Figure 3-12 (a) confirms that in each recording, after the inhibition period, the grating modulation begins with an initial *quasi* linear growth. Such linear behavior then changes to exponential, and the modulation of the refraction index reaches saturation values of Δn_{sat} = 0.0055-0.0062. The analysis of this initial linear growth leads to determination of the reaction order δ, which was done as it follows.as shown in Fig. 2-12 (b). First, we considered, for the different recordings of Fig. 2-10, the diffraction efficiency value range $0 \leq \eta \leq 1\%$. Next, from the different recordings in that value range we extracted the initial grating growth rates $C_1 I_o^{\delta}$. Then, we plotted the measured values of the initial grating growth rate $C_1 I_o^{\delta}$, having as abscissa, in logarithmic scale, the average recording intensity, Fig.2-12 (b). In this figure, the reaction order δ is the slope of the interpolating line. By least-square fit of the data in Fig.2-12 (b), we found the value of the reaction order $\delta = 0.74 \pm 0.01$, which we will use through the rest of this dissertation.

2.9.3 Determination of the Polymerization Function $k_R(t)$

Having experimentally found the value of the reaction order δ, the only unknown part of the HFMD model is the function $k_R(t)$. As already indicated, the function $k_R(t)$ physically depends on the ratio between the polymerization rate constant and the termination rate constant as in the characteristic ratio of Eq. 2-5. In viscous polymers with a polymeric binder, such as DuPont photo-

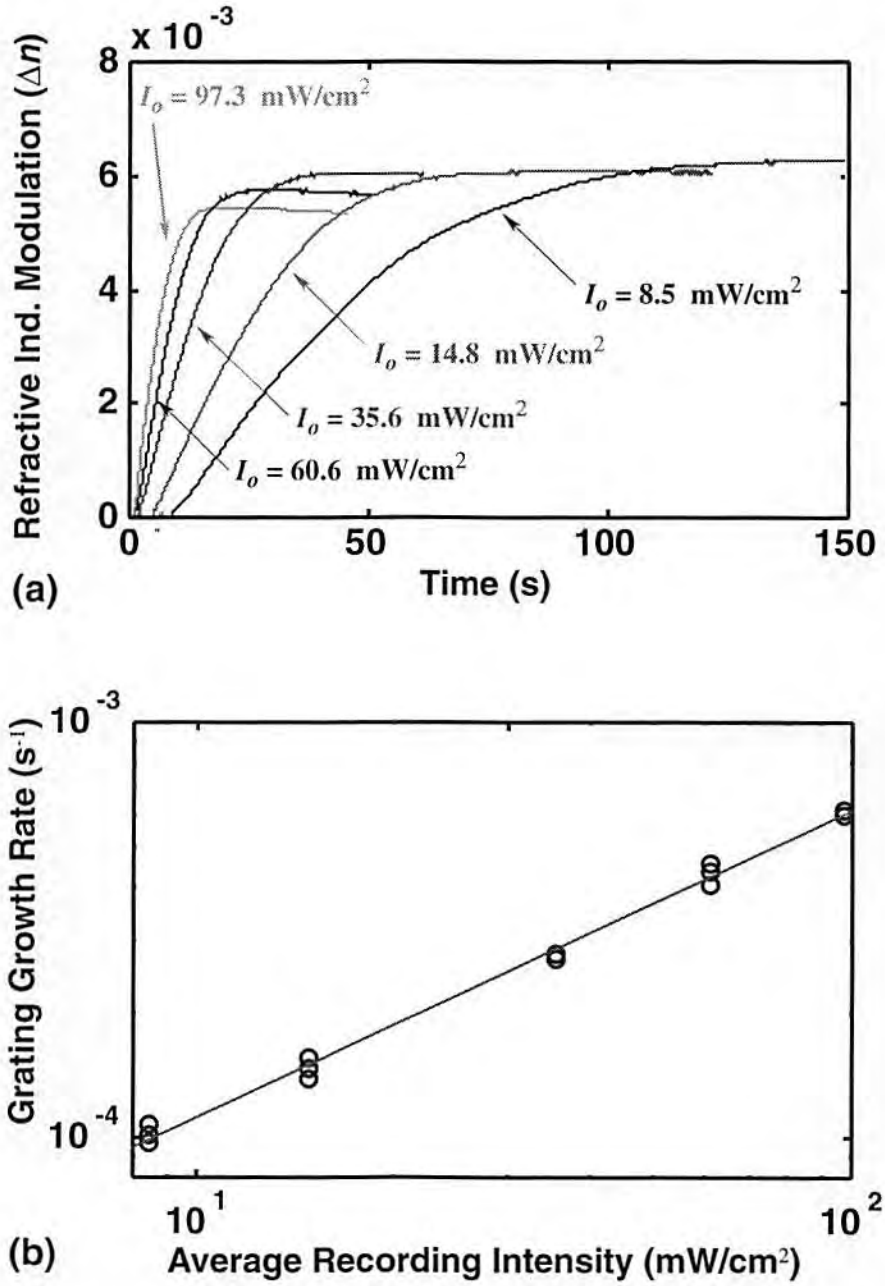

Figure 2-12. **(a)** Temporal evolution of the refractive index modulation. Each curve corresponds to a different value of average recording intensity, having constant $m = 0.8$. The curves present an initial linear phase, and then the reach saturation with an exponential like behavior. **(b)** Determination of the reaction order δ. In logarithmic scale are indicated the value of the initial growth rate of the index modulation (o) vs. average recording intensity. According to Eq. 2-23 the slope of the interpolation line indicates the value of the reaction order. From the above data, least-square fit gives $\delta = 0.74 \pm 0.01$.

polymers, the material experiences during polymerization a number of changes of its status (viscosity, temperature). Particularly, material viscosity increases during photopolymerization, which leads to a dramatic reduction of the termination process and the of the termination coefficient k_t [Reiser, 1989]. As result of this progressive decrease of k_t, the characteristic ratio increase during photopolymerization, which is reflected in an increment of $k_R(t)$ in time. A general analytical expression of $k_R(t)$ is unknown. Moreover, different polymers behave differently; however, a way to determine a functional dependency of $k_R(t)$ is by proper analysis of the data of Fig. 2-10 collected during exposure. To accomplish this goal, we followed this procedure. First, from the experimental curves of Fig. 2-10 we have extracted the normalized time evolutions of the different modulation terms, $f(t)$, from the measurements, as

$$f(t) = 1 - \exp\left(I_o^{\delta} \int_o^t k_R(\tau)\, d\tau \right), \tag{2-24}$$

where $f(t)$ depends on the average recording intensity. Therefore a different time evolution of $f(t)$ is expected for different values of I_o. Next, we have isolated the time evolution of the argument of the exponential in Eq. 2-24, $I_o^{\delta} \int_o^t k_R(\tau)\, d\tau$. The different time evolutions, $I_o^{\delta} \int_o^t k_R(\tau)\, d\tau$, are shown in Fig. 2-13, where there are three curves for each of the different values of I_o, relevant to the time interval where $f(t)$ is confined in the range $0 \leq f(t) \leq 0.9$. Among the different functional dependencies that were tested (linear, quadratic) to characterize those curves in Fig. 2-13, the best agreement was obtained using the exponential form

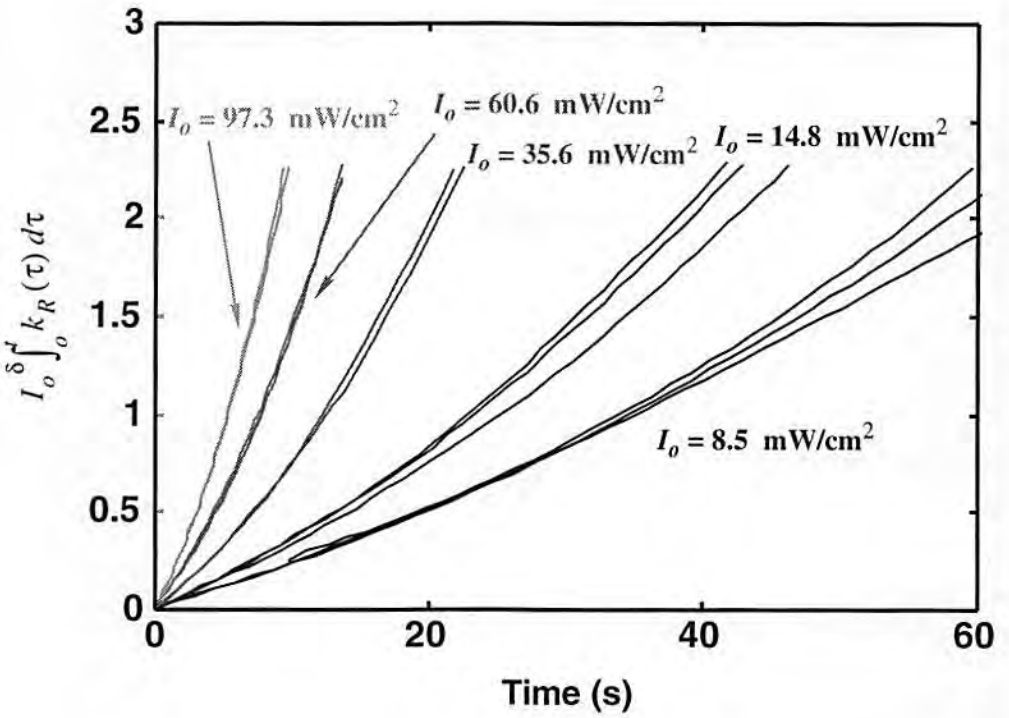

Figure 2-13. Plots of the integral form $I_o^{\delta}\int_o^t k_R(\tau)\,d\tau$. Three curves for each average recording intensity are depicted. The beam intensity modulation term is constant, m =0.8. For the purpose of modelling the function $k_R(t)$, each of the above curves are approximated as an exponential. An optimization routine is used to find the relevant parameters. The inhibition period is omitted.

$$c_1\,(1-\exp(c_2 t)) \;=\; I_o^{\delta}\int_o^t k_R(\tau)\,d\tau\,, \qquad (2\text{-}25)$$

in which c_1 (dimensionless) and c_2 (s^{-1}) are constants. The determination of these two constant yielded crucial results for the characterization of $k_R(t)$.

An optimization procedure was run to find the optimum matching values for c_1 and c_2. This procedure consisted of minimizing the normed value of the difference between the measured data and the exponential curve (RHS of Eq. 2-25), for each single experimental curve (three curves for each values of I_o). The

unconstrained optimization routine 'fmins' in MATLAB [MATLAB, 1992] was used for such procedure. The obtained data for c_1 are depicted in Fig. 2-14 (a). The interesting property about the distribution of the data of c_1 is that these values are independent of I_o, and they appear to be localized around an average value $<c_1>$ =1.52. If we assume c_1 to be constant with varying average recording intensity, this consequently implies that c_2 must be dependent on I_o as $c_2 = \varphi I_o^{\delta}$, with φ constant (dimensionally $[s(mW/cm^2)^{\delta}]^{-1}$) and $\delta = 0.74$. The c_2 values are indicated in Fig. 2-14 (b), where the circles indicate c_2 values obtained during the optimization routine, and the solid curve represents the best matching$c_2 = \varphi I_o^{\delta}$ for an optimum $\varphi = 0.0032$ (dimensionally [s(mW/cm2)d]-1). Again, the unconstrained optimization routine 'fmins' in MATLAB was used for determining φ from the data in Fig. 2-14 (b). As a result, we can express the function $k_R(t)$ as

$$k_R(t) = k_o \exp\left(\varphi I_o^{\delta} t\right), \tag{2-26}$$

where $k_R(0) = k_o = \varphi<c_1>$, and $\varphi = 0.0032$ is a constant.

Before we use such a result to determine the grating dynamics in closed form, we must remind the reader that these findings are strictly relevant to the HR-150-38 photopolymer. Different photopolymer materials from DuPont (or other manufacturers) should be expected to show different behavior when exposed, and therefore a specific analysis about the functions $f(t)$ and $k_R(t)$ must be undertaken when working with different materials. In this subsection, however, we have shown a methodology that can be applied to the characterization of different photopolymers. Moreover, we must consider that photopolymeriza-

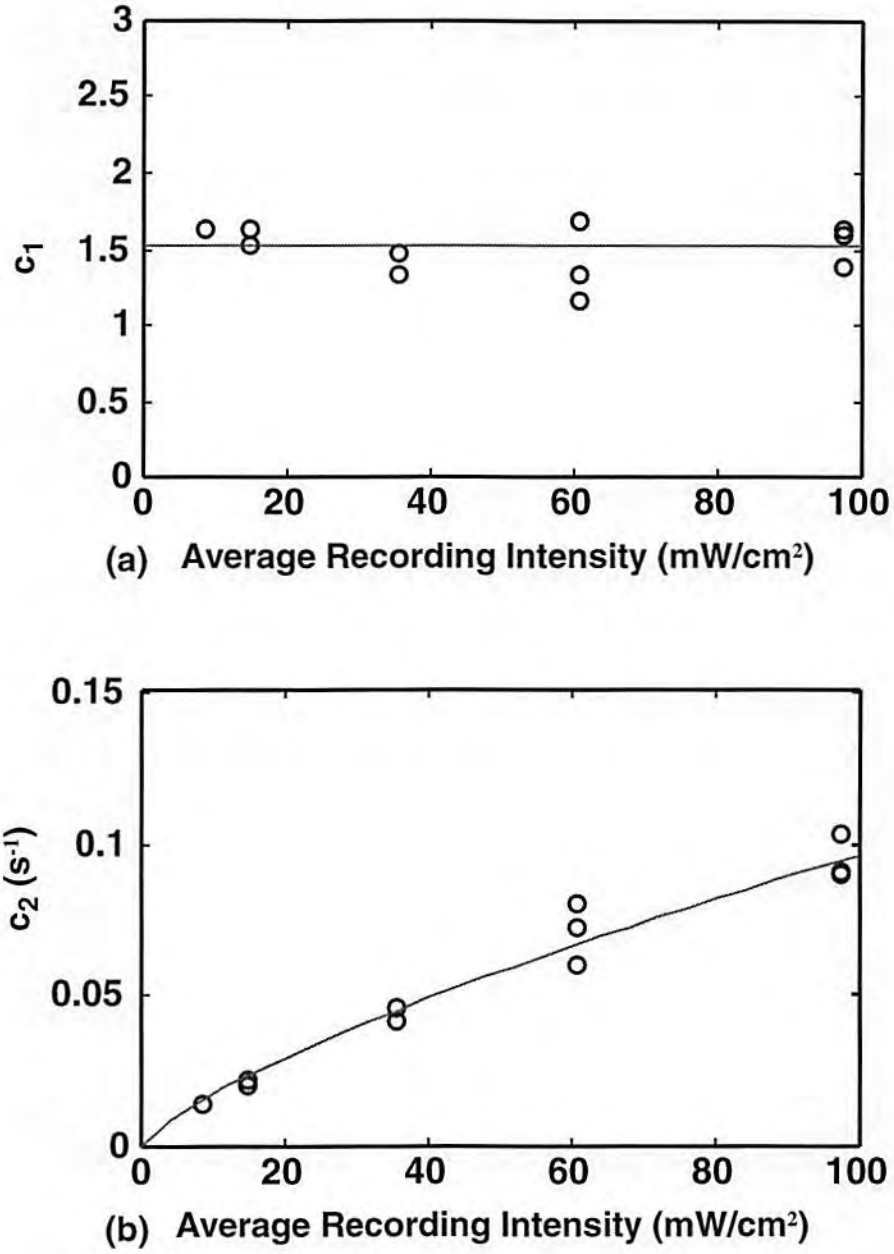

Figure 2-14. Determination of the parameters c_1, and c_2. (**a**) The optimized values of the parameter c_1 (circles) appear to be independent of the average recording intensity, I_o, with an average value $< c_1 > = 1.52$ (solid line). (**b**) The optimized values of the parameter c_2(circles) are I_o dependent. The solid curve corresponds to the fit $c_2 = \varphi I_o^{\delta}$, with $\varphi = 0.0032$ (dimensionally $[s(mW/cm^2)^{\delta}]^{-1}$).

tion can be sensitive to a number of different external variables, such as temperature and recording wavelength. The understanding the dependency of $k_R(t)$ on such variables may represent an interesting material for future investigations.

2.9.4 Grating Formation Phase and the Prediction of the Grating Time Dynamics

Once we have determined the reaction order δ, and the function $k_R(t)$, we can express in closed form the temporal evolution of the refractive index modulation. After substituting into Eq.2-13 and Eq. 2-14 the functional dependency of $k_R(t)$, given by Eq. 2-26, we can derive the solution of the differential equations which describe the free monomer depletion, and formation of the refraction index modulation, respectively as

$$[M]\,(t) \;=\; [M]_o \exp\left[\gamma\left(1 - \exp\left(t/\tau\right)\right)\right] \tag{2-27}$$

$$\Delta n\,(t) \;=\; m\Delta n_M \left\{1 - \exp\left[\gamma\left(1 - \exp\left(t/\tau\right)\right)\right]\right\}, \tag{2-28}$$

in which $\gamma = 1.52 = k_o/\varphi$is a positive constant responsible for the time evolution, $\tau = (\varphi I_o^{\delta})^{-1}$ is a time constant, the inverse of which (not surprisingly, as also seen in [Curtis and Psaltis, 1994]) depends sublinearly on the average recording intensity.

A significant consequence of the closed form expression of the temporal evolution of the grating modulation is shown in Fig 2-15. Here the curves in Fig. 2-10 are plotted using a 'pseudoexposure' variable defined as $I_o^{\delta}t$ [dimensionally $(\mathrm{mW}/\mathrm{cm}^2)^{0.74}\mathrm{s}$] as the new abscissa, which is proportional to the

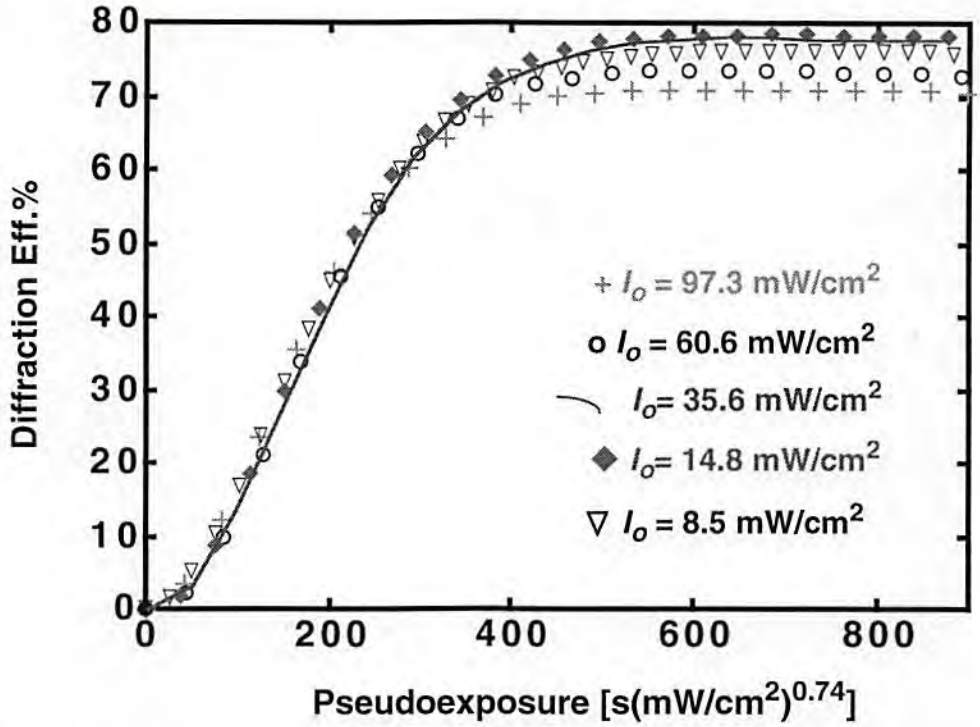

Figure 2-15. Experimental diffraction efficiency of holograms recorded with $m = 0.8$ and I_o as a parameter. The data are plotted using as abscissa the pseudoexposure $I_o^{\delta} \cdot t$, dimensionally corresponding to $(mW/cm^2)^{0.74}s$. For the sake of better visualization only one recording for each value of I_o is shown.

recording time normalized by the time constant. In agreement with theory all the curves look alike, confirming the dependence of τ on I_o given above.

Another result of Eq. 2-28 is that, once the parameters γ and τ have been extracted from a curve at a given I_o, the time evolution of η at any other I_o can be predicted by appropriately scaling $\tau = (\varphi I_o^{\delta})^{-1}$. This principle is shown in Fig. 2-16. We first extracted $\tau = 13.7s$, from the curves recorded at $I_o = 97.3$ mW/cm^2 by minimizing the sum of the absolute values of the difference between experimental data points and theoretical predictions for each experi-

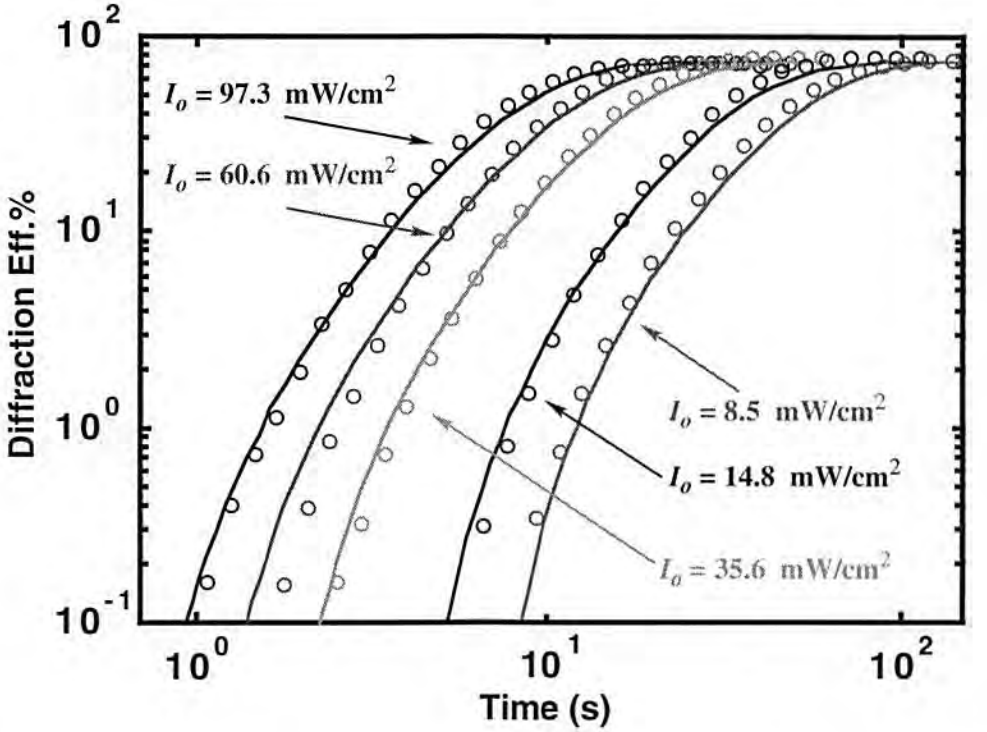

Figure 2-16. Prediction of the diffraction efficiency of the holograms recorded with $m = 0.8$ and I_o as a parameter. First the values of $\gamma = 1.52$ and $\tau = 13.7$ s were extracted from the leftmost curves of Fig. 2-10, which corresponds to three recordings at $m = 0.8$ and $I_o = 97.3$; then using the model of Eq. 2-28 *ff.*, we calculated the time constants at different I_o values; finally the predictions (solid curves) and the measured values (circles) are plotted and compared. For the sake of better visualization, only one recording for each value of I_o is shown.

ment, and then averaging the three obtained values of τ^{-1}. By scaling the value of τ, we reconstructed and compared the predicted evolutions of $\eta(t)$ (solid line) (for an average $\eta_{sat} = 75\%$ which implies $\beta = 1.32$) to the corresponding measured values (o) at other values of I_o.

2.10 HFMD Model: Conclusive Remarks

The HFMD model directly originates from a few basic photopolymerization concepts, which were introduced at the beginning of this chapter, and describes the single grating formation in photopolymers. Some issues regarding limitations to the model must be addressed. First, we noticed that at higher recording intensity, for a constant beam intensity modulation, the saturation value of the refraction index modulation tends to decrease. A possible explanation for this is that at high recording intensity, the photopolymerization is so intense that the diffusing free monomers cannot replace those polymerized. A more accurate model, therefore, might result from taking into consideration the impact of a limited free monomer diffusion during the recording of holographic grating. This issue will be explored in Chap. 5.

Another important issue that we did not consider during the modelling, is the variation of the material transmissivity during exposure. In fact, during holographic exposure, the material not only responds to the light with the grating creation, but also with the bleaching of the dye. Because of the material bleaching, the light intensity within the hologram increases during exposure, and cannot be assumed constant. To understand the impact of this process on the model we exposed a hologram, with $m = 1$ and $I_o = 21$ mW/cm^2 ($\lambda = 0.514$ nm) and we probed the material variation of transmissivity with a beam at a wavelength $\lambda = 0.514$ nm but incoherent respect to the writing beams (see Fig. 3-1). The incoherent beam was also off Bragg with the recording beams. To avoid affecting the polymerization process with the probe beam, its intensity

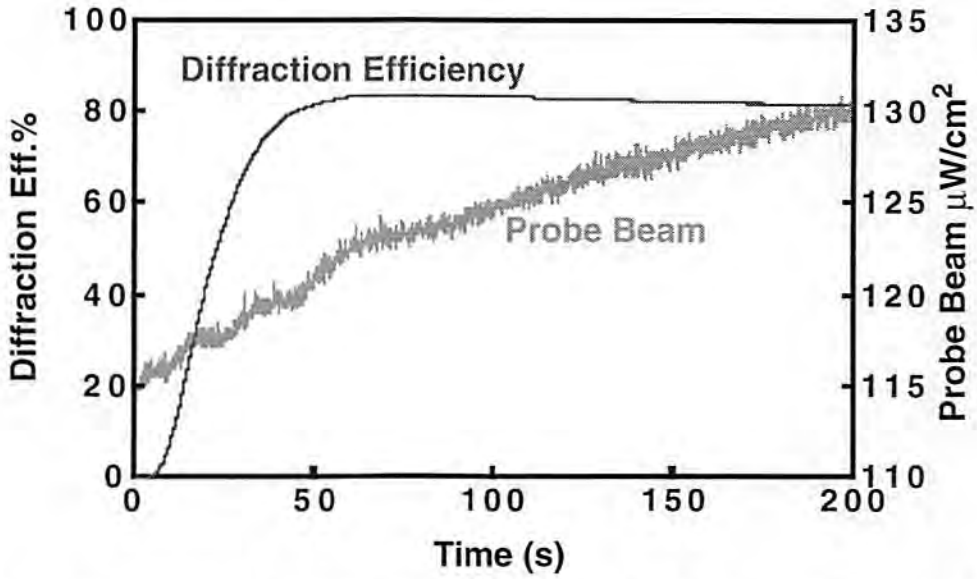

Figure 2-17. Variation of a detected probe beam at $\lambda = 0.514$ nm and of 191 mW/cm^2 of intensity, while recording with $I_o = 21$ mW/cm^2, m = 1. The probe beam is incoherent with respect to the recording beams, and because of its low intensity, it does not significantly affect the polymerization process. Due to the bleaching action of the writing beams, the material transmissivity shows a cumulative change of 4% at saturation, here 50 s after illumination starts, and of 13% after 200 s.

was chosen substantially less than the average recording intensity, as $I_b = 191$ μW/cm^2. Fig. 2-17 depicts the results of the experiments, by conjunctively depicting the evolution of the diffraction efficiency and the probe beam intensity at the hologram output. After 200 s of exposure the output probe beam intensity increases by 13%. The grating saturation time occurs, however, only within 50 s, and at this time the corresponding increase of the probe beam is only of 4%, indicating that during polymerization the variation of transmissivity is relatively limited. Such a small variation of transmissivity does not significantly affect the results of the HFMD model and therefore we can ignore the effect of material beaching for the HRF-150-38. Per contra, this last consider-

ation does not apply for photopolymer samples much thicker than the 38 micron-thick material used in our experiments. In fact, for very thick samples, the recording light can experience a more dramatic change of transmissivity (or of material absorption) within the volume hologram as photopolymerization progresses, and it may happen that near the first surface of incidence the material reaches saturation, while at the opposite end of the material photopolymerization may just begin. In this condition, the HFMD model validity is questionable, and the material transmissivity variation must be included in the model itself, without any guarantee that a simple mathematical description of grating formation (as that of the HFMD model) can be obtained.

Finally, we must address that the HFMD model as introduced in this chapter is only able to satisfactorily characterize the recording of a single holographic grating, while holographic optical storage and multiplexed volume holography is based on the concept of multiplexing a large number of holograms in the same area or volume of the medium. Extension of the HFMD model in order to characterize and predict these more complex recording scenarios is ineluctably needed. This extension, therefore, is the topic of the next chapter.

2.11 Bibliography

Bjorklund, G. C., D. M. Burland, and D. C. Alvarez, "A Holographic Technique for Investigating Photochemical Reactions," J. Chem. Phys., **73**(9), 4321-4329, (1980).

Cerquaglia Luca, Personal Communication, 1992

Colburn, W. S. and K. A. Haines, "Volume Hologram Formation in Photopolymer Materials," Appl. Opt., **10**(7), 1636-1641, (1971).

Curtis, K. and D. Psaltis, "Characterization of the DuPont Photopolymer for Three-Dimensional Holographic Storage," Appl. Opt., **33**(23), 5396-5399, (1994).

Kurtz, R. L. and R. B. Owen, "Holographic Recording Materials-A Review," Opt. Eng., 14(5), 393-405, (1975).

Kozna, A., "Effects of Film-Grain Noise in Holography," J. Opt. Soc. Amer. **58**, 436, (1968)

"MATLAB Reference Guide", The MathWorks Inc., August 1992

Odian, G., *Principles of Polymerization*, John Wiley & Sons, Inc., (1991).

Reiser, A.,*Photoreactive Polymers*, John Wiley & Sons, Inc., (1989).

Shultz, A. R. and M. G. Joshi, "Kinetics of Photoinitiated Free-Radical Polymerization," J. Polym. Sci. Polym. Phys. Ed.,**22**,1753-1771 (1984)

Shankoff, T. A., "Phase Holograms in Dichromated Gelatin," Appl. Opt., 7(10), 2101-2105, (1968).

Smothers, W. K., B. M. Monroe, A. M. Weber, and D. E. Keys, "Photopolymers for Holography," Proc. Soc. Photo-Opt. Inst. Eng., **1212**, (1990).

Torodov, T., P. Markovsky, and V. Dragostinova, "Photopolymers - Holographic Investigations, Mechanism of Recording and Applications," Opt. Quant. Elect., **16**, 471-476, (1984).

Weber, A. M., W. K. Smothers, T. J. Trout, and D. J. Mickish, "Hologram Recording in DuPont's New Photopolymer materials," Proc. Soc. Photo-Opt. Inst. Eng., **1212**, (1990).

Wei, Y., Y. Sun, and X. Tang, "Autoacceleration and Kinetics of Electrochemical Polymerization of Aniline," J. Phys. Chem., **93**, 4878-4881, (1989).

Wopschall, R. H. and T. Pampalone, "Dry Photopolymer Film for Recording Holograms," Appl. Opt., **11**(9), 2096-2097, (1972).

Chapter 3

Extension of the HFMD Model

3.1 Introduction

In this chapter we study the case of complex recording scenarios in photopolymers, and validate the HFMD model by using it to predict the grating formation process. The definition of a complex recording scenario used here is a holographic exposure system which departs from the simple recording of a single holographic grating. Two main cases that will be analyzed both theoretically and experimentally are the recording of a single grating with incoherent light addition (ILA recording), and the parallel recording of angularly multiplexed gratings using incoherent/coherent (I/C) illumination. For the sake of completeness, the theoretical treatment of multiple sequential recording will be presented as well. Before proceeding with the rest of this chapter, we point out for sake of clarity that new symbols will be introduced to describe the key parameters governing the recording process in photopolymers. For the single grating these parameters (as illustrated in Chap. 2) are the average recording intensity, I_o, the beam modulation intensity m, and the and time constant τ, for the ILA recording these same parameters are respectively indicated as I_{oi}, m_i, and τ_i, while for the I/C recording they are termed I_{oT}, m_j, and τ_T.

3.2 ILA Recording in Photopolymers

By properly applying the HFMD model results, one can describe the recording of a single holographic grating in the presence of an additional light beam which is mutually incoherent respect to the recording beams. In these conditions, however, such parameters as the beam intensity modulation and the average recording intensity must be redefined, and with them the figures of merit of the process. Still under the HFMD hypothesis, and with the appropriate adjustment of semantics, we will show how the solution to this problem is esthetically and mathematically similar to that of the single grating recording previously formulated in Chap. 2.

3.2.1 ILA Recording in Photopolymers: the Theory

When recording a single holographic grating in photopolymer using two coherent beams of intensity I_1 and I_2, in presence of a mutually incoherent light beam with intensity I_i, the total light intensity in the material is

$$I(x) = \left(I_1 + I_2 + I_i + 2\sqrt{I_1 I_2}\cos(K_g x) \right). \tag{3-1}$$

Only the coherent beams I_1 and I_2 interfere contribute to the interference pattern. We suppose that all three beams have the same wavelength, and the beam I_i can be of either of incoherent or coherent nature, in the latter case I_i must be mutually incoherent with respect of I_1 and I_2. If we express the above equation in terms of beam intensity modulation, it yields

$$I(x) = I_{oi}[1 + m_i \cos(K_g x)]. \tag{3-2}$$

Esthetically the above expression is similar to Eq. 2-9 which gives the intensity term in the absence of I_i. The average recording intensity is now redefined as

$$I_{oi} = I_1 + I_2 + I_i, \tag{3-3}$$

and the beam intensity modulation is m_i, which takes into account the presence of I_i, so that

$$m_i = \frac{2\sqrt{I_1 I_2}}{I_1 + I_2 + I_i} < m = \frac{2\sqrt{I_1 I_2}}{I_1 + I_2}. \tag{3-4}$$

As a first consequence of this recording scenario, one notes that the m_i term is less than the relative intensity beam modulation term, m, for the single grating recording (Eq. 2-10), due to the presence of the I_i in the denominator of Eq. 3-4. The fact that $m_i < m$ can be considered an early indication that ILA recording is less efficient than single grating recording.

By using the above formulation, it is now possible to model the grating formation during ILA recording. Substituting the new definitions of average recording intensity and beam intensity modulation in Eq. 2-7 and Eq. 2-8, which describe the variation of the free monomer density and refractive index during exposure, and using the approximations which lead to Eq. 2-12, we obtain the fundamental equations describing the temporal evolution of the refractive index modulation, $\Delta n_i(t)$, during ILA recording as

$$\frac{d}{dt}\Delta n_i(t) = m_i \delta c_n k_R(t) [M](t) I_{oi}^{\delta}, \tag{3-5}$$

for the grating variation, and for the monomer depletion, we have the following

$$\frac{d}{dt}[M](t) = -k_R(t) [M](t) I_{oi}^{\delta}. \tag{3-6}$$

Solving the above differential equations, using the polymerization function $k_R(t) = k_o \exp\left(\varphi I_{oi}^{\delta} t\right)$, with the boundary conditions $\Delta n_i(0) = 0$, and $[M](t) = [M]_o$, we get

$$[M](t) = [M]_o \exp[\gamma(1 - \exp(t/\tau_i))], \text{ and} \tag{3-7}$$

$$\Delta n_i(t) = m_i \Delta n_M \{1 - \exp[\gamma(1 - \exp(t/\tau_i))]\}. \tag{3-8}$$

As already defined in the previous chapter, $\Delta n_M = \delta c_n k_o [M]_o$ is the largest attainable value of grating modulation, $\gamma = k_o/\varphi$ is a constant, and the time constant τ_i is

$$\tau_i = (\varphi I_{oi}^{\delta})^{-1} < \tau = (\varphi I_o^{\delta})^{-1}. \tag{3-9}$$

The above results clearly indicate that the addition of the mutually incoherent beam of intensity I_i causes a faster photopolymerization and recording process (smaller time constant) when compared to the single grating recording (RHS of the inequality sign).

In essence, the presence of I_i influences both the modulation of the refractive index at saturation and the temporal evolution of the grating. At saturation the modulation of the refractive index is

$$\Delta n_{i-sat} = m_i \Delta n_M < m \Delta n_M \,, \tag{3-10}$$

which is less than the corresponding refractive index modulation for the single grating case. At the same time, the time constant relation in Eq. 3-9 indicates that the presence of I_i will cause a faster process, reducing the time to reach saturation.

The preceding rationale suggests a sets of experiments which can be organized according to the following steps.

(1) Measure the diffraction efficiencies of a number holograms recorded with a given m and intensities I_1, and I_2, in absence of the mutually incoherent beam of intensity I_i.

(2) Measure the diffraction efficiencies of a number holograms recorded with the addition of I_i which is mutually incoherent with the respect to the recording beams I_1, and I_2. The presence of I_i will induce an increase of the average recording energy as I_{oi}, and a decrease of the modulation beam intensity as m_i.

(3) Finally, we may verify our expectation for step **(2)**. Given the data recorded in **(1)**, we first simulate the addition of I_i, and then compare the saturation diffraction efficiency and the temporal dynamics of these new calculated data with the data measured in **(2)**. In other terms, by means of computer simulation, we can change the m in step **(1)** to m_i, as indicated in Eq. 3-4, and then compare the obtained saturation diffraction efficiencies with those measured in **(2)**. The temporal dynamics of **(1)** (once m is changed to m_i) and **(2)** can be compared by plotting the time evolution of the measured diffraction efficiencies

using the pseudoexposure as abscissa (as in Fig. 2-15). According to theory, these graphs should have the same dynamics. In the following subsections w describe in greater details the experiments and the theory related to steps **(1)** through **(3)**.

3.2.2 ILA Recording: Experimental Sep-Up

To verify experimentally this extension of the high free monomer diffusion model to hologram recording in the presence of a mutually incoherent beam, we devised the experiment depicted in the set-up of Fig. 3-1 (a). The two grating recording beams, I_1 and I_2, generated by an argon-ion laser with a wavelength of 514 nm, interfere in the HRF-150-38 photopolymer sample. The recording beams are symmetrically interfering with an angle of incidence from the normal to the of holographic plate of 22° in air. These beams are polarized normal to the plane of incidence. At the same time the beam I_i, which is of coherent nature but mutually incoherent with respect to I_1 and I_2, is generated by splitting part of the light from the argon-ion beam, and by reflecting this beam off a mirror whose position is modulated by a piezo-electric transducer. In this way I_i is phase modulated and, therefore, it is mutually incoherent with respect to the recording beams I_1 and I_2. The polarization of I_i is rotated by 90° by a half wave plate. This polarization rotation further guarantees that I_i cannot interfere with the recording beams during the writing of the grating. All the beams (I_1, I_2, and I_i) are coplanar, and I_i is incident at 10° from the normal to the holographic plate. A Bragg matched red beam (λ_b = 633 nm), from a Helium-Neon

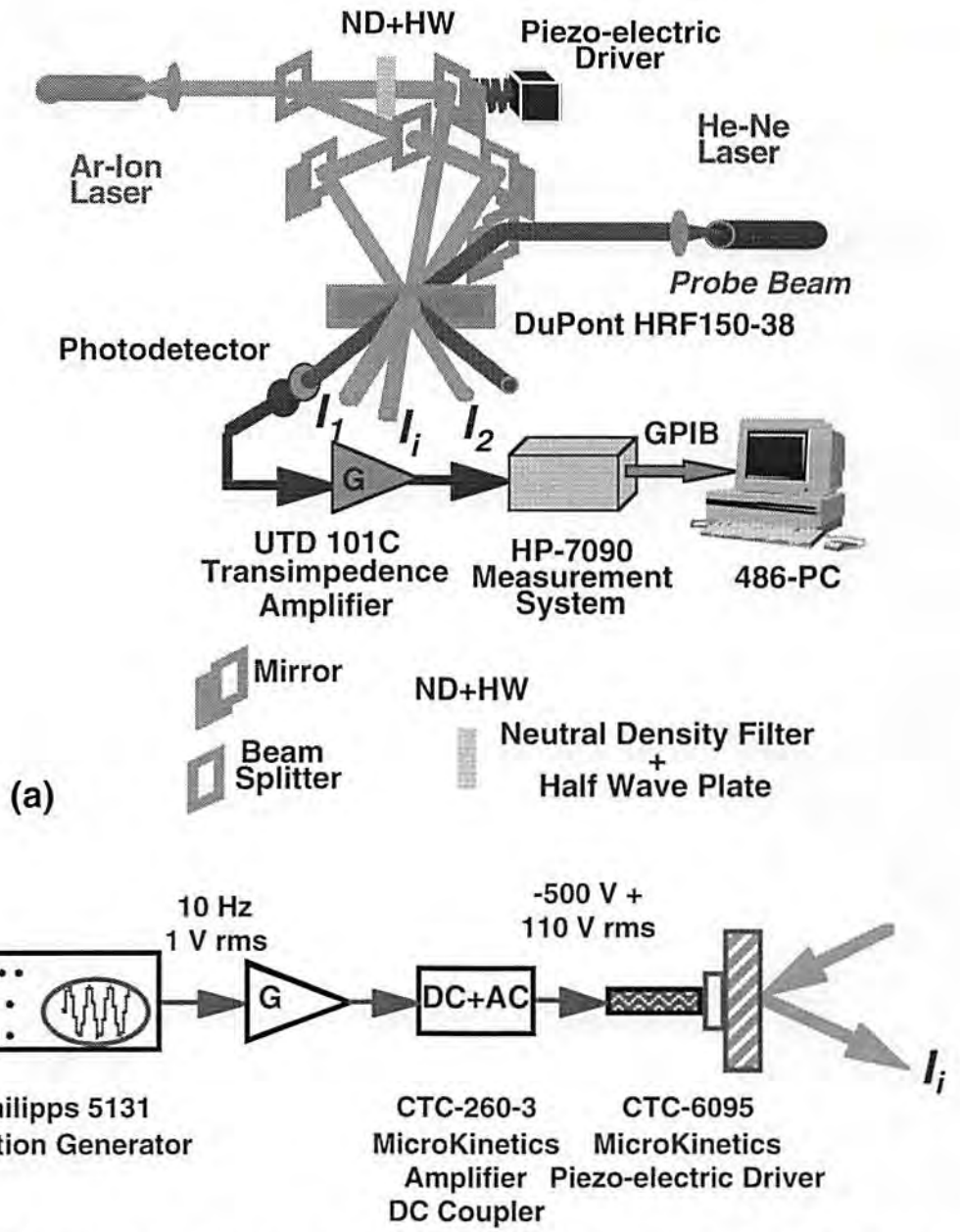

Figure 3-1. Experimental set-up for recording a single holographic grating in the presence of incoherent light. **(a)** Two coherent beams, I_1 and I_2, interfere in the medium. At the same time, an incoherent beam, I_i, is incident on the material. The incoherent beam is generated by modulating its phase when it is reflected by the mirror mounted on a vibrating piezo-electric driver. **(b)** Piezo-electric driver system set-up. A sinusoidal signal at 10 Hz is produced by a Phillips 5131 function generator and is amplified and coupled with a DC polarization voltage via a Micro Kinetics CTC-260-3 DC coupler. The output signal, -500 V + 110 V rms, activates a Micro Kinetics CTC-6095 piezo-electric driver, which experiences a maximum position shift of 1.5 μm per cycle.

laser is used to monitor the grating's temporal evolution by measuring in real time the diffracted red light.

Figure 3-1 (b) depicts the arrangement of the piezo-electric driver. A Phillips 515 function generator provides a 10 Hz sinusoidal wave, which is amplified and DC coupled through a Micro Kinetics CTC-260-03 coupler. The output of the coupler is -500 V DC (bias voltage) with an associated sinusoidal wave of 110 V rms. The piezo-electric driver is a Micro Kinetics CTC-6095 capable of a maximum extension of -5 μm at -1000 V bias. Given these characteristics, the piezo-electric driver elongation is 1.5 μm per cycle (0.1 s), which is sufficient to decorrelate I_i from the recording beams, since the recording process takes time of the order of seconds.

3.2.3 ILA Recording: Experimental Results and Discussion

Given the theoretical results and the experiments suggested at the end of Sec. 3.2.1, and using the experimental set-up described in the previous subsection, we recorded and compared the results obtained by two sets of grating recordings, which were carried out without and with the addition of the mutually incoherent beam I_i. During the set of recordings without I_i, the beam intensity modulation was $m = 1$, and $I_o = 20.6$ mW/cm^2 (*i.e.* $I_1 = I_2 = 10.3$ mW/cm^2). In such conditions, two separated exposures were recorded in two different samples, and the resulting data are depicted in Fig. 3-2 (a), which indicates that saturation diffraction efficiencies of 90% and 84% were reached after approximately 50 s.

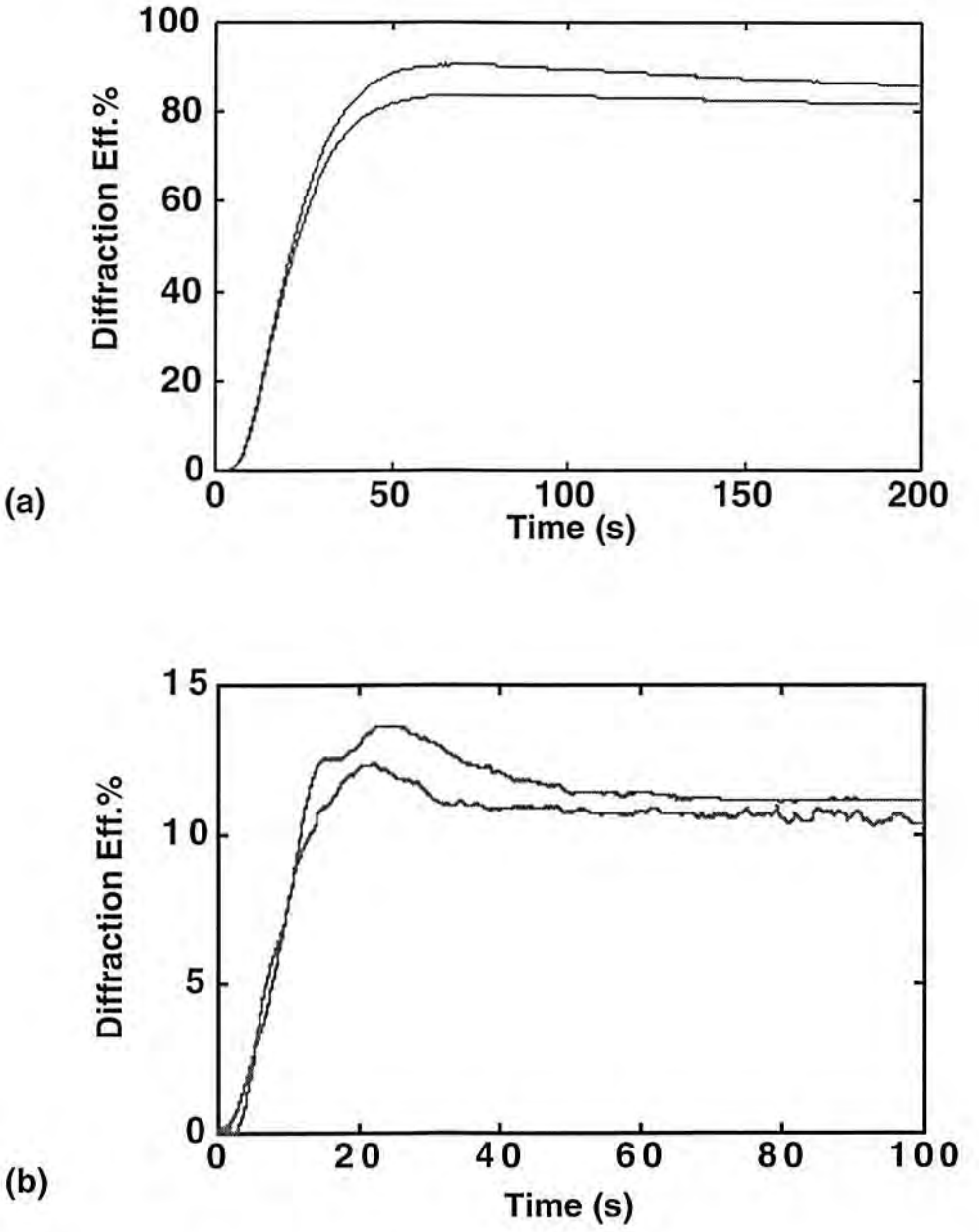

Figure 3-2. **(a)** Recording of a single grating, $m = 1$, I_o =20.6 mW/cm^2. Two exposures are shown. The saturation diffraction efficiencies are 90% and 84% after 50s of exposure time. **(b)** Recording a single grating in presence of an incoherent light. Two exposures are shown. The recording intensities are $I_1 = I_2 = 10.3$ mW/cm^2, and I_i = 45mW/cm^2 with an associated m_i =0.314. After 24s saturation is reached with associated diffraction efficiencies of 12.5% and 13.6%.

The second set of two separated holograms were exposed in two different samples of HRF-150-39 with $I_1 = I_2 = 10.3$ mW/cm^2, and the mutually incoherent beam of intensity $I_i = 45$ mW/cm^2. The average recording intensity was therefore $I_{oi} = 65.6$ mW/cm^2, and the beam modulation intensity was $m_i = 0.314 < m = 1$. In these circumstances, the saturation diffraction efficiencies in the two exposures were 12.5%, and 13.6%. Saturation was reached after 24 s, as presented in Fig. 3-2 (b).

Recurring to the methodology indicated at the end of Sec. 3.2.1, a way to compare the theoretical versus the experimental results is to verify how well the data from the single grating can predict the behavior of the material when an incoherent beam is added during recording. To perform the verification we used the following procedure. From the temporal evolution of the diffraction efficiencies in Fig. 3-2 (a), $\eta_{m=1}(t)$, we extracted the temporal evolution of the refractive index modulation $\Delta n_{m=1}(t)$, which is obtained by

$$\Delta n_{m=1}(t) = \frac{\lambda_b \cos(\theta_b)}{\pi T} \operatorname{asin}\left(\sqrt{\eta_{m=1}(t)}\right), \tag{3-11}$$

where $\eta_{m=1}(t)$ is here indicated in units (not in percent), and $\Delta n_{m=1}(t)$ is proportionally dependent on the beam modulation intensity m as indicated by Eq. 2-9. Thereafter, to predict and simulate the action of the presence of I_i during recording, it is necessary to normalize by m (here $m = 1$), and multiply by the beam modulation intensity m_i =0.314, corresponding to the incoherent light addition case:

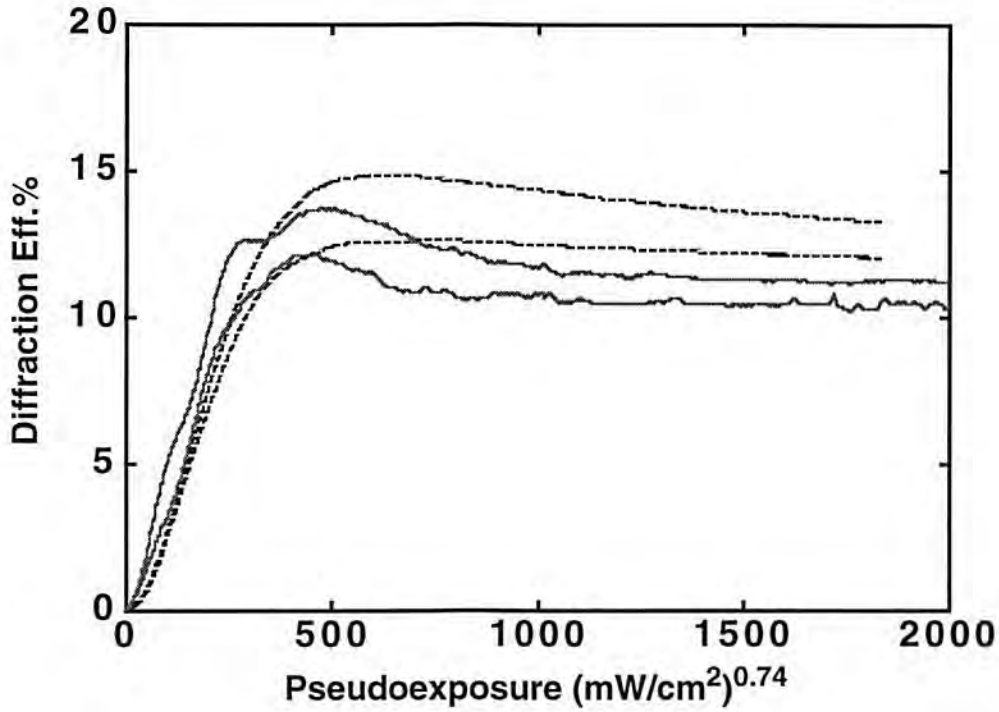

Figure 3-3. Model prediction for incoherent light addition. From the data of Fig. 3-2 a) the incoherent light addition has been simulated via software by changing the beam intensity modulation to m_i=0.314 (dashed curves). The predicted results (dashed curves) and the measured ones (solid curves) are therefore compared using the 'pseudoexposure' as abscissa, which normalizes the time constant of all the curves. The inhibition period is not shown in the figure.

$$\Delta n_{m_i}(t) = \frac{m_i}{m}\Delta n_{m=1}(t) \,. \tag{3-12}$$

Once we obtain $\Delta n_{m_i}(t)$, we can reconstruct the predicted diffraction efficiency for the ILA recording as

$$\eta_{m_i}(t) = \sin^2\left(\frac{\pi \Delta n_{m_i}(t)\, T}{\lambda_b \cos(\theta_b)}\right) \tag{3-13}$$

which may predict the diffraction efficiency at saturation. One must notice,

however, that the time constant of the temporal evolution of $\eta_{m_i}(t)$ is still $\tau = (\varphi I_o^{\delta})^{-1}$, but when I_i is present, as for the measures in Fig. 3-2 (b), the time constant is instead $\tau_i = (\varphi I_{oi}^{\delta})^{-1}$. Therefore, to properly compare the predicted values of $\eta_{m_i}(t)$ and the experimentally measured ones, we must use as abscissa the 'pseudoexposure', which is a normalization of the temporal evolution of the diffraction efficiency by the process time constant (Chap., 2 Fig. 2-15). These concepts are finally depicted in Fig 3-3, where the predicted diffraction efficiencies (dashed curves) derived from the measurements of Fig. 3-2 (a), and the measured ones (solid curves) for the incoherent addition case are compared. Beside a noisier behavior for the measured case, the predicted and the observed diffraction have a common evolution, with a saturation diffraction efficiency in the range 12.6-14.8%, which occurs at a 'pseudoexposure' value of 500 $(mW/cm^2)^{0.74}s$.

Before concluding this section, we make an important remark about the polymerization response to incoherent light. The validity of the ILA recording model is limited to the case in which I_i has the same wavelength as the grating writing beams I_1 and I_2. In this case, each intensity term contributes in the same fashion to the polymerization through the function $k_R(t)$, which is wavelength sensitive because it is related to the initiation efficiency of the process. Hence, if the incoherent beams were to have a different wavelength than the writing beams, the model would need readjustment. In this model readjustment, therefore, we would have to incorporate the quantitatively different contributions to polymerization of the writing beams and of the incoherent light.

3.3 Recording of Multiple Gratings in DuPont Photopolymers

So far we have modelled the recording mechanism of a single grating formation in DuPont photopolymer. If one wishes, however, to use holographic photopolymers to store a large amount of data or to perform dense optical interconnections, then it is necessary to develop an exposure technique which is capable of multiplexing a large number of gratings in the holographic material [Kostuk, 1989]. In these conditions, the HFMD model that we introduced for single grating formation is no longer sufficient. In fact, an adaptation of the HFMD model to the different recording techniques is deeply embedded in the physical implementation of these techniques. Therefore, before proceeding with the description and the solution of this problem, we provide a concise overview of recording techniques for grating multiplexing.

There are different ways to superimpose a number of holograms in a holographic material, a taxonomy of which usually divides them into either spatial or angular multiplexing. Spatial multiplexing consists of storing a number of single holograms, or sub-holograms (usually of limited spatial dimensions), in an assigned space [Tao *et al.*, 1993]. In such a technique each sub-hologram is essentially independent of the adjacent one. Therefore, by applying our HFMD model for each sub-hologram, one can predict and control its grating formation, and predict its diffraction efficiency. Angular multiplexing is usually used when one desires to store a large number of sub-holograms in a single area (or volume) of the material [Mok, 1993]. Here a number of sub-holograms are overlapped in the same space, and the ability of to put multiple gratings within the

same space comes at the expense of a reduced (single and overall) diffraction efficiency. Grating cross-talk is prevented by having the gratings angularly spaced by an angular distance greater than their corresponding Bragg selectivity.

There are two main strategies used to record angularly multiplexed volume holograms, serial recording and parallel recording. Curtis and Psaltis [Curtis and Psaltis, 1992] analyzed the problem of serial recording a number of holograms in HRF-150-38. They found that by properly scaling the duration of each single exposure, it is possible to serially record sub-holograms having approximately the same diffraction efficiency. Curtis and Psaltis considered sequential recording with a beam intensity modulation of unity. In the next section, we instead propose an analysis of the problem, which takes into account the results of the HFMD model, and extends control of sequential recordings in photopolymers to any beam modulation values and recording intensity.

By parallel recording, we mean the technique which incorporates simultaneous exposure of all the angularly multiplexed holograms. The convenience of this method is in its exposure schedule, which is less complicated than the serial exposure. At the same time, parallel exposure presents the drawback of creating cross-talk gratings that can destroy the fidelity of reconstruction. Furthermore, it may require more complex optical hardware.

To circumvent this last problem, there is a simultaneous recording technique termed incoherent/coherent (I/C) [Jenkins *et al.*, 1990] which requires an array of coherent sources (one source per hologram) which are mutually

incoherent. The mutually incoherent sources can be obtained by using a VCSEL array [Jewell *et al.*, 1990], or by optically transforming a single laser beam. This single laser beam transformation into an array of I/C sources can be provided by splitting a propagating the beams at different coherence lengths [Piazzolla *et al.*, 1992], by phase modulating the beams with the help of an acoustic optic device [Hong *et al.*, 1995], or as previously shown in Fig. 3-1 (b), with the help of vibrating mirrors modulated by piezo-electric drivers. Upon the recording, each source generates a pair of mutually coherent beams which interfere and write the corresponding grating in the material. At the same time, the mutual incoherence of the other sources prevents the recording of cross-talk gratings. An example of the results of this technique are shown in Fig. 3-4, where three simple holographic gratings were recorded in dichromated gelatin using a simple argon-ion laser source. Figure 3-4 (a) depicts the recording geometry of the three mutually incoherent pairs of beams I_{A1}-I_{A2}, I_{B1}-I_{B2},and I_{c1}-I_{c2}. Figure 3-4 (b) is a photograph of the reconstruction of one of the three holograms, where the reconstruction of the first order, as is the absence of noise as well. For the sake of comparison, the same experiment was repeated using fully coherent recording beams. Visual inspection of the picture in Fig. 3-4 (c) shows the resulting noisy reconstruction which helps to understand the different performances of I/C and fully coherent technique. Because of our interest in I/C recording (whose main architectural advantages will be illustrated in Chap. 6 which is dedicated to the argument of hologram copying), we extend the HFMD model to the recording of multiplexed holograms using I/C exposure with theoretical modelling and experimental verification.

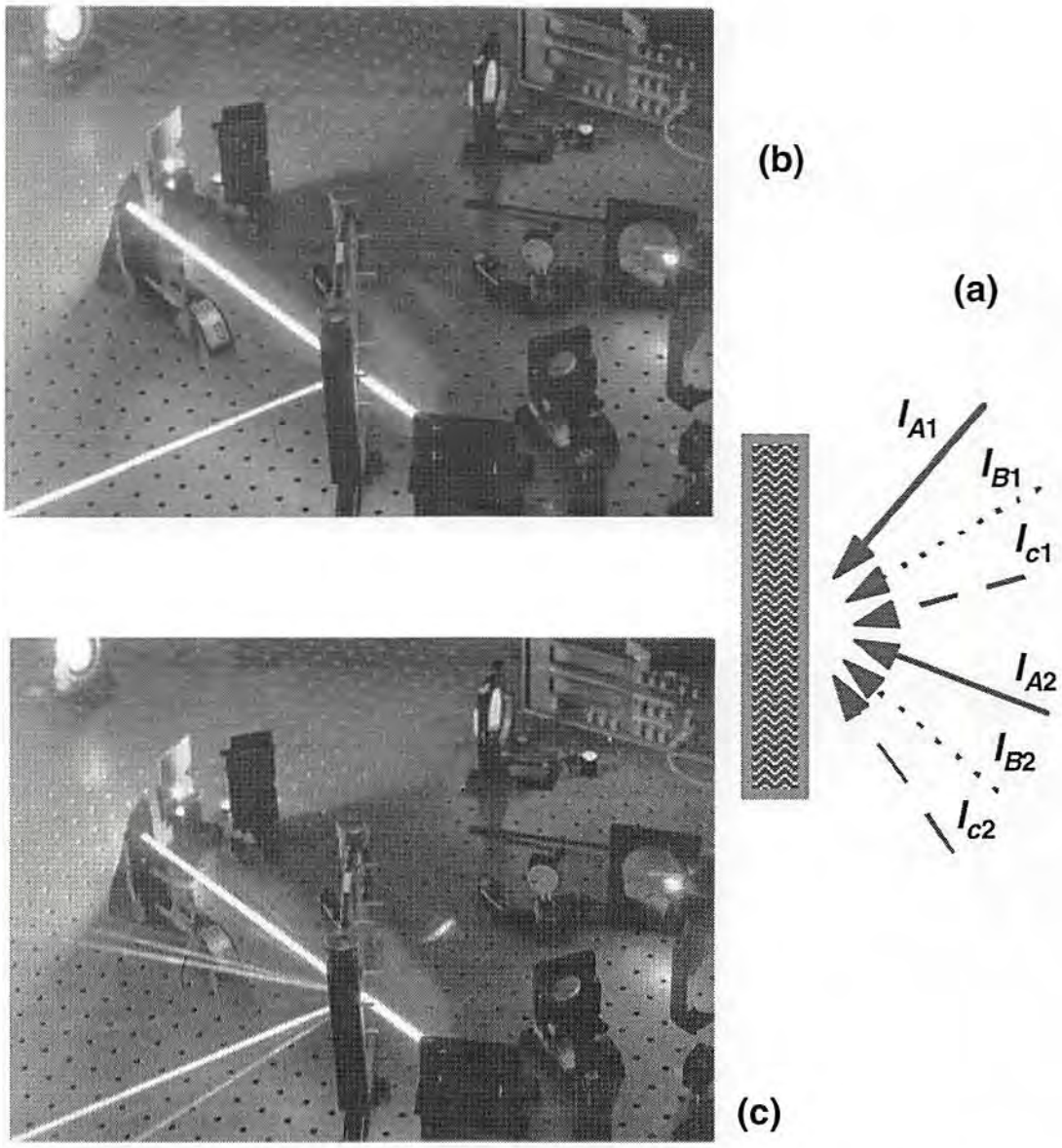

Figure 3-4. Pictures from an experiment of incoherent/coherent recording. **(a)** A schematic showing the recording of three multiplexed holograms in dichromated gelatin, corresponding to the interference of the beams I_{A1} and I_{A2}; I_{B1} and I_{B2}; I_{C1} and I_{C2}, which are depicted as solid, dotted, and dashed lines, respectively. **(b)** I/C recording. The reconstruction of one hologram. Only the corresponding first order is recalled. **(c)** Fully coherent recording. In this case, one beam recalls its corresponding first order and all the other beams as well, because of the presence of cross-talk gratings.

3.4 Modelling Sequential Multiple Exposures in Holographic Photopolymers

In this section we indicate how to extend the results of the HFMD model to describe sequential recordings. When a multiplexed volume hologram is sequentially recorded, the individual holograms are recorded one at a time. Therefore, let's consider the case of the sequential recording of a number of independent holograms each with a target refractive index modulation Δn_t, given an average recording intensity I_o, and a relative beam intensity modulation m. For the sake of simplicity, we suppose that the inhibition period is not present, which in practice means that the material has been pre-exposed with the amount of energy necessary to eliminate all the radical scavengers.

According to the results of the HFMD model, during the holographic exposure, the grating modulation grows as

$$\Delta n\,(t) \;=\; m\Delta n_M \{\, 1 - \exp\left[\gamma\,(1 - \exp\,(t/\tau))\,\right]\,\}\,, \tag{3-14}$$

where $\Delta n_M = \delta c_n k_R [M]_o$ is proportional to the monomer concentration at the time $t = 0$. Due to the algorithm derivation, we prefer to indicate here the initial maximum grating modulation as $\Delta n^{(0)} = \Delta n_M$, where the integer superscript is related to the exposure (or hologram) number. From Eq. 3-14, one obtains the exposure time interval, $\Delta t = \Delta t^{(1)}$, which produces the recording of the desired modulation index as $\Delta n(\Delta t^{(1)}) = \Delta n_t$, with

$$\Delta t^{(1)} \;=\; \tau \log\left[\, 1 - \frac{1}{\gamma}\log\left(\, 1 - \frac{\Delta n_t}{m\Delta n^{(0)}}\,\right)\right]. \tag{3-15}$$

After $\Delta t^{(1)}$ seconds, according to Eq. 2-27 which describes the variation of monomer concentration during photopolymerization, the monomer concentration is

$$[M]_1 = [M]_o \exp\left[\gamma\left(1 - \exp\left(\Delta t^{(1)}/\tau\right)\right)\right] < [M]_o . \qquad (3\text{-}16)$$

A consequence of the first exposure is that the next hologram to be recorded will have its maximum attainable refractive index modulation $\Delta n^{(1)} = \delta c_n k_R [M]_1 < \Delta n^{(0)}$. If $\Delta n_t < m\Delta n^{(1)}$, the time interval for the second exposure is

$$\Delta t^{(2)} = \tau \log\left(1 - \frac{1}{\gamma}\log\left(1 - \frac{\Delta n_t}{m\Delta n^{(2)}}\right)\right), \qquad (3\text{-}17)$$

with $\Delta t^{(1)} < \Delta t^{(2)}$, and a final monomer concentration (still as a consequence of Eq. 2-27)

$$[M]_2 = [M]_1 \exp\left[\gamma\left(1 - \exp\left(\Delta t^{(2)}/\tau\right)\right)\right] < [M]_1 < [M]_o . \qquad (3\text{-}18)$$

This procedure continues just prior to the *n-th* exposure where the recording is halted because it is verified that $\Delta n_t > m\Delta n^{(1)} = \delta c_n k_R [M]_{n-1}$, where $[M]_{n-1}$ is the monomer concentration after the $(n-1)$-th exposure.

In this recording strategy, the number N of multiplexed sub-holograms depends on the target value of the grating modulation, and, furthermore, on the beam intensity modulation m satisfying $N = m\Delta n^{(0)}/\Delta n_t$. Therefore, the higher the beam intensity modulation, the better is the storage capability of the material, and the shorter is each single exposure time. This last concept is fully depicted in Fig. 3-5, which illustrates the theoretical results of two sets of

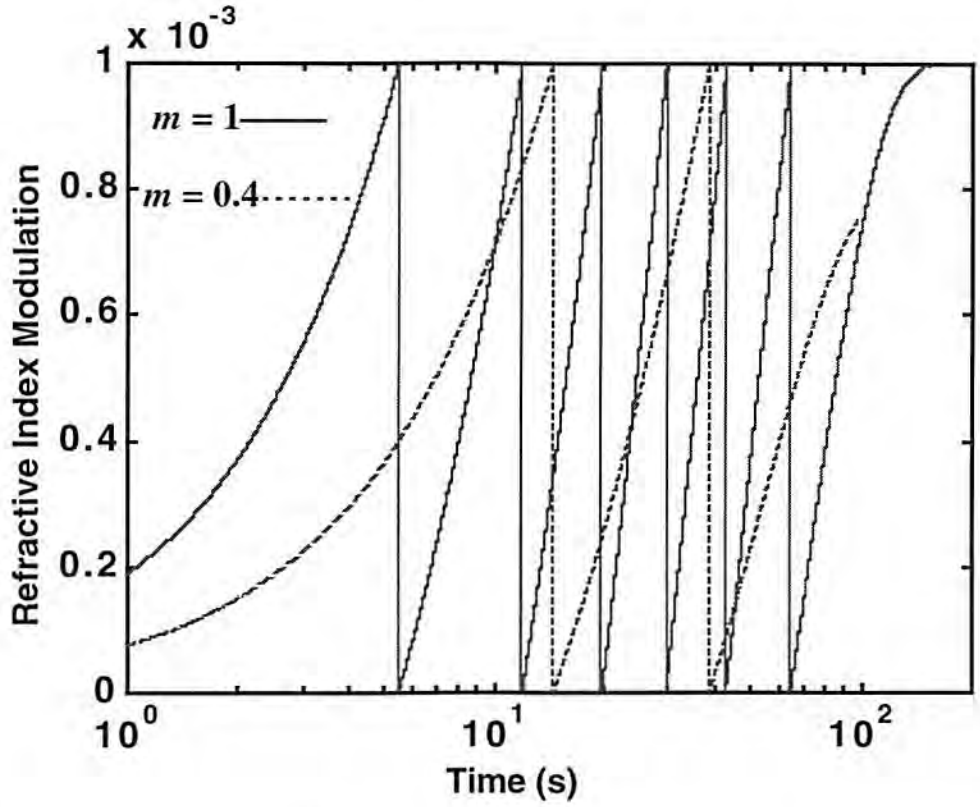

Figure 3-5. Sequential recording of multiple sub-holograms. The target grating modulation is $\Delta n_t = 0.001$, with a maximum attainable grating modulation $\Delta n_M = 0.007$. Two recording schemes are depicted, using $m = 1$ (solid line), and $m = 0.4$ (dashed line). As shown in the picture, recording with unitary beam intensity modulation is more convenient in term of material storage capability ($N = 7$) in comparison with $m = 0.4$ and $N = 2$.

sequential recordings for two different values of beam intensity modulation ($m = 1$, and $m = 0.4$), and for a target $\Delta n_t = 0.001$ with $\Delta n^{(0)} = 0.007$. To define the time dynamics we used the constant $\gamma = 1.52$, as found in the previous chapter.

As we stated earlier, and theoretically demonstrated, the sequential recording technique suffers from a cumbersome exposure schedule, because each sub-hologram exposure has to be calculated, and the total exposure time can be too

long, which, *per se*, is a drawback when a large number of holograms have to be recorded and mass produced. Furthermore self diffraction can affect sequential recording unpredictably when $m \neq 1$. In fact, when very thick holograms are sequentially recorded, the presence of self diffraction makes controlling the grating modulation and the grating orientation difficult, as well as the resulting diffraction efficiency. Self diffraction in photopolymers will be discussed in the next chapter.

Finally, photopolymers, and to our knowledge solely the photopolymers, present an additional inconvenience which is caused by the so called run-off effect, or dark diffusion increment. As described later (Chap. 5), the refractive index modulation in photopolymers can continue to increase until it reaches a stable value for a number of seconds, even after the exposure is completed. The extension of this index modulation growth depends mainly on the average recording intensity and the beam intensity modulation used during recording, and is caused by monomer diffusion. As a consequence of this effect the final value of the modulation gratings is unpredictable, which causes recording errors which may badly affect the performance of an optical system containing the multiplexed hologram.

3.5 Modelling the I/C Exposure in Holographic Photopolymers

During I/C recording a number of sub-holograms are exposed simultaneously. Each sub-exposure consists of a pair of beams interfering in the material and the beams interfering in the materials can be considered as

plane waves polarized normal to the plane of incidence. If we have a total of N beam pairs, the total intensity pattern is

$$I(x) = \left(\sum_{j=1}^{N} I_{j1} + I_{j2} + 2\sqrt{I_{j1} I_{j2}} \cos(K_{gj} x) \right), \tag{3-19}$$

where K_{gj} is the grating wave-vector of the specific sub-hologram j (for $j = 1, 2, 3, 4,...,N$). Due to the I/C recording, the formation of cross-talk gratings is prevented and, therefore, the wave-vectors related to such gratings do not appear in Eq. 3-19. A more efficient way to express the total interference pattern is by rewriting it in terms of the different beam modulation intensities

$$I(x) = I_{oT} + I_{oT} \sum_{j=1}^{N} m_j \cos(K_{gj} x), \tag{3-20}$$

in which I_{oT} is the total intensity DC term, or total average recording intensity, which is equal to

$$I_{oT} = \sum_{j=1}^{N} I_{j1} + I_{j2}, \tag{3-21}$$

and the beam intensity modulation term of the j-th sub-hologram, m_j, is

$$m_j = \frac{2\sqrt{I_{j1} I_{j2}}}{I_{oT}} < 1, \tag{3-22}$$

where by definition $0 < m_j < 1$ (for $j = 1, 2, 3, 4,...,N$).

Having defined the total average recording intensity and the beam modulation intensity, one can describe the photopolymerization process and the grat-

ing formation using the methodology established for the single grating case under the HFMD hypothesis. The rate of monomer polymerization is given by

$$\frac{d}{dt}[M]\,(t) = -k_R(t)\,[M]\,(t)\,I^{\delta}_{oT}\,. \tag{3-23}$$

The refractive index variation due to photopolymerization and instantaneous monomer diffusion is

$$\frac{\partial}{\partial t}n\,(x,t) = c_n k_R\,(t)\,[M]\,(t)\,I\,(x)^{\delta}\,. \tag{3-24}$$

The above equation can rearranged after using the binomial expansion of the intensity term, so that

$$I\,(x)^{\delta} = I_{oT}{}^{\delta}\left\{1+\delta\left[\sum_{j=1}^{N} m_j\cos\,(K_{gj}x)\right]+\frac{\delta\,(\delta-1)}{2!}\left[\sum_{j=1}^{N} m_j\cos\,(K_{gj}x)\right]^2\right. \tag{3-25}$$
$$\left.+\frac{\delta\,(\delta-1)\,(\delta-1)}{3!}\left[\sum_{j=1}^{N} m_j\cos\,(K_{gj}x)\right]^3+HOT\right\}.$$

In this case where $\sum_{j=1}^{N} m_j < 1$, we approximate the above equation by truncating the series expansion to its first term, which leads us to rewrite the refractive index variation equation of Eq. 3-25 as

$$\frac{\partial}{\partial t}n\,(x,t) = c_n k_R\,(t)\,[M]\,(t)\,I_{oT}{}^{\delta}\left[1+\delta\sum_{j=1}^{N} m_j\cos\,(K_{gj}x)\right]. \tag{3-26}$$

The total variation of the refractive depends on N harmonics terms, each one associated with the corresponding j-th hologram having a beam intensity modulation m_j and grating wave vector K_{gj}. The corresponding grating modulation, $\Delta n_j(t)$, grows as

$$\frac{d}{dt}\Delta n_j(t) = m_j c_n \delta k_R(t)\,[M]\,(t)\,I_{oT}{}^{\delta}, \tag{3-27}$$

for $j = 1, 2, 3, \ldots, N$. By introducing the polymerization function, $k_R(t)$, defined here as

$$k_R(t) = k_o \exp\left(I_{oT}{}^{\delta} t \right) \tag{3-28}$$

we can solve the Eq.'s 3-23 and 3-27. In fact, using the boundary conditions $[M](0) = [M]_o$, and $\Delta n_j(0) = 0$, for $j = 1, 2, 3, 4, \ldots, N$, we can describe in closed form the free monomer depletion, and the grating evolution in HRF-150-38 DuPont photopolymer using I/C illumination respectively as

$$[M]\,(t) = [M]_o \exp\left[\gamma\left(1 - \exp\left(t/\tau_T\right)\right)\right], \text{ and} \tag{3-29}$$

$$\Delta n_j(t) = m_j \Delta n_M \left\{1 - \exp\left[\gamma\left(1 - \exp\left(t/\tau_T\right)\right)\right]\right\}, \text{ for } j = 1,2,3,\ldots, N; \tag{3-30}$$

in which the time constant, τ_T, depends on the total average recording intensity according to $\tau_T = (\varphi I_{oT}{}^{\delta})^{-1}$. At saturation, the grating modulation is

$$\Delta n_j = m_j \Delta n_M \text{ , for } j = 1,2,3,\ldots, N, \tag{3-31}$$

in which the term $\Delta n_M = \delta c_n k_o [M]_o$ stands for the maximum refractive index modulation achievable by a single grating recording with a beam intensity modulation of unity.

From interpreting the theoretical model of Eq.'s 3-30 and 3-31, a number of important of characteristic features can be deduced from multiple grating recording using I/C exposure. While the grating modulation of each sub-hologram apparently looks like that of the single grating case, the presence of other

gratings manifests itself by reducing the value of the beam intensity modulation through the total average recording intensity in the denominator of Eq. 3-22. This implies that when N sub-holograms are recorded with N pairs of beams of identical intensity, the final grating modulation at saturation will be scaled by a factor N^{-1} (and N^{-2} for the diffraction efficiency) if compared to the grating modulation at saturation of the single grating recording case as indicated in Eq. 2-17. Moreover, the temporal evolution of each multiplexed sub-hologram is ruled by the same time constant τ_T, and therefore all the gratings must show similar temporal evolution, once scaled by the corresponding beam intensity modulation term m_j.

It is interesting to note that the apparent formal similarity among the solutions of the single grating recording model, the ILA recording, and the I/C multiple recording it is, indeed, more precisely a different expression of the same general model. In fact, the single grating model and the ILA model can be seen as subsets of a general I/C recording model, where the number of the recording pair is $N = 1$ for the single grating recording, and for the ILA, $N = 2$, with the associated $I_{2J} = I_i$ and $I_{22} = 0$.

There is a parallel between I/C recording in photopolymers and photorefractive crystals. Even though photorefractive crystals are governed by different physics, it has been shown that they exhibit the same N^{-1} scaling factor of the grating modulation (and N^{-2} for the diffraction efficiency) when exposed to simultaneous recording [Malinoff and Johnson, 1991]. This scaling factor badly affects the performance of the materials because it limits their storage

capacity. At the same time, knowledge of this characteristic may be used to achieve desirable results. In Chap. 6, which is dedicated to the study of hologram copying, we illustrate that this scaling factor is the fundamental requisite in a copying technique called blind copying, which can be performed independently if the materials used are photorefractive crystals or photopolymers.

3.5.1 I/C Multiple Grating Recording: Experimental Set-Up

The experimental set-up designed to test out theoretical model of I/C recording in HRF-150-38 is depicted in Fig. 3-6. An argon-ion laser with a wavelength of 514 nm provided the recording light, which, through a system of beam splitters, yielded $N = 2$ couples of recording beams. In order to create the mutual incoherence, part of the argon-ion beam, after a first beam splitter, was reflected from a mirror whose position was modulated by a piezo-electric driver. The set-up and the data referring to the piezo-electric transducer, and its modulation, are the same as those presented in a previous section regarding ILA recording. This phase modulated beam was split by the beam splitter '*A*', thus generating beams I_{A1} and I_{A2}, (with an associated intensity beam modulation m_A) which recorded the grating '*A*'. The other couple of recording beams, I_{B1} and I_{B2}, originated at the beam splitter'*B*'; the associated beam intensity modulation was termed as m_B, with the corresponding grating '*B*'. During each recording, a couple of neutral density filters were used to change the value of I_{B1} and I_{B2}, which therefore induced a change of m_A and m_B according to Eq. 3-22. The intensities of the recording beams I_{A1} and I_{A2} remained unchanged

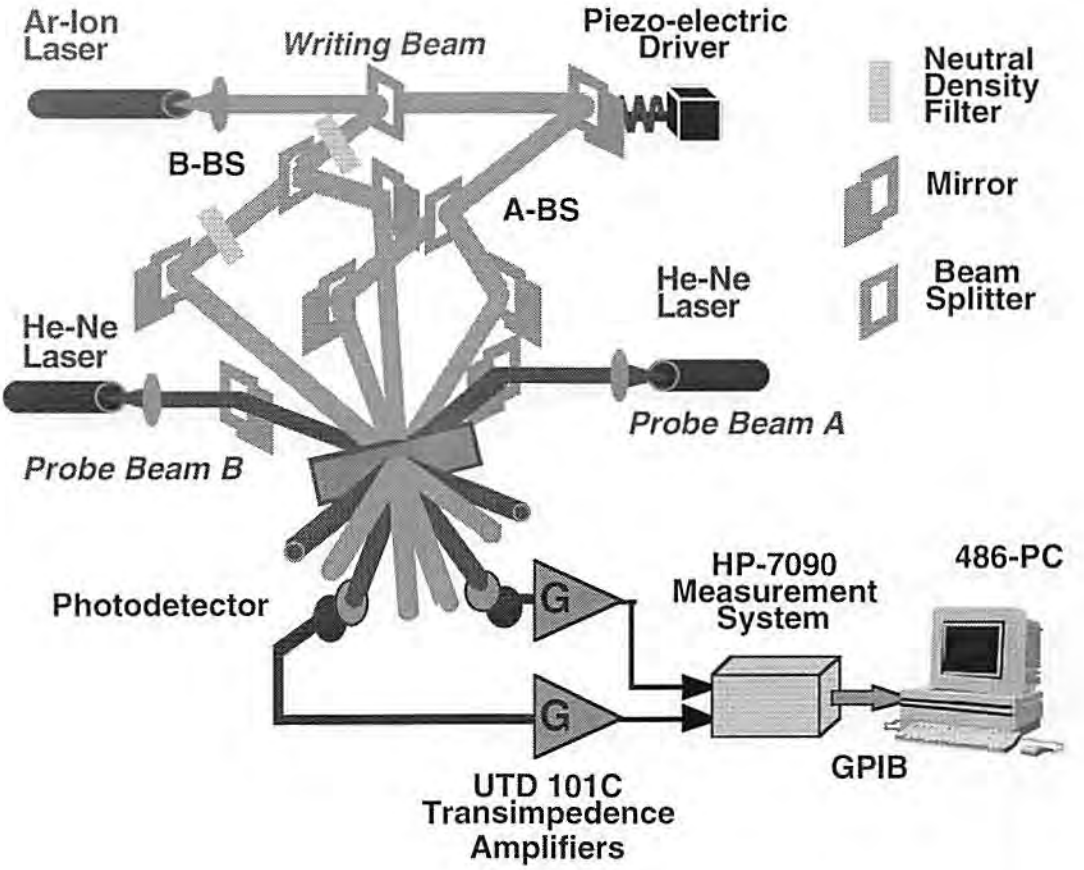

Figure 3-6. Experimental set-up for the simultaneous recording of two gratings using the I/C recording. A single argon-ion laser, at a wavelength of 514 nm, generates the recording light, which is split to form the *A*-couple and *B*-couple of beams, generated at the beam splitters '*A*' and '*B*'. The beam couple '*A*' is phase modulated by a mirror mounted on a piezo-electric transducer. The intensity of the beam couple '*B*' is modulated by two neutral density filters, as indicated in the picture. The formation of the two gratings is monitored by the probe beams '*A*' and '*B*', properly Bragg matched which are generated by two different Helium-Neon lasers, at a wavelength of 633 nm. The reading of the first orders of the probe beams are detected, and stored in a 486-PC.

throughout the experiments. Because it was needed to monitor in real time the recording of the two gratings, two helium-neon lasers provided the Bragg matched probe beams *'A'* and *'B'* at a wavelength of 633 nm. The first-orders of the diffracted probe beams were read out in real time by two corresponding photodetectors, whose readings were stored in a personal computer.

A more detailed representation of the recording scenario is depicted in Fig. 3-7. The *'A'* and *'B'* beam pairs interfere in specular symmetry around the normal to the holographic film. Each recording couple had an angular span of 50°.

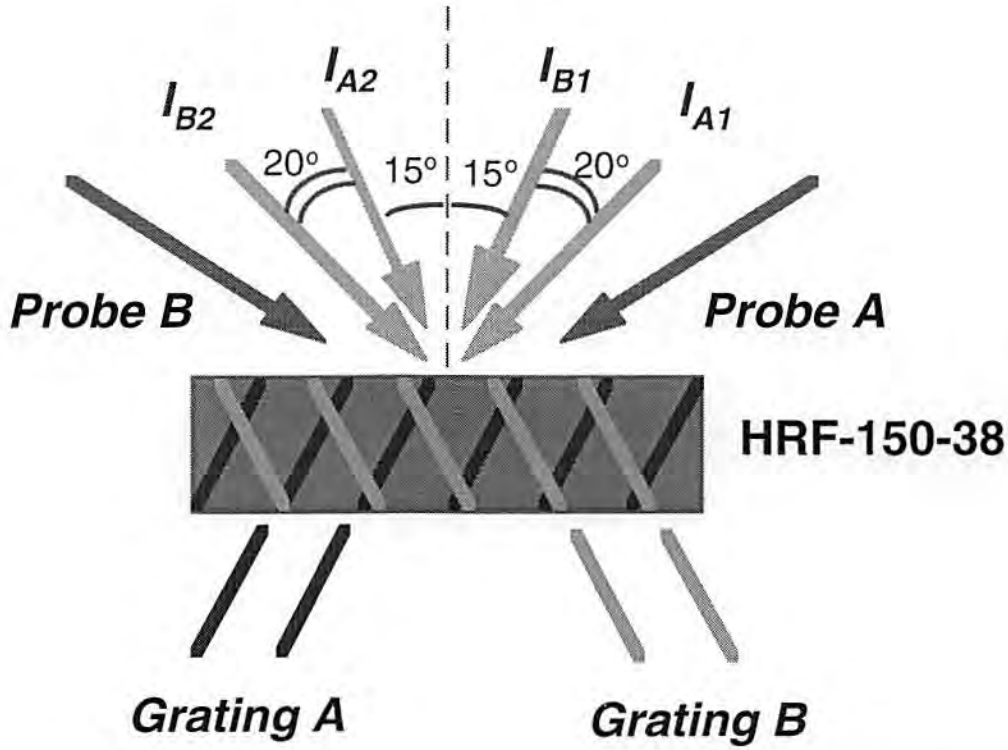

Figure 3-7. Allocation of the incident recording beams. The two couples of recording beams impinge symmetrically upon the HRF-150-38 film. The total angle within each beam pair is 50°, with their bisect at ± 10° with respect to the film normal. The probe beams are Bragg matched to the beams I_{A2}, and I_{B2}.

The line bisecting each recording pair was tilted ±10° with respect to the normal. The resulting gratings were symmetrically slanted with an internal angle obtained by Snell's law of ±6.2°. This allocation of the angles incidence of the recording beams prevented any form of off-Bragg couplings, which can be highly detrimental during the recording and monitoring of grating formation. The probe beams'A' and'B' were Bragg matched to the external writing beams I_{A1} and I_{B2}, respectively.

3.5.2 Experimental Results of I/C Recording in Photopolymers

According to theory, I/C recording should produce gratings which grow in sync, and which reach a saturation value proportional to the respective beam intensity modulation values, as in Eq. 3-31. To confirm these basic predictions of the theory, we carried out a number of exposures in which we varied the intensity I_{B2} (Exp. # 1), and then the intensities of both the I_{B1} and I_{B2} (Exp. # 2) while keeping, in this latter case, their ratio constant. The beam intensity of the A-couple was kept constant: $I_{A1} = 2.14$ and $I_{A2} = 3.3$ mW/cm^2. As indicated by the theory, a change of the magnitude of the intensity of a single beam is reflected in a change of the total intensity, I_{oT}, and consequently each of beam intensity modulation values will change according to Eq. 3-22. This two sets of experiments served to prove that, in I/C multiple recording, the only parameter that controls the saturation value of the gratings is the values of their beam intensity modulations, and not the values of the single recording intensities. In other terms, we can say that the saturation values of the different

refractive index modulations depend only on their corresponding beam intensity modulation values m_A and m_B (Eq. 3-31), but not on the specific intensities I_{A1}, I_{A2}, I_{B1}, and I_{B2}.

In the presence of an asymmetric recording geometry with slanted gratings, it was necessary to express the impinging intensities with the magnitude of their Poynting vector to calculate the values of the beam intensity modulations, m_A and m_B. To have a consistent statistics, for each pair of values (m_A and m_B), we recorded three or four different exposures. The total intensity was kept relatively low, $I_{oT} < 21$ mW/cm^2, in order to ensure the validity of the HFMD model.

A summary of the data resulting from Exp. # 1 is presented in Table 2, where the last two columns indicate the range of saturation diffraction efficiency corresponding to each pair of m_A and m_B values.

Table 2: Multiple Grating Recording: Experiment # 1

I_{A1} (mW/cm^2)	I_{A2} (mW/cm^2)	I_{B1} (mW/cm^2)	I_{B2} (mW/cm^2)	m_A	m_B	$\eta_{Sat\text{-}A}$%	$\eta_{Sat\text{-}B}$%
2.14	2.3	7.1	9.36	0.24	0.74	5.1-6.8	42.5-46.8
2.14	2.3	7.1	8	0.26	0.73	7.6-9.0	38.2-50.2
2.14	2.3	7.1	5.8	0.29	0.70	7.8-11.8	38.2-48.1
2.14	2.3	7.1	3.4	0.34	0.63	11.8-12.4	33.3-39.7
2.14	2.3	7.1	0.81	0.41	0.37	13.0-14.7	9.9-12.5

The temporal evolution of these recordings are depicted (only one exposure for each couple of m_A and m_B values) in Fig. 3-8. As shown in the figure,

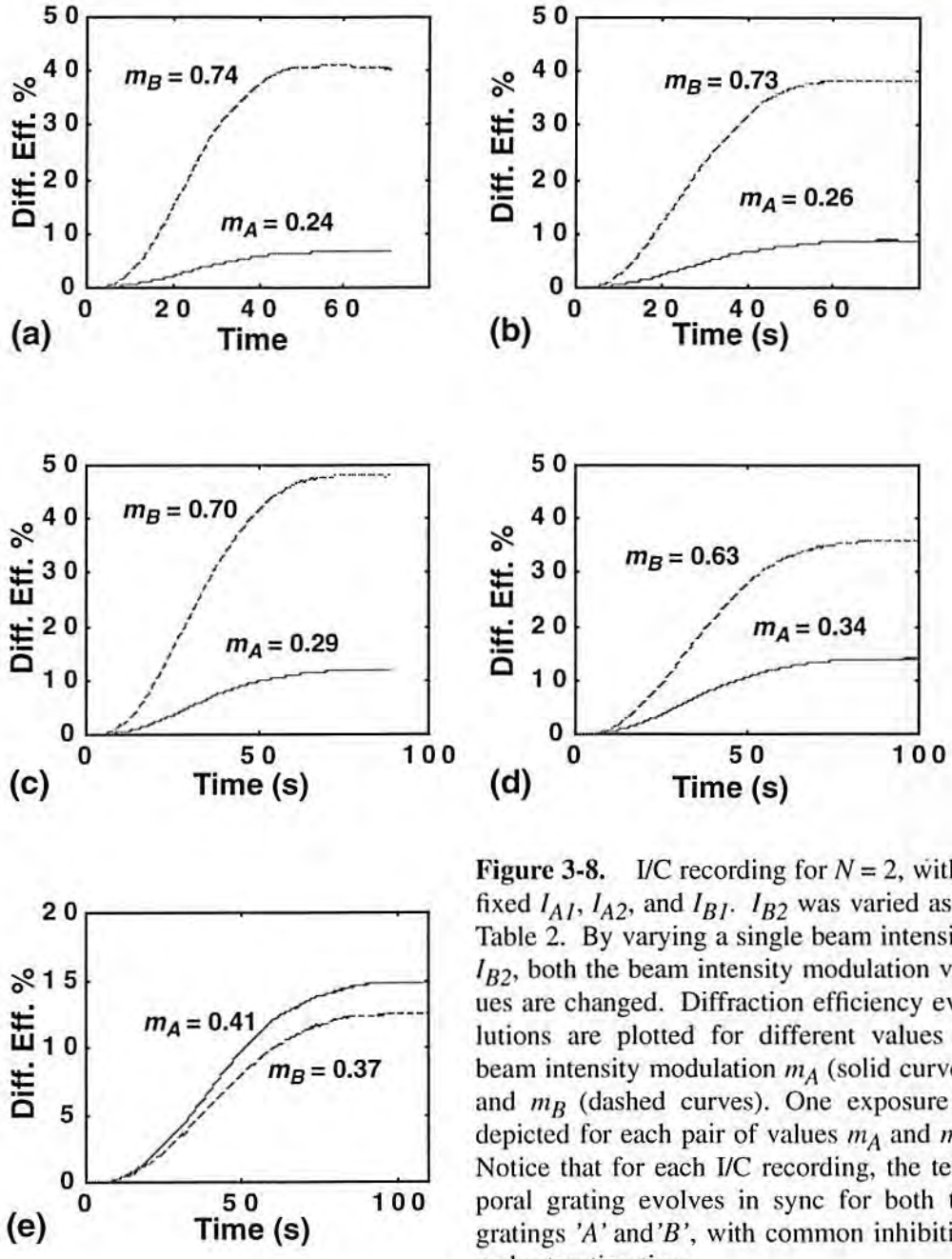

Figure 3-8. I/C recording for $N = 2$, with a fixed I_{A1}, I_{A2}, and I_{B1}. I_{B2} was varied as in Table 2. By varying a single beam intensity, I_{B2}, both the beam intensity modulation values are changed. Diffraction efficiency evolutions are plotted for different values of beam intensity modulation m_A (solid curves) and m_B (dashed curves). One exposure is depicted for each pair of values m_A and m_B. Notice that for each I/C recording, the temporal grating evolves in sync for both the gratings *'A'* and *'B'*, with common inhibition and saturation time.

during exposure the formation of the 'A' and 'B' gratings begins and ends in unison, with a common inhibition time interval and common saturation time. It can be shown that the temporal evolution of the diffraction efficiencies for the gratings 'A' and 'B' are the same, once normalized by their corresponding saturation diffraction efficiency values. As evidenced by the plots, the grating written with the highest beam intensity modulation consistently has the highest saturation diffraction efficiency, while in Fig. 3-8 (e) both the recorded gratings have similar dynamics, and comparable diffraction efficiency at saturation since the beam intensity modulations are similar in magnitude ($m_A = 0.41$, and $m_B = 0.37$).

The numerical results of Exp. # 2 are summarized in Table 3.

Table 3: Multiple Grating Recording: Experiment # 2

I_{A1} (mW/cm^2)	I_{A2} (mW/cm^2)	I_{B1} (mW/cm^2)	I_{B2} (mW/cm^2)	m_A	m_B	η_A%	η_B%
2.14	2.3	7.3	9.3	0.24	0.74	6.9-8.5	42.5-50.9
2.14	2.3	6.36	8.1	0.26	0.71	6.6-10.2	39.6-48.0
2.14	2.3	4.6	5.8	0.33	0.65	12.6-14.2	37.7-39.0
2.14	2.3	0.67	0.87	0.76	0.22	38.1-47.3	5.1-6.7
2.14	2.3	2.24	2.8	0.50	0.48	21.5-30.1	19.5-26.3

During this set of experiments, the ratio $I_{B2}/I_{B1} \approx 1.2$ was kept (almost) constant, while the neutral density filter in front of the beam splitter 'B' changed the total intensity of the 'B' recording beam pair. Figure 3-9 depicts the temporal evolution of the diffraction efficiencies for the different values of m_A and

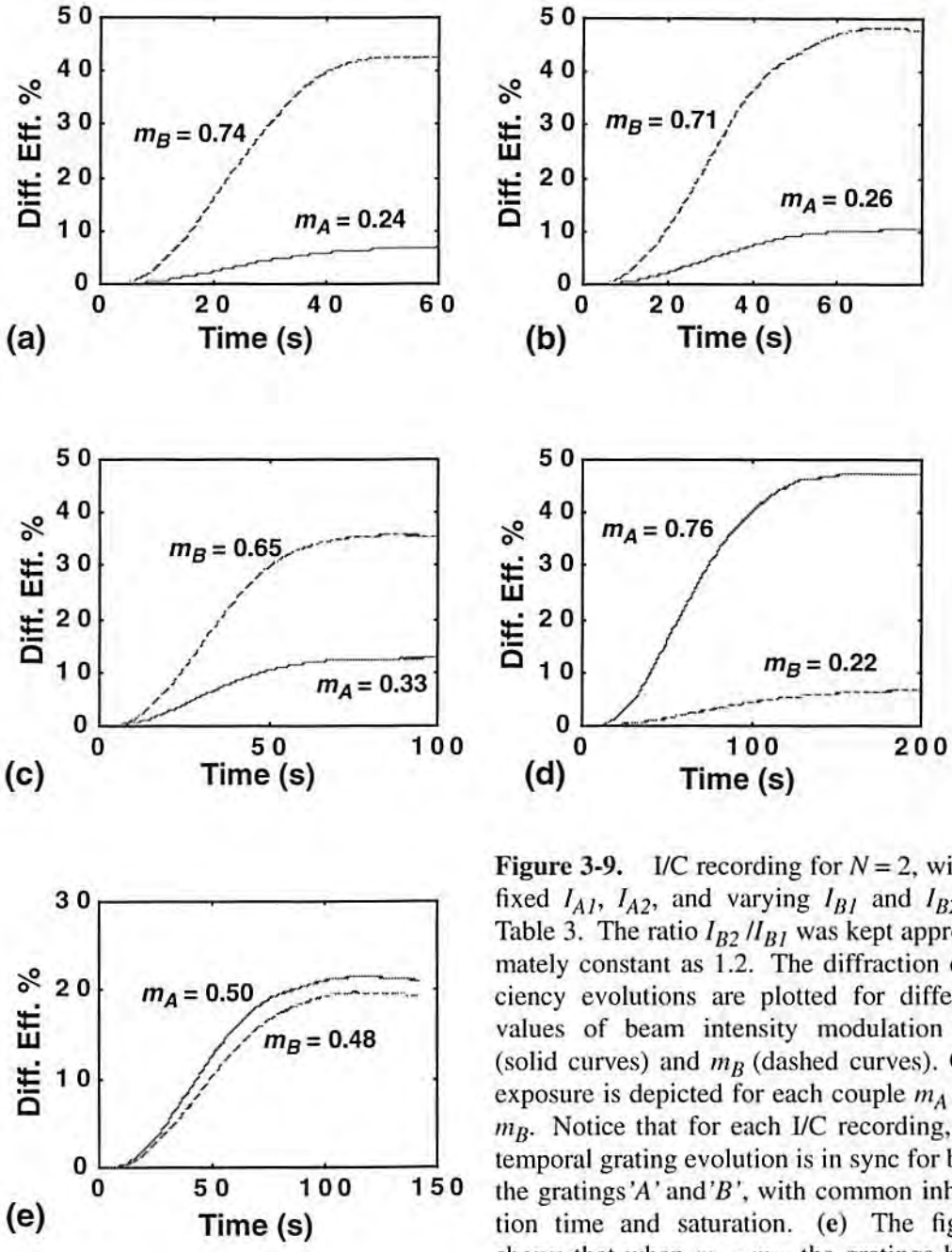

Figure 3-9. I/C recording for $N = 2$, with a fixed I_{A1}, I_{A2}, and varying I_{B1} and I_{B2} in Table 3. The ratio I_{B2}/I_{B1} was kept approximately constant as 1.2. The diffraction efficiency evolutions are plotted for different values of beam intensity modulation m_A (solid curves) and m_B (dashed curves). One exposure is depicted for each couple m_A and m_B. Notice that for each I/C recording, the temporal grating evolution is in sync for both the gratings 'A' and 'B', with common inhibition time and saturation. (**e**) The figure shows that when $m_A \approx m_B$, the gratings have almost the same diffraction efficiency evolution.

m_B. As qualitative proof of the validity of the theory, Fig. 3-9 (e) shows the temporal evolution of the diffraction efficiencies for two gratings when $m_A \approx m_B$. In agreement with theory, both the gratings have the same temporal evolution and similar saturation value of their diffraction efficiencies.

To further test the theoretical treatment of the I/C recording, it is essential to confirm that all the saturation diffraction efficiency values obey to Eq. 3-31 independently of the way that the pair m_A and m_B is generated. In other words, a cumulative plot of the saturation diffraction efficiencies measured during Exp. # 1 and Exp. # 2 must agree with the theoretical result of the coupled wave theory, which indicates that the diffraction efficiency of a slanted phase grating hologram (like those of our experiments) varies as [Kogelnik, 1969]

$$\eta_{jsat} = 100\frac{\cos(\theta_S)}{\cos(\theta_R)}\sin^2\left(\frac{\pi m_j \Delta n_M T}{\lambda_p\sqrt{\cos(\theta_R)\cos(\theta_S)}}\right), \qquad (3\text{-}32)$$

in which $T = 38$ μm is the material thickness, $m_j = m_A$ or m_B, and the angles θ_R and θ_S are the incidence angles of the (reference and signal) beams inside the photopolymer, respectively. From our experimental data, we first calculated the cosine ratio (for both the gratings '*A*' and '*B*') of the above equation $\cos(\theta_S)/(\cos(\theta_R)) = 1.09$. Furthermore, to compare the theoretical behavior and the experimental one we extracted from our measurements (using Eq. 3-32) the constant term $\pi\Delta n_M T/\left(\lambda_p\sqrt{\cos(\theta_R)\cos(\theta_S)}\right)$ from each of the recording from Exp. # 1, and Exp. # 2, whose average gave $\pi\Delta n_M T/\left(\lambda_p\sqrt{\cos(\theta_R)\cos(\theta_S)}\right) = 0.988$. Again, the reader should notice that the above constant parameter is relevant to the probe beams with wavelength

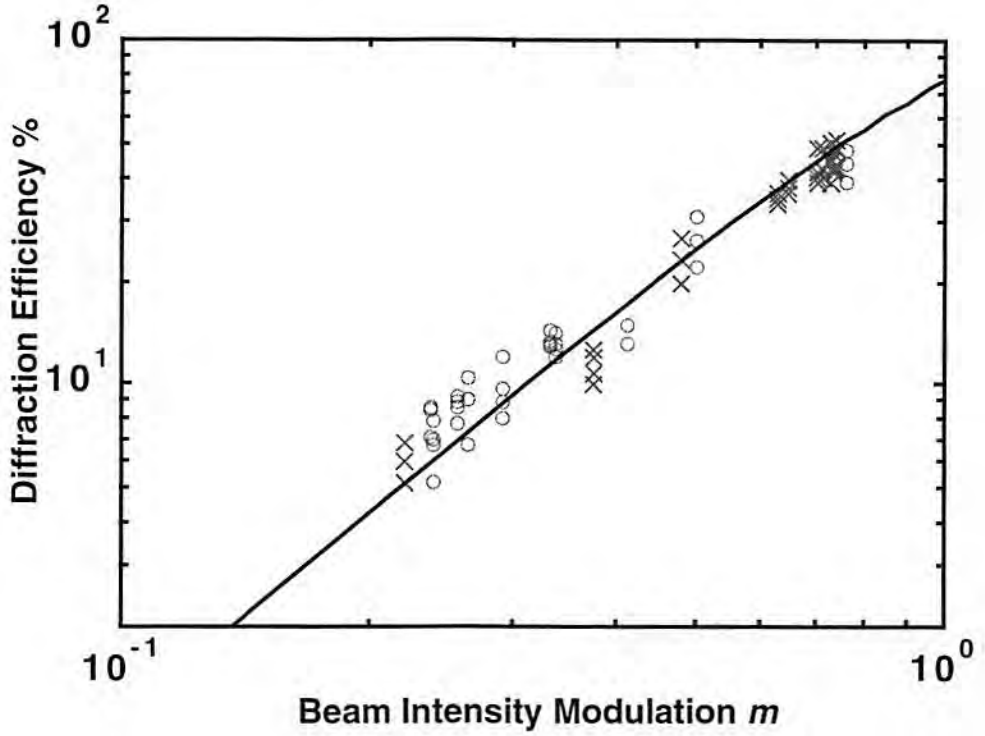

Figure 3-10. Cumulative results from Exp. # 1 and Exp. # 2. The measured saturation diffraction efficiencies are plotted versus their corresponding beam intensity modulation. The open circles (o) correspond to data from Exp. # 1, and the crosses (x) are data from Exp. # 2, while the solid line shows the theoretical prediction. At low values of m, the experimental data tend to be slightly higher than the theory prediction, probably due to a monomer diffusion mechanism during recording.

λ_p = 633 nm which reconstruct the holograms associated with the gratings '*A*', and '*B*'. Finally, in Fig. 3-9 is depicted the saturation diffraction efficiency with the beam modulation intensity. The complete data from Exp. # 1 (o) and Exp. # 2 (x) are reported in the figure versus the theoretical behavior (solid line). Independently of experimental sets, the measured saturation diffraction efficiencies follows the theory. There is a tendency, however, to present for

lower m_j values to result in saturation diffraction efficiency values slightly higher than expected. We relate this tendency toward higher efficiency at lower m_j by postulating a different material response to the two grating formation processes. To better visualize this concept, consider a recording scenarios with $N = 2$ and $m_A > m_B$, which implies a larger intensity peak for the grating '*A*'. The material viscosity changes during polymerization, therefore, during I/C recording, the material will tend to be more viscous in the region of the intensity peaks of grating '*A*'. This favors the migration of free monomers toward the bright peaks of the grating '*B*' (where the material is less viscous), with consequent photopolymerization, and a growth of the refractive index modulation of grating '*B*' larger than expected. A simple solution to this problem is to expose with a very low total average recording intensity, I_{oT}. In this condition, not only the HFMD assumption is stronger, but the change of material viscosity is so slow (see Chap. 2) that the monomer diffusion competition between different gratings cannot occur.

3.6 Conclusive Remarks

In this chapter we have illustrated and experimentally confirmed that, given the HFMD hypothesis, we can model the recording and the formation of multiple gratings in HRF-150-38 photopolymer. Moreover, we have linked in a general model the multiple grating formation, using I/C illumination, the single grating formation model, and the incoherent light addition model. The I/C model, however, is only valid when all the recording beams have the same

wavelength. In fact, the model considers that all the beams contribute in the same fashion to photopolymerization through the polymerization function $k_R(t)$, which is wavelength sensitive because it is related to the material initiation efficiency. When the recording beam pair wavelengths differ, each pair of writing beams must be associated with its own polymerization function which can have different functional dependencies. In this case, the grating evolution may not be describable in closed form.

3.7 Bibliography

Curtis, K. and D. Psaltis, "Recording of Multiple Holograms in Photopolymers Films," Appl. Opt., **31**, 7425-7428, (1992).

Hong, J. H., I. McMichael, T. Y. Chang, W. Christian, and E. G. Paek, "Volume Holographic Memory Systems: Technique and Architectures," Opt. Eng., **34**(8),1995

Jenkins, B. K., G. C. Petrisor, S. Piazzolla, P. Asthana, and A. R. T. Jr., "Photonic Architecture for Neural Nets Using Incoherent/Coherent Holographic Interconnections," Optical Computing 90, Kobe, Japan, (1990).

Jewell, J., Y. Lee, A. Scherer, S. McCall, and N. O. e. al., "Surface-Emitting Microlasers for Photonic Switching and Interchip Connections," Opt. Eng., **29**(3), 210, (1990).

Kogelnik, H., "Coupled Wave Theory for Thick Holographic Gratings," Bell System Technical Journal, **48**(9), 2909-2947, (1969).

Kostuk, R. K., "Comparison of Models for Multiplexed Holograms," Appl. Opt., **28**(4), 771-777, (1989).

Malinoff, E., S., and Johnson, "Maximized Photorefractive Holographic Storage," J. Appl. Phys. **70**(9), 4702-4707, (1991)

Mok, F. H., "Angle-Multiplexed Storage of 5000 Holograms in Lithium Niobate," Opt. Lett., **18**(11), 915-917, (1993).

Piazzolla, S., B. K. Jenkins, and J. A. R. Tanguay, "Single-step copying process for Multiplexed Volume Holograms," Opt. Lett., **17**(9), 676-678, (1992).

Tao, S., D. R. Selviah, and J. E. Midwinter, "Spatioangular Multiplexed Storage of 750 Holograms in a Fe:Li:NbO_3 Crystal," Opt. Lett., **18**(11), 912-914, (1993).

Chapter 4

Self Diffraction in Holographic Photopolymers

4.1 Introduction

When two coherent beams interfere in a real time holographic material, they write a holographic grating which simultaneously begins to couple the energy of the recording beams between each other. Because of this field coupling, the phase and the intensity of the writing beams change within the hologram and during the exposure time, while the recorded grating dynamically changes in time and space its phase and amplitude modulation in a nonlinear fashion. This process is termed self diffraction or self scattering, and intrinsically manifests itself only in real time holographic materials such as photorefractive crystals or photopolymers.

The nature of self diffraction has been extensively studied in photorefractive crystals, and it plays a key role in a number applications [Gunter and Huignard, 1988]. To our knowledge, however, no investigation has been undertaken until now to understand the effects of self diffraction in photopolymers, probably due to the quite recent introduction of more reliable photopolymer materials

and to the lack of theoretical modelling of the grating formation process in these materials. According to our findings, which are illustrated in this chapter, the effects of self diffraction can be a major obstacle when a thick photopolymer is used for applications in data storage and/or optical interconnections. Moreover, because of the generality of the problem, self diffraction can appear in future real-time volume holographic materials, and therefore the results presented in this chapter may be applicable to these future materials as well.

In this chapter, after a first qualitative and a theoretical description of this problem, we present the results of a computer simulation describing the effects of self diffraction in volume holographic photopolymers. These simulation results are also compared to experimental data that we have obtained from measurements of holograms exposed in HRF-150-38 photopolymers.

4.2 Effects of Self Diffraction in Holographic Photopolymers

A simple and pictorial way to describe the effects and consequences of self diffraction in holographic photopolymers can be attempted with the help of Fig. 4-1 (a), which depicts the recording of a transmission grating by two beams whose electric fields are described as

$$E_1(\underline{r}) = E_{1o}\exp(-j\underline{\rho}\cdot\underline{r}) \text{ , and} \tag{4-1}$$

$$E_2(\underline{r}) = E_{2o}\exp(-j\underline{\sigma}\cdot\underline{r}) \tag{4-2}$$

where E_{1o} and E_{2o} are the amplitudes of the electric fields which are here supposed to be positive real values, and $\underline{r}$ is the position vector. The holographic

material is in the region between $z = 0$ and $z = T$. Due to the symmetry of the recording, the wavevectors $\underline{\rho}$ and $\underline{\sigma}$ have the same magnitude. The recording beam amplitudes or intensities define the beam intensity ratio, BR, which is

$$BR = \frac{E_{1o}^2}{E_{2o}^2} = \frac{I_1}{I_2} . \tag{4-3}$$

For this example we suppose that the beam intensity ratio is much larger than one, $BR = (E_{1o}/E_{2o})^2 >> 1$. The interference of the two beams creates an interference pattern inside the holographic medium as

$$I(x) \propto \left|E_1(\underline{r}) + E_2(\underline{r})\right|^2 = E_{1o}^2 + E_{1o}^2 + 2E_{1o}E_{2o}\cos(K_g x) \tag{4-4}$$

in which the term $K_g = |\underline{\rho} - \underline{\sigma}|$ is the grating wavenumber, Fig. 4-1 (c). According to the theory presented in Chap. 2 Sec. 2.5, and to Eq.'s 2-10 and 2-13, we know that, during exposure holographic, photopolymers respond to the interference pattern writing a grating whose amplitude modulation spatially maps the interference pattern, while the amplitude modulation of the recording grating itself is proportional to the modulation term in Eq. 4-4. Therefore, we can consider that after time Δt the beam interference has written a holographic grating of initial amplitude modulation Δn and associated complex amplitude diffraction efficiency $\tilde{\eta}$ as [Kogelnik, 1969]

$$\tilde{\eta} = -j\sin\left(\frac{\pi\Delta nT}{\cos(\theta_b)\lambda}\right) \approx -j\frac{\pi\Delta nT}{\cos(\theta_b)\lambda}, \tag{4-5}$$

in which T is the hologram thickness, and the approximation sign is valid for low levels of diffraction. The grating amplitude modulation Δn is here a posi-

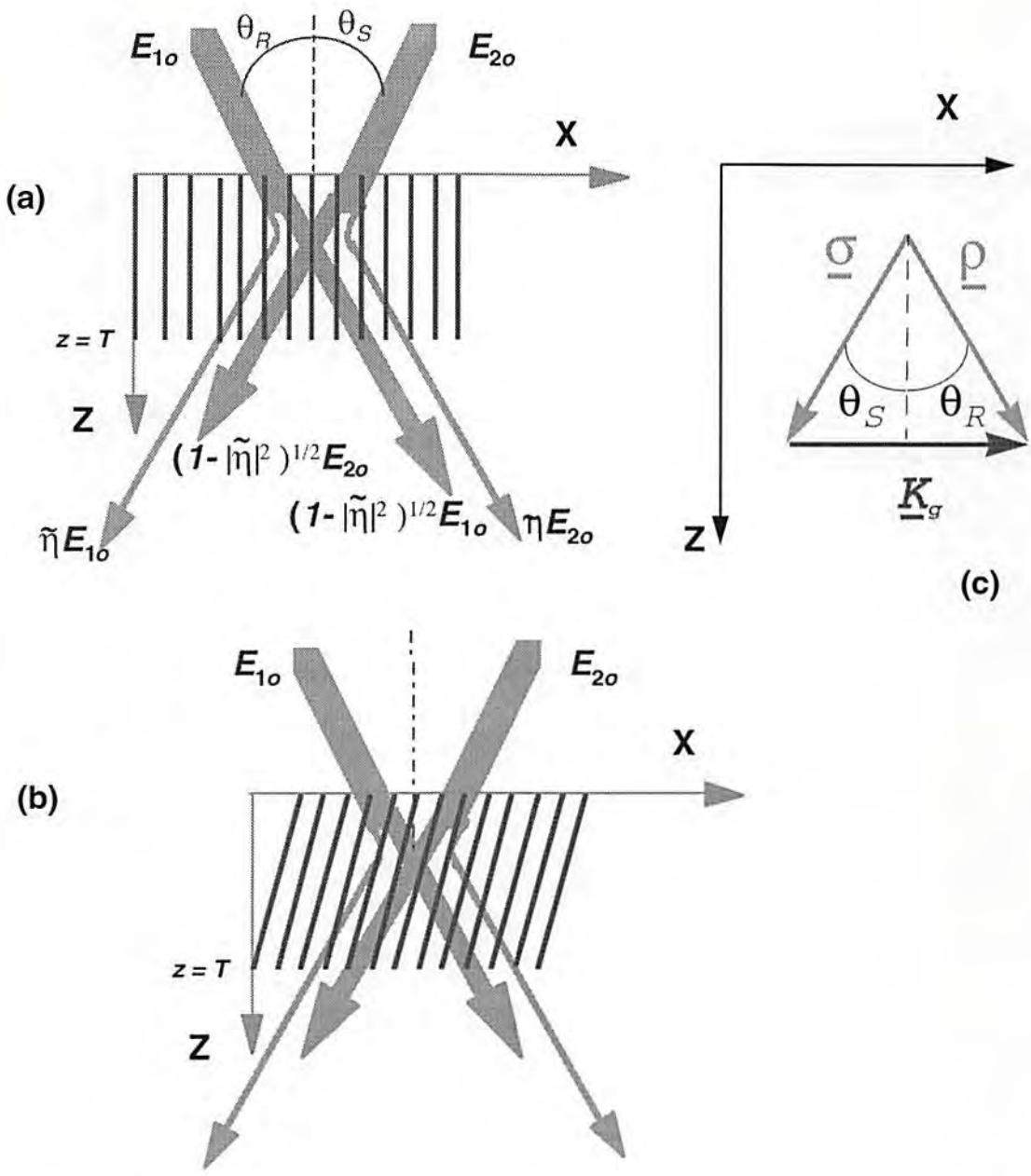

Figure 4-1. Example of self diffraction in photopolymers. **(a)** At the beginning of the grating there are two fields with amplitude E_1 and E_2. The output electromagnetic fields are changed in amplitude and phase due to diffraction. The term $\tilde{\eta}$ indicates the complex field amplitude diffraction efficiency. **(b)** During holographic exposure, self diffraction causes, among the other things, the change of grating geometry of the from unslanted to slanted. **c)** Geometrical relations among the field wavevectors and the grating wavevector.

tive number, and (for the moment) uniform within the holographic region; the grating is unslanted (at this time of the recording), Fig. 4-1 (a); the complex amplitude diffraction efficiency $\tilde{\eta}$ in Eq. 4-5 is a pure imaginary term. During holographic readout, the ratio of the amplitude of the diffracted first order (at $z = T$) over the amplitude of a readout beam at $z = 0$ defines the complex amplitude diffraction efficiency $\tilde{\eta}$.

At this instant of the exposure (time Δt) the recording process has not been completed yet, however the presence of the holographic grating with amplitude modulation Δn causes some interesting consequences. In fact, according to the coupled wave theory [Kogelnik, 1969], the complex amplitudes of the recording beams change from E_{1o} and E_{2o} at the beginning of the holographic region ($z = 0$) respectively to

$$E_{1T}(\Delta t) = \left(1 - |\tilde{\eta}|^2\right)^{1/2} E_{1o} + \tilde{\eta} E_{2o} \approx \left(1 - |\tilde{\eta}|^2\right)^{1/2} E_{1o} \text{ and} \quad (4\text{-}6)$$

$$E_{2T}(\Delta t) = \tilde{\eta} E_{1o} + \left(1 - |\tilde{\eta}|^2\right)^{1/2} E_{2o} \approx \tilde{\eta} E_{1o}\,, \quad (4\text{-}7)$$

at $z = T$, in which the approximation sign is valid because we supposed $BR >> 1$ and $\tilde{\eta}$ large enough to allows such approximations. This change of the complex field amplitudes of the recording beams within the holographic regions also indicates that the modulation term of the interference pattern changes in amplitude and phase within the holographic region as

$$2E_{2o}E_{1o}\cos(K_g x)\,, \text{ at } z = 0; \quad (4\text{-}8)$$

$$2|\tilde{\eta}|\left(1-|\tilde{\eta}|^2\right)^{1/2}E_{1o}^2\cos\left(K_g x+\frac{\pi}{2}\right),\ \text{at } z=T. \tag{4-9}$$

Again, according to the HFMD model, the material must respond to the wave interference, writing a grating update which has phase 'locked' to the interference pattern, and amplitude modulation value proportional to the modulation term of the interference. Therefore in the next Δt seconds the grating update will be modulated in amplitude and phase along the z-axis, and if we consider the total recorded grating (the integration of the preexisting grating with the grating update) after $2\Delta t$ seconds, it can appear modulated in amplitude and phase, which changes, among the other things, the hologram geometry from unslanted to slanted. The slanting inclination angle is related to the BR and the recording geometry, for example for $BR >> 1$ and for the recording geometry in Fig. 4-1 (a), the inclination of the slanting angle is as in Fig 4-1 (c).

This process of interaction among the recording waves and the written grating continuously changes (in space and time) the beam intensity ratio within the holographic region which we indicate as $BR(z,t)$. The absence of coupling effect at $z = 0$, however, causes the following identities

$$BR = BR(0,t) = BR(0,0). \tag{4-10}$$

This energy coupling tends to locally equalize the intensity of the recording waves through the material, which causes $BR(z,t)$ to decrease until it reaches a value of unity. At $BR(z,t) = 1$, a recording equilibrium is reached during the process. By recording equilibrium we mean the state during the exposure at which, even in presence of coupling between the recording beams, the intensity of the recording beams does not change. In fact, if $BR(z,t) = 1$ the grating is

coupling an equivalent amount of energy from each beam to the other, resulting in a recording equilibrium. Moreover, to a beam intensity ratio of value of unity corresponds a beam intensity modulation, m, of value of unity, being

$$m(z,t) = \frac{2\sqrt{BR(z,t)}}{BR(z,t)+1}, \tag{4-11}$$

and according to the indication Eq. 2-17, such value of m compels the grating to reach a maximum attainable modulation value.

In essence, self diffraction is a dynamical process of interaction between matter (holographic photopolymers) an energy (recording beams), which can be summarized as it follows:

(1) two interfering waves write a holographic grating in a photopolymer;

(2) the grating couples the recording waves, changing their phase, amplitude, and the resulting beam intensity ratio, $BR(z,t)$, within the holographic region;

(3) the modified waves interfere and write a grating update, which may be not in phase with the preexisting one, and may be not uniform in amplitude within the holographic region;

(4) the process continues as in step **(2)** and **(3)** until saturation is reached, while the two recording waves tend to even in intensity within the holographic region, and $BR(z,t)$ tends to a value of unity;

(5) the final written grating may be bent (we show that sometimes this bending may be approximated to a slanting angle) with nonuniform amplitude modulation;

(6) because of the coupling symmetry, for an initial $BR(0,0) = 1$, self diffraction cannot take place.

We conclude this section with a short comparison between the nature of self diffraction in photorefractive crystals and in holographic photopolymers. Essentially there is one physical difference (and different consequences) between self diffraction in photopolymers and photorefractive crystals, and this is due to the different nature of the materials. In photopolymers the grating recording is a permanent process, and the newly forming gratings are continuously added to the old ones. Instead, photorefractive crystals are erasable media, as such, when self diffraction occurs, newly interfering beams partially erase the old grating, and at the same time a new grating is written. Because of this write/erase process, self diffraction has been used in a number of optical applications [Yeh *et al.*, 1989] as optical amplification and wave mixing, which cannot be extended therefore to permanent media as photopolymers.

4.3 Basic Equations Ruling Self Diffraction in Photopolymers

In this section we present our analysis that describes holographic grating recording in photopolymers in presence of self diffraction. To carry out this analysis we dynamically combine the theoretical approach of the coupled wave theory [Kogelnik, 1969] with the results of the HFMD model (Chap. 2). In order to accomplish this goal, we first introduce and define (and sometimes redefine with respect to the notions introduced in Chap. 2) the physical variables of the problem, and then we proceed with the theoretical treatment.

The geometry of the problem is depicted in Fig. 4-3. Within the holographic region the total electromagnetic field, $E_T(\underline{r}, t)$, is the combination of two TE polarized plane waves with field of amplitude $E_1(\underline{r}, t)$ and $E_2(\underline{r}, t)$, which are interfering in the material, the angles that the two waves make with the z-axis being θ_R and θ_S, respectively. The symbol $\underline{r}$ is the position vector. The waves write a phase transmission hologram in a lossy medium. One may notice that in this treatment we prefer to use the complex amplitude of the electromagnetic fields, instead of the field intensity (as previously done in Chap. 2 and 3) to describe the grating formation process. The reason for this different approach is the need to retain the phase information of the recording waves and of the grating, while keeping the analytical treatment mathematically simple (to the extent).

Within the holographic grating region, which we are going to characterize, the propagating (and recording) waves can be described in complex notations as

$$E_1(\underline{r}, t) = R(z, t) \exp(-j\underline{\rho} \cdot \underline{r}) \text{ , and} \tag{4-12}$$

$$E_2(\underline{r}, t) = S(z, t) \exp(-j\underline{\sigma} \cdot \underline{r}) \text{ ,} \tag{4-13}$$

where the complex amplitude terms, $R(z,t)$ and $S(z,t)$, change in time because of fields interaction with the growing diffractive grating, with the relations

$$R(0, t) = R(0, 0) = E_{1o} \text{ and } S(0, t) = S(0, 0) = E_{2o} \text{ .} \tag{4-14}$$

The wavevectors, $\underline{\rho}$ and $\underline{\sigma}$, are related to the grating wavevector by the Bragg vector relation

$$\underline{K}_g = \underline{\rho} - \underline{\sigma} \tag{4-15}$$

as visualized in Fig. 4-3 (c), standing the relation

$$|\underline{\rho}| = |\underline{\sigma}| = \beta n_o = \frac{2\pi}{\lambda} n_o \tag{4-16}$$

in which β is the wavenumber *in vacuo*, n_o is the average refractive index of the material, and λ is the wavelength *in vacuo*.

Because of the time varying recording waves, the total recording intensity varies in time and in space too. According to Eq. 4-12, and Eq. 4-13, the total recording intensity within the material is then

$$\begin{aligned} I(\underline{r}, t) &= \frac{\varepsilon_r v}{2} |E_1(\underline{r}, t) + E_2(\underline{r}, t)|^2 \\ &= \frac{\varepsilon_r v}{2} (|R(z,t)|^2 + |S(z,t)|^2 + R(z,t)\, S^*(z,t)\, e^{-j\underline{K}_g \cdot \underline{r}} + cc) \\ &= I_o(z)\ (1 + \tilde{m}(z,t)\, e^{-j\underline{K}_g \cdot \underline{r}} + cc)\,, \end{aligned} \tag{4-17}$$

in which v is the light velocity in the material, ε_r is the average material electric permittivity, *cc* denotes complex conjugate of the preceding term, the asterisk indicates the complex conjugate operator, and $I_o(z)$ is the average recording intensity (as also defined in Eq. 2-9) which varies within the hologram because of absorption. The term $\tilde{m}$ is the complex beam amplitude modulation, and is the analogous to the beam intensity modulation m, but, differently this varies in time and space during the exposure. It is given by

$$\tilde{m}(z,t) = 2\frac{R(z,t)\, S^*(z,t)}{|R(z,t)|^2 + |S(z,t)|^2}\,. \tag{4-18}$$

Self diffraction causes the recording of a refractive index modulation of the holographic grating with varying magnitude and phase (due to the grating bend-

ing during recording) along the z - axis. Therefore, $n(\underline{r}, t)$ is here described in terms of its complex amplitude $\tilde{n}(z, t)$, as

$$n(\underline{r}, t) = \frac{1}{2}[\tilde{n}(z, t)\exp(-j\underline{K}_g \cdot \underline{r}) + \tilde{n}^*(z, t)\exp(j\underline{K}_g \cdot \underline{r})] , \qquad (4\text{-}19)$$

in which, after deriving Eq.'s 2-13, 2-28, and 2-16 with the use of the complex beam amplitude modulation in Eq. 4-18, $\tilde{n}(z, t)$ varies during polymerization as

$$\frac{d}{dt}\tilde{n}(z, t) = \tilde{m}(z, t)\,\Delta n_M \frac{\gamma e^{t/\tau} e^{\gamma(1-e^{t/\tau})}}{\tau}, \qquad (4\text{-}20)$$

where (as already introduced in Chap. 2) τ is a time constant depending on the average recording intensity, k_o is the initial value of the polymerization function as $k_o = k_R(0)$, and Δn_M is the largest attainable value of the refractive index modulation.

At this point in the discussion all the physical variables necessary to describe the recording of a transmission phase grating in photopolymers in the presence of self diffraction have been defined. To analytically characterize the dynamical interaction among the forming grating and the writing beams we have now to solve the wave equation

$$(\nabla^2 + q^2) E_T = 0 \qquad (4\text{-}21)$$

where q is the propagation constant, which can be written in terms of the wave-number, the attenuation constant and the grating modulation as

$$q^2 = \left[\beta^2 (n^2{}_o + 2n_o n(\underline{r}, t)) - j2\beta\alpha\right], \qquad (4\text{-}22)$$

having already approximated the varying electric permittivity of the material,

$\varepsilon(\underline{r}, t) = (n_o + n(\underline{r}, t))^2$, as $\varepsilon(\underline{r}, t) \approx n^2{}_o + 2n_o n(\underline{r}, t)$ because $|n_o| \gg |n(\underline{r}, t)|$, while α is the attenuation constant [Kogelnik, 1969].

Solving the above, isolating the harmonic terms and neglecting the waves which do not satisfy the Bragg vector relation, the following system of differential equation holds

$$\frac{\partial^2}{\partial z^2}R(z,t) - j2\rho_z\frac{\partial}{\partial z}R(z,t) - \rho^2 R(z,t) + (\beta n_o)^2 R(z,t) - j2\alpha\beta R(z,t) + \beta n_o \tilde{n}(z,t) S(z,t) = 0, \quad (4\text{-}23)$$

$$\frac{\partial^2}{\partial z^2}S(z,t) - j2\sigma_z\frac{\partial}{\partial z}S(z,t) - \sigma^2 S(z,t) + (\beta n_o)^2 S(z,t) - j2\alpha\beta R(z,t) + \beta n_o \tilde{n}^*(z,t) R(z,t) = 0 \quad (4\text{-}24)$$

in which ρ_z and σ_z are the scalar products of the wavevectors along the z-axis being $\rho_z = \frac{2\pi}{\lambda} n_o \cos(\theta_R)$ and $\sigma_z = \frac{2\pi}{\lambda} n_o \cos(\theta_S)$, respectively.

The above equations can be sensibly simplified once we neglect the second order derivatives by applying the SVA (Slow Varying Amplitude) approximation, that is

$$\left|\frac{\partial^2}{\partial z^2}R(z,t)\right| \ll \left|2\rho_z\frac{\partial}{\partial z}R(z,t)\right|, \text{ and} \quad (4\text{-}25)$$

$$\left|\frac{\partial^2}{\partial z^2}S(z,t)\right| \ll \left|2\sigma_z\frac{\partial}{\partial z}S(z,t)\right|. \quad (4\text{-}26)$$

Furthermore, if we consider the identities of Eq. 4-16, rewrite the complex amplitude of the refractive index modulation in integral form, after Eq. 4-20 and Eq. 4-18, and simplify algebraically, the system of differential equations is then reduced to the following

$$\frac{d}{dz}R(z,t) = -\frac{\alpha}{\cos(\theta_R)}R(z,t) - j\frac{\pi\tilde{n}(z,t)}{\lambda\cos(\theta_R)}S(z,t), \quad (4\text{-}27)$$

$$\frac{d}{dz}S(z,t) = -\frac{\alpha}{\cos(\theta_S)}S(z,t) - j\frac{\pi\tilde{n}^*(z,t)}{\lambda\cos(\theta_S)}R(z,t) \ . \qquad (4\text{-}28)$$

At the same time the above equations can be dynamically expressed in terms of the recording/interfering/diffracting waves as

$$\frac{\partial}{\partial z}R(z,t) = -\frac{\alpha}{\cos(\theta_R)}R(z,t) - j\frac{2\gamma\pi\Delta n_M}{\lambda\cos(\theta_R)}S(z,t)\int_0^t \frac{R(z,t_o)\,S^*(z,t_o)}{|R(z,t_o)|^2 + |S(z,t_o)|^2}\frac{e^{t_o/\tau}\,e^{\gamma\left(1-e^{t_o/\tau}\right)}}{\tau}dt_o, \quad (4\text{-}29)$$

$$\frac{\partial}{\partial z}S(z,t) = -\frac{\alpha}{\cos(\theta_R)}S(z,t) - j\frac{2\gamma\pi\Delta n_M}{\lambda\cos(\theta_S)}R(z,t)\int_0^t \frac{S(z,t_o)\,R^*(z,t_o)\,\Delta n_M}{|R(z,t_o)|^2 + |S(z,t_o)|^2}\frac{e^{t_o/\tau}\,e^{\gamma\left(1-e^{t_o/\tau}\right)}}{\tau}dt_o \ . \quad (4\text{-}30)$$

The above system of partial differential equations are the coupled wave equations describing the variation of the field complex amplitudes during recording in the presence of self diffraction. The solutions of these coupled wave equations, $R(z,t)$ and $S(z,t)$, not only correspond to the complex amplitude of the waves but also determine, through Eq. 4-20 and Eq. 4-18, the coupling functions and the evolution of the modulation of the diffraction index.

It is not difficult to convince anybody that to find the closed form solutions to these coupled wave equations can be a topic of a lifetime unsuccessful thesis. Therefore, in the following sections, we focus our effort on solving this problem numerically and experimentally verifying the numerical findings.

4.4 Simulation of Grating Formation in Photopolymers in the Presence of Self Diffraction

The numerical program that we designed to simulate the effects of self diffraction during the recording of holographic gratings in photopolymers is entirely derived from the theory that we presented in the previous section. There are two main difficulties we faced during the preparation of this simulation: the solution waves, $R(z,t)$ and $S(z,t)$, are jointly functions of time and space and these system solutions dynamically determine in a nonlinear fashion the system coefficients, as indicated in Eq. 4-29 and Eq. 4-30. To numerically manage this dynamical system of partial differential equation, the independent variable domain was considered as a two dimensional grid of uniform increments Δt and Δz. At each instant t, belonging to the time grid, was solved the coupled wave equation as in Eq. 4-27 and 4-28 and found $R(z,t)$ and $S(z,t)$. The coupling term of the coupled wave equations at the time t was calculated taking into account the solutions of the previous time step, being $R(z,t\text{-}\Delta t)$ and $S(z, t-\Delta t)$. The time increment Δt was selected depending on the value of τ, which is related to the average recording intensity. A good heuristic estimate was $\Delta t = \tau/100$ which gives low residual errors while giving a good numerical resolution. The complex wave amplitudes were vectorized along the z-axis with uniform interval Δz. To determine the thickness increment, we considered the medium as a cascade of contiguous transmission volume holograms having the smallest required thickness, Δz, to diffract in volume regime. Determination of Δz was calculated with the help of Klein's thickness parameter Q [Gaylord and

Moharam, 1981], which is

$$Q = \frac{2\pi\lambda\Delta z}{n_o \Lambda_g^2}, \tag{4-31}$$

in which Λ_g is the grating period. According to theory, for $Q \approx \pi^2$ the hologram reconstruction is in volume regime, therefore given Eq. 4-31 we were able to select the proper Δz which we used in the simulation as

$$\Delta z = \pi \frac{n_o \Lambda_g^2}{2\lambda}. \tag{4-32}$$

The flow chart of the simulation is in Fig. 4-2. The core of this simulation is explained in more detail in the following.

(1) Grating Initial condition. Considering the instant t, the complex amplitude of the grating modulation is not supposed to change, being $\tilde{n}(z)$. For $t = 0$, $\tilde{n}(z) = 0$.

(2) Diffraction. Considering the instant t, and the associated grating modulation $\tilde{n}(z)$, the complex wave amplitudes, $R(z,t)$ and $S(z,t)$, are calculated through a coupled wave equation system having grating modulation described in step (**1**). The boundary conditions are $R(0,t) = E_1(0,0)$, and $S(0,t) = E_2(0,0)$. When very thick holograms are analyzed ($T >> 100$ μm), variation of the attenuation constant must be taken into account.

(3) Grating update. The complex amplitude of the refractive index modulation is updated for the next temporal step. Note that this new update is necessary because the waves diffracted as in step (**2**), contribute now to modify the grating modulation amplitude. After Eq. 4-20, the grating update is

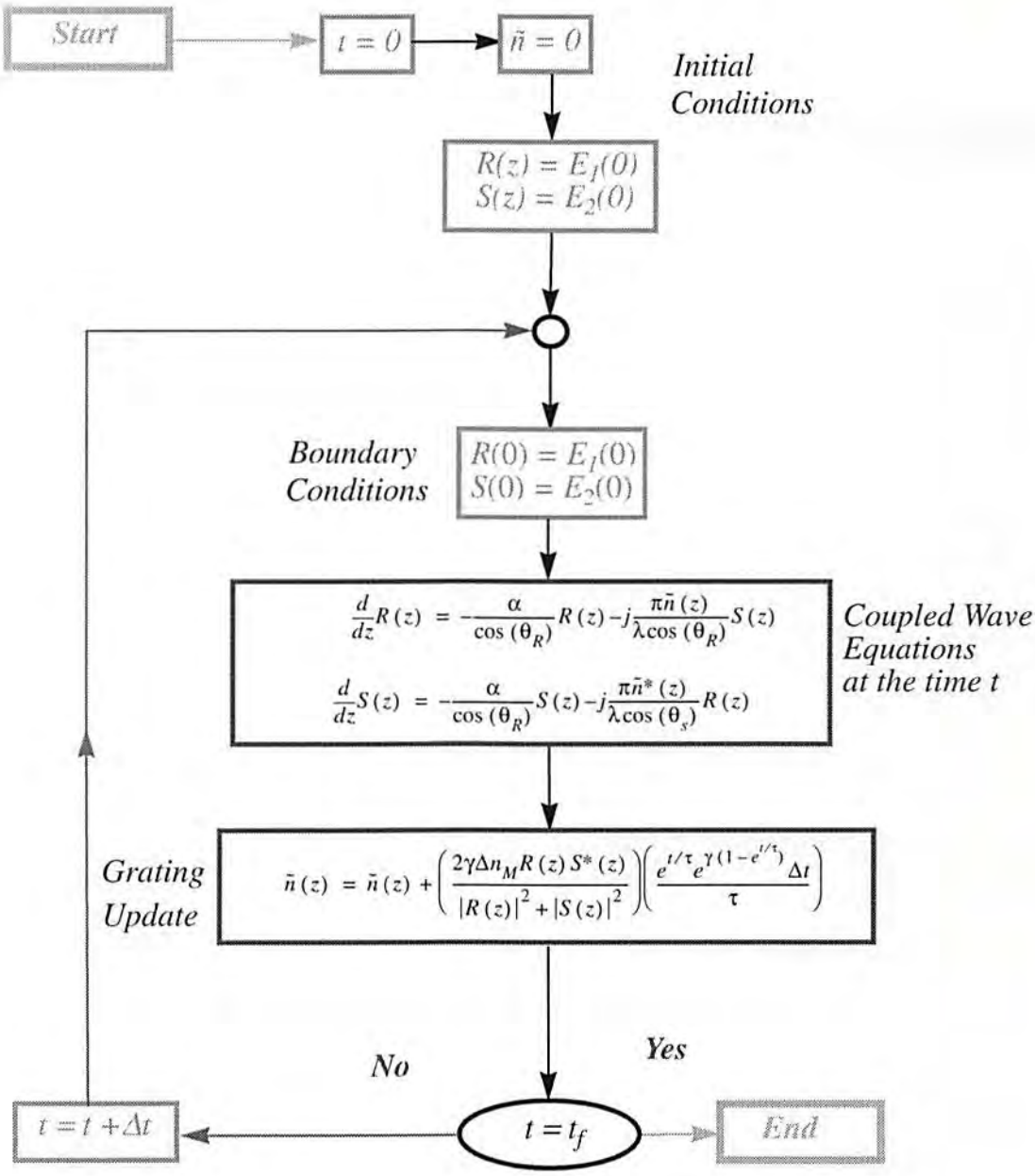

Figure 4-2. Flow chart of the program simulating the recording of a transmission hologram in photopolymers in presence of self diffraction. The loop is related to the time increment, during which the complex amplitude of the refractive index modulation is updated.

$$\tilde{n}(z) = \tilde{n}(z) + \frac{2\gamma\Delta n_M R(z) S^*(z)}{|R(z)|^2 + |S(z)|^2} \frac{e^{t/\tau} e^{\gamma(1-e^{t/\tau})} \Delta t}{\tau}. \qquad (4\text{-}33)$$

The update is here written in programming syntax, to be consistent with the instructions in the flow chart of Fig. 4-2.

(4) Time update. Once the grating complex amplitude along the whole thickness of the volume hologram is updated, the next time increment $t = t + \Delta t$ is taken. Afterwards the algorithm goes to step (**1**). The program stops when the final exposure time t_f is reached.

The output data were the spatial-temporal evolutions of the refractive index modulation, and of the recording waves ($\lambda = 514$ nm). At the same time, the evolution of the diffraction efficiency read by a Bragg matched probe beam ($\lambda_p = 633$ nm) was simulated, in order to better compare the simulation with any experimental data.

The software was developed in the Matlab programming language ant was run on a SUN SPARC-5 machine. For a 300 μm thick hologram, recorded with an average recording intensity of 16 mW/cm^2, the computational budget was 10^{10} FLOP's (floating point operations).

4.5 Simulation of Self Diffraction in HRF-150-38 Photopolymer

In this section we present results of computer simulations helpful to quantify and understand the effects of self diffraction in photopolymers. For the moment we restrict our consideration to the case of a 38 μm thick photopoly-

mer, which is the thickness of DuPont HRF-150-38 photopolymer film. The material figures of merit (reaction order $\delta = 0.74$, the constant $\gamma = 1.52$) are those indicated in Chap. 2. The maximum attainable refractive index modulation value used in the simulations is $\Delta n_M = 0.006$, to be consistent with what we measured in the specific batch of photopolymer films that we exposed during the experimental verifications (presented later in this chapter) of the theory. For the simulation (and for the experiments as well) the Bragg angle of the recording beams in air is 20°. The wavelength of the recording beams is $\lambda = 514$. For these data, and according to Eq. 4-32, we get that $\Delta z = 0.75$ μm ($n_o = 1.5$). The average recording intensity is $I_o = 16$ mW/cm^2, which is consistent with the HFMD assumption. As a first example, we simulate the holographic exposure with input beam intensity ratio $BR(0,0) = 20$ (beam intensity modulation $m = 0.426$) at the face of incidence of the film. A simulation with this high value beam intensity ratio can illustrate more effectively the consequences of self diffraction during hologram recording, such as the spatial-temporal variation of the refractive index modulation (in phase and amplitude) and the spatial-temporal variation of the beam intensity ratio within the holographic region. Results of this first simulation are depicted in Fig. 4-4, and Fig. 4-4. Figure 4-4 represents the evolution of the refractive index modulation at three different stages during the exposure at $t = 1$ s, $t = 30$ s, $t = 80$ s; Fig. 4-4 illustrates in three dimensional plots the spatial-temporal variation of the grating modulation (magnitude and phase), of the beam intensity ratio $BR(z,t)$, and the diffraction efficiency read by a Bragg matched probe with $\lambda = 633$ nm. Figure 4-4 (a) and (b) respectively describe the time evolution of the grating amplitude (in a

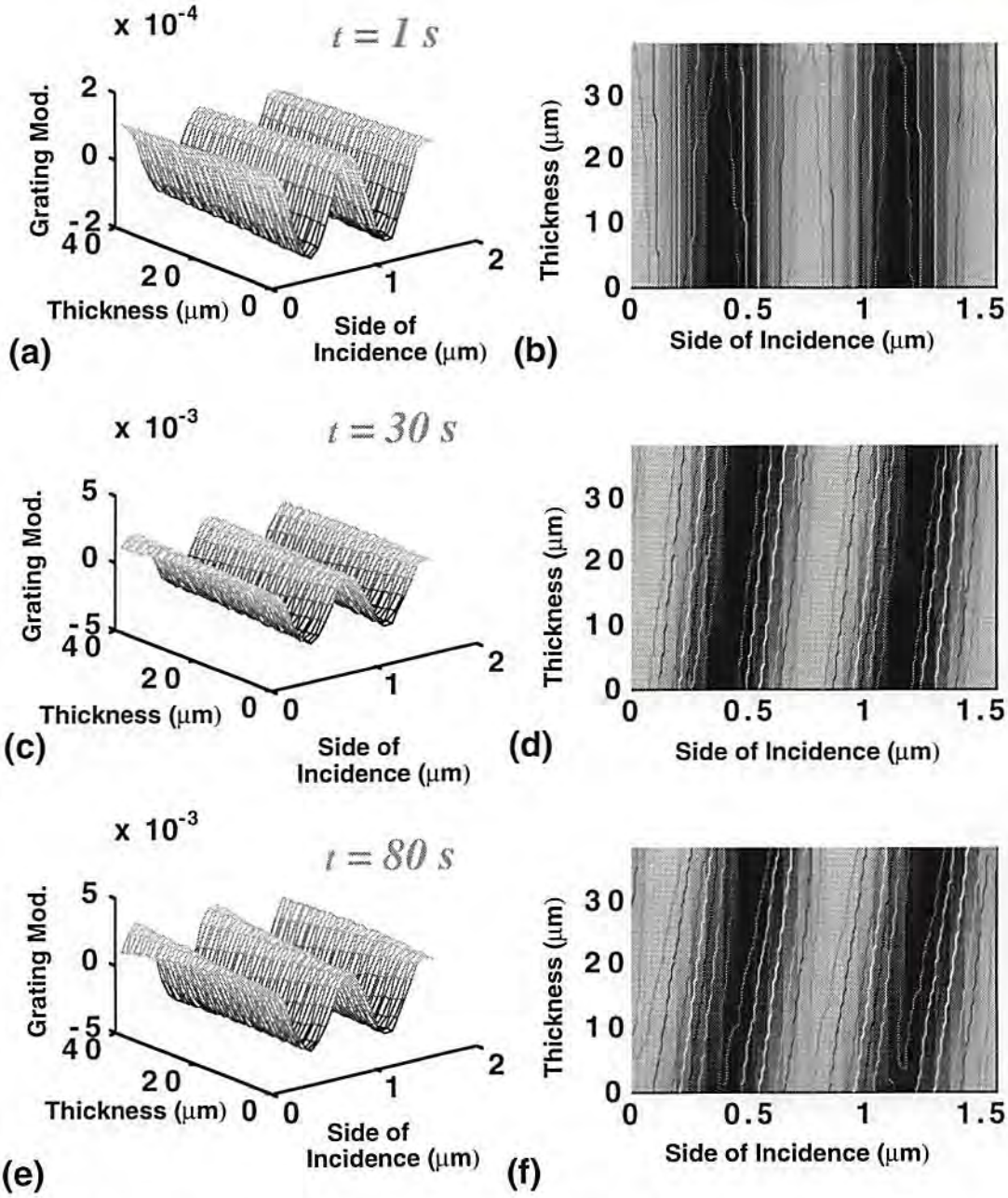

Figure 4-3. Evolution of the refractive index modulation at three distinct moments during the holographic exposure, illustrating self diffraction. Two symmetrically incident beams with a Bragg angle of 20° and wavelength $\lambda = 514$ nm in air write a hologram with $I_o = 16$ mW/cm^2 and $BR(0,0) = 20$. The figures indicate the refractive index modulation after 1, 30, and 80, seconds in three dimensional plots. The contour plots better visualize the grating bending during these three different stages of the recording.

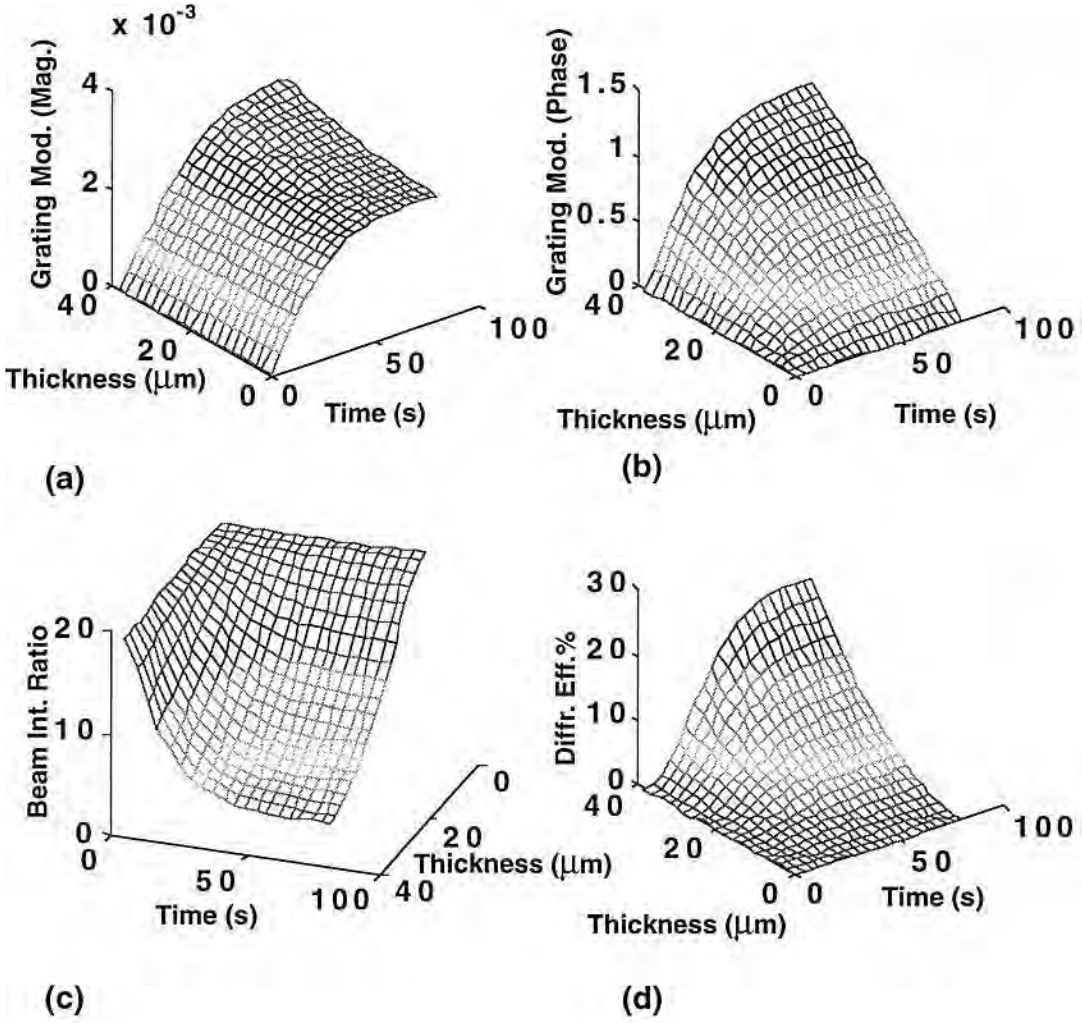

Figure 4-4. Recording of holographic grating in HRF-150-38, with symmetrically incident waves with wavelength $\lambda = 514$ nm, Bragg angle in air of 20°, average recording intensity $I_o = 16$ mW/cm^2, and beam intensity ratio $BR(0,0) = 20$. The three dimensional plots depict in time and space (along the z-axis) the variation of the following parameters: **(a)** Magnitude of the refractive index modulation. **(b)** Phase variation of the refractive index modulation. **(c)** Beam intensity ratio. **(d)** The diffraction efficiency read out by a Bragg matched beam having wavelength $\lambda = 633$ nm.

three dimensional plot) and of the grating orientation (the contour plot) after the first second of exposure (the inhibition time is not included). At this moment the grating bending is not yet visible, due small value of grating modulation amplitude ($\Delta n \approx 1.5\text{x}10^{-5}$) which does not allow a strong coupling between the recording waves. This situation is definitely different at $t = 30$ s, as indicated Fig. 4-4 (c) and (d). Here the grating modulation amplitude is approximately constant within the material with $\Delta n \approx 2.16\text{x}10^{-3}$. After 30 seconds the grating is bent, as indicated in the contour plot in Fig. 4-4 (d), with the associated phase reaching the value of $\psi = 0.9$ rad at 38 μm, Fig. 4-4 (b). At saturation, $t = 80$, the effect of self diffraction are magnified, Fig. 4-4 (e) and (f). The magnitude of the refractive index modulation is not anymore constant within the hologram, and so the beam intensity ratio which, as expected from the theory, tends to reach an unitary value, Fig. 4-4 (a), Fig. 4-4 (c). From the initial $\Delta n \approx 2.55\text{x}10^{-3}$ at $z = 0$ the grating modulation index reach a value of $\Delta n \approx 3.2\text{x}10^{-3}$ at $z = 38$ μm. Conjunctively, the phase of the refractive index modulation grows within the holographic region up to $\psi = 1.16$ rad at $z = 38$ as depicted Fig. 4-4 (b).

One of the consequences of the phase shift can be apparent during hologram reconstruction. Typically, the diffraction efficiency of the reconstruction of the hologram is optimized with an illuminating beam incident at the Bragg angle. In this case, however, the reconstruction is optimized when the illuminating beam is angularly shifted from the Bragg angle by an additional angle related to the grating bent caused by self diffraction, Fig. 4-1 (b). For the case simulated, the inclination of the grating can be calculated by approximating a

linear grating phase shift within the holographic region. Therefore, one can calculate the grating position shift, Δx, along the x-axis at $z = 38$ μm from the grating phase shift at $t = 80$ s as

$$\psi = \frac{2\pi\Delta x}{\Lambda_g}, \tag{4-34}$$

which for $\psi = 1.16$ yields $\Delta x = 0.138$ μm. The grating angle of inclination is therefore $\Delta\phi \approx \Delta x/38$ rad, which corresponds, for a reconstructing beam, to an angular shift from the Bragg incidence of $\Delta\phi = 0.20^{o}$ inside the material, or $\Delta\phi = 0.30^{o}$ in the air. One must notice that the initial beam intensity ratio determines not only the amount of phase shift, but also its sign, or, more practically, the direction of the grating bending. In fact for a hypothetical recording with an initial ratio $BR(0,0) = 1/20$, we should aspect now a phase shift of $\Delta\phi = -1.16$ rad, which corresponds to an angular shift of $\Delta\phi = -0.30^{o}$ in air.

As earlier said in this section, another noticeable effect of the self diffraction is the spatial-temporal variation of the beam intensity within the holographic region during exposure, as depicted in Fig. 4-4 (c). Particularly, the time variation of the output beam intensity ratio, $BR(38\ \mu m,t)$ is one of the manifestation of self diffraction that can be monitored during recording. In this simulation the output beam intensity ratio starts from an initial value $BR(38\ \mu m,0) = 20$, and then decreases in time reaching at saturation the value of $BR(38\ \mu m,80) = 3.6$. Generally the final value of the output beam intensity ratio depends on the value of the diffraction efficiency reached during recording (or better on the material thickness and on the Δn_M value), and, of course, on

$BR(0,0)$: the higher the diffraction efficiency (related to a thicker material and a higher Δn_M) the higher is the coupling which ultimately evens the recording beam intensities within the holographic region. At the same when $BR(0,0) \approx 1$, a lower amount of wave coupling (and diffraction efficiency) is necessary to even the recording beam intensities within the holographic region, and therefore self diffraction effects are less apparent. For the simulation so far presented, the relatively low value of Δn_M and of the scarce hologram thickness prevented to reach such equilibrium ($BR(38\ \mu m,80) = 1$) for an initial $BR(0,0) = 20$.

In order to present a better understanding and an easier visualization of the results, part of the data of Fig. 4-6, are shown in Fig. 4-5, where the two dimensional graphs show the evolution in time and space of the refractive index modulation, in Fig. 4-5 (a) and (b), the output beam intensity ratio, in Fig. 4-5 (c), and the temporal evolution of the diffraction efficiency, in Fig. 4-5 (d).

Finally, it is interesting to compare this recording with $BR(0,0) = 20$ with a recording scenario relative to a beam intensity modulation $BR(0,0) = 1$. When recording with $BR(0,0) = 1$, because of the symmetry of the process, the grating couples the same amount of energy between one writing wave and the other, and this symmetrical coupling prevents the variation in phase and amplitude of the modulation term of the interference pattern within the holographic region. In essence, self diffraction virtually is not existing when the writing beams present initial unitary beam index modulation or initial unitary beam intensity ratio, $BR(0,0) = 1$. This recording scenario is illustrated in Fig. 4-6, where are presented the spatial-temporal dynamics of the grating modulation, output

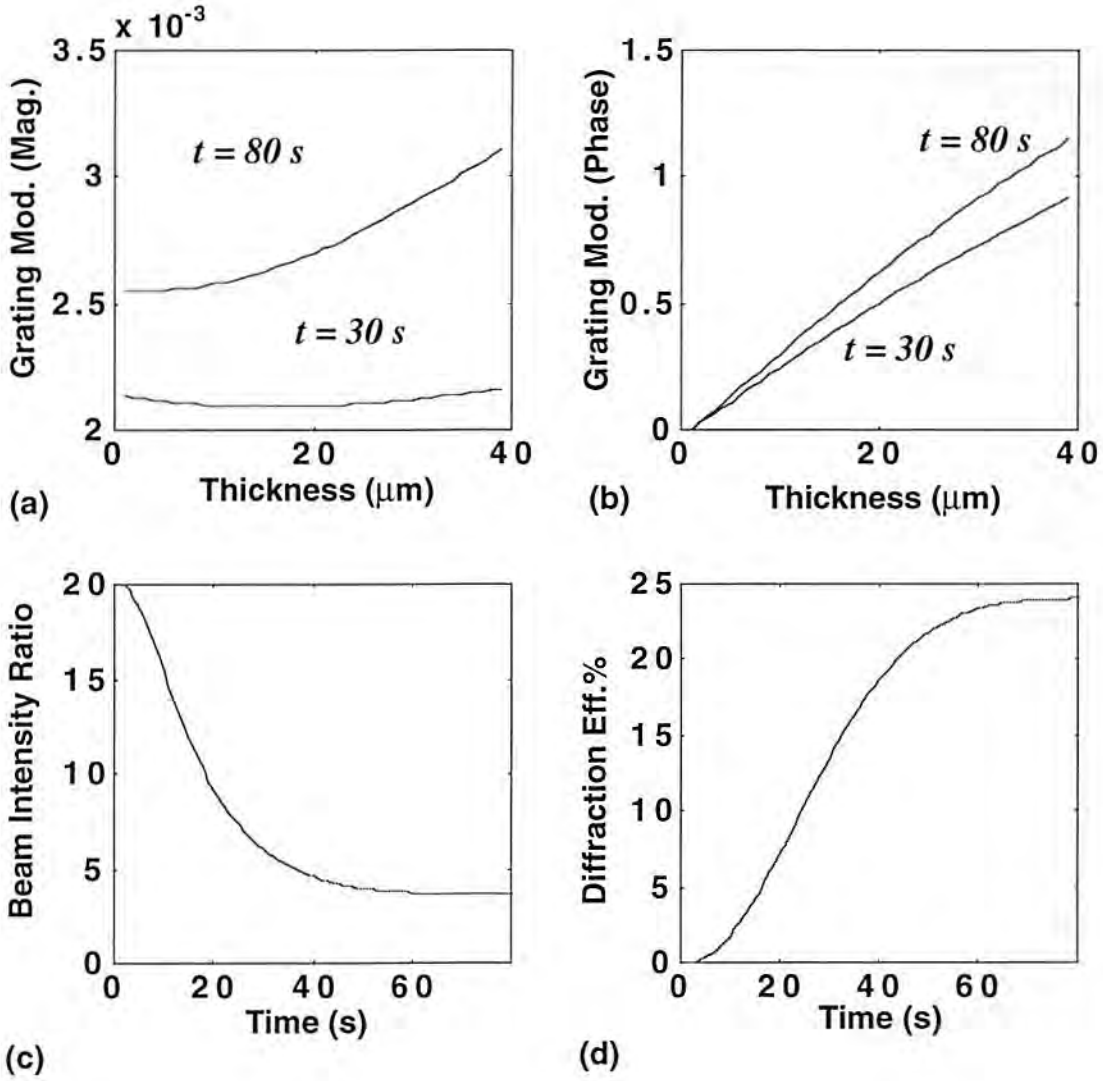

Figure 4-5. Recording of holographic grating in HRF-150-38, with symmetrically incident waves having wavelength $\lambda = 514$ nm, a Bragg angle of 20° in the air, average recording intensity I_o =16 mW/cm^2, and beam intensity ratio $BR(0,0)$ =20. **(a)** Magnitude of the refractive index modulation within the holographic region after 30 s and 80 s. **(b)** Phase variation of the refractive index modulation within the holographic region after 30 s and 80 s. **(c)** Temporal variation of the output beam intensity modulation at $z = 38$. **(d)** Temporal variation of the diffraction efficiency at $z = 38$ reading out with a Bragg matched probe beam with $\lambda_p = 633$ nm.

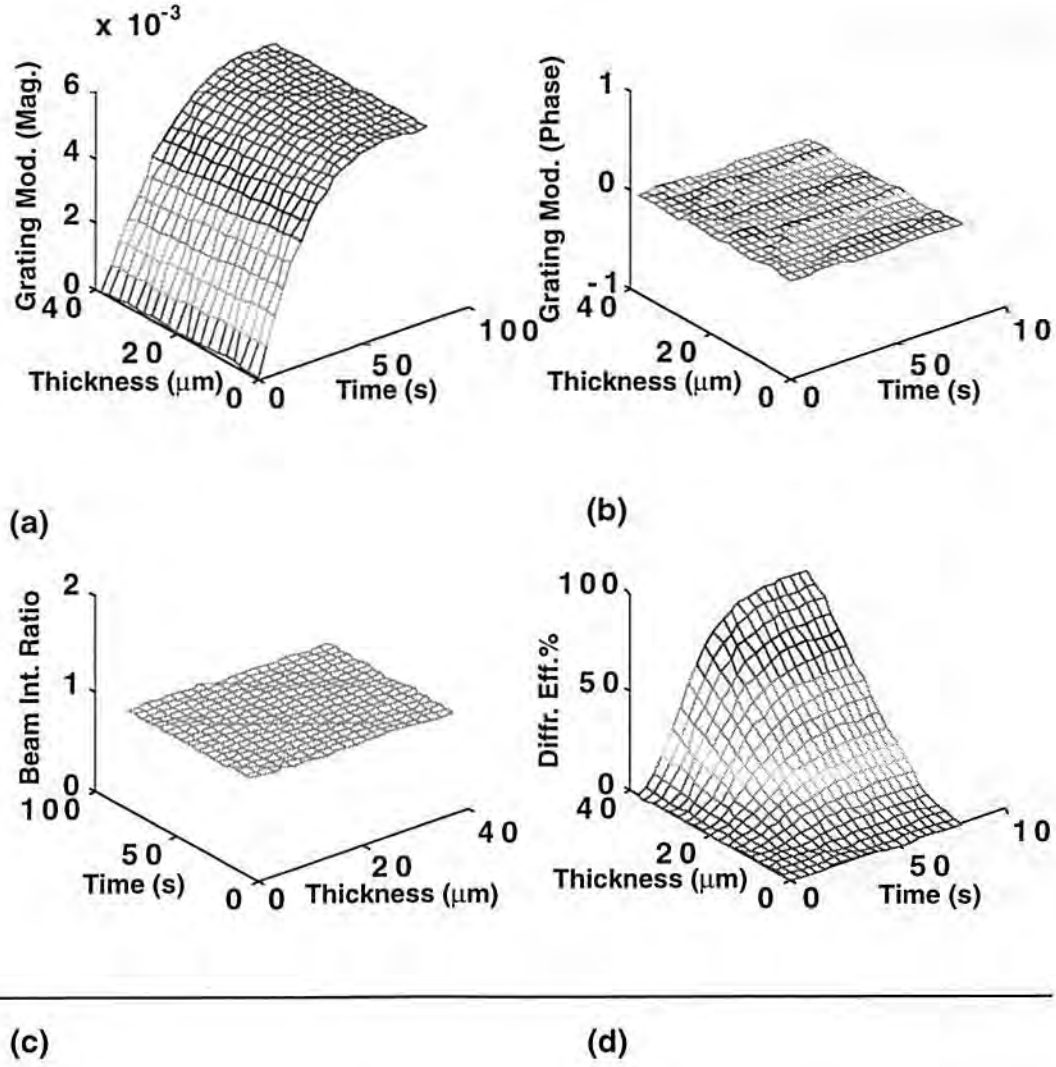

Figure 4-6. Recording of holographic grating in HRF-150-38, with symmetrically incident waves (wavelength $\lambda = 514$ nm), Bragg angle of 20^{o} in the air, average recording intensity $I_o = 16$ mW/cm^2, beam intensity ratio $BR(0,0) = 1$. The three dimensional plots depict in time and space along the z-axis the following parameters: **(a)** Magnitude of the refractive index modulation. **(b)** Phase variation of the refractive index modulation (here absent). **(c)** Beam intensity ratio, here constant within the holographic region. **(d)** The diffraction efficiency read out by a Bragg matched beam at wavelength $\lambda_p = 633$ nm.

intensity beam ratio, and diffraction efficiency of a 38 μm thick photopolymer sample exposed with I_o = 16 mW/cm². By comparing these data with those of Fig. 4-4, one can observe that for $BR(0,0) = 1$ there is, beside the higher saturation diffraction efficiency, Fig. 4-6 (d), respect to the case in Fig. 4-4 (d) (a result which, however, was already foreseen by the HFMD model), the total absence of variation (in space and time) of the phase modulation of the recorded grating and of the output beam intensity modulation. Moreover, the amplitude of the grating modulation Fig. 4-6 (a), is constant within the holographic region, differently form what is depicted in the plots of Fig. 4-5 (a) and Fig. 4-4 (a) for $BR(0,0) = 20$.

4.6 Experimental Observation of Self Diffraction in HRF-150-38 Photopolymer

A way to monitor the self diffraction is to measure the output beam intensity ratio (or better, the recording beam intensities at the output of the holographic grating), whose temporal evolution, per se, is an indication of the presence of self diffraction itself. To perform such measurements we used an experimental set up as in Fig. 2-6, with the addition of two additional detectors dedicated to measure in real time the output intensities of the recording beams. The diffraction efficiency was read by a Bragg-matched probe beam at λ_p = 633 nm; the recording beams, with the associated λ = 514 nm, where symmetrically incident, each with a Bragg angle of 20° in air; a number exposures with different beam intensity modulation m values were performed; the holographic mate-

rial was DuPont HRF-150-38. The beam intensity modulation values were m = 1, 0.968, 0.687, 0.426, which corresponded to an input beam intensity ratio $BR(0,0)$ = 1, 1.66, 1/6.3, 20, according to the geometry of Fig. 4-1 (a). Such a spread of values of m's and $BR(0,0)$'s is helpful to verify the theory for a significant number of different holographic exposure conditions. For example, we chose to record a set of holograms with $BR(0,0) = 1/6.3 < 1$ (different from the all other exposures with $BR(0,0) \geq 1$), because we could corroborate better the theory which predicts that to different values of $BR(0,0)$ correspond different inclinations of the grating slant angle. The average beam intensity was kept constant at I_o = 16 mW/cm^2. Each exposure was also simulated via software in order to compare simulation results and experimental data of the time evolution of both the beam intensity ratio and the diffraction efficiency.

4.6.1 Experimental Data on Self Diffraction: Discussion

Figures 4-7 and 4-8 compare the results of the computer simulations and experimental exposures. As usual, the holographic medium is the HRF-150-38 photopolymers 38 μm thick. For each value of input beam intensity ratio (or beam intensity modulation) the temporal evolution (the inhibition period is not included) of the diffraction efficiency and of the output beam intensity ratio (BR(38 μm,t)) of the measured data (solid curve) and of the computer simulation (dashed curve) is presented.

The theory indicates that self diffraction is prevented by an unitary input beam intensity ratio, and this can be confirmed by the observation of an

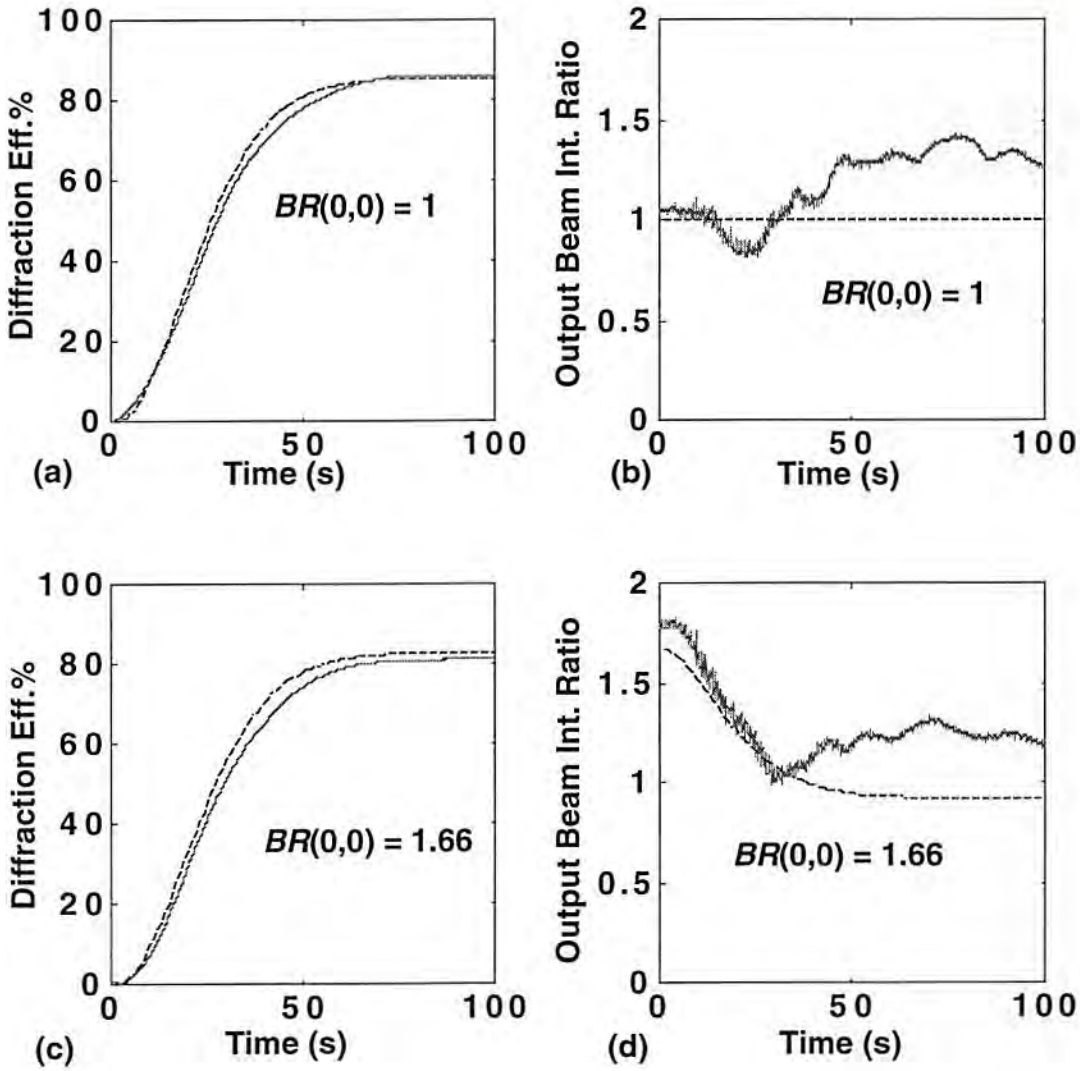

Figure 4-7. Computer simulations (dashed curves) and experimental measurements (solid curves) of the diffraction efficiency, and of the output beam intensity ratio in HRF-150-38 photopolymer: (**a**) and (**b**) $BR(0,0) = 1$, (**c**) and (**d**) $BR(0,0) = 1.66$.

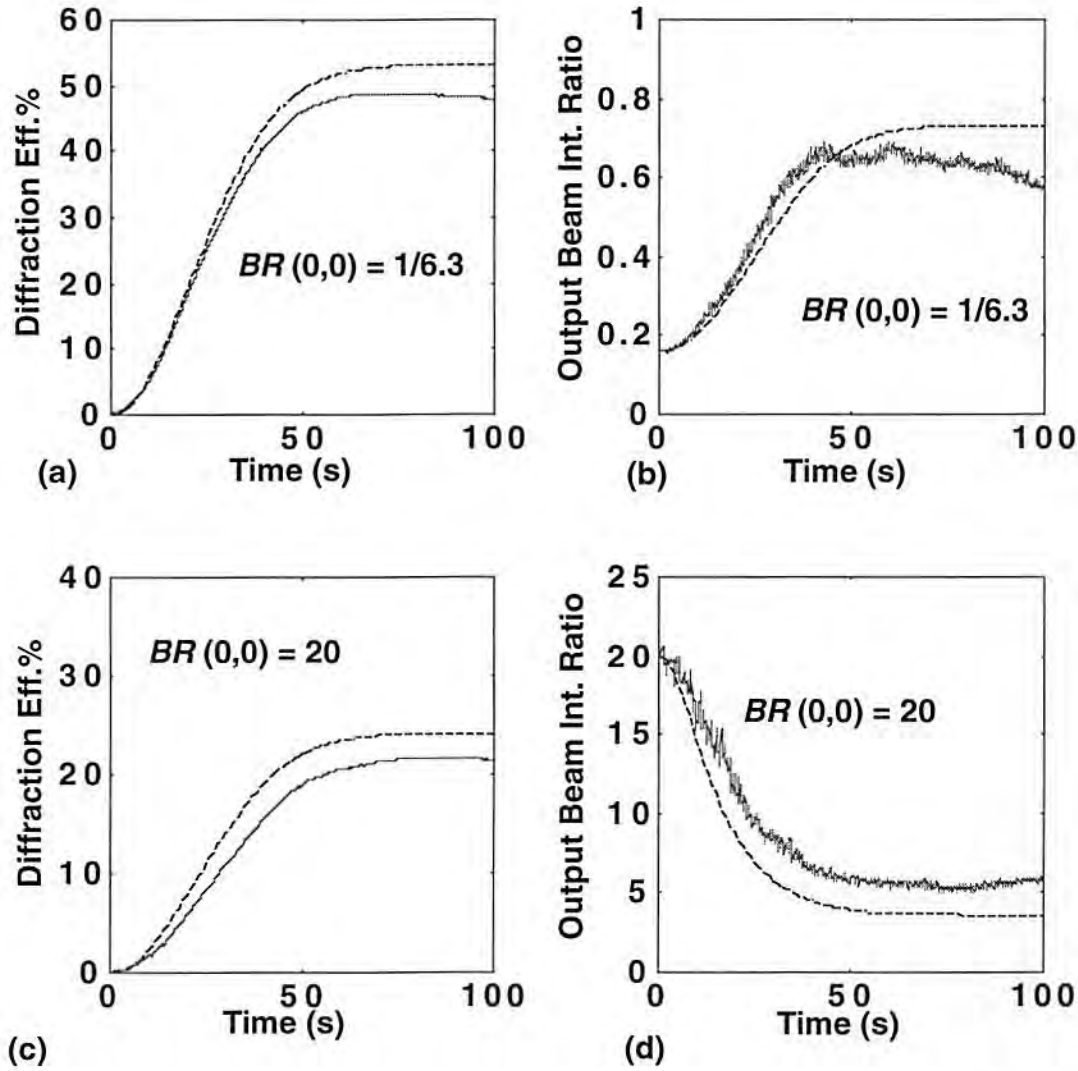

Figure 4-8. Computer simulations (dashed curves) and experimental measurements (solid curves) of the diffraction efficiency and of the output beam intensity ratio in HRF-150-38 photopolymer: **(a)** and **(b)** $BR(0,0) = 1/6.3$, **(c)** and **(d)** $BR(0,0) = 20$.

unchanged temporal evolution of the output beam intensity ratio for $BR(0,0) = 1$. In fact, Fig. 4-7 (b) shows how the output beam intensity ratio varies around the unitary value during exposure (actually in the recording $BR(0,0) = 1.1$), but it does not significantly change. The noise in the experimental curve of the output beam intensity ratio in Fig. 4-7 (b) (and all the others as well) may have been caused by the argon ion laser power fluctuations. Moreover, the reading of the writing beam intensities at the hologram output is an interferometric measurement, and, therefore, it is more sensitive to environmental noise source (air fluctuation, vibration etc.).

The effects of self diffraction are definitely detectable when a hologram is exposed with recording beams having input beam intensity ratios of value different from unity. As depicted in Fig. 4-7 (d), 4-8 (b) and 4-8 (d), the initial beam intensity ratio during recording decreases (or increases for $BR(0,0) = 1/6.3$) until saturation, when this output intensity ratio is practically constant. Only in the case of $BR(0,0) = 1.66$ the beam intensity ratio reaches the equilibrium, this happens because the $BR(0,0)$ value is very close to one, while the for the other recordings we can observe that $BR(38\text{ mm},100)$ is 0.6 and 5.2 for the corresponding $BR(0,0)$ values of 1/6.3 and 20.

The simulation can predict with good accuracy the temporal evolution of the diffraction efficiency and of the output beam intensity ratio for all four recording conditions. It must be noticed, however, that for the relatively low Δn_M value and the reduced thickness of the holographic material, the HFMD model results can also predict with the same accuracy the time evolution of dif-

fraction efficiency, avoiding therefore the heavy elaborations required to simulate self diffraction in photopolymers. Unfortunately, this is not any longer valid for thicker samples, where the effects of self diffraction must be taken into account to correctly predict the spatial-temporal evolution of the diffraction efficiency during a holographic exposure in photopolymers.

4.6.2 Self Diffraction in a Double Layer Sample

To characterize the self diffraction effects in thicker photopolymers, a second set of exposures was recorded. In order to prepare thicker photopolymer films, a stack of two films were attached on a slide glass as indicated in Fig. 4-9. The total thickness of these samples was therefore 38+38 μm.

Figures 4-10 and Fig. 4-11 depict the experimental measurements and the computer simulations of a set exposures using these 38+38 μm films, at the same recording condition of the earlier experiments: $I_o = 16$ mW/cm^2, $BR(0,0) = 1, 1.6, 1/63, 20$;

Figures 4-10 (a) and (b) indicate the results of an exposure in absence of self diffraction, or more correctly with $BR(0,0) = 1$. In this case, because of the larger thickness, the diffraction efficiency reaches overmodulation, and therefore after reaching a maximum of $\eta \approx 99\%$ decreases to saturation value of $\eta \approx 62\%$. This result is predicted by theory, even if the overmodulation time in the simulation (dashed line) is anticipated by 2 seconds. The measured output beam intensity ratio starts at $BR(76\ \mu m,0) = 1.1$ and ends at $BR(76\ \mu m,100) = 1.2$, fluctuating around these values during the duration of the

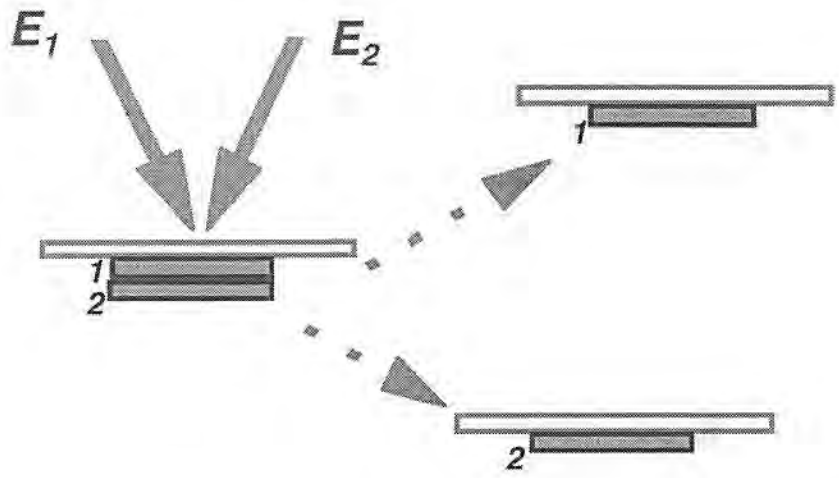

Figure 4-9. Double layer of HRF-150-38. First two films are laminated in top of each others, on a glass slide support. Next this 38+38 μm of holographic film is exposed, while it is measured the temporal evolution of the diffraction efficiency and of the output beam intensity ratio. After the exposure, the second layer is removed and laminated on an other glass slide (2). The angular selectivities of the holograms (1) and (2) is then measured.

exposure.

Particularly, the best match between simulation and experimental data can be found for higher value of beam intensity modulation, where the theory quite accurately predict the evolution of the diffraction efficiency and of the output beam intensity ratio. Interestingly, if we consider the recording for $BR(76\ \mu m,0) = 1/6.3$, we can notice that the final value is not unity but $BR(76\ \mu m,100) = 2.2$ (theoretical 1.6), which means that the initial weak beam (here, E_1 according to Fig. 4-1 (a)), at the end of exposure surpasses in intensity the other beam. This process is termed beam coupling, [Faiman *et al.*, 1986], and it manifests only if a determined condition between the phase of the two recording waves and the grating is met. Beam coupling has been extensively studied

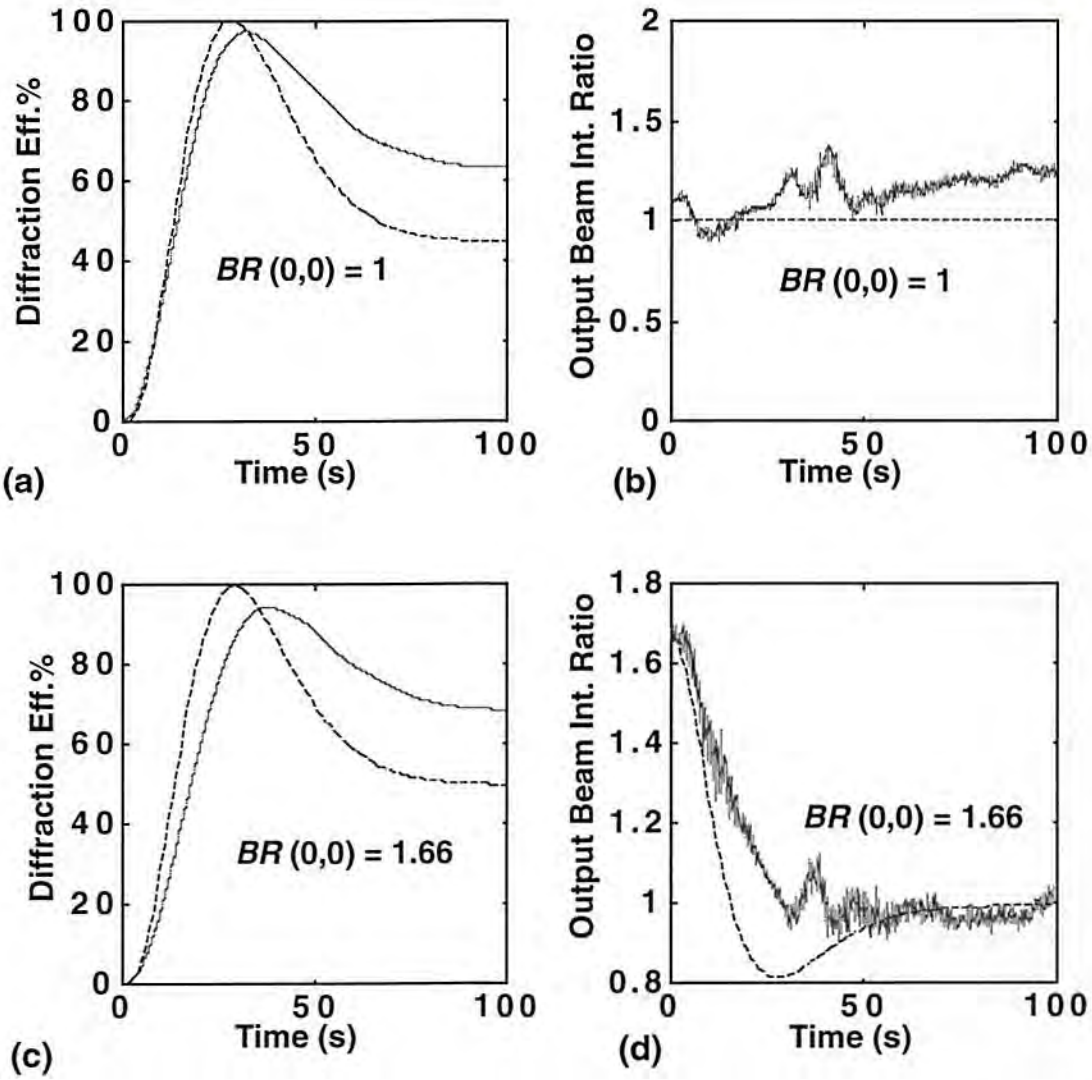

Figure 4-10. Computer simulations (dashed curves) and experimental measurements (solid curves) of the diffraction efficiency, and of the output beam intensity ratio in a double layer of HRF-150-38 photopolymer: $BR(0,0) = 1$ (**a**) and (**b**), and $BR(0,0) = 1.66$ (**c**) and (**d**).

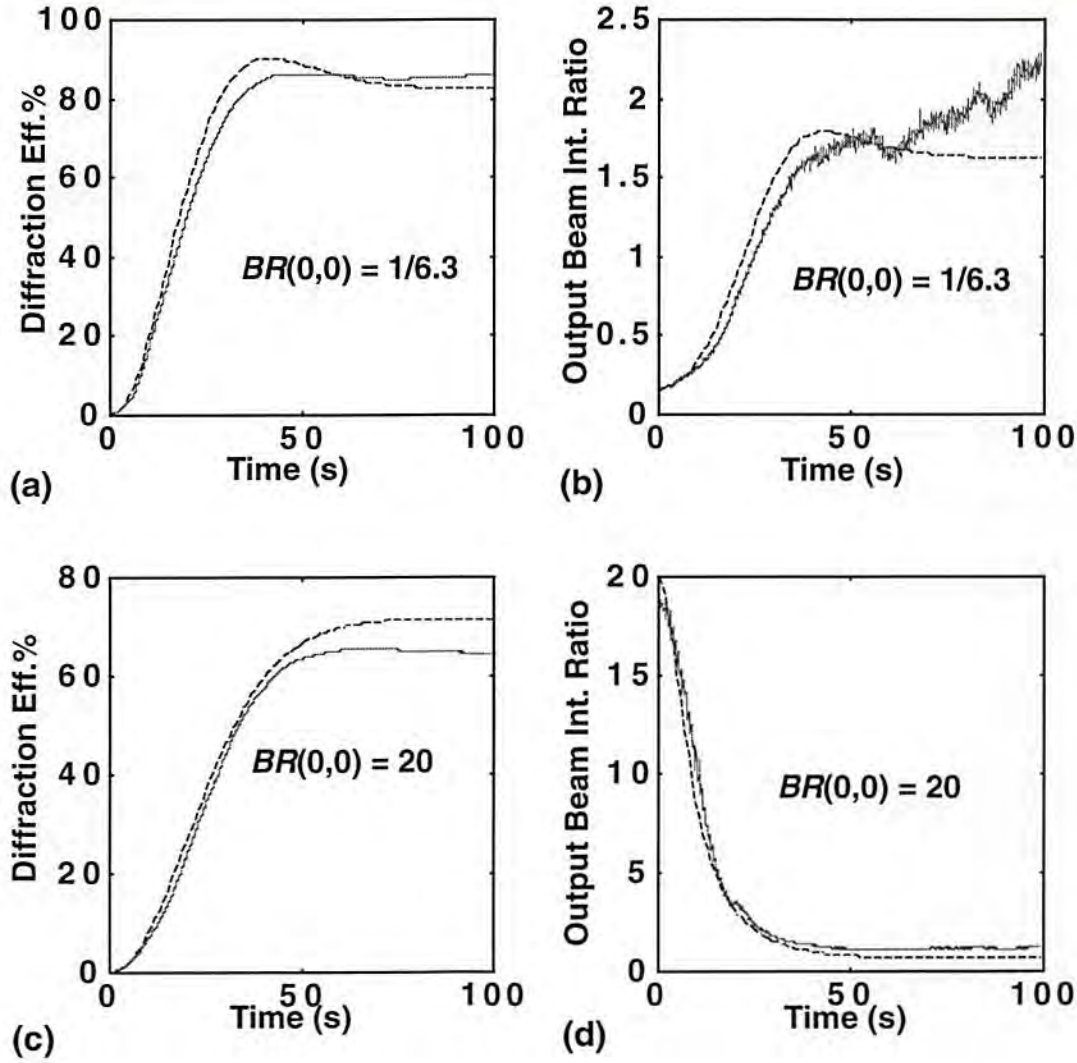

Figure 4-11. Computer simulations (dashed curves) and experimental measurements (solid curves) of the diffraction efficiency and of the output beam intensity ratio in a double layer of HRF-150-38 photopolymer: $BR(0,0) = 1/6.3$ **(a)** and **(b)**, and $BR(0,0) = 20$ **(c)** and **(b)**.

in photorefractive crystals, and, actually, until now beam coupling was considered a characteristic peculiar to such materials. To our knowledge this is the first time that a form of this physical process has been observed in photopolymers.

Particularly, the double stack film geometry offers an additional advantage for the sake of better characterization of self diffraction effect in the material. After exposure, it is possible to remove the second film and to laminate it on a second glass slide, as in Fig. 4-9. In this way it is possible to measure the diffraction efficiency, the angular selectivity, and the different inclination angle of the slanted grating in each exposed layer. This last concept can be better explained with the help of Fig. 4-19, which presents the results of computer simulations describing the phase and magnitude of the grating modulations at saturation recorded with the different $BR(0,0)$ values. Because of self diffraction, the phase and amplitude of the recorded grating vary within the holographic region for nonunitary$BR(0,0)$'s. Hypothetically, if we divide the film in two slides of 38 μm, we can notice, as a consequence of self diffraction, that first slide ($0 \leq z \leq 38$) experiences lager phase variation (larger slanted angle), while the magnitude of the grating modulation is larger in the second slide ($38 \leq z \leq 76$). The curve indicating the negative phase shift, Fig. 4-19 (b), is related to the initial input beam intensity ration less than one, $BR(0,0) = 1/6.3$, which shows an inversion of the direction of fringe bending respect to the other recordings for $BR(0,0) > 1$.

The simulation results relevant to the diffraction efficiencies, grating mod-

ulations, and fringe slant angles, for each of the slides are shown in Table 4. These data were experimentally verified by measurements of the grating selectivity of the recorded holograms. To measure the angular selectivity we used the experimental set-up as in Fig. 4-13, where the 486-PC controlled the angular rotation of a rotatory stage and collected the data concerning the reading of the zero and first order beam diffracted by the holographic grating.

Table 4: Simulation Results of the Double Stack Holograms

Fist Layer	$BR(0,0)=1$	$BR(0,0)=1.66$	$BR(0,0)=1/6.3$	$BR(0,0)=20$
Phase Shift	0	0.23 rad	-0.865 rad	1.165 rad
Air Slant Angle	0	0.061^{o}	-0.235^{o}	0.31^{o}
Average Δn	0.006	0.0057	0.0042	0.0025
Ave. Diff.Eff.%	86	81	54	22
Sec. Layer				
Phase Shift	0	0.03 rad	-0.135 rad	0.545 rad
Air Slant Angle	0	≈ 0	-0.036^{o}	0.15^{o}
Average Δn	0.006	0.0058	0.005	0.0035
Ave. Diff. Eff.%	86	83	69	42

Figure 4-14 depicts the results of these measurements for each of the double layer holograms recorded with $BR(0,0) = 1$, 1/6.3, and 20. The exposure with $BR(0,0) = 1.66$ has been omitted for the sake of better clarity of the figure, in fact the results of this recording are too close to those with $BR(0,0) = 1$. In the figure the solid curves indicate the measurements concerning the first layers, the second layer data are depicted by the dashed curves. The $BR(0,0) = 1$ first

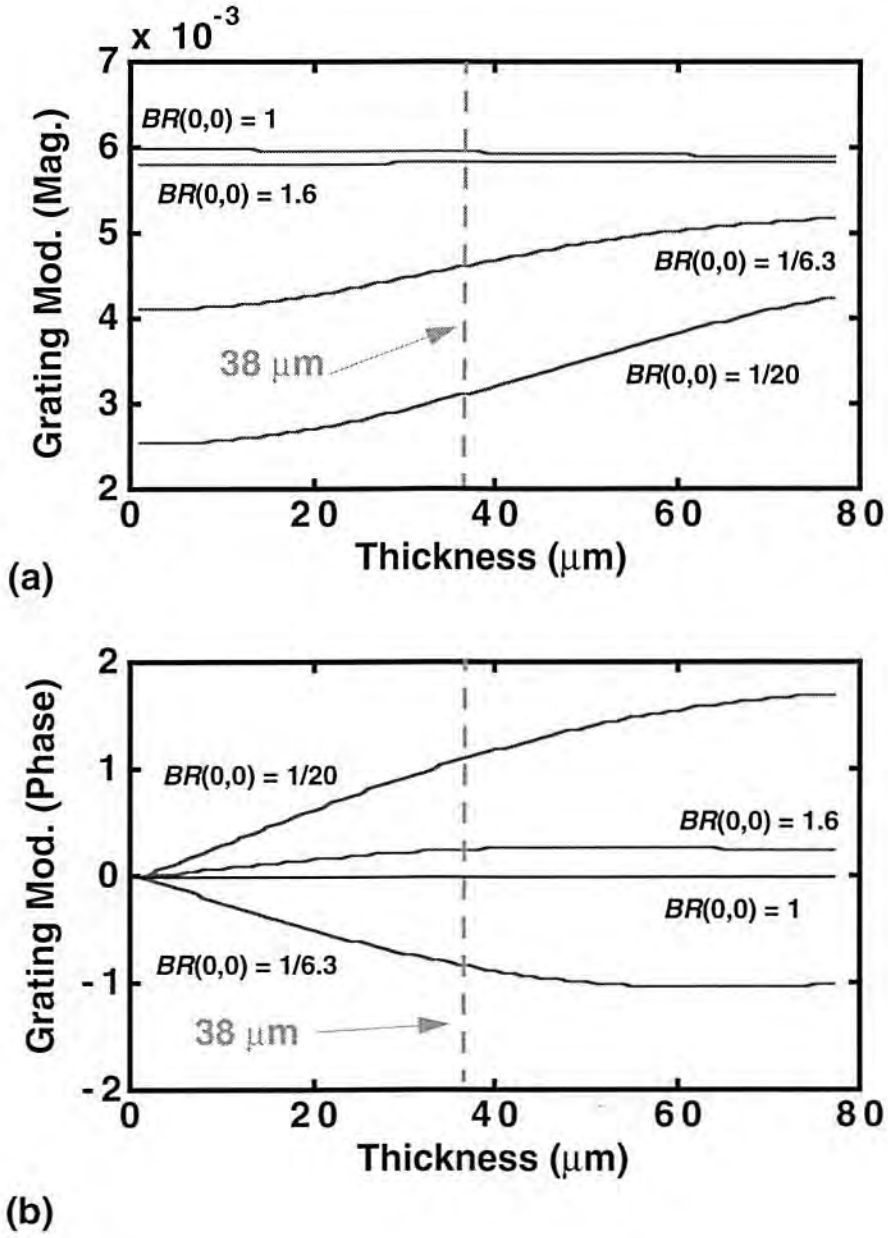

Figure 4-12. Simulation results depicting: **(a)** Amplitude of the refractive index modulation within the holographic region at different values of input beam intensity modulation, $BR(0,0)$. **(b)** Phase of the refractive index modulation within the holographic region a different value of input beam intensity modulation, $BR(0,0)$. The figures are referred to a HRF-150-38 photopolymer, after 100 s of exposure with an average recording intensity $I_o = 16$ mW/cm^2.

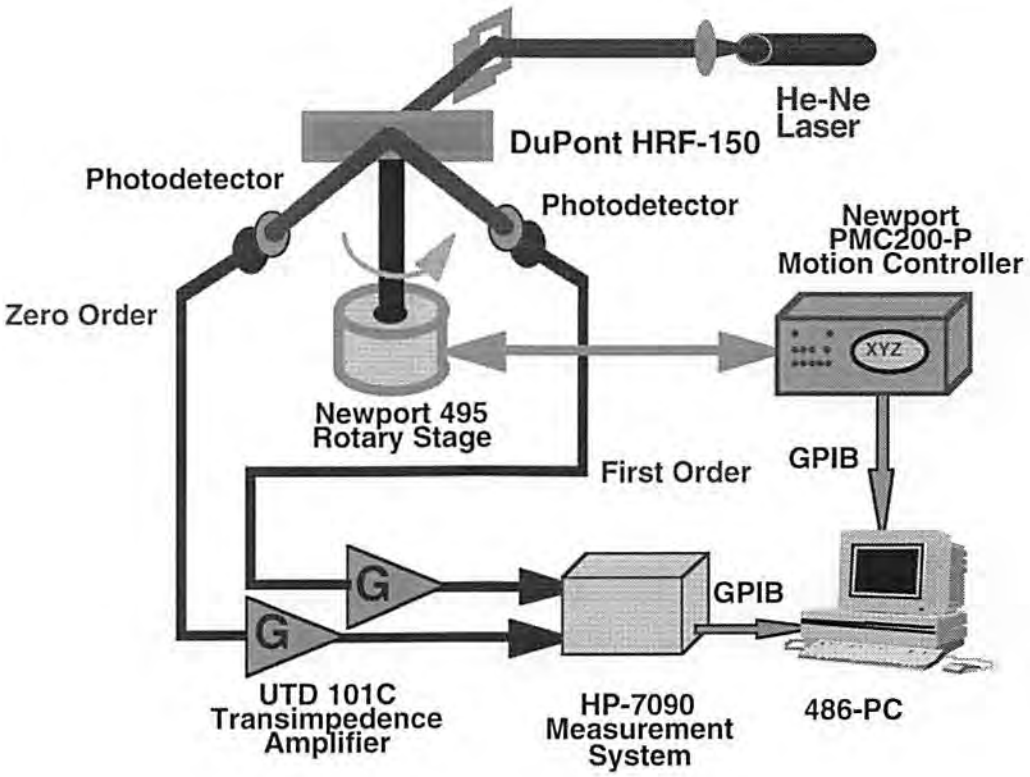

Figure 4-13. Experimental set-up for the measurement of the angular selectivity of a holographic grating. A He-Ne laser beam impinges on the photopolymer film, while two detectors read out the light intensity of the zero and first order. These data, amplified by two UTD 101C transimpedence amplifiers, reach the HP-7090 measurement system, and then are stored in a personal computer via GPIB bus connection. The personal computer controls a motion controller and a rotary stage which shifts 0.05^{o} counterclockwise after every measurement of the diffraction efficiency.

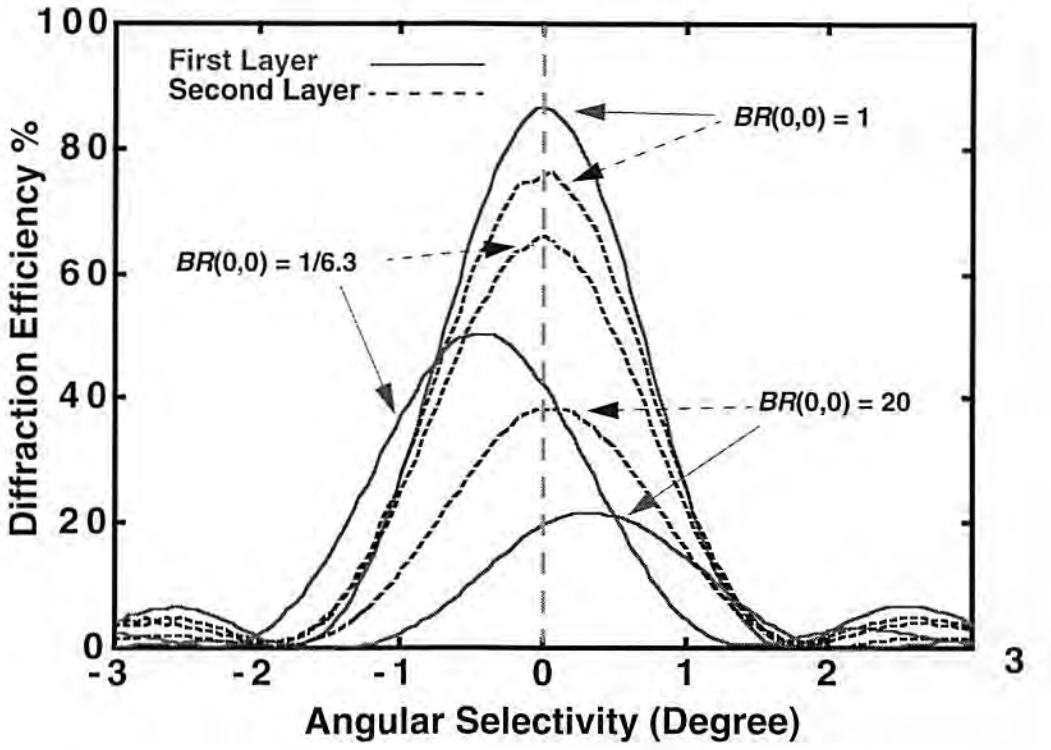

Figure 4-14. Measurements of the angular selectivity of three different double layer holograms. The solid curves describe the first holographic layers, the dashed ones the second ones. The angular references are the curves corresponding to $BR(0,0) = 1$, where the main lobes are centered at 0^{o}, and, according to theory, are not angularly shifted respect to each others. For $BR(0,0) \neq 1$, the first layer are angularly distant from 0^{o}, while the second layer diffraction efficiency is larger than the corresponded first layer. All these measurements are theoretically predicted.

main lobe has been positioned to the center of the plot as reference. Because all the gratings are related same thickness holograms, the main lobe angular width is 3.5^{o} for all the curves, which is in agreement with the coupled wave theory [Kogelnik, 1969] results in which $2n_o\Lambda_g/T = 0.059$ rad is the main lobe width in air, (T, as usual, indicates the hologram thickness), once transformed in degree (3.4^{o}) such value it makes approximately the measured value. It is noticeable how for the recording related to $BR(0,0) = 1/6.3$ first layer lobe is shifted -

0.35^{o}, opposite to the $+0.3^{o}$ of $BR(0,0) = 20$ first layer, confirming the data of Table 4. The angular shift is however largely reduced for the second layer as also indicated by the theory. Moreover, it is worthy to observe, as further validation of the simulation results, as the second layers maximum diffraction efficiencies for $BR(0,0) = 1/6.3$, and $BR(0,0) = 20$ (respectively 66.1%, and 38.6%) are larger than the corresponded first layers diffraction efficiencies (respectively 50.7%, and 21%)) in agreement with the predicted values of Table 4.

4.7 Material Limitations due to Self Diffraction

The effects of self diffraction can be more severe and discernible when a holographic grating is recorded in a very thick photopolymer material. To illustrate better this concept we present, with the help in Fig. 4-15, the simulation results concerning two distinct holograms recorded in two distinct thick photopolymer samples $T = 300$ μm and $\Delta n_M = 0.006$. The holograms are supposed to be recorded with input beam intensity ratios respectively as $BR(0,0) = 20$, and $BR(0,0) = 50$, while the average recording density was $I_o = 16$ mW/cm^2. Effectively, Fig. 4-15 (a) describes and compares the variation of the saturation diffraction efficiencies within the holographic region (along the z-axis) among recordings affected by self diffraction (solid curves), and of other holograms hypothetically recorded (in the same material and at similar recording conditions) in absence of self diffraction (dashed curves). It is noticeable how the presence of self diffraction can badly affect the performances of the material in a number of different fashions. The recorded holograms (in presence of self

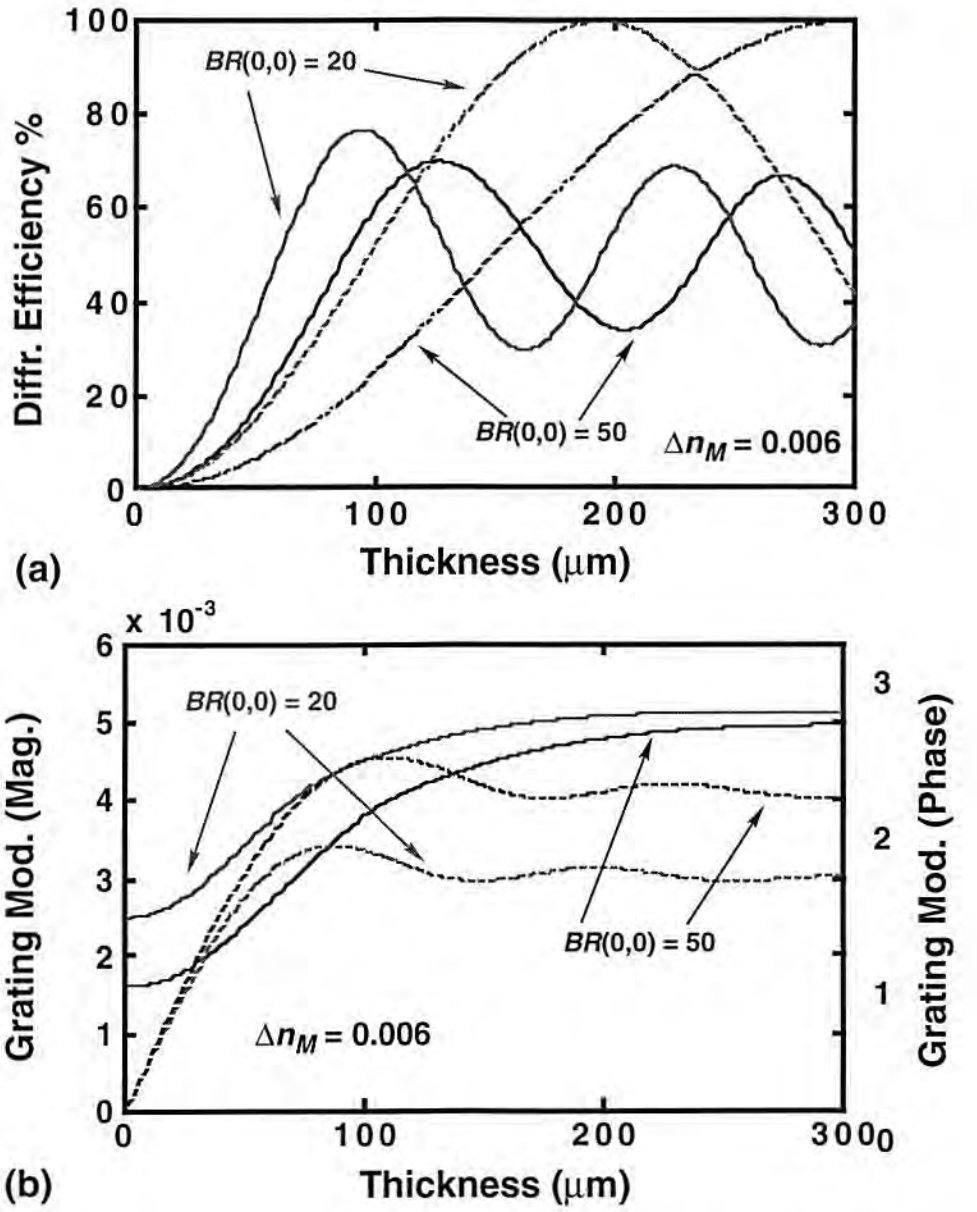

Figure 4-15. Simulation results describing the effects of self diffraction on a 300 μm thick photopolymer at different input beam intensity ratios, with $\Delta n_M = 0.006$, and writing beams at a Bragg angle of 20°, and a wavelength $\lambda = 514$ nm. The average recording intensity was $I_o = 16$ mW/cm^2, in each recording. The simulation is taking into account the variation of the loss due to dye bleaching. **(a)** Diffraction efficiency read out by a Bragg matched probe beam at $\lambda_p = 633$ nm. The values related to the action of self diffraction (solid curves) are compared to those in absence of self diffraction (dashed curves). **(b)** Variation of the phase (dashed curves) and amplitude (solid curves) of the grating due to self diffraction within the holographic region.

diffraction) fail to reach hypothetical maximum of 100% diffraction efficiency while the maximum value is instead bounded well below the 80% value. Moreover, along the material thickness, the variation of the diffraction efficiency is *quasi* sinusoidal, with a period different from the hypothetical one (in the absence of self diffraction) seen from the dashed curves. Concurrently, Fig. 4-15 (b) (solid curves) indicates how the amplitude grating modulations grow along the z-axis almost converging at $z = 300$ μm. In both the recordings, Fig. 4-15 (b) dashed curves, the variations of the grating phases shows similar trends: first they reach the maximum values, and next they are almost constant along the z-axis. Of course, even in these cases, the variation of the grating phases and amplitudes are far different from what we would expect if we hypothetically recorded the same holograms in absence of self diffraction. In fact, because the recording beams are symmetrically incident with a Bragg angle of 20°, in the absence of self diffraction one would expect no grating phase variation (a constant phase of zero) and constant modulation amplitude within the hologram.

Clearly, from a critical understanding of the results of these simulations, one may deduce that self diffraction may jeopardize the use of very thick photopolymers for high storage application. In fact, the results seen in Fig. 4-15 (a) indicate that can be difficult to predict and control the response of the material in term of diffraction efficiency in very thick samples. Moreover, the fringe orientations bending can change the redout Bragg angle of the recorded holograms, which may severely affect the hologram readout in a detrimental fashion. To better clarify this last statement, one may consider the example of

the recording of angularly multiplexed holograms which are storing optical information or implementing optical interconnections. If this change (or better the shift) of the Bragg angle occurs, a recalling beam, during readout, may now be (after recording in presence of self diffraction) Bragg matched with a different (from the original recording) grating, delivering, therefore, the wrong information or activating the wrong interconnections, with devastating consequences on the performance of the holographic element.

Of course, a simple way to limit these effects caused by self diffraction is to record holograms preventing self diffraction, which for the case of angularly multiplexed holograms, may be to record the holograms via sequential exposures, using input intensity beam ratios of unity. It has been already said, that this sequential technique can be cumbersome and it may be too prolonged in time, but it also presents an additional number of other inherent drawbacks, which are more strictly related to the nature of the physics of photopolymers. Dark diffusion transient it is one of these drawbacks, as extensively described in Chap. 5. Moreover, in recording where a signal beam is carrying a complex information or image a recording with beam ratio of unity has been demonstrated to write holograms which originate noisy reconstructions [Collier *et al.*, 1971]. Another drawback is related to the consequences of nonuniform bleaching of the light absorbing dye during recording. In sequential recording, the dye is progressively bleached in a fashion which is spatially nonuniform along the z-axes. In fact, because of the light absorption, the initial recordings will be able to bleach the region closer to the surface ($z = 0$) of the incident writing beams with:

(1) a grating amplitude modulation which is decaying along the z-axis;

(2) the more intense bleaching of the initial holographic region originates a spatially varying absorption coefficient as $\alpha(z = 0) << \alpha(z = T)$;

(3) because of **(2)**, the photopolymerization will be more intense at the beginning of the holographic region, which will saturate earlier respect to end of the region ($z = T$), causing the a different monomer concentrations along the z-axis, with $[M](z = 0,t) << [M](z = T,t)$.

As the sequential recording progresses, the last exposures will record gratings whose amplitude modulations will grow along the z-axis, contrary to what seen in **(1)**, as a consequence of **(3)**. Therefore, in these conditions the control of each sequentially recorded grating diffraction efficiency is a challenging project. Thus, the theory which describes the exposure time schedule in sequential exposures, discussed in Chap. 3, cannot apply for these very thick photopolymers.

As is well known, one of the conditions which favor the use of thick holographic material as an effective high storage media is to have a large Δn_M. At the same time a large Δn_M, ineluctably, magnifies the effects of self diffraction on the recordings. To better visualize this argument, we have depicted in Fig. 4-16 and Fig. 4-17 the simulation results of recordings of holograms in 300 μm thick photopolymers, progressively with larger $\Delta n_M = 0.002$, 0.006, Fig. 4-16, and $\Delta n_M = 0.01$, 0.015, Fig. 4-17. The input beam intensity ratio was the same for all the recordings, $BR(0,0) = 20$, and, as well, it was considered the same photopolymerization process with the values of parameters (γ, δ, and τ) in all

the four cases. The average recording intensity was $I_o = 16$ mW/cm^2. Similarly to what was depicted earlier, the figures present a comparison of the variation, at saturation, of the diffraction efficiencies in presence of self diffraction (solid curves), in absence of self diffraction (dashed curves), of amplitudes of the grating modulations (solid curves), and of the phases of the grating modulations (dashed curves). The figures clearly indicate that for larger Δn_M values the effects of self diffraction are more evident, as clearly seen in Fig. 4-17 (a) which depicts such variations for $\Delta n_M = 0.01$ and 0.015, and in Fig. 4-16 (a) for $\Delta n_M = 0.006$. Here, for both the holograms, once the diffraction efficiencies reach a maximum of ~ 80%, they start oscillating within the holographic region going never below 25%. It is noticeable that the oscillation period is smaller for a larger Δn_M value (while it is not apparent for the $\Delta n_M = 0.002$ recording), and this oscillation starts right after the grating phases reach the largest value. Interestingly, a simple analysis of the grating formation of this thick material can allow us to define the reason of this (almost unpredictable) behavior of the diffraction efficiency and to determine the period of this oscillations. The analysis can be carried out as it follows.

For the moment we can restrict out attention to the recordings in Fig. 4-17 and Fig. 4-16, relevant to the holograms for $\Delta n_M = 0.01$, 0.015, and 0.006. Hypothetically, each of these holograms can be thought as the combination of two holographic layers in cascade: the first sub-hologram includes the region between $z = 0$ and the phase grating peak at $z = z_1$; the second sub-hologram in interval $z_1 \leq z \leq 300$ μm includes the region where the grating phase and grating amplitude are (almost) constant. When a Bragg matched probe beam at

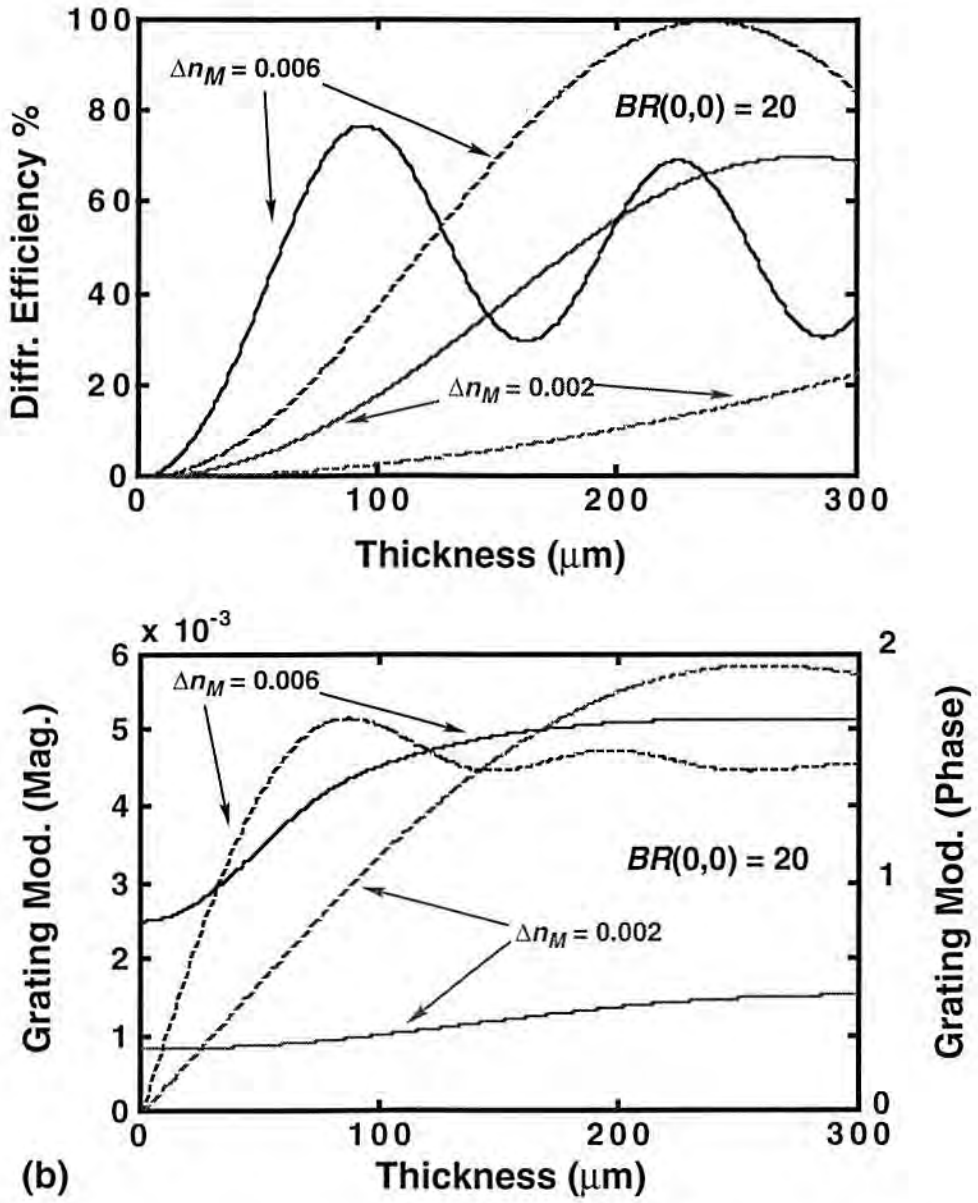

Figure 4-16. Simulation results describing the effects of self diffraction on 300 μm thick photopolymers having respectively $\Delta n_M = 0.006$ and 0.002. The writing beams are at a Bragg angle of 20° with a wavelength $\lambda = 514$ nm. The average recording intensity was $I_o = 16$ mW/cm^2, in each recording, with $BR(0,0) = 20$. The simulations are taking into account the variation of the absorption loss due to dye bleaching. **(a)** Diffraction efficiency read out by a Bragg matched probe beam at $\lambda_p = 633$ nm. The values related to the action of self diffraction (solid curves) are compared to those in absence of self diffraction (dashed curves). **(b)** Variation of the phase (dashed curves) and amplitude (solid curves) of the grating due to self diffraction within the holographic region.

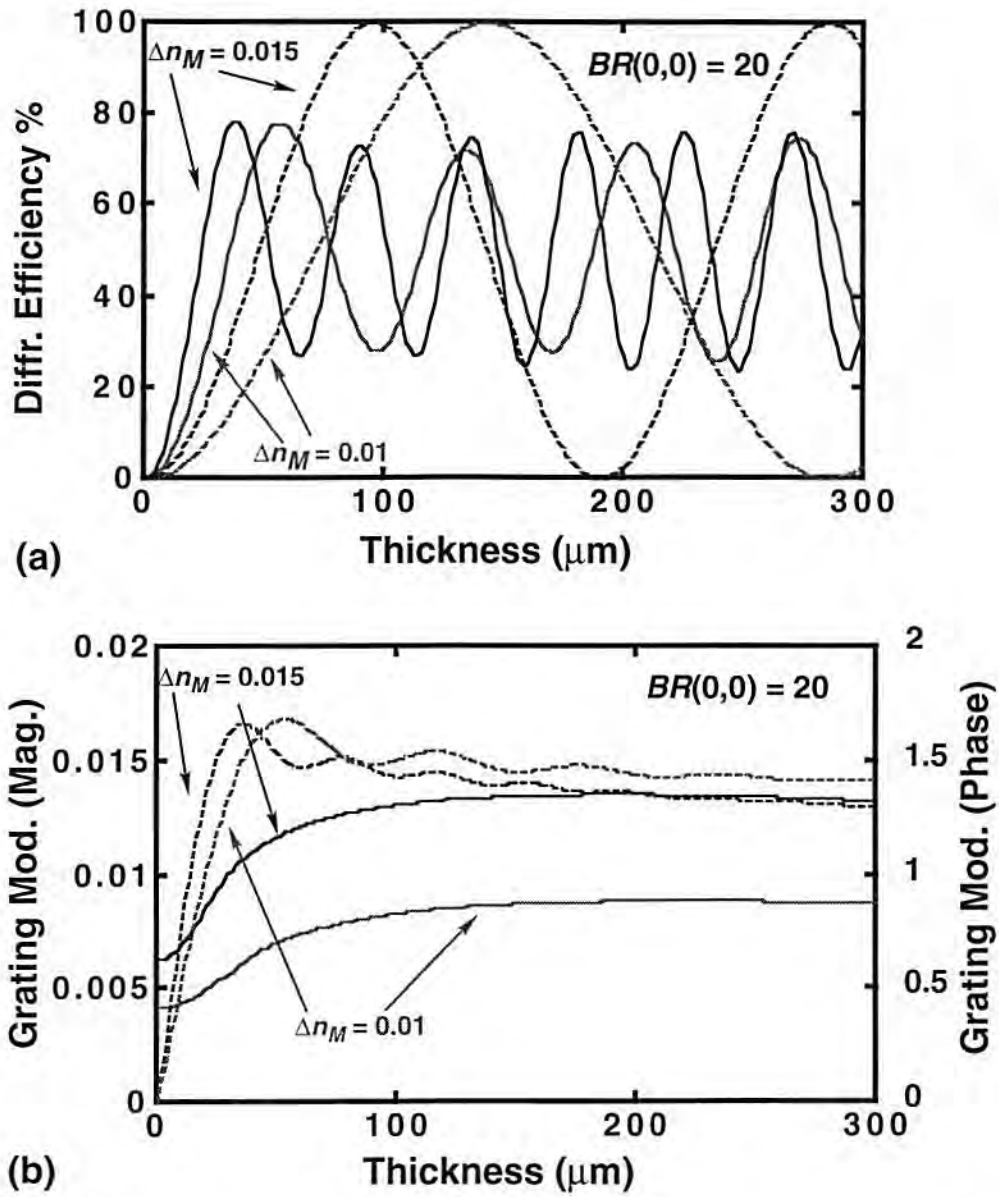

Figure 4-17. Simulation results describing the effects of self diffraction on 300 μm thick photopolymers having respectively $\Delta n_M = 0.01$ and 0.015. The writing beams are at a Bragg angle of 20° with a wavelength $\lambda = 514$ nm. The average recording intensity was $I_o = 16$ mW/cm^2, in each recording, with $BR(0,0) = 20$. The simulations are taking into account the variation of the absorption loss due to dye bleaching. **(a)** Diffraction efficiency read out by a Bragg matched probe beam at $\lambda_p = 633$ nm. The values related to the action of self diffraction (solid curves) are compared to those in absence of self diffraction (dashed curves). **(b)** Variation of the phase (dashed curves) and amplitude (solid curves) of the grating due to self diffraction within the holographic region.

$\lambda_p = 633$ nm of field amplitude E_p impinges on the hologram, the total field at the output of the first sub hologram is composed of first and second diffracted order respectively as

$$\tilde{\eta}_1 E_p \text{ and } \left(1 - |\tilde{\eta}_1|^2\right)^{1/2} E_p, \tag{4-35}$$

in which the term $\tilde{\eta}_1$ is the complex amplitude diffraction efficiency of the first sub-hologram. For these recordings, the magnitude of the field diffraction efficiency $\tilde{\eta}_1$ is approximately equal to $|\tilde{\eta}_1|^2 \approx 0.8$. The total output field of the first sub-hologram illuminates now the second sub-hologram. As already motivated, we will approximate this second sub-hologram as a simple grating with constant modulation index and zero phase variation, which according to Eq. 4-5 corresponds to a complex amplitude diffraction efficiency

$$\tilde{\eta}_2(z) = -j\sin\left(\frac{\pi \Delta n_2 z}{\cos(\theta_p)\lambda_p}\right) \text{ for } z_1 \le z \le 300, \tag{4-36}$$

in which Δn_2 is the modulation of the grating in this second sub hologram. Therefore, according to the canonical solution of the Kogelnik's coupled wave theory [Kogelnik, 1969], we can express the variation of the overall diffraction efficiency inside this second sub-hologram as

$$\eta(z) = \frac{\left|\tilde{\eta}_1 E_p \cos\left(\frac{\pi \Delta n_2 z}{\cos(\theta_p)\lambda p}\right) - j\left(1 - |\tilde{\eta}_1|^2\right)^{1/2} E_p \sin\left(\frac{\pi \Delta n_2 z}{\cos(\theta_p)\lambda p}\right)\right|^2}{|E_p|^2} . \tag{4-37}$$

Rearranging the above, with the proper algebraic inspiration, we can obtain the following more comfortable writing

$$\eta(z) = \frac{1}{2} + \frac{2\left|\tilde{\eta}_1\right|^2 - 1}{2}\cos\left(\frac{2\pi\Delta n_2 z}{\cos(\theta_p)\lambda p}\right) - \frac{\left|\tilde{\eta}_1\right|\left(1 - \left|\tilde{\eta}_1\right|^2\right)}{2}\sin\left(\frac{2\pi\Delta n_2 z}{\cos(\theta_p)\lambda p}\right), \quad (4\text{-}38)$$

which for an approximated $\left|\tilde{\eta}_1\right|^2 \approx 0.8$, defines a sinusoidal oscillation of the diffraction efficiency along the z-axis, within 80% and 20%, as seen in the computer simulations of Fig.'s 4-16 and 4-17. Moreover, Eq. 4-38 specifies the period of the diffraction efficiency oscillation cycles as

$$\Lambda_o = \frac{\cos(\theta_p)\lambda p}{\Delta n_2}, \quad (4\text{-}39)$$

which for the case of the recording with $\Delta n_M = 0.01$, 0.015,(in Fig. 4-17) and $\Delta n_M = 0.006$ (in Fig. 4-16) is respectively $\Lambda_o = 46$, 75 and 120 μm, in total agreement with the numbers that we can evince from the simulation data.

Differently, the simulation data for $\Delta n_M = 0.002$ Fig. 4-16, does not show the same behavior of the other recordings at higher Δn_M. Of course, the reason of this different behavior because the grating phase variation barely reaches it maximum at the end of the hologram, and therefore the simple analysis shown above cannot be applied.

Intuitively, the above discussions and comparisons are helpful in suggesting some new rules of thumb to be used when recording angularly multiplexed volume holograms in very thick photopolymers:

(1) to choose a low Δn_M;

(2) to avoid reaching the maximum phase modulation within the holographic region;

(3) to limit the phase variation of the recorded grating in the Bragg angular selectivity range (explained later in this section).

I/C recording may be able to satisfy the above three rules of thumb. In fact, it has been shown in Chap. 3 that one of the consequences of simultaneously recording a number of holograms in photopolymers is to reduce the value of Δn_M as $\Delta n_M / N$, being N the number of multiplexed holograms, which can satisfy the above rule **(1)** and possibly, as a consequence, rule **(2)**. This last concept is better demonstrate in Fig. 4-18, where the results concerning the I/C recording of gratings with $BR(0,0) = 2$, and $BR(0,0) = 20$ are presented. It was supposed that $N = 10$ gratings, each one with an associated $I_o = 16$ mW/cm^2,are simultaneously recorded in the material a 300 μm thick photopolymer with $\Delta n_M = 0.006$. The HFMD assumption is still supposed valid. Fig. 4-18 (a) demonstrates how, during I/C recording, the detrimental effects of self diffraction are largely limited, because the diffraction efficiencies of the two recordings (solid curves) follow very closely the hypothetical case in which self diffraction is absent (dashed curves). This agreement between the ideal case and the self diffraction case is explained by an analysis of the data in Fig. 4-18 (b), which is depicting for both the recordings the variation of the grating modulation, in magnitude and phase. The magnitude values of the gratings are approximately constant along the material profile, while the grating phases are monotonically and nearly linearly growing (differently to what seen in Fig.'s 4-16 and 4-17) to a maximum of 1.2 rad at $z = 300$ μm for the grating associated to $BR(0, t) = 20$ (the $BR(0, t) = 2$ recording shows a limited phase variation because it is closer to an input beam intensity ratio of unity in value). These last

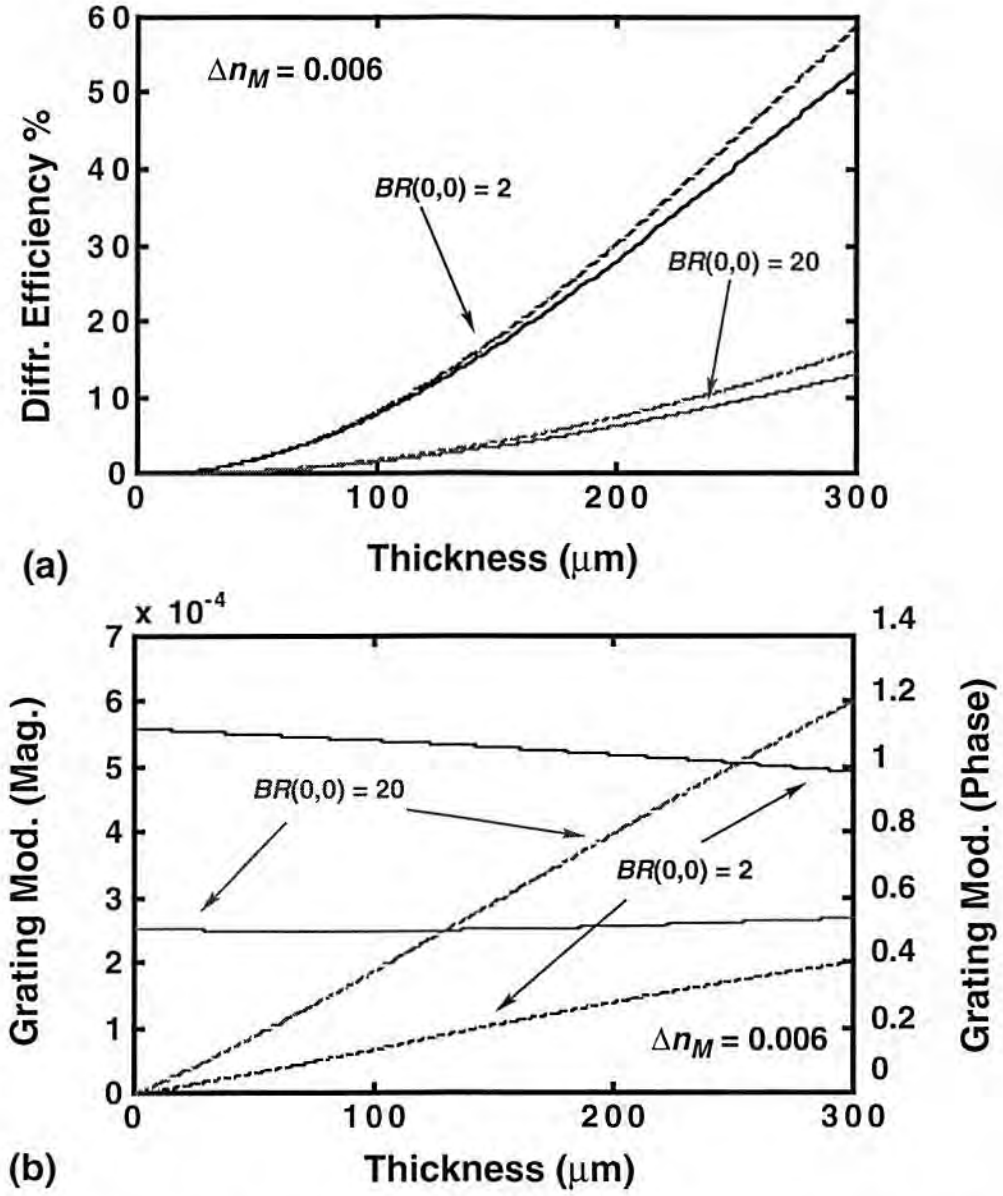

Figure 4-18. Simulation results describing I/C recording in a 300 μm thick photopolymer having $\Delta n_M = 0.006$, and $N = 10$ angularly multiplexed holograms. Two holograms are depicted, with writing beams at a Bragg angle of 20°, and writing wavelength $\lambda = 514$ nm. The average recording intensity was $I_o = 16$ mW/cm^2 for each beam couple, with $BR(0,0) = 20$, and $BR(0,0) = 2$. The simulations are taking into account the variation of the absorption loss due to dye bleaching. **(a)** Diffraction efficiency read out by a Bragg matched probe beam at $\lambda_p = 633$ nm. The values related to the action of self diffraction (solid curves) are compared to those in absence of self diffraction (dashed curves). **(b)** Variation of the phase (dashed curves) and amplitude (solid curves) of the grating due to self diffraction within the holographic region.

data indicate that, in essence, almost ideal gratings have been recorded in the medium and it is reasonable that the diffraction efficiency must closely follow the canonical case, as confirmed in Fig. 4-18 (b). According to the indication of rule **(3)**, however, for sake of better holographic reconstruction, it is important that spatial variations of the grating phases do not lead to inclination of the gratings which will eventually require an off Bragg illuminating beams to maximize the readouts. In other terms, given $\Delta\phi$ the inclination of the grating originated by the phase variation, it is required that $\Delta\phi$ is less than the hologram angular selectivity as

$$\Delta\phi < \frac{\Lambda_g}{T}, \tag{4-40}$$

where the angles are referred in the material [Kogelnik, 1969]. For the holograms Fig. 4-18 (b), we can approximate linearly the variation of the grating phases within the hologram, and given a maximum phase value of ψ at $z = T$, one can rewrite the above condition, after calculating $\Delta\phi$ according to the procedure previously shown by Eq. 4-34, as

$$\frac{\psi\Lambda_g}{2\pi T} < \frac{\Lambda_g}{T}, \tag{4-41}$$

which can be reduced to the simpler condition

$$\psi < 2\pi, \tag{4-42}$$

which is clearly true for the cases of Fig. 4-18.

4.8 Conclusions

In this chapter we have described the origin and the consequence of self diffraction during holographic recording in photopolymers. Self diffraction can affect, sometimes in a very complicated way, the performances of holograms recorded in photopolymers, especially when very thick materials with high $\Delta n_M$are used. In this chapter, however, we have indicated a number of way to limits the effects of self diffraction, such as to use input beam intensity ratios close to unity during the exposure. In the case of hologram multiplexing, we have discussed how I/C recording may limit the drawbacks of self diffraction in certain circumstances.

Importantly, in this chapter it was presented a methodology to study self diffraction in permanent real time holographic material, which can potentially be extended to any kind of permanent real time holographic material already existing, or eventually available in the next future.

4.9 Bibliography

Collier, R. J., C. B. Burckhardt, and L. H. Ling, *Optical Holography,* Academic Press, (1971).

De Lalla Giuseppe, Personal Communication, 1994

Faiman, Y., E. Klancnik, and S. E. Lee, "Optical Coherent Image Amplification

by Two-Wave Coupling in Photorefractive $BaTiO_3$," Opt. Eng., **25**(2), 228-234, (1986).

Gaylord, T. K. and M. G. Moharam, "Thin and Thick Gratings: Terminology Clarification," App. Opt., **20**(19), 3271-3273, (1981).

Gunter, P. and J. P. Huignard, ed. *Photorefractive Materials and Their Applications*, Springer-Verlag, Berlin, (1988).

Kogelnik, H., "Coupled Wave Theory for Thick Holographic Gratings," Bell System Technical Journal, **48**(9), 2909-2947, (1969).

Yeh, P., A. E. Chiou, J. Hong, P. Beckwitt, T. Chang, and M. Khoshnevisan, "Photorefractive Nonlinear Optics in Optical Computing," Opt. Eng., **28**(4), 328-343, (1989).

Chapter 5

A Diffusion Model for the Holographic Grating Formation in Photopolymers

5.1 Introduction

Free monomer diffusion is, with the nonuniform spatial illumination and photopolymerization, one of the basic physical process that makes possible the recording of holograms in photopolymer materials. As early as 1971, practically when the investigation on holographic photopolymers began, Colburn [Colburn *et al.*, 1971] indicated that the grating modulation is practically created by free monomer migration in each 'bright fringe' spots where they are likely to be polymerized. This accumulation of polymeric molecules in the proximity of such illuminations peaks gives rise to a nonuniform material concentration which, in optics terms, acts as a phase grating. The same argument was confirmed by the observations of Wopschall [Wopschall and Pampalone, 1972], while working at DuPont Experimental Station Laboratory on materials that can be considered as the legitimate grandparents of those photopolymers investigated in this thesis. More closely related to the DuPont HRF-150-38 is, the material studied by Booth [Booth, 1975], at DuPont Experimental Station

Laboratory, which practically presented the first attempt to characterize holographic photopolymers in terms of noise, shelf life, sensitivity, and diffusion mechanism. While Booth agreed with Colburn that monomer diffusion is essential for the creation of a grating modulation, he did not share with Colburn some basic intuitions and observations on the dynamics of the grating evolution. Booth observed a positive monotonic evolution of the grating formation (as we do), in contrast to what Colburn *et al.* reported (thinking that it was due to free monomer diffusion), which was at first $\Delta n(t)$ returning to zero after a small growth, and finally its growth to saturation. Probably this behavior was more inherent to the peculiar nature of the material investigated by Colburn and it did not have any relation with the monomer diffusion itself. In more recent literary outputs, monomer diffusion has been indicated as one of the causes of the hologram recording process in photopolymers, [Weber *et al.*, 1990] and [Smothers *et al.*, 1990], while, to our knowledge, the first mathematically sound effort to analyze the interaction of free monomer diffusion and nonuniform photopolymerization during holographic exposure has been presented in a work by Zhao [Zhao and Mourolis, 1994]. Zhao developed a mathematical model based on the study of the higher order harmonics of the holographic grating and of the diffusion terms. According to the results of our investigation, higher order harmonic theory may be attractive but it requires a demanding mathematical effort which can be superfluous. In fact, in this chapter we propose a simpler diffusion model which considers the physical description of the monomer concentration as the combination of its DC and its first harmonic term which both contribute to the formation of the first harmonic term of the grating modu-

lation (essentially $\Delta n(t)$) during holographic exposure. This model is inspired and is supported by experimental observations, and it can predict a number of physical processes that occur during holographic exposure in photopolymers, such as the relation between the average recording intensity and saturation diffraction efficiency, and dark diffusion transient which is for the first time presented and simulated in this dissertation. Before we continue with a careful presentation of our diffusion model, we must clarify how the next described diffusion model can include the HFMD model which was presented previously in this thesis. The HFMD model takes into account free monomer diffusion. We supposed, however, that such diffusion process was ideal for the hologram recording, which means that free monomer diffusion could be considered very fast (hypothetically 'instantaneous') when compared to grating formation process at certain average recording intensity. Conversely, when the diffusion cannot be considered no longer as 'instantaneous', or better at higher average recording intensities where the grating formation process is very fast a more rigorous mathematical and physical modelling of the grating formation is necessary, which must include the mathematical description of the spatial-temporal varying free monomer concentration. The rest of this chapter describes the diffusion model and the supporting experimental measurements follows an introductory and qualitative discussion of our diffusion model, which we present in the next section.

5.2 Modelling the Monomer Diffusion During Holographic Exposure

With the help of Fig. 5-1, we can illustrate the principles of a diffusion model able to depict the interaction among the free monomer diffusion, photopolymerization, and the grating formation during holographic exposure. The figure illustrates a holographic exposure in a photopolymer, where two coherent waves, I_1 and I_2, interfere in the material creating an illumination pattern $I(x) = I_o[1+m\cos(K_g x)]$ (note that, unless specified, most of the following symbology is borrowed from Chap. 2). Because of this sinusoidal interference pattern, photopolymerization is more intense in the proximity of the bright fringe spots, and so is the concentration of the created polymeric molecules. This spatially varying concentration of polymeric molecules gives rise to a sinusoidal modulation of the refractive index of the material whose time varying amplitude modulation is indicated as $\Delta n_g(t)$ in Fig. 5-1. At the same time the monomer concentration, $[M](x,t)$, varies in time and space because of polymerization. In fact, this concentration is depleted in time as the photopolymerization progresses and, because of the nonuniform illumination, the depletion is more vigorous where the intensity peaks are located. The immediate consequence of this nonuniform monomer depletion is that the monomer concentration has a harmonic component of amplitude $[M]_1(t)$, which is 180^o out of phase with the refractive index modulation. Because of the presence of the two spatially modulated concentrations (*i.e.* those of the free monomers and the polymers) within the holographic region, the instantaneous grating modulation, $\Delta n(t)$, can be approximately considered (at the moment, with the license to be more rigorous

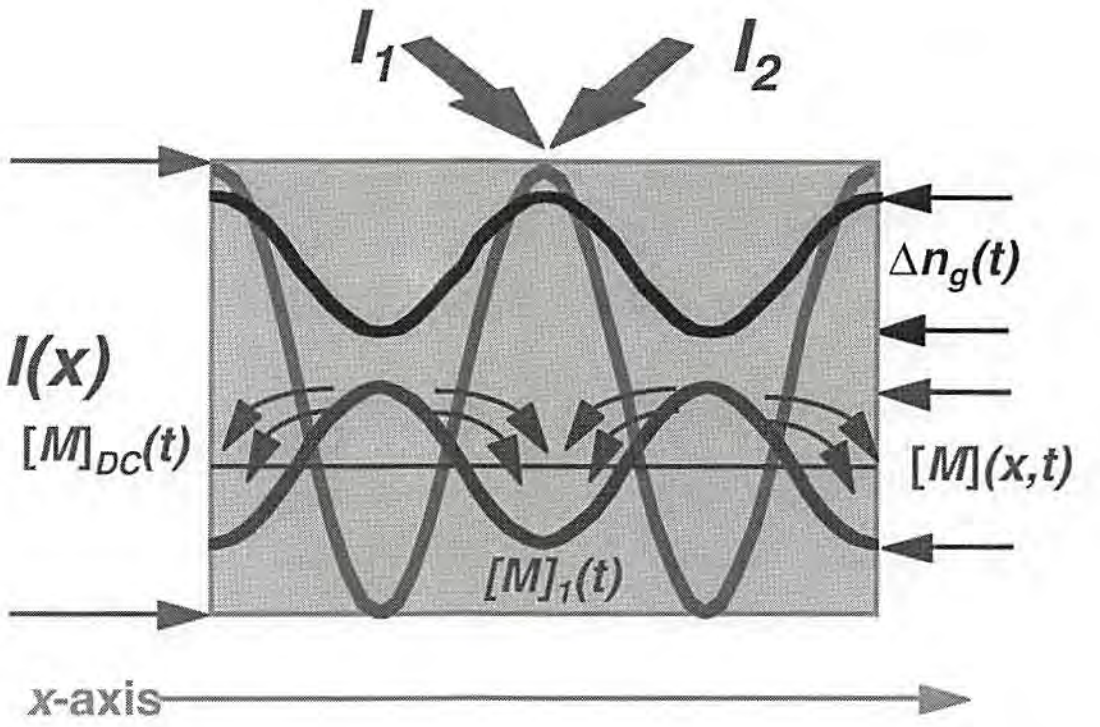

Figure 5-1. Model of the interaction between monomer diffusion and grating formation during holographic exposure in photopolymers. During exposure, a polymeric chain is created along each fringe of the recording light intensity $I(x)$: this leads to a growing index modulation $\Delta n(t)$. The monomer consumption is higher along the illumination peaks, then the monomer concentration is 180° out of phase with the index modulation. $[M](x,t)$ is the monomer concentration, with a DC term $[M]_{DC}(t)$, and $[M]_1(t)$ as its modulation term. The total grating index modulation is the combination of the two sinusoids: $\Delta n_g(t)$-$c_o[M]_1(t)$. Because of monomer diffusion, $[M]_1(t)$ tends to 0.

in a later section of this chapter) as the combination $\Delta n_g(t) - c_o[M]_1(t)$, where c_o is a constant. At the same time, free monomer diffusion tends to level out the free monomer gradient moving free monomers from the 'dark regions', where polymerization is less effective (local minima of $I(x)$ and local maxima of $[M](x,t)$), to the 'bright regions' (local maxima of $I(x)$ and local maxima of the refractive index)), where the free monomer depletion is more intense.

Free monomer diffusion makes the grating formation process possible. In fact, if the free monomer diffusion were absent, or much slower than the polymerization rate, in a short time photopolymerization could deplete all the free monomers that existed in the bright regions, and after that polymerization would start to propagate into the 'dark regions', without creating an effective grating modulation. On the contrary, when the monomer diffusion is much faster than photopolymerization, a continuous supply of free monomers is funneled into the 'bright regions' where free monomers themselves are polymerized. This continuous transfer of free monomers builds up the grating modulation because it spatially changes the material density. At the same time, when free monomer diffusion is very fast, the growth of $[M]_1(t)$ is inhibited with $[M]_1(t) \approx 0$. This last case corresponds to the HFMD model earlier described in this thesis which, in the rest of this chapter, is integrated in the diffusion model by combining it with Flick's diffusion laws [Banks, 1994]. Before we begin the mathematical description of the diffusion model, in the next section we present some experimental observations that can corroborate the theory so far discussed.

5.2.1 Physical Evidence of Free Monomer Diffusion During Holographic Exposure in Photopolymers

There are a number of experimental observations that can confirm our modelling of the free monomer diffusion (and of the presence free of monomer diffusion) during hologram recording in photopolymers. Some of these experi-

mental observations are briefly presented in this section.

As previously indicated, we should expect that a low average recording intensity can favor a higher diffraction efficiency. This condition was already observed in Chap. 2 and Fig. 5-2 better depicts this scenario comparing two exposures having respectively I_o = 166 and 44 mW/cm^2, while the beam intensity modulation, in both recordings, was m = 0.97. In these experiments, as in all in the other experiments presented this chapter, the writing wavelength is 514 nm, the diffraction efficiency is read by a Bragg matched probe beam with wavelength λ_p = 633 nm, while the writing Bragg angle is (unless specified differently) 20^o and DuPont HRF-150-38 is the material used for both the experiments and the simulations. As shown in the figure, at 166 mW/cm^2, the saturation diffraction efficiency (71%) is noticeably inferior to that one recorded at lower recording intensity (83%). This different outcome of the saturation diffraction efficiency for the two different recording conditions can be credited to the interaction between grating formation rate and free monomer diffusion rate (the definition of the grating formation rate and diffusion rate is given in a more rigorous fashion in the next section). In fact, at higher recording intensity the free monomer diffusion rate is too slow when compared to the grating formation rate. This difference between the two rates indicates that there is scarce supply of free monomers in the bright regions of the interference pattern, with the consequence that the refractive index modulation cannot build up as efficiently. This may not be true at lower recording intensity, as witnessed by the 83% diffraction efficiency for I_o = 44 mW/cm^2. The first implication of this result is that for large values of average recording intensity, such as 166

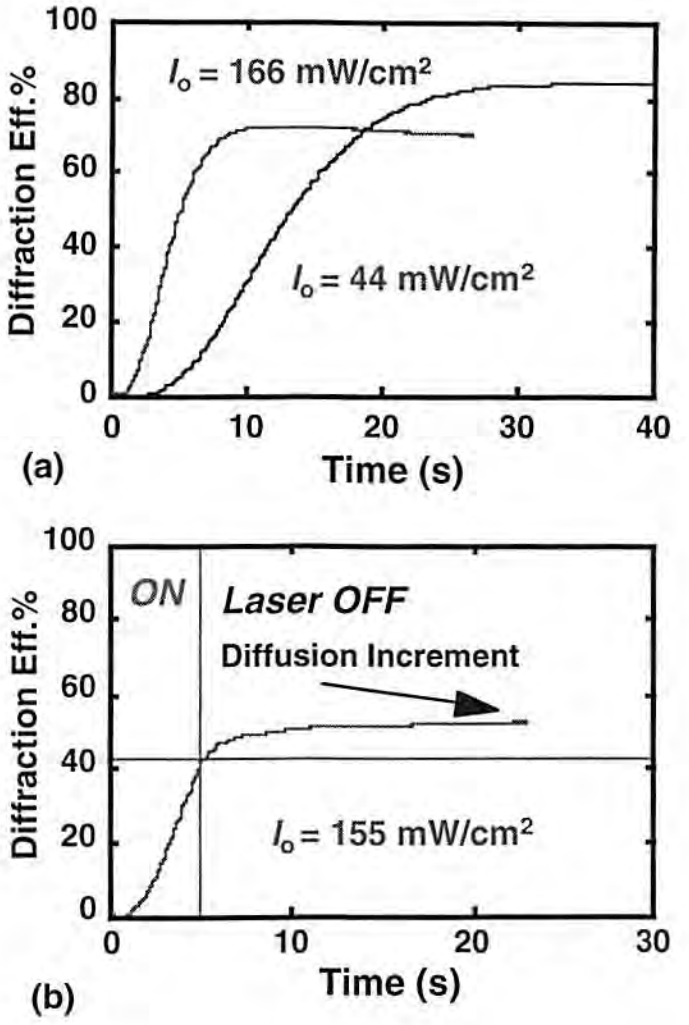

Figure 5-2. Physical evidence of the action of free monomer diffusion during holographic exposures. For the shown recordings the beam intensity modulation was $m = 0.97$ the writing Bragg angle was 20^o, the writing and reading wavelengths were respectively 514 and 633 nm. HRF-150-38 photopolymer was used. **(a)** A higher recording intensity induces a lower saturation diffraction efficiency. At higher intensity, the grating formation time is faster than the monomer diffusion time, therefore after their initial depletion the free monomers are not polymerized any longer along the bright spots. This reduces the efficiency of the process. **(b)** Dark diffusion transient or run off. After exposing, during the 'Laser OFF' period, a monomer gradient ($[M]_1(t) \neq 0$), which is 180^o out of phase with $\Delta n(t)$, exists. Because of monomer diffusion, $[M]_1(t)$ tends to zero, and this leads to an increment of the grating modulation (and of the diffraction efficiency). This diffusion transient period allows the measurements of the diffusion time constant τ_D.

mW/cm^2, the HFMD model is no longer valid, and a new mathematical model capable to take into account the limited free monomer diffusion rate is needed.

A characteristic (and somehow unexpected) behavior of photopolymers is depicted in Fig. 5-2 (b), which shows the temporal evolution of the diffraction efficiency relevant to an exposure in which the recording beams have been halted after 5 s, at $\eta = 40\%$. The experimental observation for $t > 5$ s, and therefore in absence of the recording beams, shows that the diffraction efficiency increases up to 50% at t = 20 s. An explanation of this transient behavior, termed run off or dark diffusion transient, is related to the action of the diffusing free monomers. According to what was presented in the previous section, during recording, the total existing holographic grating can be considered as a combination between the refractive index written because of nonuniform free monomer photopolymerization, $\Delta n_g(t)$, and the amplitude of the sinusoidal modulation of the free monomer concentration, as $\Delta n_g(t) - c_o[M]_1(t)$. In the figure, after 5 s, when the recording illumination is turned off, the grating modulation is therefore $\Delta n_g(5) - c_o[M]_1(5)$. For $t > 5$ s, because of free monomer diffusion, the free monomer concentration tends to become spatially uniform, with $[M]_1(t)$ decaying to zero in time, which causes the grating modulation to tend asymptotically to the value of $\Delta n_g(5)$. Interestingly, this behavior may be more apparent for larger values of average recording intensity. In fact, a higher exposure intensity can imparts a higher $[M]_1(t)$, whose decay leads to a larger and more visible dark diffusion transient. An immediate drawback of this run off effect can be during sequential recording of multiplexed holograms, because it may be very difficult to anticipate the diffraction incre-

ment of each run off after each single exposure.

Another direct, and very useful for the sake of our investigation, consequence of this transient behavior is the possibility to measure during photopolymerization the diffusion time constant at different polymerization levels or at different diffraction efficiency values. In fact, during the dark diffusion transient one can approximate the diffraction efficiency transient to an exponentially growing function, and then estimate the diffusion time constant [Hervet *et al.*, 1978]. The analysis of such measurements indicates that the diffusion time constant mainly depends on the diffraction efficiency values (corresponding to the moment when the illumination is halted), and it increases (the diffusion process slows down) with the larger diffraction efficiency. The explanation of this diffusion time constant variation may be related to the changes that the material experiences during free monomer photopolymerization. As earlier described in this work, Chap. 2, as free monomers photopolymerization progresses, the material viscosity increases which slows down free monomer diffusion with a consequent hike of the diffusion time constant.

Figure 5-3 compares the variation of the measured grating formation time constants with the variation of the measured diffusion time constant pertinent to two different exposure condition: with high (155 mW/cm^2), Fig. 5-3 (a), and low (19 mW/cm^2), Fig. 5-3 (b), average recording intensity. In both these cases the beam intensity modulation was $m = 0.97$. It must be noticed that we used the hologram diffraction efficiency as the abscissa of these plots to better emphasize the relation between grating formation and diffusion time constant.

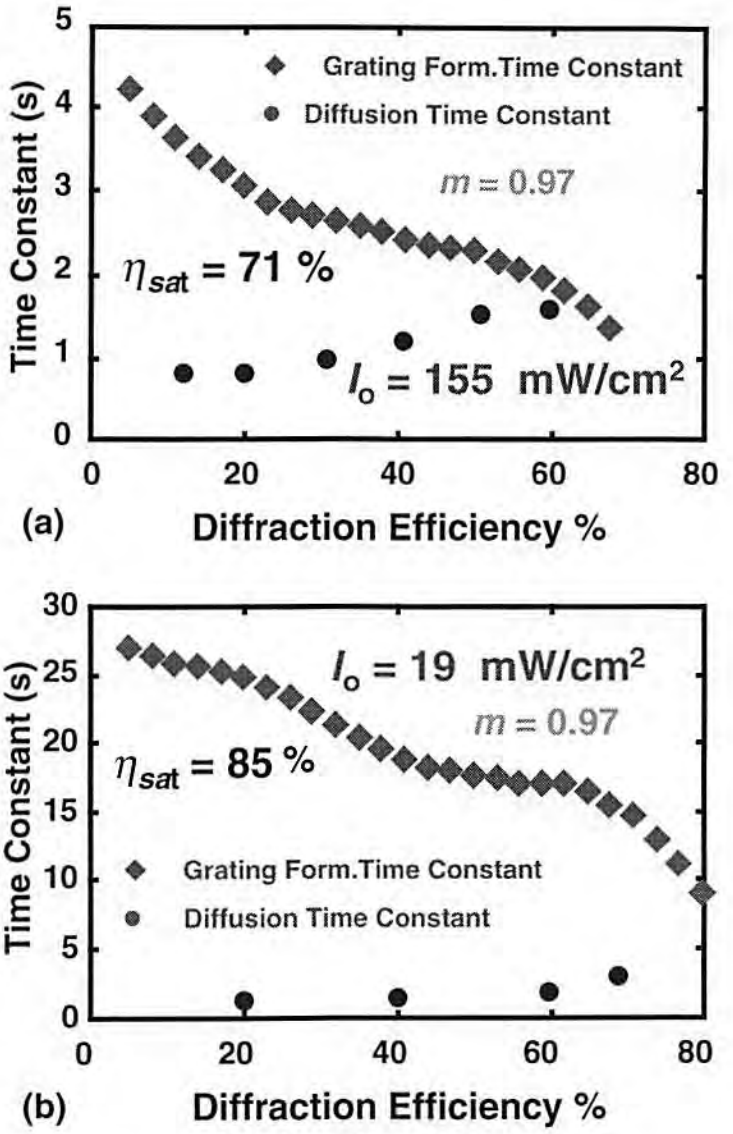

Figure 5-3. Comparison between grating formation time constant and monomer diffusion time constant at different average recording intensities. A higher recording intensity leads to a faster grating formation. The grating formation time constant accelerates during exposure. Conversely, the free monomer diffusion slows down during exposure. This effect may be caused by the increasing viscosity of the media during photopolymerization. **(a)** Recording with $I_o = 155$ mW/cm^2 and $m = 0.97$. The grating formation practically ends when the grating formation time constant is equal to the monomer diffusion time constant. The measured saturation diffraction efficiency is $\eta_{sat} = 71\%$. **(b)** Recording with $I_o = 155$ mW/cm^2 and $m = 0.97$. The grating formation ceases when all the monomers are polymerized: the grating formation time constant is always larger than the diffusion time constant with a higher saturation diffraction efficiency, $\eta_{sat} = 85\%$.

An interpretation of the data of Fig. 5-3 is instrumental to understand better and to validate the interaction between grating formation and monomer diffusion so far illustrated. For the case of high recording intensity of Fig. 5-3 (a), the grating formation time constant is approximately 4.2 s at $\eta = 5\%$ and then the formation process accelerates as witnessed by the decreasing time constant. The point in the plot where the increasing diffusion time constant and the decreasing grating formation time constant intersect, $\eta = 60\%$ and $\tau_D = 1.5$ s, approximately indicates the ending of the grating formation process. According to our theory at this point in this exposure the photopolymerization is very fast and the monomer diffusion is not sufficiently fast to allow migration of free monomers from the dark spots to the bright spots where with their photopolymerization contribute to increase the grating modulation. In fact, shortly thereafter at 71% the diffraction efficiency reaches its saturation value.

Per contra, the holographic exposure with low average recording intensity of Fig. 5-3 (b) (which is within the framework of the HFMD model) yields higher saturation diffraction efficiency. Here even with the behavior of a decreasing grating formation time constant (which is approximately 28 s at $\eta = 5\%$), and increasing diffusion time constant, these two parameters never intersect during recording. In these conditions (*i.e.* the HFMD hypothesis) the majority of the free monomers are able to migrate to the fringe bright spots, and therefore positively contribute to build up a larger grating modulation with their consequent binding in polymeric chains.

5.3 Mathematical Solution of the Diffusion Model

In this section we present the body of the mathematical theory of the diffusion model. This theoretical treatment is entirely based on the information introduced in the discursive description of the diffusion model presented in the previous two sections and it has the aim to combine photopolymerization, coupled wave equations, and Flick's diffusion laws, in order to formulate a functional mathematical expression (hopefully in closed form) able to describe the grating formation in photopolymers.

5.3.1 Basic Equations of the Diffusion Model

As explained in Sec. 5.2 and depicted in Fig. 5-1, when two coherent plane waves of intensity I_1 and I_2 interfere within the holographic medium an intensity pattern is created, $I(x) = I_o[1+m\cos(K_g x)]$, which initiates a nonuniform polymerization, which, according to what indicated in Sec. 2.5, is

$$\left(\frac{\partial}{\partial t}[M]\ (x,t)\right)_{Ph} = -k_R(t)\, I^{\delta}(x)\ [M]\ (x,t)\,, \tag{5-1}$$

where the subscript Ph indicates that the above equation solely describes the variation of the free monomer concentration due to photopolymerization.

Because of this nonuniform photopolymerization, the consumption of the free monomer is more intense where the intensity peaks are located, which leads us to assume and to approximate that the spatial concentration of the free monomers as sinusoidal with phase shift of 180^0 with the intensity pattern,

which gives

$$[M]\ (x,t)\ =\ [M]_{DC}(t) - [M]_{1}(t)\cos\left(K_g x\right), \tag{5-2}$$

where $[M]_1(t)$ is the amplitude of the harmonic term (180° out of phase with the intensity modulation pattern) of the monomer concentration and $[M]_{DC}(t)$ indicates the DC term of the free monomer concentration.

According to the results of the Flick's law [Banks, 1994], we can assume the free monomers move from the regions with high free monomer concentration and low photopolymerization (dark regions) to the areas with low monomer concentration and high photopolymerization with the following rate

$$\left(\frac{\partial}{\partial t}[M]\ (x,t)\right)_{Diff} = \frac{\partial}{\partial x}D\frac{\partial}{\partial x}[M]\ (x,t), \tag{5-3}$$

where the proportionality factor D (dimensionally m^2/s) is the diffusion coefficient which may generally depend on the free monomer concentration and on other physical characteristics of the material (*i.e.* viscosity). The subscript in LHS of the above equation indicates that such equation describes only the time variation of free monomer concentration due to free monomer diffusion.

At this point, we can combine Eq.'s 5-1 and 5-3, and finally describe the total monomer variation rate as

$$\frac{\partial}{\partial t}[M]\ (x,t)\ = -k_R(t)\,I^{\delta}(x)\ [M]\ (x,t) + \frac{\partial}{\partial x}D\frac{\partial}{\partial x}[M]\ (x,t)\,. \tag{5-4}$$

It is necessary now to mathematically describe the variation of the refractive index. Photopolymerization, *per se*, does not change locally the refractive index modulation. In fact, photopolymerization links locally existing free

monomers in polymeric chains, and while this process may change the bulk value of the refractive index, indeed it does not spatially modulate the material density, which is the condition to create a phase grating. The refractive index modulation is related to the local variation of material mass density which is originated by the continuous migration of free monomers (when a monomer concentration gradient is present) within the holographic region. Consequently, we claim that the rate of variation of the refractive index is proportional to the rate of diffusion of the free monomers as

$$\frac{\partial}{\partial t} n\,(x,t) \;=\; c_n \frac{\partial}{\partial x} D \frac{\partial}{\partial x} [M]\;(x,t)\,. \tag{5-5}$$

in which c_n is a constant.

The differential equations 5-4 and 5-5 are the necessary information that can describe the temporal dynamics of the grating formation process in photopolymers, and their solutions give the mathematical description of such process. Because the mathematical complexity of the problem, to solve these equations we introduce a number of approximations which are instrumental in simplifying the mathematical nature of the diffusion model. The errors that these approximations originate are estimated in a subsequent section.

As a first approximation, we suppose that the diffusion coefficient D is constant (in time and space) during the exposure, then we use the binomial series approximation to express the intensity interference term as we also presented during the formulation of the HFMD model. Next, we derive Eq. 5-4 using the definition of free monomer concentration of Eq. 5-2, which leads to

the following expression of the free monomer variation rate during holographic exposure

$$\frac{d}{dt}\left([M]_{DC}(t) - [M]_1(t)\cos(K_g x)\right) \qquad , \quad (5\text{-}6)$$
$$= -k_R(t)\, I_o^{\delta}[1 + m\delta\cos(K_g x)]\,\{ [M]_{DC}(t) - [M]_1(t)\cos(K_g x)\} + \frac{[M]_1(t)}{\tau_D}\cos(K_g x)$$

where the monomer concentration is described as a function containing DC and harmonic terms, and the term τ_D is the diffusion time constant which is equal to $\tau_D = 1/DK_g^2$ as obtained by deriving Eq. 5-3. From Eq. 5-6 we can isolate the rate of variation of the free monomer concentration according to its DC term and the amplitude of the first harmonic, which are

$$\frac{d}{dt}[M]_{DC}(t) = -k_R(t)\, I_o^{\delta}\{ [M]_{DC}(t) - \frac{m\delta}{2}[M]_1(t)\}\text{, and} \qquad (5\text{-}7)$$

$$\frac{d}{dt}[M]_1(t) = k_R(t)\, I_o^{\delta}\{m\delta\,[M]_{DC}(t) - [M]_1(t)\} - \frac{[M]_1(t)}{\tau_D}. \qquad (5\text{-}8)$$

A few comments to assign physical meanings to the RHS terms of the above differential equations may be helpful to the reader. The RHS of Eq. 5-7 indicates that the temporal variation of $[M]_{DC}(t)$ is given by the combination of the rate of disappearance (therefore the negative sign) of this DC term of the free monomer concentration due to photopolymerization and rate of consumption of free monomers that cannot diffuse because of their photopolymerization during the migration towards the bright spots (the term $m\delta k_R(t)\, I_o^{\delta}[M]_1(t)$). Because of its physical definition, we have that $[M]_1(t) < [M]_{DC}(t)$. Moreover, in most of the recordings we can verify that $0.5\delta m << 1$, therefore in describing the variation of $[M]_{DC}(t)$ we can use the approximation

$[M]_{DC}(t) - \frac{m\delta}{2}[M]_1(t) \approx [M]_{DC}(t)$, which leads to

$$\frac{d}{dt}[M]_{DC}(t) = -k_R(t)\, I_o^{\delta}\, [M]_{DC}(t) , \tag{5-9}$$

which is an instrumental equation in finding a closed form solution to the diffusion equation.

Essentially the RHS of Eq. 5-8, which describes the variation of $[M]_1(t)$ during exposure, is composed of a (negative) contribution due to diffusion as $[M]_1(t)/\tau_D$ (which is rate of the decay $[M]_1(t)$), while the photopolymerization continuously builds up $[M]_1(t)$ itself through the term $k_R(t)\, I_o^{\delta}\{m\delta\,[M]_{DC}(t) - [M]_1(t)\}$. Here the term $k_R(t)\, I_o^{\delta} m\delta\,[M]_{DC}(t)$ indicates the rate of creation of $[M]_1(t)$ due to nonuniform photopolymerization, while the term $-k_R(t)\, I_o^{\delta}\,[M]_1(t)$ represents the rate of disappearance of $[M]_1(t)$ due to the detrimental photopolymerization outside of the bright fringe regions.

By considering a constant diffusion coefficient, the refractive index variation has a sinusoidal functional dependence, whose amplitude modulation, $\Delta n(t)$, varies with the following rate

$$\frac{d}{dt}\Delta n(t) = c_n \frac{[M]_1(t)}{\tau_D} . \tag{5-10}$$

Basically Eq. 5-9, 5-8, and 5-10 are the core of the mathematical treatment of the diffusion model. Next, we solve these equations providing first a functional description of the time variation of the free monomer concentration and later of the refractive index modulation.

5.3.2 Solution of the Free Monomer Concentration Equations

The solutions of Eq. 5-9 and 5-8 provide the mathematical description of the temporal evolution of the monomer concentration during holographic exposure in photopolymer. It must pointed out that these solutions are also conducive to determining the temporal evolution of the grating modulation, as presented in the next subsection.

Once we introduce the functional dependence of the polymerization function as $k_R(t) = k_o \exp\left(\varphi I_o^{\delta} t\right)$ (as seen in Chap. 2, Eq. 2-26), we can solve the equations describing the monomer concentration (initial conditions are $[M]_{DC}(0) = [M]_o$, and $[M]_1(0) = 0$) respectively as

$$[M]_{DC}(t) = [M]_o e^{[\gamma(1-\exp(t/\tau))]}, \text{ and} \tag{5-11}$$

$$[M]_1(t) = \frac{m\delta\gamma\tau_D}{\tau_D+\tau}[M]_o e^{[\gamma(1-\exp(t/\tau))]}\left(e^{t/\tau} - e^{-t/\tau_D}\right). \tag{5-12}$$

in which the term $\tau = 1/\varphi I_o^{\delta}$ is the polymerization time constant as also indicated during the presentation of the HFMD model (Chap.2, Sec. 2.9), $\gamma = k_o/\varphi$ is a constant, and $[M]_o$ is the initial free monomer concentration.

While the temporal variation of the DC term is identical to the same expression that we formulated during the studying of the HFMD model, the expression of the first harmonic represents something new which deserves a careful description. The amplitude of the first harmonic of the free monomer concentration can be dissected into a constant amplitude term which multiplies some time dependent expressions. The amplitude term $\frac{m\delta\gamma\tau_D}{\tau_D+\tau}[M]_o$ is (obvi-

ously) proportional to the initial monomer concentration $[M]_o$ and to the beam intensity modulation. This last result is motivated by the fact that a higher m induces a more efficient photopolymerization at the bright fringe spots, with a creation of a consequent larger first harmonic modulation term. Both the average recording intensity and the diffusion time constant influence the multiplicative term and the temporal dynamics of $[M]_1(t)$ in a non linear fashion. As I_o and/or τ_D tends to zero, so it does $[M]_1(t)$: in essence these conditions correspond to a fast free monomers diffusion and to a slower grating formation speed which both contribute to the assumption the of the HFMD model which therefore envisions $[M]_1(t) \approx 0$. Significantly, the temporal dynamics of $[M]_1(t)$ is the combination of three exponential terms, each one related to a different physical process that occurs in the material during exposure. The first multiplicative decaying exponential form, $\exp[\gamma(1-\exp(t/\tau))]$, is linked to the depleting level of the DC concentration available: the lower is the level of $[M]_{DC}(t)$, than the lower is the level of $[M]_1(t)$. The difference between the other two exponential forms, $\left(e^{t/\tau} - e^{-t/\tau_D}\right)$, describes the competition between the creation of the gradient of the free monomers due to nonuniform photopolymerization (first exponential) and its disappearance due to the free monomer diffusion (second exponential). All this reasoning can be visualized in Fig. 5-4, where we depicted the evolution of $[M]_1(t)$ during exposure for a variable average recording intensity and a fixed diffusion time constant $\tau_D = 0.9$ s (part (a)) and, vice versa, for a fixed $I_o = 16$ mW/cm^2, and a varying τ_D (part (b)). The evolution of the amplitude modulation is here normalized by the initial free monomer concentration, and the beam intensity modulation

term. As a confirmation to what said, Fig. 5-4 (a) shows that at a higher values of I_o corresponds a higher peak value of $[M]_1(t)$, which may indicate that a low saturation refractive index modulation is likely. Therefore, if during a recording a large $[M]_1(t)$ is created (to $I_o = 300$ mW/cm^2 and $\tau_D = 0.9$ s corresponds a maximum $[M]_1(t)$ as 12% of $[M]_o$) and the diffusion speed is not adequately fast, the monomers are polymerized far from the bright region which reduces the attainable grating modulation. Concurrently, in recordings with a low τ_D (fast diffusion), Fig. 5-4 (b), $[M]_1(t) \approx 0$ and $[M](x,t) \approx [M]_{DC}(t)$, which practically are the conditions required by the HFMD model.

5.3.3 Closed Form Solution of the Refractive Index Modulation

Once the variation of $[M]_1(t)$ during exposure is determined, by inserting the results of Eq. 5-12 into Eq. 5-10 we can write and try to solve the equation of the variation of the amplitude of refractive index modulation which is

$$\frac{d}{dt}\Delta n(t) = \frac{c_n m \gamma \delta}{\tau_D + \tau}[M]_o\left(e^{[\gamma(1-\exp(t/\tau))]}e^{t/\tau} - e^{[\gamma(1-\exp(t/\tau))]}e^{t/\tau_D}\right). \quad (5\text{-}13)$$

A closed form solution of the above is possible only after the following approximation of the second product between the exponential form in the RHS of Eq. 5-13

$$e^{[\gamma(1-\exp(t/\tau))]}e^{-t/\tau_D} \approx e^{-\gamma t/\tau}e^{-t/\tau_D}, \quad (5\text{-}14)$$

which was obtained by expanding in Taylor's series the exponential exp(t/τ), and then retaining the first two terms of such series expansion. Using such

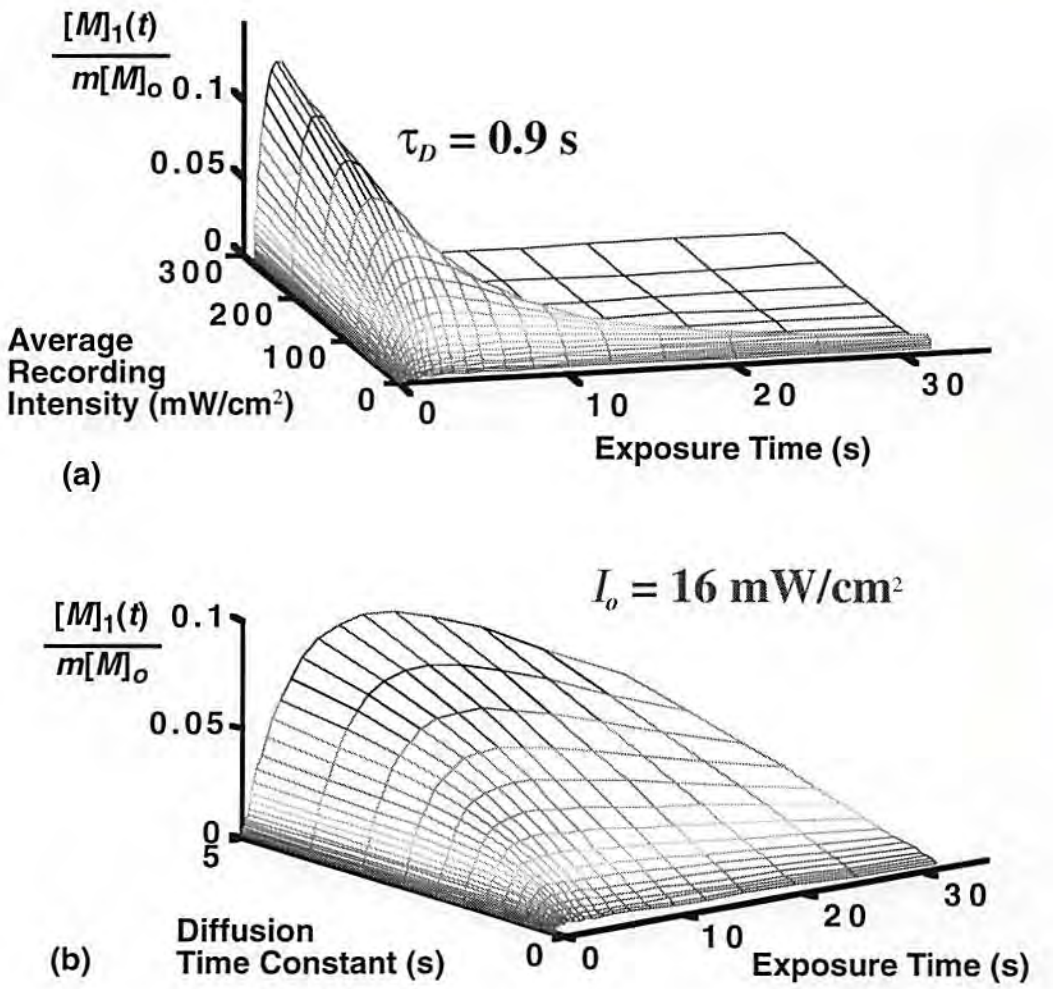

Figure 5-4. Variation of the first harmonic of the free monomer concentration during holographic exposure. **(a)** The diffusion time constant is fixed as $\tau_D = 0.9$ s and the average recording intensity is varying as I_o = 1-300 mW/cm^2. Higher I_o corresponds higher $[M]_1(t)$ modulation, which is detrimental when one wants to reach the largest possible grating modulation value. **(b)** The time constant is varied as $\tau_D = 0.25$-5 s and the average recording intensity is fixed at $I_o = 16$ mW/cm^2. At lower τ_D values, the conditions for the HFMD model are better met because of $[M]_1(t) \approx 0$.

approximation for Eq. 5-13, the variation of the $\Delta n(t)$ is written as

$$\frac{d}{dt}\Delta n(t) = \frac{c_n m\gamma\delta [M]_o}{\tau_D + \tau}\{e^{[\gamma(1-\exp(t/\tau))]}e^{t/\tau} - e^{-\gamma t/\tau}e^{-t/\tau_D}\}. \qquad (5\text{-}15)$$

The solution of the above equation, given the initial condition $\Delta n(0) = 0$, is then

$$\Delta n(t) = \frac{m\tau\Delta n_M}{\tau_D + \tau}\left\{\left(1 - e^{[\gamma(1-\exp(t/\tau))]}\right) - \frac{\tau_D\gamma}{\tau_D\gamma + \tau}\left(1 - e^{-\frac{\tau_D\gamma+\tau}{\tau\tau_D}t}\right)\right\}, \qquad (5\text{-}16)$$

in which $\Delta n_M = c_n\delta[M]_o$ is the largest attainable amplitude of the grating modulation, according to what also indicated during the discussion of the HFMD model solution. The time evolution of the refractive index modulation, included in the curly braces, is composed essentially of the difference of two exponential functions. The function $\left(1 - e^{[\gamma(1-\exp(t/\tau))]}\right)$ (which is in common with the HFMD model solution) is essentially describing the evolution of grating modulation caused by the polymeric chain formation, which in Fig. 5-1 has indicated as $\Delta n_g(t)$. More interestingly, the second exponential function

$$-\frac{\tau_D\gamma}{\tau_D\gamma + \tau}\left(1 - e^{-\frac{\tau_D\gamma+\tau}{\tau\tau_D}t}\right), \qquad (5\text{-}17)$$

is the, overall negative, contribution to the grating formation due to the presence of the free monomer modulation term $[M]_1(t)$ which is 180° out of phase with $\Delta n_g(t)$. Practically, the term of Eq. 5-17 originates from the inhibition to the grating formation process caused by a limited (certainly not instantaneous) free monomer diffusion. As the diffusion time constant tends to zero (instantaneous diffusion of the free monomers) so does the term of Eq. 5-17, and the solution to

$\Delta n(t)$ converges to the HFMD solution, which proves that the HFMD solution is just a special case of the diffusion model.

At saturation, the amplitude modulation of the refractive index is

$$\Delta n_{sat} = \frac{m\tau\Delta n_M}{\tau_D + \tau}\left(1 - \frac{\tau_D\gamma}{\tau_D\gamma + \tau}\right), \tag{5-18}$$

which is a term depending proportionally on m as also in agreement with the results of the HFMD model shown in Fig. 2-9. Moreover, we can see that Δn_{sat} depends on the diffusion time constant and on the average recording intensity through the polymerization time constant τ in a nonlinear fashion. Figure 5-5 (a) depicts the variation of the saturation diffraction efficiency for a varying τ_D = 0.25-5 s and I_o = 1-200 mW/cm^2 while we have constant m = 1. From the set of experiments that we carried out to verify experimentally theoretical findings of this chapter, an average Δn_M = 0.0063 was measured and this value has been used in all the numerical simulations of this chapter. The initial flat area around 89% is the region of the HFMD model. At higher values of average recording intensity and/or higher values of diffusion time constants, the saturation diffraction efficiency drops. Of course, the front curve, corresponding to the highest diffusion time constant with τ_D = 5 s, has almost none of this initial flat region due to an excessively slow diffusion process which hampers the grating formation process. An experimental verification to these data is in Fig. 5-5 (b). In this figure, the measured saturation diffraction efficiencies (◆) at various average recording intensities for m = 0.97 are compared with the theoretical curve (solid line) for τ_D = 0.9 s. Such value of the diffusion time constant was

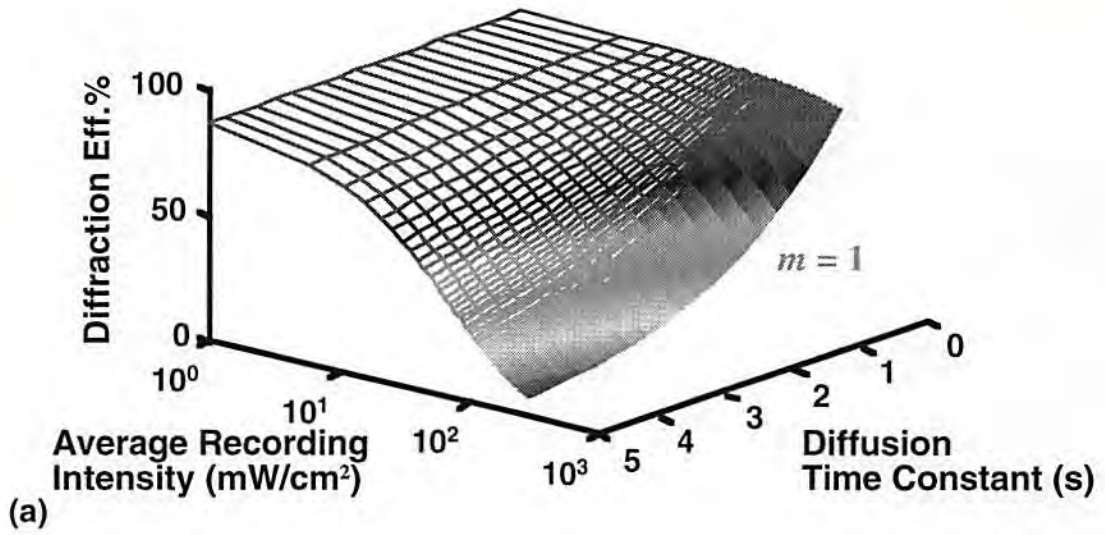

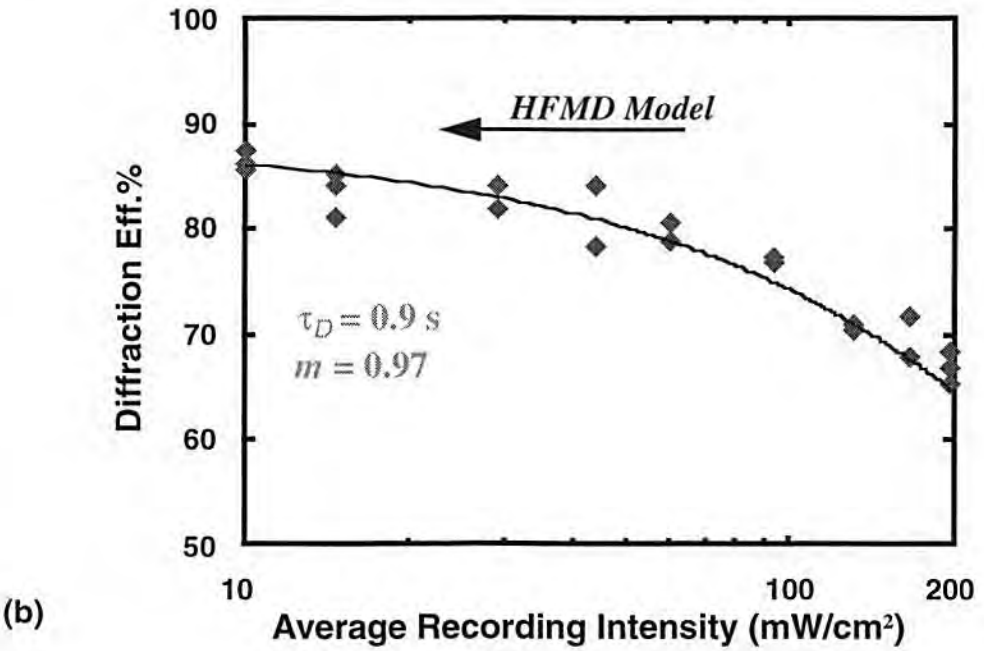

Figure 5-5. Saturation diffraction efficiency according to the diffusion model. (**a**) The three dimensional plot indicates the saturation diffraction efficiency according to the diffusion model, in exposure with 20° of Bragg angle, the writing and the reading wavelength are 514 and 633 nm with $m = 1$. The following parameters are varied: $\tau_D = 0.25$-5 s, and I_o =1-300 mW/cm^2. (**b**) The theory (solid curve), for $m = 0.97$ and $\tau_D = 0.9$ s, is compared with experimental data (u). This constant value of τ_D is an average of the diffusion time constants measured in the experiments of Fig.5-3.

extracted from the measurements shown earlier in Fig. 5-3. By inspection of Fig. 5-5 (b), one can easily notice that theory is perfectly capable of foreseeing both the HFMD model boundary zone, where $\Delta n_{sat} \approx c_n m \delta [M]_o = m \Delta n_M$ and $\eta = 86\%$, corresponding to $I_o < 70$ mW/cm^2, and the decrease of the saturation diffraction efficiency at higher values of I_o.

Once the solution of $[M](x,t)$ and of $\Delta n(t)$ is determined, it is beneficial, for the sake of a better visualization of the diffusion model, to end this section with Fig. 5-6, where we present and compare the evolution of the amplitude of the refractive index modulation versus the time variation of the free monomer concentration. These plots were calculated from Eq.'s 5-11, 5-12, and 5-16. These simulation results are pictorially describing the variation of $[M](x,t)$, and $\Delta n(t)$, while the material is exposed with $m = 1$, $I_o = 200$ mW/cm^2. After 2.1 s $[M]_1(t)$ reaches maximum value of 11% of $[M]_0$ as indicated by the spatial modulation of $[M](x,t)$, while, because of the high recording intensity, the Δn_{sat} is limited to 71% of its maximum value Δn_M. As the exposure progresses, $[M]_1(t)$ tends to disappear and so does the spatial modulation of $[M](x,t)$.

5.4 Assessment of the Approximation Errors

To obtain a functional closed form of the equations describing the temporal dynamics of the monomer concentration and the grating modulation of the diffusion model, we introduced some instrumental approximations whose impact on our model derivation is assessed and discussed in this section.

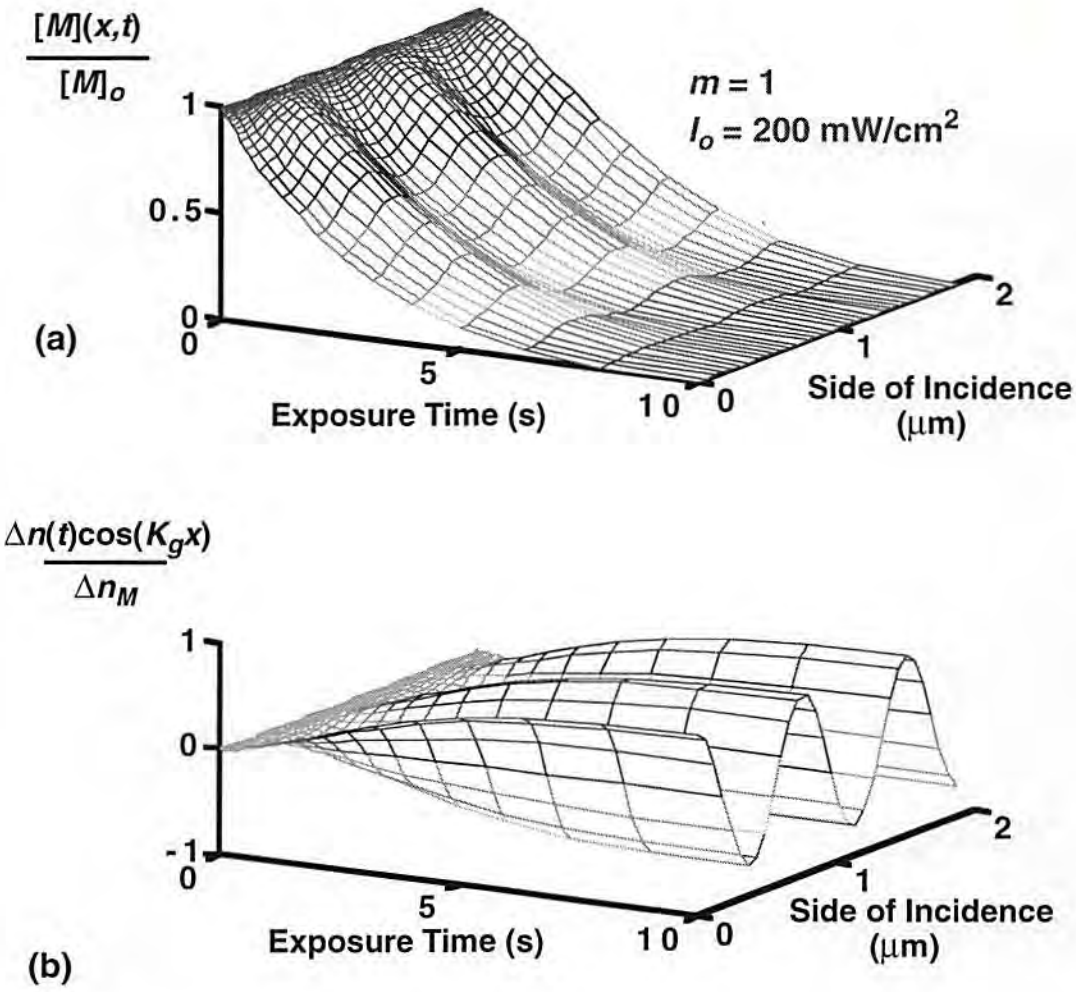

Figure 5-6. Simulation of spatial temporal dynamics of the free monomer consumption and of the refractive index modulation during holographic exposure in photopolymer. The data are referred to an exposure with a pair of beams having $m = 1$, $I_o = 200$ mW/cm^2, Bragg angle of 20° and writing beam wavelength of 514 nm. **(a)** Free monomer consumption during photopolymerization. As photopolymerization progresses, the depletion of the free monomer concentration is spatially modulated and out of phase with $\Delta n(t)$. Such modulation reaches its peak value 11% of $[M]_o$ after 2.1 s. **(b)** The modulation index is built up as the monomer concentration is depleted. Because of the high recording intensity, and the limited diffusion time constant, the refractive index modulation can reach only 71% of the maximum value which is $\Delta n_M = c_n \delta[M]_o$ (*i.e.* the HFMD model limit).

Basically, there are three approximations that we have considered during the development of our diffusion model, which we present here in the same sequence as their introduction

(1) the diffusion coefficient D was considered constant, and consequentially the diffusion time constant τ_D during photopolymerization has a constant value;

(2) the DC term of the monomer concentration is much larger than the modulation term, allowing simplification of Eq. 5-7 as Eq.5-9, using $[M]_{DC}(t) - \frac{m\delta}{2}[M]_1(t) \approx [M]_{DC}(t)$;

(3) to obtain a closed form solution for $\Delta n(t)$, we approximated the exponential form $e^{[\gamma(1-\exp(t/\tau))]}e^{-\tau/\tau_D} \approx e^{-\gamma t/\tau}e^{-\tau/\tau_D}$ in Eq. 5-13.

It is quite immediate to understand that the requirements of approximation **(2)** are met for low values of m and I_o. For $m << 1$, recalling that physics restrictions already impose that $[M]_{DC}(t) > [M]_1(t)$, it is *a fortiori* true that $[M]_{DC}(t) \gg \frac{m\delta}{2}[M]_1(t)$. At the same time, at low I_o the rate of creation of $[M]_1(t)$ is low, and monomer diffusion may easily cancel any concentration gradient, thus physically validating the necessary condition $[M]_{DC}(t) \gg \frac{m\delta}{2}[M]_1(t)$.

Unfortunately, it is not easy to dissect and comment about the impact of approximations **(1)** and **(3)** on the solutions of the model. Therefore, we carried out a number of computer simulations and experimental exposures to understand the validity and the accuracy of the model. Fig. 5-7 and Fig. 5-8, and compare the evolution of $[M]_{DC}(t)$, $[M]_1(t)$, $\Delta n(t)$ and of the diffraction effi-

ciency (in %) of the numerically calculated exact solution (dashed curves), the approximated closed form solution (solid curves), jointly with the measured valued of the diffraction efficiency (dotted curves), at different value of I_o (166 and 44 mW/cm^2), for a constant $m = 0.97$. For each value of I_o are plotted the evolution of two experimental recordings, in this way the theoretical results are also compared with the possible variations of experimental measurements. The exact solution is obtained by numerically solving Eq. 5-7, 5-8, and 5-5, and considering a varying diffusion time constant as measured in Fig. 5-3. The action of this time varying diffusion time constant can be easily detected in the evolution of $[M]_1(t)$ in Fig. 5-7 (b) and Fig. 5-8 (b). One may notice that the exact solution of $[M]_1(t)$ does not reach the peak value of the approximated solution because we have experimentally noticed that at the beginning of the grating formation, with a lower material viscosity, the diffusion time constant is smaller (faster diffusion), which inhibits the growth of $[M]_1(t)$. As we already know, a reduced $[M]_1(t)$ leads to a more efficient grating formation process, and, of course, to a higher saturation diffraction efficiency which explains why the exact solution shows higher diffraction efficiency at saturation than the approximated one. This indication is confirmed in the simulation, and it appears very detectable for the high intensity recording at $I_o = 166$ mW/cm^2, where we have for the exact and approximated solution respectively 68% and 65% of saturation diffraction efficiency, while the measurements indicate 71.8% and 68%. Still emphasizing on the evolution of the diffraction efficiency of Fig. 5-7 (d) and of Fig. 5-8 (d), we can positively observe a good agreement among the exact and the approximated solutions, and as they follow almost exactly the experimen-

tally measured data. Noticeably, as a consequence of approximation **(2)**, at lower I_o the match between the exact solution and the approximated is the better (83% and 82% respectively the exact solution and the approximated, while the measured values indicate 84% and 78.5% for I_o = 44 mW/cm^2).

Finally, a more global visualization of the approximation errors is offered in Fig. 5-9 which depicts the variation of the diffraction efficiency errors, for a varying I_o = 1 - 200 mW/cm^2, and m = 0.1 - 1. To define the approximation error (in%) we used the following relationship between diffraction efficiencies of the approximated solution η_{Ap} and the exact numerical solution η_{Es}

$$\eta_{err} = 100\frac{\eta_{Es} - \eta_{Ap}}{\eta_{Es}}. \qquad (5\text{-}19)$$

The figure confirms that the error is reduced at lower is I_o, and is almost nonexistent at I_o = 1 mW/cm^2 (because we are in the realm of the HFMD hypothesis condition), while it increases with I_o. The 15% error at m = 1 and I_o = 200 mW/cm^2 is deceiving. First, we do not recommend recording a hologram at such high intensity because of the low attainable saturation diffraction efficiency. Next, because of such low saturation diffraction efficiency, the actual error difference, η_{Es} -η_{Ap}, is so small in value that can be meaningless when compared with the actual fluctuations of the diffraction efficiency values that can be seen during experimental exposure, as also shown in Fig. 5-8 (d).

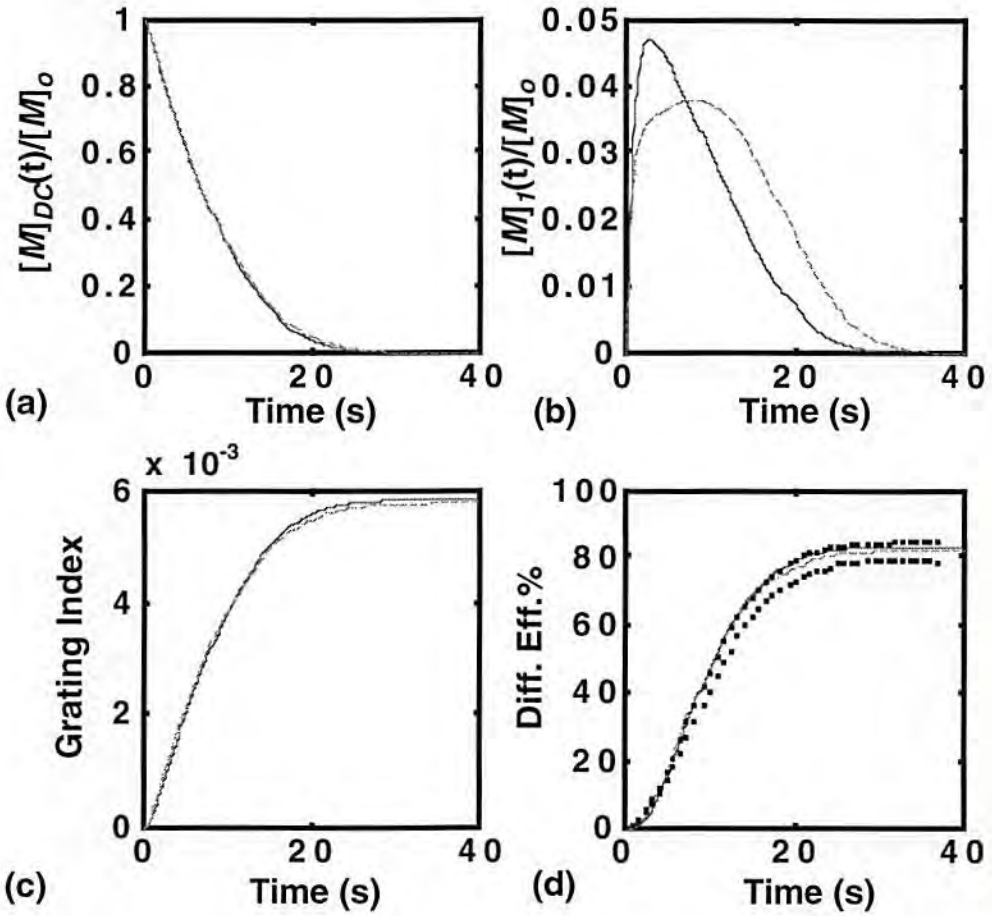

Figure 5-7. Comparison between the exact solutions of the diffusion model (dashed line) and its approximated solution (solid line). The exposure is recorded with $I_o = 44$ mW/cm^2, $m = 0.97$; the Bragg angle is 20°, while the writing and reading out wavelength are respectively 514, and 633 nm. The inhibition period is not shown. **(a)** Temporal variation of the free monomer concentration DC term. This variation is normalized to $[M]_o$. **(b)** Temporal variation of the amplitude of the first harmonic of the free monomer concentration. This variation is normalized to $[M]_o$. **(c)** Temporal variation of the modulation of the refractive index. **(d)** Temporal variation of the diffraction efficiency. The dotted curves refer to two experimental measurements.

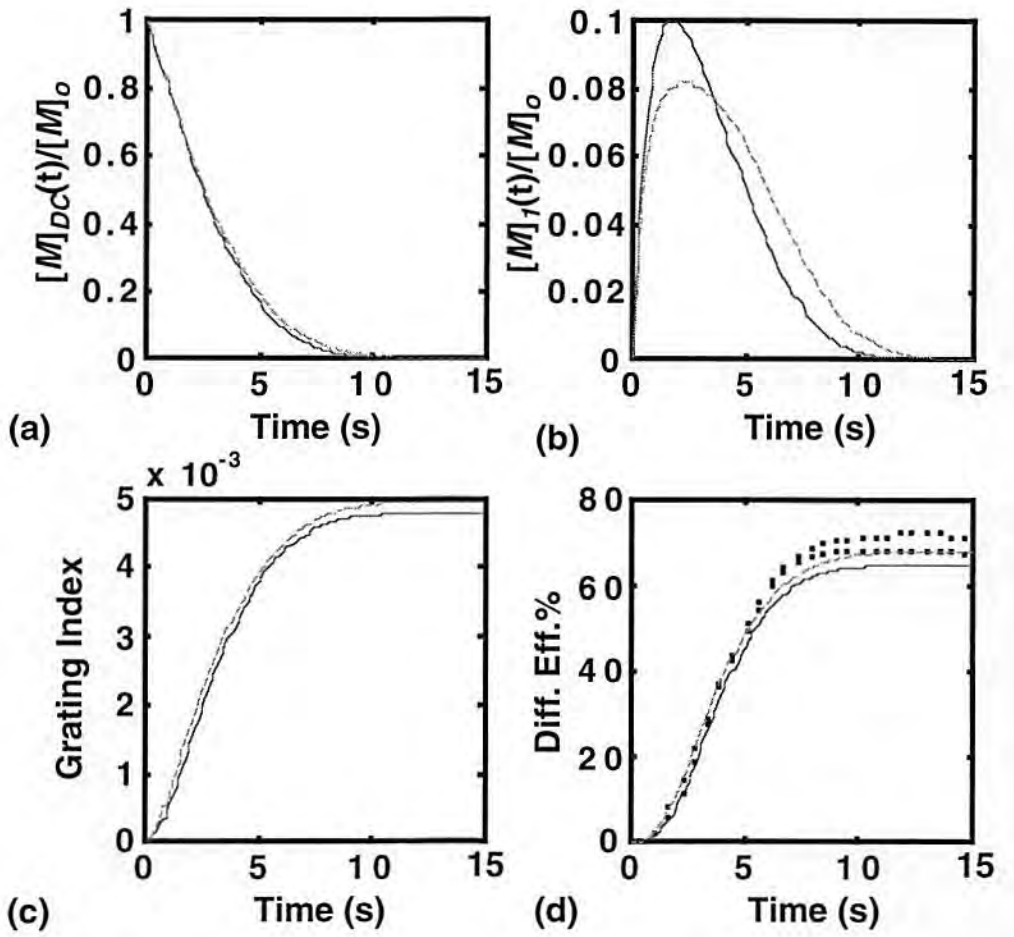

Figure 5-8. Comparison between the exact solutions of the diffusion model (dashed curves) and its approximated solution (solid curves). The exposure is recorded with I_o = 166 mW/cm^2, m = 0.97; the Bragg angle is 20°, while writing ad reading out wavelength are respectively 514 and 633 nm. The inhibition period is not shown. **(a)** Temporal variation of the free monomer concentration DC term. This variation is normalized to $[M]_o$. **(b)** Temporal variation of the amplitude of the first harmonic of the free monomer concentration. This variation is normalized to $[M]_o$. **(c)** Temporal variation of the modulation of the refractive index. **(d)** Temporal variation of the diffraction efficiency. The dotted curves refer to two experimental measurements.

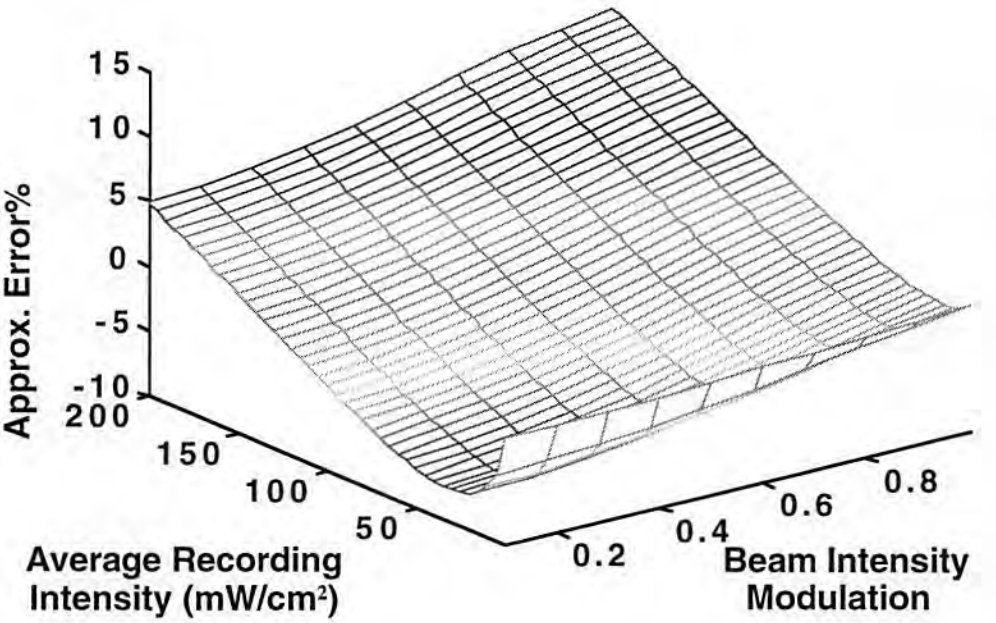

Figure 5-9. Approximation errors of the closed form solution of the diffraction efficiency according to the diffusion model. At lower intensity recording the error is virtually nonexistent, due to the convergence of the exact solution, the approximated solution, and the HFMD model solution.

5.5 Characterization of the Dark Diffusion Transient

As already discussed, photopolymers have the peculiar characteristic that (in certain circumstances) the diffraction efficiency can increase for few seconds after the interruption of the illuminating exposure. This process was termed dark diffusion transient, and we pointed out that the origins of this transient need to be searched in the action of the free monomer diffusion. The earlier qualitative description of the nature of this physical process is treated in a

more rigorous fashion in this section as follows.

Consider the recording of a hologram as in Fig. 5-1. According to the mathematical solution of the diffusion problem (presented in this chapter so far), after an exposure lasting t_o seconds (the inhibition period is here not considered), the free monomer concentration (in its DC and its harmonic term) and the grating modulation are respectively (form Eq.'s 5-11, 5-12, and 5-16)

$$[M]_{DC}(t_o) = [M]_o e^{[\gamma(1-\exp(t_o/\tau))]}, \tag{5-20}$$

$$[M]_1(t_o) = \frac{m\delta\gamma\tau_D}{\tau_D+\tau}[M]_o e^{[\gamma(1-\exp(t_o/\tau))]}\left(e^{t_o/\tau}-e^{-t_o/\tau_D}\right), \text{ and} \tag{5-21}$$

$$\Delta n(t_o) = \frac{m\tau\Delta n_M}{\tau_D+\tau}\left\{\left(1-e^{[\gamma(1-\exp(t_o/\tau))]}\right)-\frac{\tau_D\gamma}{\tau_D\gamma+\tau}\left(1-e^{-\frac{\tau_D\gamma+\tau}{\tau\tau_D}t_o}\right)\right\}. \tag{5-22}$$

When the exposure is turned off at $t = t_o$, a monomer gradient exists with $[M]_1(t_o) \neq 0$, because of this monomer gradient, the free monomers keep diffusing, until $[M]_1] = 0$. Using the mathematical tools that govern the diffusion model equations, we can therefore describe the variations of free monomer concentration and diffraction efficiency that take place during the dark period ($I_o = 0$) for $t \geq t_o$ as

$$\frac{d}{dt}[M]_{DC}(t) = 0, \tag{5-23}$$

$$\frac{d}{dt}[M]_1(t) = -\frac{[M]_1(t)}{\tau_D}, \text{ and} \tag{5-24}$$

$$\frac{d}{dt}\Delta n(t) = c_n \frac{[M]_1(t)}{\tau_D}. \tag{5-25}$$

The solutions of the above differential equations, where the initial boundary conditions at $t = t_o$ as in Eq.'s 5-20, 5-21, and 5-22, are therefore for $t \geq t_o$

$$[M]_{DC}(t) = [M]_{DC}(t_o) \tag{5-26}$$

$$[M]_1(t) = [M]_1(t_o)\, e^{-\frac{t-t_o}{\tau_D}}, \text{ and} \tag{5-27}$$

$$\Delta n(t) = \Delta n(t_o) + c_n [M]_1(t_o) \left[1 - e^{-\frac{t-t_o}{\tau_D}}\right]. \tag{5-28}$$

Finally, thanks to Eq. 5-28 the dark diffusion transient is mathematically explained. In fact, the function in the square brackets of this equation is an exponential function which asymptotically grows in time, and it is related to the disappearance of the free monomer gradient, Eq. 5-27, which was generated by the previous exposure. It must be pointed out that the magnitude of the diffusion increment can vary largely from exposure to exposure. In fact, the magnitude of such an increment (in refractive index modulation) is linearly dependent on the magnitude of $[M]_1(t_o)$. We can determine that one can expect a very limited diffusion increment when a hologram is exposed with low average recording intensity or the exposure is halted close to saturation. Justifications to these assertions, which are confirmed by experimental observations, are immediate. At low I_o values, the recording process is in the HFMD hypothesis, where photopolymerization is slow compared to the speed of free monomer diffusion,

which therefore instantaneously levels out any concentration gradient. Then, for a low I_o it corresponds a reduced $[M]_1(t_o)$ and a consequential reduced diffusion increment. Similarly, when the exposure is close to saturation the depletion of free monomers is almost completed, consequently the free monomer gradient is largely reduced, and so is the possible diffusion increment.

Interestingly, this diffusion transient can be positively used to increase the saturation diffraction efficiency when the photopolymer is exposed with a high average recording intensity. As already illustrated, one of the main limiting factor in achieving large diffraction efficiency during exposure with high average recording intensity is that the free monomers can be polymerized far from bright spots. Concurrently, the higher the free monomer spatial gradient, the higher the likelihood that this unwanted polymerization happens. A way to circumvent such a problem, at high exposure intensities, is to alternate cyclically the exposure and the dark diffusion transient. In such way, first the free monomers are allowed to build up a large $[M]_1(t_o)$) next, during the dark diffusion transient, there is a diffraction efficiency increment without possibility of unwanted polymerization far from the bright spots. This process of alternating photopolymerization and diffusion transient can therefore be repeated until saturation occurs.

A visualization of the alternate illumination recording approach is proposed in Fig. 5-10. Here is depicted the simulation (solid curves) and the experimental measurement (dotted curve in Fig. 5-10 (d)) of a holographic exposure with $I_o = 166$ mW/cm^2, and $m = 0.97$. The exposure schedule was the follow-

ing: the first exposure period 0 - 4.6 s, the first diffusion transient 4.6 - 25 s, the second exposure 25 - 33 s, the final diffusion transient 33 - 40 s. Fig. 5-10 (a) depicts the variation of DC term of the monomer concentration and Fig. 5-10 (b) depicts the variation of the modulation term of first harmonic of the free monomer concentration while Fig. 5-10 (d) compares the temporal dynamic of the diffraction efficiency with that one of an experimental recording. The first exposure ends after 4.6 s, with an associated diffraction efficiency of 50%, and, according to the simulation, $[M]_1$ (4.6) = 7% of $[M]_o$. As $[M]_1(t)$ decays to zero, the first diffusion transient generates an increment of diffraction efficiency of 11% in the measured data and 8% in the simulation results, as witnessed in Fig. 5-10 (d). After this, another exposure/diffusion cycle takes place. The second and final diffusion transient originates a reduced diffraction efficiency increment because too close to saturation with $[M]_1(t) \approx 0$. As seen in Fig. 5-10 (b), being near saturation, the amplitude modulation of the free monomer concentration is very low, and therefore the subsequent diffusion transient increment is very small, Fig. 5-10 (d). The final indication of this experiment is a measured saturation diffraction efficiency of 80% and a simulated of 75%. It is meaningful to compare these data with those in Fig. 5-8, depicting the exposure of hologram with continuous illumination. At saturation, where the alternate illumination is used, the increment of the diffraction efficiency is evident: there is a diffraction efficiency is increase of 10% in value in the experimental data and about 8% in the simulation with respect to the analogous recording of Fig. 5-8 (in which was used a continuous illumination with $I_o = 166$ mW/cm^2 and $m = 0.97$).

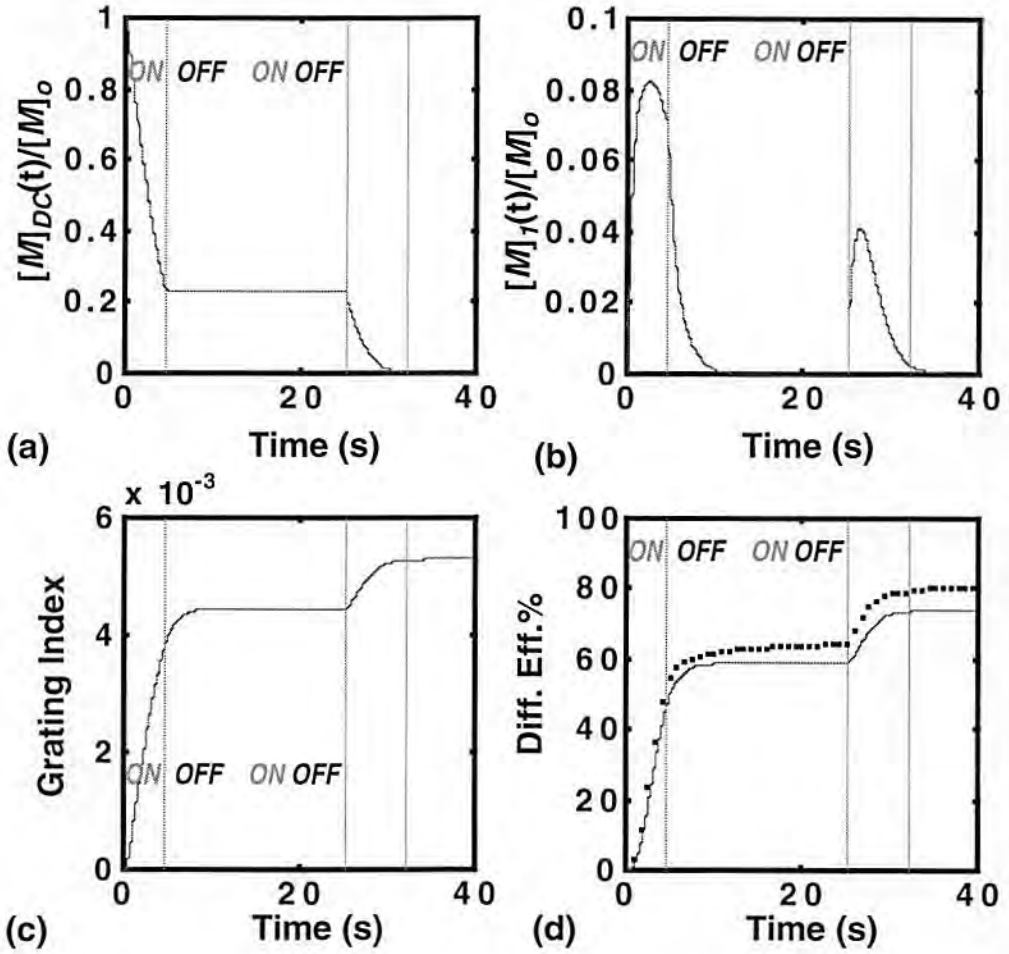

Figure 5-10. Diffraction efficiency during alternate illumination. The experimental curve (dotted curves) and the simulations (solid curves) are relative to an exposure with I_o = 166 mw/cm^2, m = 0.97, Bragg angle of 20°, write and read wavelengths respectively 514 and 633 nm. The exposure duty cycle is the following: first illumination 0-4.6 s, dark period 4.6-25 s, second illumination 25-33 s, final dark period 33-40 s. The inhibition period is omitted. **(a)** Variation of the DC component of the free monomer concentration, here normalized. **(b)** Variation of the first harmonic component of the free monomer concentration. Notice that as the illumination is halted, the free monomers keep diffusing, asymptotically eliminating the spatial gradient of the monomer concentration. **(c)** Variation of the refractive index amplitude modulation. **(d)** Variation of the diffraction efficiency. At the first dark period, the diffusion increment is as large as 11% in diffraction efficiency in the actual measurement and 8% in the simulation. This large increment is due to the large free monomer concentration gradient after 4.6 s of exposure. Because at the beginning of the second dark period the free monomer population is almost completely depleted, the subsequent increment is reduced.

5.6 Diffusion Model and Bragg Angle Dependence

During the mathematical treatment of the diffusion model we assumed that the diffusion coefficient D in Eq. 5-3 is constant time and space, which originated the following expression of the diffusion time constant

$$\tau_D = \frac{1}{DK_g^2} = \frac{\lambda^2}{4\pi^2 D \sin^2(\theta_b)}, \tag{5-29}$$

in which λ and θ_b are respectively the wavelength of recording beams and the associated Bragg angle in air. In the above equation the grating wavevector is expressed in term of the wavelength and of the Bragg angle as $K_g = 4\pi \sin(\theta_b)/\lambda$. The results of the diffusion model indicate that the saturation diffraction efficiency of a holographic exposure greatly depends on the value of the diffusion time constant Fig. 5-6 (a) which for low values of τ_D favors the largest possible saturation diffraction efficiency. Conversely, a reading of Eq. 5-29 indicates that a larger Bragg angle induces τ_D to decrease (because of the multiplicative factor $1/\sin^2(\theta_b)$) which, therefore, favors a larger saturation diffraction efficiency. To verify experimentally this indication, we performed a number of exposures at the following Bragg angles in air (of the writing beams): $\theta_b = 10^o, 20^o, 30^o, 40^o$. Great care was taken to keep the same average recording intensity for each exposure, therefore the Poynting vector at different Bragg angles was constant in magnitude, with an associated $I_o = 58$ mW/cm^2. The beam intensity modulation was $m = 0.88$. A number of exposures were made for each θ_b, and the measurements of these experiments with

the simulation predictions are plotted in Fig. 5-11. The figures compares the experimentally measured diffraction efficiencies (u), Fig. 5-11 (a), and the refractive index modulations (l), Fig. 5-11 (b), with their respective simulation results (solid curves) assuming $\tau_D = 0.9$ s at $\theta_b = 20^o$ and a functional dependence from Bragg angle as in Eq. 5-29 and a saturation modulation index as in Eq. 5-18. It is here beneficial to remind the reader that the grating modulation is related to the measured diffraction efficiency η_{sat} (in%) by

$$\eta_{sat} = 100 \sin^2\left(\frac{\pi \Delta n_{sat} T}{\lambda_p \cos(\theta_p)}\right) \tag{5-30}$$

where the probe beam wavelength is $\lambda_p = 633$ nm and θ_p is the internal Bragg matched angle of the probe beam. It must be noted that the variation of the Bragg angle manifests itself also in Eq. 5-30 due to the presence of θ_p. In fact, a larger θ_b corresponds a larger θ_p which enhances the diffraction efficiency values through the increasing factor $1/\cos(\theta_p)$. According to the simulation curves, however, there is a great difference form the predicted theoretical results (the solid curves in Fig. 5-11) and the experimental data. In fact, we can observe that the measured diffraction efficiency variation with the Bragg angle is almost flat, while theoretical prediction indicated a saturation diffraction efficiency as low as $\eta_{sat} = 34\%$ at $\theta_b = 10^o$ which increases (due to a decreasing τ_D and an increasing θ_p) to $\eta_{sat} = 84\%$ at and $\theta_b = 40^o$. Even more in disagreement are, however, the data comparing the measurements of a decreasing amplitude of the grating modulation with a larger θ_b versus its theoretical predictions. A number of causes and speculations can be introduced here to comment on these unex-

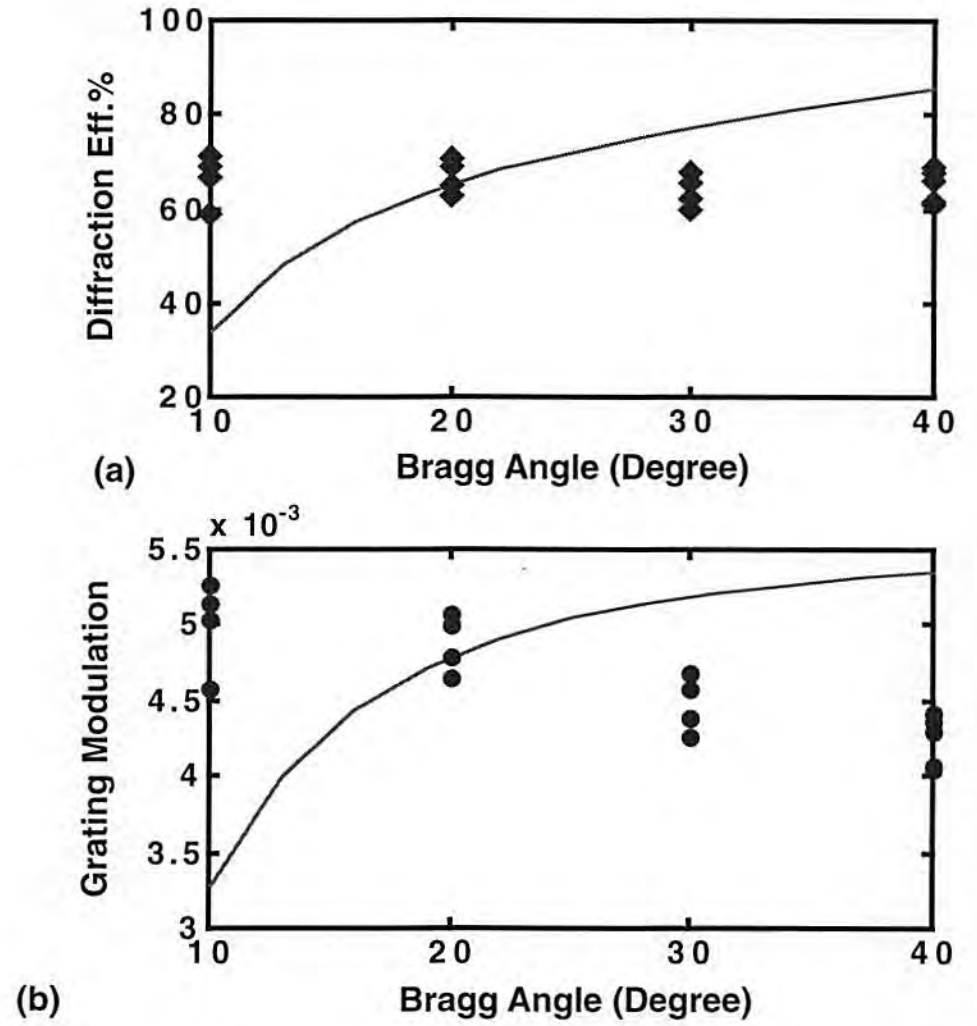

Figure 5-11. Hologram recordings at different Bragg angles with $I_o = 58$ mW/cm^2 and $m = 0.88$. The Poynting vector of the average recording intensity was constant in magnitude at the different Bragg angles. The writing recording wavelengths were respectively 514 and 633 nm, and $\tau_D = 0.9$ s at 20° of the Bragg angle. **(a)** Variation of the saturation diffraction efficiency variations with the Bragg angle. The measurements of the saturation diffraction efficiencies (◆) are compared with the predictions which consider τ_D varying as $1/\sin^2(\theta_b)$ (solid curve). **(b)** Variations of the grating modulations at saturation. The measurements of the saturation values of the grating modulation (●) are compared with those values predicted for a τ_D varying proportionally to $1/\sin^2(\theta_b)$ (solid curve).

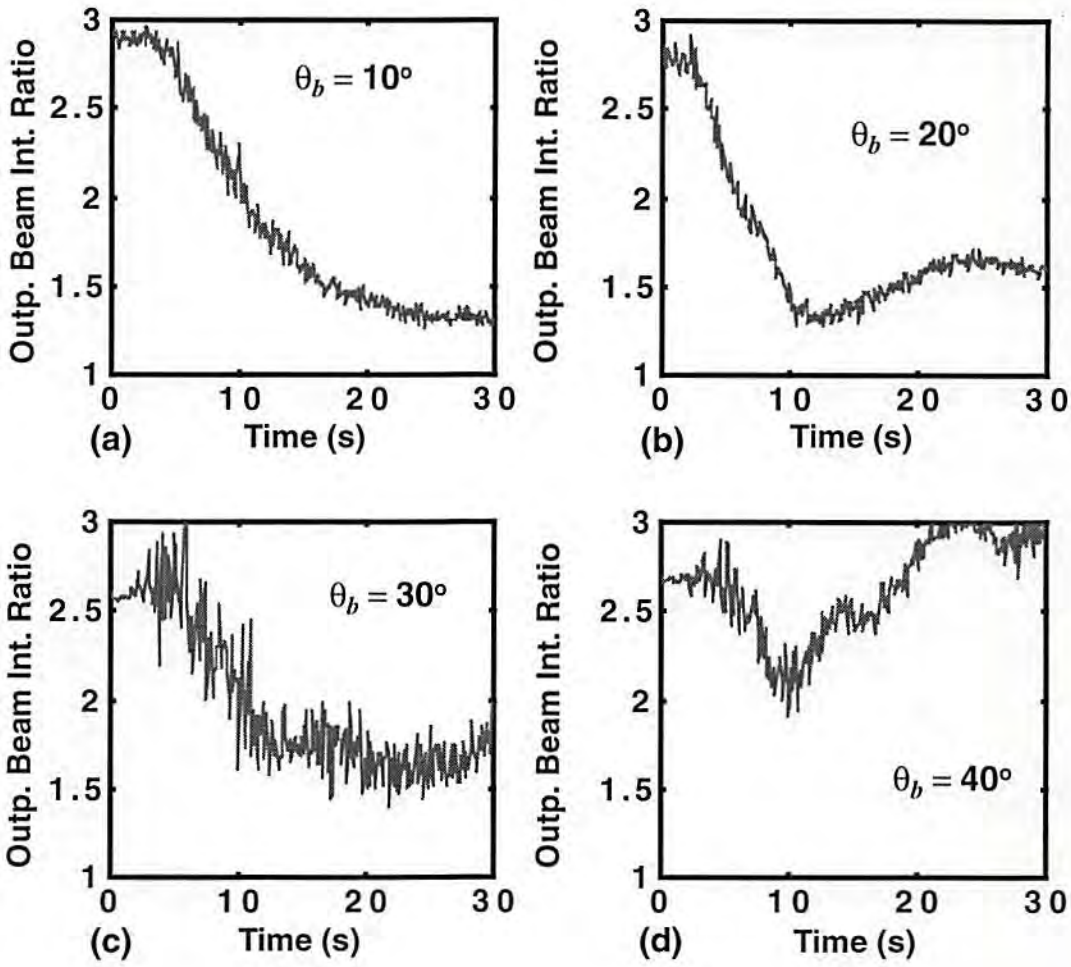

Figure 5-12. Experimentally measured variations of the output beam intensity ratio, $BR(38\ \mu m,t)$, for holographic exposure recorded with four different Bragg angles, as: **(a)** $\theta_b = 10^o$, **(b)** $\theta_b = 20^o$ **(c)** $\theta_b = 30^o$, **(d)** $\theta_b = 40^o$. As the Bragg angle increases, the different temporal dynamics of the output beam intensity ratios indicates that self diffraction is more effective at lower θ_b values.

pected results. The most immediate justifications still may be related to the fact that to obtain a closed form solution in our model we have considered a constant diffusion coefficient D, and then a constant τ_D, differently from what was experimentally seen in the indications of Fig. 5-3. Therefore, it may be not rigorous to calculate an average τ_D and scale such a value to different Bragg angles using Eq. 5-29. Another important consideration that can be helpful in understanding the disagreement between theoretical predictions and experimental results as seen in Fig. 5-12 is related with self diffraction. Self diffraction may be also dependent on the Bragg angle and this different behavior can cause the recording of gratings with different amplitude modulations.

In Chap. 3 we have also indicated that a way to understand and estimate the action of self diffraction is by evaluating the variation of the output beam intensity ratio during recording. Therefore we selected four recordings from those shown in Fig. 5-11 and then we reported their temporal variations of the output beam intensity ratio in Fig. 5-12. Interestingly, one can easily observe how the temporal evolution of the output beam intensity ratio during recording can greatly vary with Bragg angle. At larger values of the Bragg angle as $\theta_b = 40^o$, Fig. 5-12 (d), self diffraction is less apparent because the output beam intensity ratio does not substantially change from its initial values and it does not monotonically decrease as we may expect. Instead for $\theta_b = 10^o$ the output beam intensity ratio gradually decreases in time from an initial value $BR(38\ \mu m,0) = 2.8$ to a final $BR(38\mu m,30\ s) = 1.3$ indicating that self diffraction occurs during recording. According to what we learned in Chap. 4, a consequence of self diffraction is to enhance the amplitude of the grating

modulation which can justify the disagreement between theoretical and experimental data that we have observed in Fig. 5-11. The reasons for this different action of self diffraction for a varying Bragg angle in holographic photopolymers have not been studied to date and without a doubt they constitute an critical topic for future investigation.

5.7 Conclusions and General Remarks on the Diffusion Model

In this section we presented a model which combines photopolymerization kinetics with the free monomer diffusion to describe the recording of holographic gratings in photopolymers. The theoretical predictions of the model were compared with experimental data from holographic exposure in DuPont HRF-150-38 photopolymers. In essence, this model can characterize the interaction between free monomer diffusion (physically represented by its time constant τ_D) and the grating formation evolution (physically represented by its time constant τ) during exposure with high average recording intensity ($I_o > 70$ mW/cm^2). This model, however, is also inclusive of the previously described HFMD model at lower average recording intensity ($I_o < 70$ mW/cm^2). As an extension of the model, we discussed and simulated the recording of a holographic grating when the photopolymer is exposed with alternate (on then off) illumination. In this recording condition, a period of photopolymerization is alternated with a period of free monomer diffusion which, uniquely for holographic photopolymers, contributes to increase the amplitude of the grating modulation. While we observed a variation of the recorded grating modulation

with the Bragg angle, our model was not capable of predicting such variation, particularly at low values of the Bragg angle. Eventually, this argument can be the subject of a future investigative effort, in which we suggest focusing on the understanding of the effects of self diffraction for a varying Bragg angle jointly with a better characterization of the temporal evolution of diffusion time constant during the holographic exposure.

5.8 Bibliography

Banks, R. B., *Growth and Diffusion Phenomena*, Springer-Verlag, (1994).

Booth, B. L., "Photopolymer Material for Holography," Appl. Opt., **14**(3), 593-601, (1975).

Colburn, W. S. and K. A. Haines, "Volume Hologram Formation in Photopolymer Materials," Appl. Opt., **10**(7), 1636-1641, (1971).

Hervet, H., W. Urbach, and R. Rondelez, "Mass Diffusion Measurements in Liquid Crystals by a Novel Optical Method," J. Chem. Phys., **68**(6), 2725-2729, (1978).

Alfonso Maria Pendenza, Personal Communication, 1996

Smothers, W. K., B. M. Monroe, A. M. Weber, and D. E. Keys, "Photopolymers for Holography," Proc. Soc. Photo-Opt. Inst. Eng., **1212**, (1990).

Weber, A. M., W. K. Smothers, T. J. Trout, and D. J. Mickish, "Hologram Recording in Du Pont's New Photopolymer materials," Proc. Soc. Photo-Opt. Inst. Eng., **1212**, (1990).

Wopschall, R. H. and T. Pampalone, "Dry Photopolymer Film for Recording Holograms," Appl. Opt., **11**(9), 2096-2097, (1972).

Zhao, G. and P. Mourolis, "Diffusion Model of Hologram Formation In Dry Photopolymer Materials," Journal of Modern Optics, **41**(10), 1929-1939, (1994).

Chapter 6

Copying of Multiplexed Volume Holograms

6.1 Introduction

This chapter describes our proposed technique to copy angularly multiplexed volume holograms. Particularly, we address the principal issues concerning the copying of multiplexed volume holograms such as cross talk reduction, fidelity of the copy, material compatibilities, and blind copying, which we define as a copying technique which does not require *a priori* knowledge of the information content of the master hologram.

The copying technique requires a set of self coherent but mutually incoherent optical sources (incoherent/coherent or I/C recording) [Piazzolla *et al.*, 1992], and the copy can be performed in a single exposure step on to a secondary holographic material. The use of the I/C recording reduces cross talk noise that usually affects simultaneous recording (and copying) of multiplex holograms. By presenting experimental results, we validate our copying technique with a practical demonstration of three angularly multiplexed holograms recorded and copied in HRF-150-38 photopolymer. Later in this chapter, an

analysis and an extension is derived, whose results indicate the conditions to successfully incorporate the blind copying of anglularly multiplexed holograms in the copying technique.

6.2 Related Works and Motivation

Since its invention, holography has been considered a resourceful field to be explored and exploited for high density storage applications. Until recently, however, hologram copying was not a relevant attractive research and technological issue. Reasons for such scarce interest probably include the success of existing electronic and magnetic based storage systems which completely satisfied the requirements of available computational systems; however this is no longer true. Particularly in multimedia applications, commercial technology largely relies on optical based CD-ROM's (compact disk read only memories), and more recently on DVD's (digital video disk) as reliable, inexpensive, and durable high storage memory systems. As technology progresses, having already seen the limitations of the current optical memory systems, interest in holographic systems is increasing and undergoing a renaissance. In fact, holography is changing from an almost academic exercise to a cutting edge technological and probable future field for commercial products [Zech, 1992], and this is confirmed by the number of firms that are taking into consideration the commercial development of holographic storage devices [Holoplex]. Once a holographic memory (or holographic interconnection) is created, there is the problem of copying or duplicating it in a simple and inexpensive fashion. A

number of copying techniques have been developed in the past, which we will briefly comment on and describe in the remainder of this section.

Classically, the hologram copying techniques are either mechanical or optical based [Vanin, 1978].

In mechanical copying, the surface relief of a superficial diffractive grating is printed over a negative master. Then, the copies are manufactured by casting the holographic material over the master. Unfortunately, mechanical copying is suitable only for the duplication of thin holograms having maximum spatial frequency limited to ~ 2000 lines/mm due to mechanical restrictions, which reduces the complexity of the stored patterns. Because these holograms yield low storage capacity, their implementation is quite limited and technologically unattractive.

The principle behind optical holographic copying is to expose a photosensitive material with the virtual wavefronts reconstructed from a master hologram. Among the optical techniques, optical contact printing was the most largely used in the past. Here the master hologram is in contact with an unexposed secondary holographic medium, where the hologram is going to be copied. The copy is therefore recorded with the interference of the reference beam and the object wavefront recalled from the master. Some drawbacks are encountered when this technique is used. When thin films are exposed, noise (ghost images) deriving from duplicate images can negatively affect the copy. Moreover, during the exposure the intensity ratio between the object and the reference wavefront is not adjustable, and therefore the copy diffraction effi-

ciency is not controllable. In addition to this, the physical contact between the two holographic plates (master and copy) can damage the master hologram, which limits the number of the possible subsequent duplications. This last problem can be circumvented by separating the master and copying material by a short Fresnel distance. In in this last case, however, the source spatial and temporal coherence and the control of the recording region (in the copy) are cause of a number of concerns [Vanin, 1978].

Interestingly, hologram copying offers the advantage that the diffraction efficiency of the duplicated hologram can be substantially larger than that of the master when is properly chosen a copy medium with larger modulation of the refractive index of the master. An application of this principle is described by [Brady *et al.*, 1990]. Brady presented an experiment in which holographic interconnections are copied back and forth from a photorefractive crystal, to circumvent the effect of the grating decay during neural weight training. To our knowledge this is one of the few works in the literature about utilization of a hologram duplication in a fully optical architecture.

In a more recent paper [Campbell *et al.*, 1995], the fundamental limitations in multiplexed hologram copying were analyzed. This work presented different copying techniques (including one which states the specific argument of this chapter and in [Piazzolla *et al.*, 1992]), for comparing their limitations in terms of storage capability and length of the exposure time. According to Campbell, the sequential recording technique yields the best performance;, however Campbell did not consider other aspects pertinent to the copying.

Such issues as cross talk noise and the implementation of blind copying represent a main concern when a large number of holograms are likely to be copied.

6.3 Optical Architecture for Hologram Copying

Herein we introduce our technique that permits single-exposure copying of multiplexed volume holograms, while maintaining the desired independence of the holograms. This technique assumes that the master hologram can be reconstructed with angularly multiplexed reference beams that are separated in angle by more than the angular sensitivity of the holograms, that each hologram reconstructs its corresponding waveforms independently of the other holograms, and is intended to likewise remain independent in the copy. The master hologram may have been made by a set of sequential exposures or by a single simultaneous exposure. The copying technique utilizes a set of individually coherent sources that are mutually incoherent, which we have already termed I/C technique. Each source generates two relative reference beams, one at the master hologram and one at the copy holographic medium; the reconstructed object beam from the master interferes with the reference beam at the copy to record a hologram. By turning on all sources simultaneously, their mutual incoherence prevents the recording of undesired cross-coupling gratings, and therefore independence of the different holograms is maintained in a single step exposure.

Fig. 6-1 shows the proposed architecture that provides for single-step copying. A set of individually coherent, but mutually incoherent, sources gen-

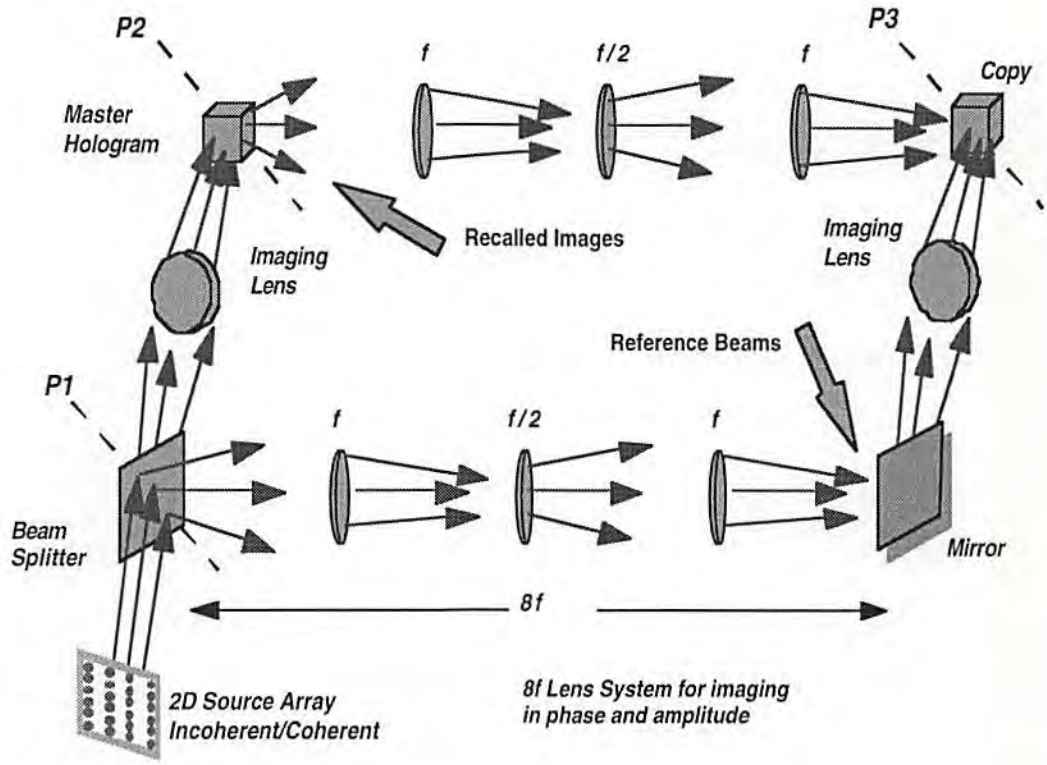

Figure 6-1. Architecture of the optical system for single step copying. A source array generates coherent beams that are mutually incoherent. The beam splitter generates the path of master reference beams, which readout the information in the master, and the path of copy reference beams. The reference beams at the planes P2 and P3 are identical. The upper 8*f* lens system duplicates, in phase and amplitude, the readout images at the copy plane where they interfere with their corresponding reference beams. The mutual incoherence of the sources assures the absence of cross talk.

erates a set of reference beams. These beams are intended to duplicate, at the master hologram, the angles, phases, and locations of the reference beams that were used to expose the master hologram. For cases in which the reference beams are incident in a regular angularly multiplexed geometry, a regular 1-D or 2-D spatial array of sources can generate the beams. Such an array of mutually incoherent sources can be either fabricated (VCSEL) [Jewell *et al.*, 1990], or generated from a single coherent source and an optical system (as it will be seen later). In the architecture, the reference beams illuminate the master hologram simultaneously, recalling all of the stored holograms in parallel. The source array is imaged so that it generates an identical set of reference beam phasefronts on the secondary (copy) holographic medium. Because of the lens imaging system in the architecture of Fig. 6-1, the reference beam phasefronts in planes P2, and P3 are identical, assuming ideal lenses and in the absence of the two holographic media. Particularly, to image the readout of the master, there is an $8f$ lens system which consists of a cascade of three lenses, having focal length f, $f/2$, and f, and each consecutive pair separated by the other by a $2f$ distance. In this way the reconstructed object beams are incident on the secondary medium with amplitudes and phases identical to those incident on the primary medium during recording of the master hologram. The appropriate pairs of beams (object and reference) interfere in the secondary holographic medium, making a complete copy of the original multiplexed hologram. Because of the use of a set of mutually incoherent sources, the copy process is performed in a single exposure step.

As a demonstration of this concept, a master hologram was first exposed,

consisting of three holograms, each carrying a letter in the acronym 'USC', that were angularly multiplexed on the same region of the holographic plate. Each volume hologram was exposed by interfering the reference and object beams. The angles of both beams, with respect to the plate, were different for each hologram. The object beams were carrying the information associated with the three letters of the acronym. In this case, all three holograms were written simultaneously, but the copying process applies equally well to multiplexed master holograms that are sequentially recorded. The experimental set-up used for recording the master hologram is indicated in Fig. 6-2. An argon-ion laser, without an etalon, originated a beam (514 nm wavelength) with a coherence length of approximately 1 cm. The laser beam is expanded and collimated, and it creates the recording waves; beamsplitters BS1, BS2 and mirrors M1, M2 are used to generate 3 mutually incoherent beams of equal intensity (each corresponding to a letter of the 'USC' acronym). The path length difference between any two of these beams (measured to the holographic plate) is much greater than the coherence length. Each beam is then split into separate reference beam (mirrors M3, M4 and M5) and object beam (mirrors M6, M8, and M7, respectively) paths. The six beams are then incident on the same region of the holographic plate, H1, and they record three independent holograms.

The experimental set up for copying is shown in Fig. 6-2. The same set of reference beams (from M3, M4, and M5) illuminates the master hologram H1, and reconstructs the three object beams. The 8*f* three lens system images the amplitudes and phases of the reconstructed object beams, emerging from the

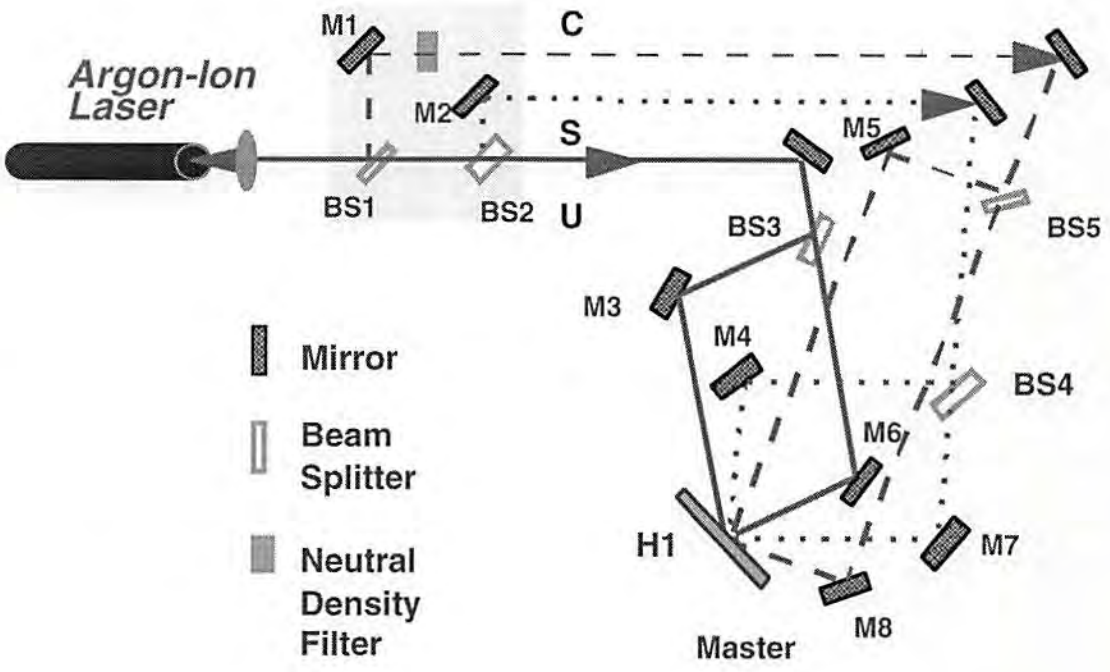

Figure 6-2. Experimental set-up for the master recording. Three object beams U, S, C, carrying the information of the acronym 'USC' interfere in the holographic plate with their respective reference beams. The recording of the three holograms is performed simultaneously. The mutual incoherence of the three couple of beams has been generated by their different paths length, as depicted by the shaded area. The beams are mutually incoherent because of their path differences are longer than the laser coherence length (for an argon - ion laser the coherent length is $\approx$ 1 cm.). Notice that, for sake of better visualization, mutually coherent couples of beams are depicted with analogous lines: solid, dashed, and dotted.

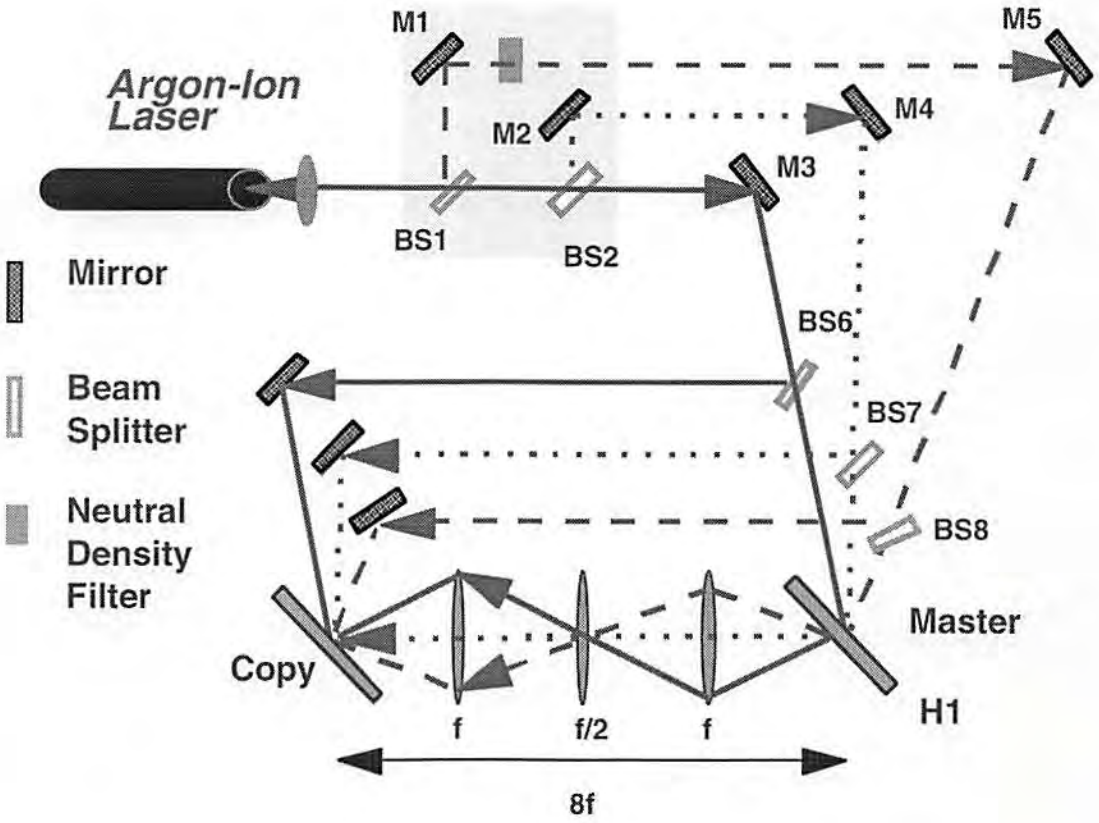

Figure 6-3. Experimental set-up for coping. Three reference beams are split up in master reference beams, and copy reference beams. The master reference beams recall each of the object beams carrying letters of the acronym 'USC', which are imaged in the copy plate and interfere with their mutual (coherent) reference beams. The 8*f* lens system images the stored information at the copy plane. For sake of better visualization, mutually coherent couples of beams are depicted with analogous lines: solid, dashed, and dotted.

master, at the copy plane. Du Pont HR-150-38 holographic photopolymer film was used for this experiment. Beamsplitters BS6, BS7, and BS8 provide the duplicates of the master reference beams at the copy hologram; the optical path lengths are kept equal, pairwise, to insure mutual coherence between each object beam and its corresponding reference beam at the copy. The results of these experiments are indicated by the pictures of Fig. 6-4. In the figure are shown pictures from the holographic reconstructions (of master and copy hologram) and it is proved the independence of the three multiplexed holograms. The picture in Fig. 6-4 (a) is the 'USC' acronym reconstructed from the master hologram. Fig. 6-4 (c) demonstrates the independence of the three angularly multiplexed sub-holograms in the master carrying the stored information. The central reference beam, reconstructing the letter 'S', is blocked, and only the letters 'U C' are reconstructed. This experiment proves that cross talk gratings, which can reconstruct the letter'S', are not recorded. As indicated in Fig. 6-3, the copy was made in a single exposure. The pictures of Fig. 6-4 (b) and 6-4 (d) show the reconstruction of the multiplexed holograms, obtained by placing the copy holograms in position H1 of Fig. 6-2, and illuminating each hologram with their respective reference beams. Again, in Fig. 6-4 (d) the central reference beam has been blocked; the independence of the reconstructions from the copy is demonstrated by the absence of the corresponding letter 'S' in the object wavefronts. No measurable cross talk was noticed among the three reconstructed objects in the master or in the copy.

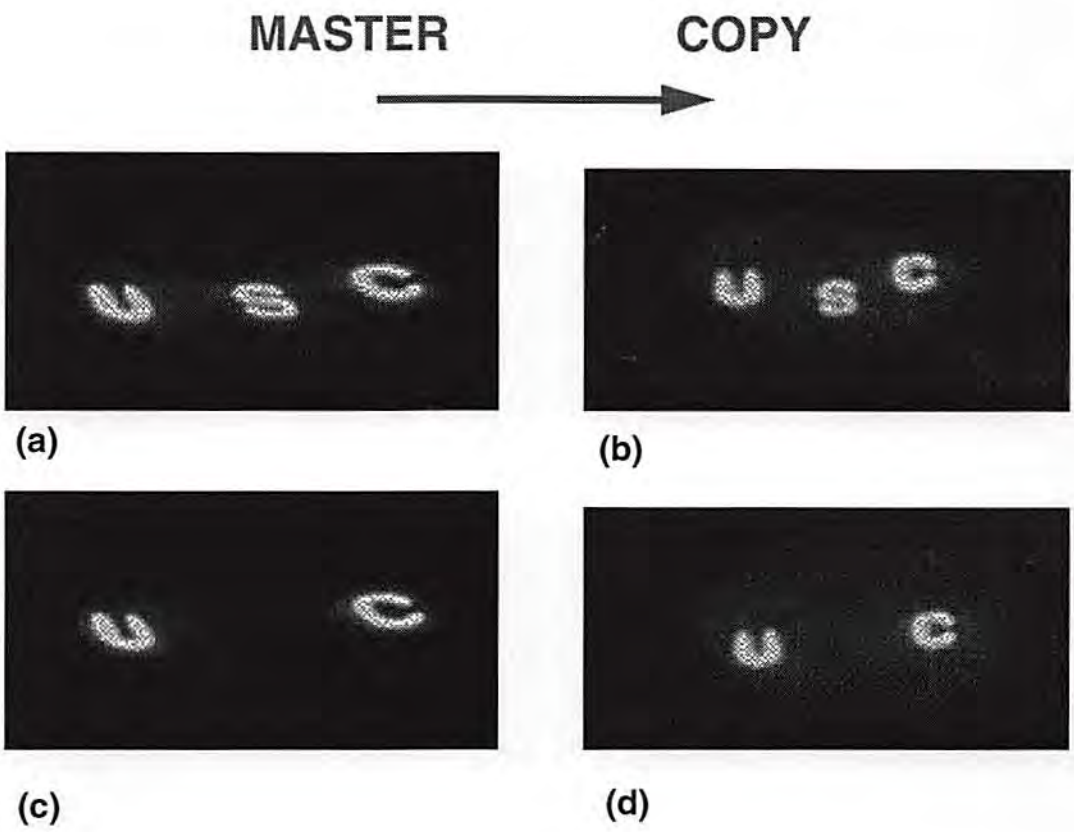

Figure 6-4. Pictures describing experimental results of hologram copying. Three angularly multiplexed holograms have been recorded as in Fig 6-2. (**a**) Master. Picture of the projection of the recalling of the three multiplexed holograms carrying the acronym'USC'. (**b**) Copy. Picture of the reconstructions from the copy hologram of the stored acronym 'USC'. (**c**) Master. It is proved the independence of the three holograms stored and angularly multiplexed in the master. The central reference beams is blocked, and only the letters 'U C' are recalled. Because of lack of cross talk, the reconstruction of the letter 'S' is absent. (**d**) Copy. It is demonstrated the independence of the three copied holograms. Again, the central reference beams is blocked, and only the letters 'U C' are recalled. Because of the lack of cross talk, the reconstruction of the letter 'S' is absent.

6.4 System Limitations and Extensions

The described hologram copying system, to our knowledge, is the first ever designed, which is able to perform single step copying of multiplexed volume hologram, and it is specifically oriented to reduce cross talk grating formation. This copying system has been successfully demonstrated in a small scale (for a 3x1 source array), however if we want to extend its application to a large number of holograms, several factors can provide bounds on its scalability and applicability. The nature of these limiting factors can be generally addressed as architectural and material dependent.

The architectural limitations are mainly due the lenses used to relay the information from the master hologram to the copy holograms. These factors can be phase aberration, and the *f*-number and space-bandwidth product, which essentially limits the number and the complexity of the holograms that can be copied in a single step. These architectural factors, however, can be analyzed with the help of geometrical optics theory and their limitation can be substantially defined. In fact, a simply analysis can be used to quantify relation between the *f*-number of the (first and last) lenses and the number of object beams that can be transmitted through the $8f$ imaging system itself. This analysis is carried out as it follows.

The distance between the master hologram and the first lens is $2f$. If D_i is the diameter of the first lens of the system, such lens is seen from the master hologram with a field of view, $\Delta\theta_w$, as

$$\Delta\theta_w = \frac{D_i}{2f} = \frac{f^o}{2}, \tag{6-1}$$

in which $f^o = D_i / f$ is the lens f-number. Note that the above relation is valid if the area, A_h, where the hologram are angularly multiplexed is much smaller than the lens area, *i.e.* $A_h << \pi D^2/2$. At the same time, requirements of angular selectivity impose that the smallest angular distance between two angularly contiguous holograms is given by their angular selectivity, $\Delta\theta_s$,which is

$$\Delta\theta_s = \frac{n_o \Lambda_g}{T} = \frac{n_o \lambda}{2\sin(\theta_b)}, \tag{6-2}$$

in which T is the material thickness, n_o is the medium refractive index, Λ_g is the grating wavelength, λ the wavelength of recording beams in air, and θ_b the Bragg angle in air, which is here assumed to be constant for all the hologram stored in the master. At this point we can indicate the number of independent holograms, N_f, that can be relayed through the $8f$ lens system as

$$N_f \leq \left(\frac{\Delta\theta_w}{\Delta\theta_s}\right)^2 = \left(\frac{Tf^o}{n_o\lambda}\sin(\theta_b)\right)^2, \tag{6-3}$$

the squared exponent indicates that the holograms are angularly multiplexed within the solid angle which is seen from the master to the first lens surface.

As the optical system, material limitations play a substantial role in our architecture, and these limitations can be characterized only if the knowledge of the physics ruling the hologram recordings in the material is available. As fairly known in photorefractive crystal and in photopolymers (which was proved in Chapter 3 of this thesis), the superposition of holograms during

recording, and the available dynamic range of the given recording material forces a trade-off between achievable diffraction efficiency and the number of holograms that overlap at each point of the holographic medium. A very similar trade-off occurs for sequentially exposed multiplex holograms. This trade-off manifests itself differently in distinct classes of materials; in the photorefractive case, for example, superposition effects due to simultaneous recording and erasure must also be taken into account [Maniloff *et al.*, 1991]. Based on these material limitations, we now present an analysis which determines the largest number of holograms that we can multiplex in a medium driven into saturation, taking into account the average diffraction efficiency η_a of the angularly multiplexed holograms. For this analysis, the copy material may be indifferently a HRF-150-38 photopolymer or a photorefractive crystal. For the case of HRF-150-38, the HFMD hypothesis is here assumed.

Let's consider that N_m holograms are angularly multiplexed in the material. Therefore, the generic i-th hologram angularly multiplexed on the copy material has diffraction efficiency

$$\eta_i = \sin^2\left(\frac{\pi\Delta n_i T}{\lambda\cos(\theta_i)}\right) \approx \left(\frac{\pi\Delta n_i T}{\lambda}\right)^2, \qquad (6\text{-}4)$$

in which Δn_i is the grating modulation of the i-th hologram. The approximation above is obtained after considering that for a large number holograms, the angularly multiplexed diffraction is likely very low ($\eta_i << 1$) and can be considered close to one the value the cosine of the (internal) angle at the denominator,*i.e.* $\cos(\theta_i) \approx 1$ for $i = 1,\ldots,N_m$. Using the above approximation, we can

express the average diffraction efficiency as

$$\eta_a = \left(\frac{\pi T}{\lambda}\right)^2 < \Delta n^2{}_i > \ , \tag{6-5}$$

where the symbol <•> indicates the operation of averaging over a discrete set of elements. According to the findings of Chapter 3, Δn_i can be written as

$$\Delta n_i = m_i \Delta n_M = \frac{2\sqrt{I_i^{\,o} I_i^{\,r}}}{\sum_{j=1}^{N_m} I_j^{\,r} + I_j^{\,o}} \Delta n_M \ , \tag{6-6}$$

where m_i is the beam intensity modulation of the i-th hologram, which depends on total intensity illuminating the material; $I_i^{\,o}$ and $I_i^{\,r}$ are respectively the intensities of the object and reference beams writing the i-th hologram; Δn_M is the largest attainable grating modulation; N_m is the number of multiplexed holograms. For the purpose of modelling the average diffraction efficiencies of the multiplexed holograms, we impose some conditions on the intensity of the recording beams. The reference beams all have the same intensity, $I_p^{\,r}$, and the object beam intensities have values uniformly distributed in the range $0 < I_j^{\,o} < I_p^{\,r}$, for $j = 1, 2, .., N_m$. Under these circumstances the sum at the denominator of Eq. 6-6, is

$$\sum_{j=1}^{N_m} I_j^{\,r} + I_j^{\,o} = \frac{3}{2} N_m I_p^{\,r} \ , \tag{6-7}$$

in which we have averaged $I_j^{\,o}$, and substituted to $I_i^{\,r}$ with a constant value $I_p^{\,r}$. Using the above result in the definition of Δn_i in Eq. 6-6, we can calculate the average of $\Delta n_i{}^2$, as

$$< \Delta n^2_i > \quad = \frac{8\Delta n^2_M}{9N^2_m} \quad . \tag{6-8}$$

Through Eq. 6-5 and 6-8, we can determine the upper limit of the number of holograms that can be angularly multiplexed for an average diffraction efficiency is η_a

$$N_m \leq \frac{4\pi T \Delta n_M}{3\lambda} \sqrt{\frac{2}{\eta_a}}. \tag{6-9}$$

It is now interesting to evaluate with the help of Fig 4-8, the optical limitations of Eq. 6-3 accordingly with the material limitations of Eq 6-9. The upper hypersurface of the three dimensional plot of Fig 4-8 (a) represents the *f*-number limitations for $f^o = 0.25$, while the other hypersurface represents the material limitations. In the figure is assumed that $\lambda = 0.514$ μm and $10 \leq T \leq 300$ μm; self diffraction effects are ignored; the average diffraction efficiency is varied as $0.1\% \leq \eta_a \leq 100\%$; the maximum attainable grating modulation is $\Delta n_M = 0.007$; the average bragg angle is $\theta_b = 20^o$. The thicker line delimits the border of the total hypersurface whose points define the largest number of holograms that the system can copy (*i.e.* the minimum value between N_f and N_m) for the given η_a and T. The copying limitation for the HRF-150-38, which has $T = 38$ μm, are more specifically indicated in Fig. 6-5 (b). In this figure are compared the cases of two *f*-number systems $f^o = 0.25$, and $f^o = 1$, while the average diffraction efficiency was varied as, $0.01\ \% \leq \eta_a \leq 100\%$. The slope in the figure indicates the material limitations. For an unitary *f*-number the main limitation are given by the material, which

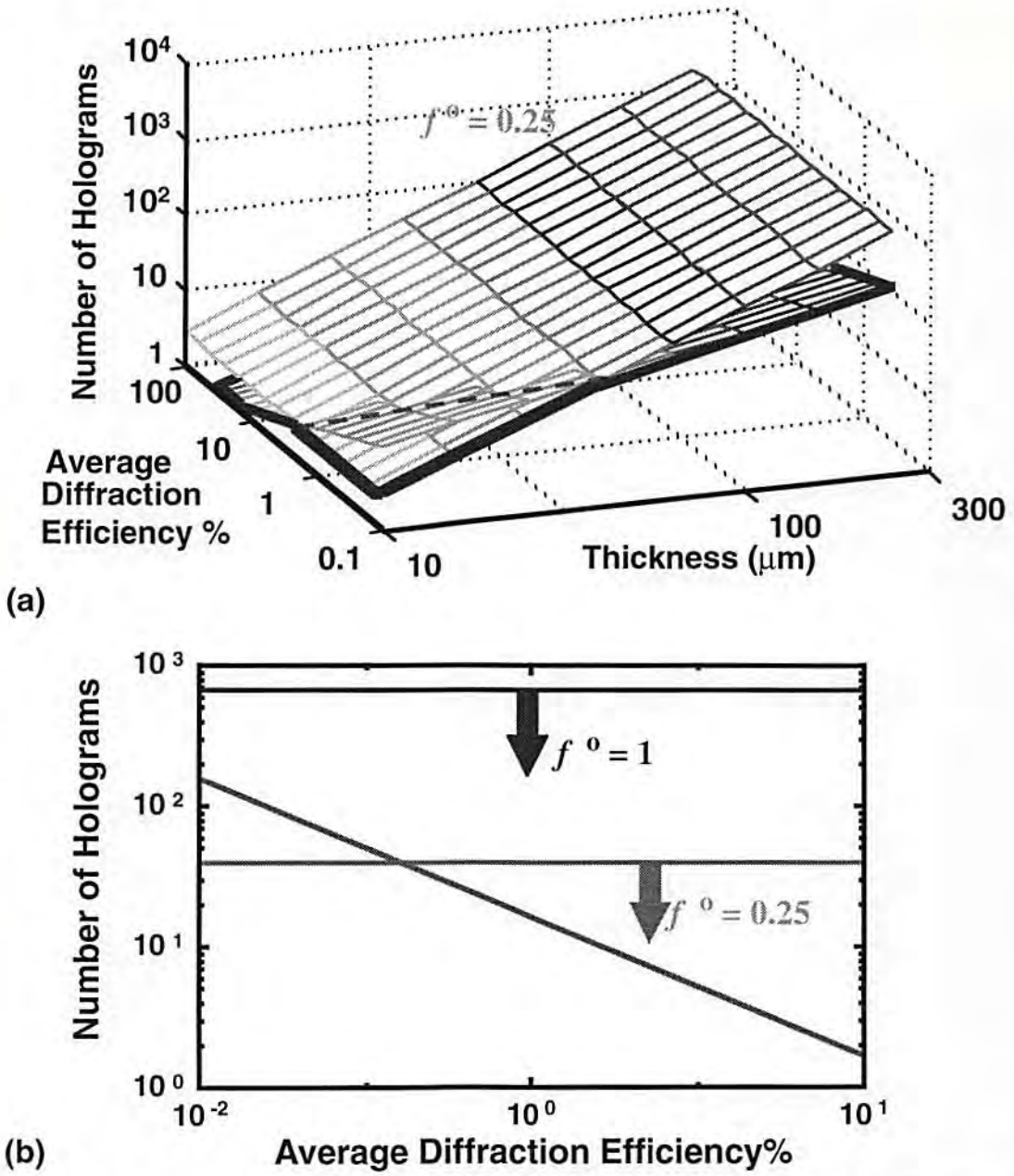

Figure 6-5. Copying limitations. (**a**) Case of $\lambda = 0.514$ μm, $\Delta n_M = 0.007$, $10 < T \leq 300$ μm, and $\theta_b = 20^o$, $f^{\,o} = 0.25$. The hypersurfaces indicate the *f*-number limitations (upper) and the material limitations (lower). The thicker line bounds the intersection hypersurface which defines the largest number of holograms that can be copied for a given η_a and T. The dashed line is the intersection between the two hypersurfaces. (**b**) Copying limitations for HRF-150-38. Two *f*-number systems are considered (horizontal lines). For $f^{\,o} = 1$, material limitations are prevailing. For $f^{\,o} = 0.25$, the limit number of holograms that can be copied is 40, due to *f*-number limitations. Both the graphs are in logarithmic scale.

imposes a maximum of 153 holograms for $\eta_a = 0.01\ \%$. Conversely for $f^0 = 0.25$, the optical limitations prevail and 40 is the largest number of hologram that we can copy given such f-number.

Considering possible extensions of our copying architecture, we must point out that the generation of non-identical copies is also possible here. For example, additional holograms can be added in conjunction with those copied from the master; the nature of the reference beams at the copy can be different from those of the master if desired; in some cases filtering can be performed on the object beam path from the master to the copy to decrease noise; magnification can potentially be inserted between the master and the copy; and the relative diffraction efficiencies can be changed by altering either each beam ratio or each beam intensity. Finally, blind copying can be incorporated in the architecture. In the next section we describe how blind copying can be performed based on the fact that all the holograms are simultaneously exposed with an I/C illumination.

6.5 Blind Copying of Multiplexed Holograms

According to our earlier definition, blind copying consists of the duplication of an angularly multiplexed volume hologram without *a priori* knowledge of the information content (grating modulation of each single multiplexed hologram) of the master hologram. This section, therefore, is dedicated to the presentation of an analysis which establishes the necessary conditions to implement blind copying in the architecture of Fig. 6-1.

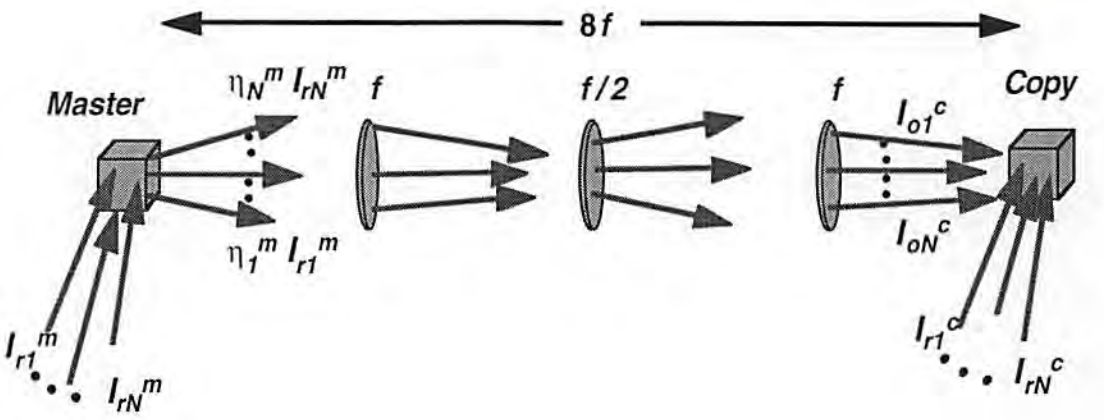

Figure 6-6. Copying set up for blind copying analysis. There are N reference beams (I_{rj}^m) retrieving the object beam wavefronts from the master, which interfere with N reference beams (I_{rj}^c) to record the copy. The j-th master and copying reference beams are coherent with respect to each other but incoherent with respect to any other i-th beams, with $i \neq j$. The purpose is to find the relation among the reference beams and the material figure of merits which will indicate how to control blind copying.

Figure 6-6 depicts in more detail a significant part of the copying system that we are going to analyze. Here N master reference beams, I_{rj}^m for $j = 1$, 2,. . . , N, are retrieving N object beam wavefronts (which may not be necessarily simple plane waves) from a master hologram. These wavefronts are imaged into the copy medium and interfere with N copy reference beams, I_{rj}^c for $j = 1$, 2,. . , N. For the moment we limit this analysis to permanent masters, where the illumination of the master reference beams do not cause a decay or an erasure of the diffraction efficiency of the stored holograms.

If the copy must be identical to the master, then it is necessary that each multiplexed hologram in the master and the copy must have identical diffraction efficiency as

$$\eta_j^m = \eta_j^c, \quad \text{for } j = 1, 2, \ldots, N; \tag{6-10}$$

in which the superscripts m and c correspondingly refer to the master and the copy hologram of the generic j-th hologram which is angularly multiplexed.

If the secondary material is a photopolymer film or a photorefractive crystal driven into saturation, and the N angularly multiplexed holograms are simultaneously exposed using I/C illumination, we can rewrite the above equation in terms of recording parameters which, according to the notations in Fig. 6-6, is

$$\eta_j^c = \sin^2\left[\frac{\pi T}{\lambda \cos(\theta_j)} \Delta n_M \frac{2\sqrt{\eta_j^m I_{rj}^m I_{rj}^c}}{\left(\sum_{i=1}^{N} I_{ri}^c + \eta_i^m I_{ri}^m\right)}\right] = G\eta_j^m, \tag{6-11}$$

in which the copy object beams are expressed as a function of the readout beams retrieved from the master; θ_j is the (internal) Bragg angle of the j-th hologram; T is the secondary material thickness; G is a gain coefficient, which can specify a desired amplification or attenuation of the master diffraction efficiencies. It is beneficial to emphasize that Eq. 6-11 is the core of blind copying, and it is only valid if all the gratings are simultaneously recorded (single step), and I/C illumination is used (cross talk gratings are reduced). As stated earlier, when a large number of holograms are angularly multiplexed, the corresponding diffraction efficiency values are very low, therefore the above equation can be approximated as

$$\eta_j^c = c_j^2 \frac{\eta_j^m I_{rj}^m I_{rj}^c}{\left(\sum_{j=1}^{N} I_{rj}^c + \eta_i^m I_{rj}^m \right)^2} = G\eta_j^m, \tag{6-12}$$

where $c_j = \frac{2\pi T \Delta n_M}{\lambda \cos(\theta_j)}$ is a coefficient whose variation for each j-th hologram depends on the angle θ_j. Remembering that θ_j is an internal (within the copying material) angle, we can assume that spreading of its values is limited. In this case, we can approximate θ_j with its average value, as $\theta_j \approx \theta_o$, and we can consider c_j as a constant coefficient

$$c_j \approx c_o = \frac{2\pi T \Delta n_M}{\lambda \cos(\theta_o)}, \tag{6-13}$$

for $j = 1, 2, .., N$. From Eq. 6-12, and using Eq. 6-11, and Eq. 6-13, we can obtain the following relation

$$c_o^2 I_{rj}^m I_{rj}^c = G\left(\sum_{i=1}^{N} I_{ri}^c + \eta_i^m I_{ri}^m \right)^2, \text{ for } j = 1, 2, \ldots, N. \tag{6-14}$$

The above equation indicates the relation between the intensities of the j - th master and reference beams necessary for blind copying. It must noted, however, that the sum operator in the RHS of Eq. 6-14 is a constant term, implying therefore that the LHS must be constant independently of the index j. A way to verify Eq. 6-14 is to have N master reference beams of constant intensity, I_r^m, and to have copy reference beams of constant intensity, I_r^c. In these conditions we can update Eq. (6-14) as

$$c_o^2 I_r^c I_r^m = GN^2\left(I_r^c + \eta_a^m I_r^m \right)^2, \tag{6-15}$$

in which $\eta_a^m = \left(\frac{1}{N}\right)\sum_{i=1}^{N}\eta_i^m$ is the average master diffraction efficiency. Considering now the ratio between the intensities of the copy and the master reference beams, we can rearrange the above as

$$c_o{}^2 I_r^c/I_r^m = GN^2\left(I_r^c/I_r^m + \eta_a^m\right)^2. \tag{6-16}$$

As usual, for a large N, the average diffraction efficiency can be very low, $\eta_a{}^m << 1$, when

$$I_r^c/I_r^m \gg \eta_a^m, \tag{6-17}$$

we can drop the average diffraction efficiency term in Eq. 6-16, and therefore express the copy/master reference intensity ratio that gives the solution to the problem as

$$\frac{I_r^c}{I_r^m} = \frac{c_o{}^2}{GN^2}. \tag{6-18}$$

In essence, the above equation indicates the incorporation of blind copying into the copying architecture when hologram diffraction efficiencies are low in value as depicted by Eq. 6-17. To performing blind copying, according to Eq. 6-18, *a priori* information about the grating modulation of each multiplexed holograms in the master is not required, but the knowledge of the Bragg angles jointly with the thickness and the maximum saturation index of the secondary medium is required. Concerning the requirement of low average diffraction efficiency, it is easy to determine how this can be usually met. As the number of holograms N increases, material limitations indicate that the average diffraction efficiency decreases as $1/N^2$. Moreover, in architectures which are

implementing a neural adaptive weights paradigm using photorefractive crystals, the training of the holographic weights causes the decay of the grating modulations and of the diffraction efficiencies [Goldstein *et al.*, 1995]. Particularly, in these applications, the condition of Eq. 6-7 is always met, and blind copying may be a very attractive solution to magnify the master hologram diffraction efficiencies when these are expected to be too low.

The plot of Fig. 6-7 depicts and summarizes the limitations in a practical example of blind copying. In this example, the material used is a photorefractive crystal (*e.g.* Lithium Niobate), 5 mm thick with $\Delta n_M = 0.001$, the average diffraction efficiency is $\eta_a^m = 1\%$. Each point in the graph corresponds to a hologram copying scenario described by the abscissa indicating the number of multiplexed holograms and by the copy/master intensity ratio in the ordinate. The fidelity zone is where Eq. 6-17 is verified, and this zone is above the horizontal line which verifies $I_r^c / I_r^m = \eta_a^m$. The distortion zone is where the Eq. 6-17 is not verified, and therefore distorted copies are expected if blind copying is performed. The set of oblique lines indicates the locus of constant diffraction efficiency gain ($G > 1$) or the attenuation ($G < 1$) for the number of gratings indicated by the abscissa. Note that the position of the unitary gain line depends solely on the physical characteristic of the copying material (T and Δn_M). If the material has a larger Δn_M or is thicker, the more distant this line is from the distortion zone, and the larger the number of gratings is that can be copied with high fidelity. Similarly, when an amplification of the diffraction efficiency is desired, the number of holograms that can be copied without distortion is reduced with respect to the case for $G \leq 1$.

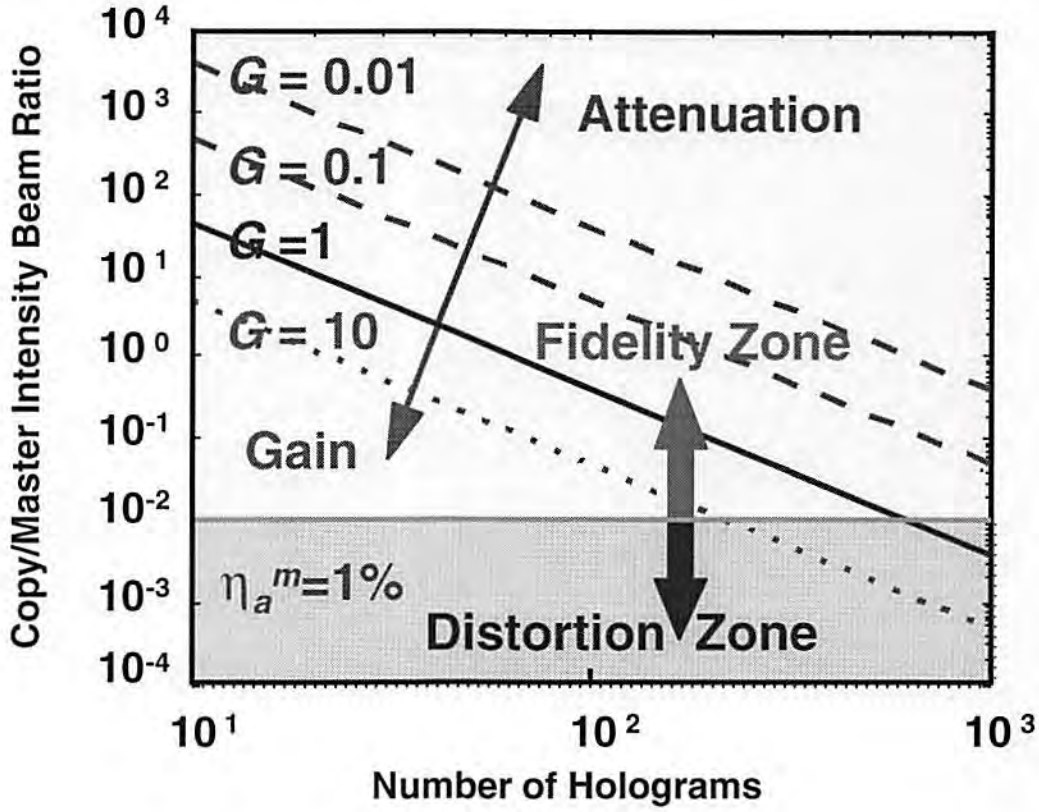

Figure 6-7. Blind copying diagram. A Lithium Niobate photorefractive crystal, 5 mm thick, with $\Delta n_M = 0.001$, is the secondary medium. The wavelength is 0.514 μm, and the average Bragg angle is 20°. After Eq. 6-17, the horizontal line is related to the average diffraction efficiency $\eta^m{}_a = 1\%$. This horizontal line divides the diagram in two zones: a distortion zone and a fidelity zone, as indicated by the arrows. The oblique solid line corresponds to the locus of the identical copies of the diffraction efficiencies for a given number of multiplexed holograms (abscissa) and copy/master intensity beam ratio (ordinate): above this line there is an attenuation zone, below there is a gain zone.

In summary, we derived a process for blind copying that can be performed by following three required steps. First, and obviously, an optical set-up as in Fig. 6-1 must be assembled or built up. Next, the system limitations must be calculated, eventually with the help of a graph as in Fig. 6-5. Finally, one must define, for a given copy materials, the copy/master intensity beam ratio, using a graph as in Fig. 6-7. It must be pointed out, however, that the last graph can describe only the system performance given a permanent master hologram and a secondary medium which is driven into saturation, and therefore any indications about the time evolution of the process are omitted here. Moreover, when the master consists of an erasable material, the grating decay, which is eventually caused by the illumination retrieving of the object wavefronts, is a factor that needs to be taken into account. To properly describe these last two issues, in the next section we introduce the concept of copy gain function.

6.6 The Copy Gain Function (CGF)

The blind copying analysis, so far derived, is only correct for master materials as dichromated gelatin or photopolymers, which does not change their recorded gratings upon illumination of the readout reference beams. Therefore, such analysis it is not correct when applied to erasable master materials, such as photorefractive crystals, whose recorded holograms experience a gradual erasure during readout (at certain wavelengths). A way to circumvent this problem is to use master readout beams whose wavelength is not absorbed by the master (a factor that prevents master erasure during readout), while

these beams at this wavelength can record holograms in a properly selected secondary medium. Clearly, this solution may be extremely advantageous because it preserves the master gratings from any form of degradation during readout, and the copying process itself can be repeated an indefinite number of times with a generation of a virtual infinite number of copies. Unfortunately, when the master material is very thick, it can be arduous to Bragg match a large number of readout beams with a different wavelength from the original recording one, because the angular selectivity of a hologram is proportional to the inverse of the material thickness (Eq. 6-2).

Another solution to alleviate this problem of grating decay is suggested by the fact that a number of photorefractive crystals, as Lithium Niobate, can be indeed turned into permanent materials after a baking process (fixing) [Carrascosa *et al.*, 1990]. Therefore, after fixing the master gratings, the production an infinite number of copies without grating decay is possible.

If the above solutions are otherwise not possible, or are not architecturally attractive, and therefore master grating erasure is unavoidable, it is necessary to characterize the transitory regime of the system (*i.e.* the temporal evolution of the copied gratings) to understand and better exploit the system performance. This section is dedicated to the study of this transitory regime. For the sake of generalization, we will consider the case of both permanent and erasable materials during such study. The study of this transitory regime during copying begins with the introduction of some basic definitions that lead to determination of the copy gain function (CGF).

Consider the copying of a master which consists of N angularly multiplexed holograms. In this case, according to the results of the blind copying process, we require N reference beams of intensity I_r^m which recall from the master N object beams. These object beams interfere in the secondary medium with N reference beams, each of them of intensity I_r^c. Because of the master readout, the amplitude modulation of each of the gratings recorded in the master decays as $\Delta n^m{}_j f_m(t)$, in which $f_m(t) \leq 1$ a monotonically decreasing function which depends on the material physical characteristics and total readout intensity, in the fashion that a larger readout intensity is responsible for a more severe decay. At the same time, we can indicate as $\eta_{jo}^m \ll 1$ the (initial) diffraction efficiency of the j-th hologram, whose temporal variation, during readout, can be approximated as $\eta_{jo}^m f_m^2(t)$. The time varying diffraction efficiency of the j-th hologram copied in the secondary medium $\eta_j^c(t)$. For $\eta^c{}_j(t) << 1$, we can approximate the time evolution of the copied diffraction efficiency of the j-th hologram as

$$\eta_j^c(t) = \left(\frac{\pi T \Delta n^c{}_j(t)}{\lambda \cos(\theta_i)} \right)^2, \tag{6-19}$$

in which the term $\Delta n^c{}_j(t)$ represents the temporal evolution of the grating modulation during copying. The temporal variation of $\Delta n^c{}_j(t)$ can be written as

$$\frac{d}{dt} \Delta n^c{}_j(t) = m_j(t) \Delta n_M f_c(t), \tag{6-20}$$

in which $f_c(t)$ is a function which depends on the copying material characteristics and on the total recording intensity, while, due to the master gratings era-

sure, $m_j(t)$ is the time varying beam intensity modulation, which for the specific j-th hologram is

$$m_j(t) = 2\frac{\sqrt{\eta^m_j I^m_r f^2{}_m(t) I^c_r}}{N\left(I^c_r + \eta^m_a I^m_r f^2{}_m(t)\right)}, \tag{6-21}$$

where the object beams are written in term of the wavefronts retrieved from the master. Using 6-20, and 6-21, we can rewrite the time evolution of the diffraction efficiency seen in Eq. 6-19 as

$$\eta^c_j(t) = \eta^m_{jo}(c_o/N)^2 \frac{I^m_r}{I^c_r}\left[\int_0^t \frac{f_m(\tau) f_c(\tau)\, d\tau}{I^c{}_r + \eta^m_a f_c(\tau) I^m{}_r}\right]^2, \tag{6-22}$$

in which c_o is the same constant obtained after the approximation of Eq. 6-13, and, as previously indicated, $\eta^m{}_a$ is the average diffraction efficiency in the master (before readout). For the condition

$$I^c_r/I^m_r \gg \eta^m_a f^2_m(t)\ , \tag{6-23}$$

we can derive from Eq. 6-22 the term $G(t)$ which consists in the ratio between $\eta^c{}_j(t)$ (time evolution of the copied diffraction efficiency) and $\eta^m{}_{jo}$ the initial master diffraction efficiency, as

$$G(t) = (c_o/N)^2 \frac{I^m_r}{I^c_r}\left[\int_0^t f_m(\tau) f_c(\tau)\, d\tau\right]^2 = \frac{\eta^c_j(t)}{\eta^m_{jo}}, \tag{6-24}$$

where $G(t)$ is termed as copy gain function (CGF).

The CGF, which depends on the physical characteristics of the master and copying material, describes the time evolution of the eventual gain or attenua-

tion that any copied grating experiences during recording. The CGF is independent of the index j, and therefore is common to each of the copied grating. Of course, different holographic materials present different dynamics, and therefore the CGF must be computed according to the specific master and the copy materials used. In the rest of this section we determine the CGF for the four possible combinations existing when photorefractive crystals and photopolymers are used as master and/or copy.

6.6.1 Copying from a Photopolymer to a Photorefractive Crystal

A photopolymer master is a permanent medium, therefore $f_m(t) = 1$. In the copy, during recording, the grating modulations grow exponentially as [Yeh, 1993]

$$f_c(t) = \frac{e^{-\frac{t}{\tau_c}}}{\tau_c}, \tag{6-25}$$

The copying time constant, τ_c, is inversely proportional to the total intensity illuminating the secondary material as [Yeh, 1993]

$$\tau_c^{-1} = \kappa_c N\left(I_r^c + \eta_a^m I_r^m\right) \approx \kappa_c N I_r^c, \quad \text{for } I_r^c / I_r^m \gg \eta_a^m, \tag{6-26}$$

where the constant κ_c is characteristic of the used crystal and the subscript c indicates that the crystal is used as secondary medium.

In this case, according to Eq. 6-24, we obtain the following CGF

$$G(t) = (c_o/N)^2 \frac{I_r^m}{I_r^c}\left[1 - \exp\left(-\frac{t}{\tau_c}\right)\right]^2, \tag{6-27}$$

which at saturation is

$$G(\infty) = (c_o/N)^2 \frac{I_r^m}{I_r^c}. \tag{6-28}$$

6.6.2 Copying from a Photopolymer to a Photopolymer

As seen in the previous subsection, the holograms multiplexed in the photopolymer are permanent, with the associated $f_m(t) = 1$. According to the HFMD solution, the gratings copied in the photopolymers grow with the function $f_c(t)$ as

$$f_c(t) = \frac{\gamma e^{\frac{\tau}{\tau_c}}}{\tau_m} e^{\gamma(1 - e^{t/\tau_c})}, \tag{6-29}$$

where the time constant is

$$\tau_c^{-1} = \left[N\varphi\left(I_r^c + \eta_a^m f_m^2(t)\, I_r^m\right)\right]^{\delta} \approx \left(N\varphi I_r^c\right)^{\delta}; \text{ for } I_r^c/I_r^m \gg \eta_a^m f_m^2(t). \tag{6-30}$$

According to these findings, the CGF will be

$$G(t) = (c_o/N)^2 \frac{I_r^m}{I_r^c}\left(1 - e^{\gamma\left(1 - e^{t/\tau_c}\right)}\right)^2. \tag{6-31}$$

At saturation, the solution is the same as in Eq. 6-28.

6.6.3 Copying from a Photorefractive Crystal to a Photorefractive Crystal

The master holograms of a photorefractive crystal are partially erased during readout. The decay that the gratings experience upon illumination is [Yeh, 1993]

$$f_m(t) = \exp(-t/\tau_m), \tag{6-32}$$

in which $\tau_m^{-1} = \kappa_m N I_r^m$ is a time constant of the master gratings, κ_m is a constant typical of the crystal used [Yeh, 1993], and the subscript m standing for master.

Considering the interaction between decaying master and growing/decay copy during exposure, we can write the CGF for this specific case as

$$G(t) = (c_o/N)^2 \frac{I_r^m}{I_r^c}\left[\int_0^t \frac{e^{-\frac{(t-\tau)}{\tau_c}}}{\tau_c} e^{-\frac{\tau}{\tau_m}} d\tau\right]^2, \tag{6-33}$$

in which and $\tau_c^{-1} \approx \kappa_c (N I_r^c)$, according to Eq. 6-26.

The close form solution of this CGF is then

$$G(t) = (c_o/N)^2 \frac{I_r^m}{I_r^c}\left[\frac{\tau_m}{\tau_m - \tau_c}\left(e^{-\frac{t}{\tau_m}} - e^{-\frac{t}{\tau_c}}\right)\right]^2, \tag{6-34}$$

which reaches a peak value at $t = \frac{\tau_m \tau_c}{\tau_m - \tau_c}[\log(\tau_m) - \log(\tau_c)]$. Interestingly, one can notice that at saturation this CGF is zero. This is related with the erasure of the master holograms. In fact, when the master holograms are erased, only the copy reference beams illuminate the secondary medium, resulting in

an exponential erasure of the copied holograms.

For the particular case of $\tau_m = \tau_c$, the CGF is

$$G(t) = (c_o/N)^2 \frac{I_r^m}{I_r^c} \left(\frac{e^{-\frac{t}{\tau_c}}}{\tau_c} t \right)^2 , \qquad (6\text{-}35)$$

which reaches a maximum at $t = \tau_c$, and then decays to zero.

Because of its particular functional dependency, few words must be spent to better describe this specific CGF. The selection of the crystal for master and copy greatly affects the CGF. In fact the maximum value of CGF depends not only on the usual copy/master reference ratio (and Δn_M), but also on the specific coefficient κ_c and κ_m. This last statement is illustrated with the help of Fig. 6-8 (a). This figure depicts the evolution of the CGF multiplied by the square of the number of the copied holograms (CGF X N^2). The master is an undoped SBN crystal, and either the faster crystal $BaTiO_3$ ($\kappa_m > \kappa_c$), or a slower ($\kappa_m < \kappa_c$) SBN:75:Ce (essentially a doped SBN) is the secondary medium. The physical data about these crystals are found in [Yeh, 1993]. A copy/master intensity beam ratio of value of unity (Eq. 6-17 and 6-18) is used during copying, and for both the copying materials $\Delta n_M = 0.001$. The total (master and copy) reference intensity beams is $NI_r^m = NI_r^c = 100$ mW/cm^2. The figure indicates how a faster secondary medium favors a CGF with a larger peak value, which is reached rapidly, with a reduced decay of the master gratings as indicated by the figure. This last factor further suggests that using a faster copy material, the master can be copied for a larger number of times

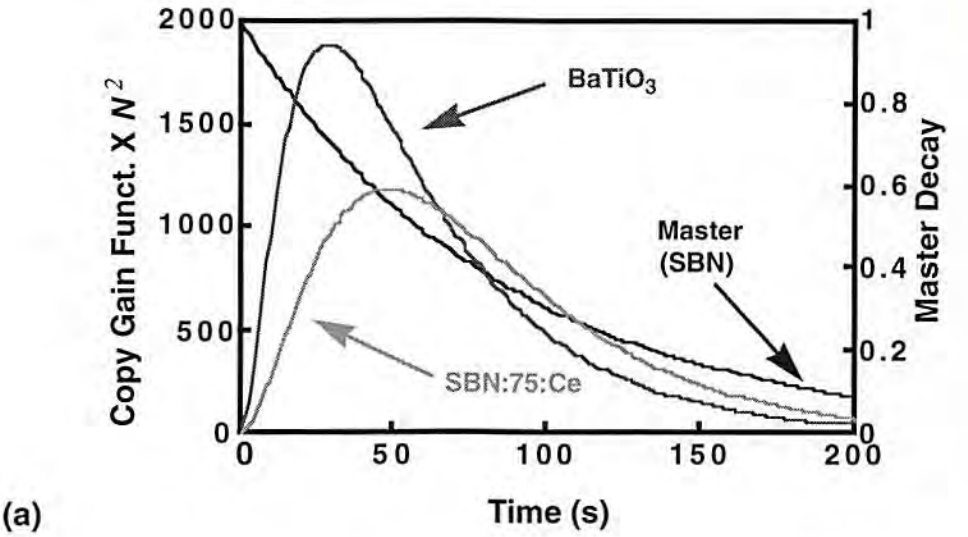

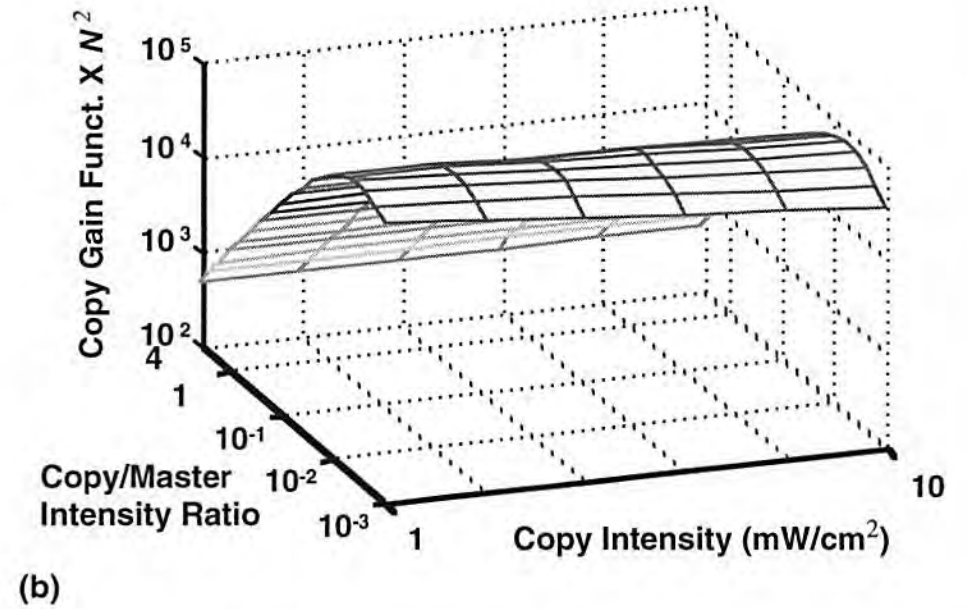

Figure 6-8. Copy gain function, having an erasable master hologram. **(a)** Master: undoped SBN. Copy: $BaTiO_3$ or SBN:75:Ce. Respectively, the $BaTiO_3$ and SBN:75:Ce are faster and slower than the master crystal. The peak maximum CGF of the SBN-$BaTiO_3$ is higher than the SBN-SBN:75:Ce system, with a lower master erasure. **(b)** Master: SBN. Copy: HRF-150, 500 μm thick. The highest CGF value is reached at lower NI_r^c, and for a copy/master intensity ratio less than 0.6.

until the gratings are totally erased. Per contra, a faster material is extremely volatile, and therefore its information contents (holograms) are easily erased during subsequent readings. Of course, this problem can be avoided by copying in the slower crystal, which is less sensitive to grating erasure, with the consequence of lower hologram diffraction efficiency, as demonstrated by the CGF of the SBN:75:Ce.

6.6.4 Copying from a Photorefractive Crystal to a Photopolymer

In this characterization we can apply results from previous CGF studies: the gratings of the master photorefractive crystal decay as in Eq. 6-32, while in the photopolymer the copied gratings grow as Eq. 6-29. Combining these last two equations, we can express the CGF from a photorefractive master to a photopolymer copy as

$$G(t) = (c_o/N)^2 \frac{I_r^m}{I_r^c}\left[\int_0^t e^{-\frac{\tau}{\tau_m}} \frac{\gamma e^{\frac{\tau}{\tau_c}}}{\tau_m} e^{\gamma(1-e^{\tau/\tau_c})}\, d\tau\right]^2 . \qquad (6\text{-}36)$$

The closed form solution of the above equation is not immediate, and to obtain such solution it is necessary some mathematical attention. Integrating by parts, the above CGF becomes

$$G(t) = (c_o/N)^2 \frac{I_r^m}{I_r^c}\left(1-e^{\gamma(1-e^{(\tau/\tau_c)})} e^{-\frac{t}{\tau_m}} - \frac{1}{\tau_m}\int_0^t e^{-\frac{\tau}{\tau_m}} e^{\gamma(1-e^{\tau/\tau_c})}\, d\tau\right)^2 . \qquad (6\text{-}37)$$

The solution of the remaining integral in Eq. 6-37 is possible once we use the following approximation (based on the retention of the first two elements of the Taylor's series expansion of the term $\exp(\tau/\tau_c) \approx 1+ \tau/\tau_c$)

$$e^{-\frac{\tau}{\tau_m}\gamma\left(1-e^{\tau/\tau_c}\right)} e \cong e^{-\frac{\tau}{\tau_{tot}}}, \tag{6-38}$$

in which $\tau_{tot} = \dfrac{\tau_m \tau_c/\gamma}{\tau_m + \tau_c/\gamma}$.

Then, by using the approximation of Eq. 6-38 in Eq. 6-37, solving the integral and algebraically rearranging it, we get the following CGF

$$G(t) \equiv (c_o/N)^2 \frac{I_r^m}{I_r^c}\left[\frac{\gamma\tau_{tot}}{\tau_c} + e^{-\frac{t}{\tau_m}}\left(\frac{\tau_{tot}}{\tau_m}e^{-\frac{t}{\tau_c}} - e^{\gamma\left(1-e^{t/\tau_c}\right)}\right)\right]^2, \tag{6-39}$$

which at saturation is

$$G(\infty) = (c_o/N)^2 \frac{I_r^m}{I_r^c}\left[\frac{\tau_m}{\tau_m + \tau_c/\gamma}\right]^2. \tag{6-40}$$

Even in this case, great care must be taken when choosing the materials and selected the intensities of the reference beams illuminating the master and the copy. For instance, if the photopolymer total recording intensity is too high and it not in the realm of HFMD model, the copied holograms will present lower diffraction efficiency than expected. To maximize the saturation CGF of Eq. 6-40, the optimal reference intensity beams must be provided, noticing, however, that GFC saturation value is related in a nonlinear fashion to the reference beam intensities and the material time constants. Fig. 6-8 (b) depicts the saturation value of the CGF when using as master material undoped SBN,

and a 500 μm thick HRF-150 (self diffraction effects are not considered here). The total intensity of the copy reference beams is varied, consistently with the HFMD hypothesis, as $1 < NI_r^c < 10$ mW/cm², the copy/master intensity beam ratio is in the interval [0.001 4], while the z-axis indicates the figure of merit CGF X N^2 at saturation. As shown in the figure, the better yield of the CGF X N^2 values is for lower NI_r^c, however critical parameter is the copy/master beam intensity ratio. In fact, the product CGF X N^2 (which we want to maximize) is higher (in the range of $\sim 10^4$) for the copy/master intensity ratio approximately lower than 0.6, then it begins to decay to the value of $\sim$ 450 for an intensity ratio of 4.

Of course, for different crystals and photopolymers, the material physical characteristics can be different from those that originated Fig. 6-8 (b), and therefore different system performance must be evaluated. In fact, when faster and more sensitive photopolymers are used, these can be driven into saturation with a reduced decay of the master gratings, which, moreover, permits reuse of the master for a subsequent number of copies until the gratings are completely erased.

6.7 Conclusions

This chapter presented and analyzed a technique to duplicate multiplexed volume holograms. It first introduced a description of a general principle inspiring the proposed copying architecture. The results of an analysis of this copying architecture indicate how to perform blind copying of multiplexed vol-

ume holograms using permanent or erasable master holographic materials. Incidentally, the presented copying architecture has already inspired practical commercial applications, [Mok *et al.*, 1996] and [Holoplex].

An aspect of the copying architecture that we did not analyze was that of the copying errors. As in every copying process, master duplication cannot be perfect, and errors are generated. The nature of copying errors and their repercussion on the system depends on the applications in which the multiplexed volume holograms are used (optical storage, optical interconnections, etc.) and, therefore, a general analysis is not possible. In the next chapter, however, we present as a study an example of this problem, which consists of the generation, duplication, and system error characterization due to copying, of a holographic based neural network.

6.8 Bibliography

Brady, D., K. Hsu, and D. Psaltis, "Periodically Refreshed Multiple Exposed Photorefractive Holograms," Opt. Lett., **15**(14), 817-819, (1990).

Campbell, S., Y. Zhang, and P. Yeh, "Material Limitations in Volume Holographic Copying," Digest of Meeting in Optical Computing (OSA, Salt Lake City), 77-79, (1995).

Carrascosa, M. and E. Aguilló-López, "Theoretical Modeling of the Fixing and Development of Holographic Gratings in LiNbO3," JOSA-B, **7**(12), 2317-2322, (1990).

Goldstein, A. A., G. C. Petrisor, and B. K. Jenkins, "Gain and Exposure Scheduling to Compensate for Photorefractive Neural-Network Weight Decay," Opt. Lett., **20**(6), 611-613, (1995).

Holoplex, at "http://www.primenet.com/holoplex/".

Jewell, J., Y. Lee, A. Scherer, S. McCall, and N. O. e. al., "Surface-Emitting Microlasers for Photonic Switching and Interchip Connections," Opt. Eng., **29**(3), 210, (1990).

Malinoff, E., S., and Johnson, "Maximized Photorefractive Holographic Storage," J. Appl. Phys. **70**(9), 4702-4707, (1991)

Mok, F., G. Zhou, and A. Chugh, "Read-Only Data Storage System," OSA Annual Meeting, Rochester, New York, (1996).

Piazzolla, S., B. K. Jenkins, and J. A. R. Tanguay, "Single-step copying process for Multiplexed Volume Holograms," Opt. Lett., **17**(9), 676-678, (1992).

Vanin, V. A., "Hologram Copying, A Review," Sov. J. Quant. Electron., **8**, 809, (1978).

Yeh, P., *Introduction to Photorefractive Nonlinear Optics*, John Wiley & Sons, Inc., (1993).

Zech, G. "Volume Hologram Optical Memories, Mass Storage Future Perfect?," Optics&Photonics News, **(8)**, 16-25, (1992)

Chapter 7

Generation and Copy of Holographic Weights: an Artificial Neural Network Application

7.1 Introduction

Depending on the applications, multiplexed volume holograms can be used as optical memories and/or optical interconnections. This inherent duality makes volume multiplexed holograms suitable in neural network applications where they can simultaneously function as axonal interconnections and synaptic memory. Therefore, as a technological application, this chapter studies, models, and presents a way to implement some basic artificial neural network functions using volume holography. Beside the design and implementation of holographic neural networks, their duplication via blind copying it is emphasized. As seen later in this chapter, holographic neural network training can be a time consuming procedure with the final values of the holographic weights embedded within the material with their values practically unknown. Therefore, when a large production of these networks is required, the blind copying of these holographic interconnects can be a viable and simple techno-

logical solution to their mass production.

Holographic copying, as an any other form of transmission, elaboration, and duplication of stored information, can be badly affected by some form of noise. Emphasizing on angularly multiplexed volume holograms, we can consider that there are three forms of noise that can damage their performances: grating degeneracy, beam degeneracy, and grating cross-talk.

Grating degeneracy arises when different beams can share the same grating. This form of noise can be prevented by positioning the incident recording beams in a fractal sampling geometry [Lee *et al.*, 1989].

Beam degeneracy originates from the rediffraction of the diffracted beam and it is reduced at low diffraction efficiency values [Goodman, 1985].

Cross-talk gratings are unwanted gratings recorded simultaneously with the main gratings which are carrying the holographic information. For instance, when the information carried by object beam is of complex nature (*i.e.* the object beam is not a simple plane wave), the internal interference of the waves composing the object beam angular spectrum record in the holographic material a set of cross-talk gratings. During readout, these cross-talk gratings act as a source of noise redistributing the energy in an undesired fashion. This form of noise will be accurately studied in this chapter, and its repercussions on the training of the neural network, and on the performances of the copying will be assessed.

The rest of this chapter is organized as it follows. A brief introduction on some basic concepts about neural networks will be followed by a description of

a holographic/optoelectronics implementation. Then we study the diffractive regime of angularly multiplexed volume holograms able to implement trainable neural interconnections. Next, a practical problem (XOR) is simulated on the holographic neural network, and the action of the cross-talk grating noise is evaluated. Finally, blind copying of the network angularly multiplexed holograms is performed. After replacing the master holograms with their copies, the network performances are characterized.

7.2 Artificial Neural Networks: Preliminary Concepts

Artificial neural networks are signal processing and computing systems inspired by biological nervous system. Essentially, artificial neural networks, and biological nervous systems as well, are composed of a large number of computing nodes (neurons) densely interconnected to other nodes via weighted interconnections (axons). In such systems the output signal fired by each neuron, after being multiplied by the weight (synapses) of the relative interconnection, may feed the input of other neurons which concurrently process their input signals (input potential) with a (generally) nonlinear transfer function. Depending on the input potential value, the transfer function determines the firing of the output signal. Because of their peculiar nature of nonlinear, dynamical, and densely parallel processing systems, neural networks are uniquely suitable for a number of applications as pattern recognition, optimization process, and artificial intelligence [Anderson, 1988].

Neural network architectures are determined by their topology, neuron

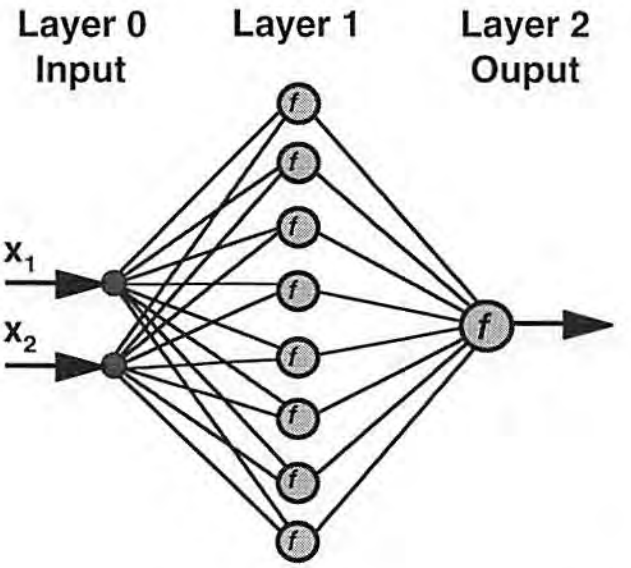

Figure 7-1. Schematic representation of two layer feed-forward artificial neural network. The are 8 neurons on the first layer and one output neuron. The input signal is a vector of two elements. The neuron transfer function used in this chapter is a sigmoid as in Eq. 7-3.

characteristics, and learning rules. A common neural network topology consists of a number of cascaded feed-forward layers of neurons, where the number of layers and the number of neurons in each layer can be related to the complexity of the problem whose solution the network is dedicated [Lippman, 1987]. Figure 7-1 depicts an example of two layer feed forward neural network. In this network, $N_r = 2$ input signals are connected to the $N_s = 8$ neurons of the second layer, and the output layer is constituted by a single neuron. Each neuron on a layer processes the input potential signal, computing an output signal as

$$x_i^l = f\left(\rho_i^l + b_i^l\right), \tag{7-1}$$

in which the superscript l indicates the layer level, the subscript i indicates the

specific neuron on the layer l, $f(\bullet)$ is the neuron transfer function, b_i^l is a bias value, and finally ρ_i^l is the input potential. The input potential is the algebraic sum of the weighted output signals of the (connected) neurons of the l -1 previous layer as

$$\rho_i^l = \sum_j w_{ij}^l x_j^{l-1} , \tag{7-2}$$

in which w_{ij}^l is the weight of the axon linking the output signal x_j^{l-1} (*i.e.* neuron j on the layer l-1) to our neuron i on the layer l. These considerations can be extended for feed-forward networks with an undefined number of layers.

For modelling the neuron response, we will assume here that the nonlinear transfer function is implemented by a sigmoid, which therefore suggests to rewrite Eq. 7-1 as

$$x_i^l = \left[1 + e^{-\frac{\left(b_i^l + \rho_i^l \right)}{b_o}} \right]^{-1} . \tag{7-3}$$

where b_o is a constant, and the firing of the output signal is limited in the range [0 1].

Similar to its biological model, the knowledge of a neural network is embedded in the values of its weights. By properly changing (or better adapting) the values of its weights, a network can be trained to solve specified tasks or problems. The learning rule is the algorithm used to update the values of the weights to converge (when it is possible) to a desired problem solution (when it exists). During an iterative learning process, a generalized learning rule can be

described by the following weight update form

$$w_{ij}^{l}(n+1) = w_{ij}^{l}(n) + \alpha(n+1)\,\delta_{i}^{l}(n+1)\,x_{j}^{l-1}(n+1) \ , \qquad (7\text{-}4)$$

where n is the index of the iteration, the term $\alpha(n+1)$ is called learning rate, $\delta_{i}^{l}(n+1)$ is an error signal. Of course, both the terms $\alpha(n+1)$ and $\delta_{i}^{l}(n+1)$ are algorithm dependent.

A historically important and successful learning algorithm, for multilayer feed-forward networks, is the backward error propagation algorithm (BEP) [Rumelhart *et al.*, 1986]. Extensively used in pattern recognition and pattern classification problems, the BEP algorithm can train a multilayer feed-forward network to recognize input patterns or training samples (in our case input vectors or training vectors) via sequential exposure of training samples and iterative attempts to reduce of the an error function. The error function, ε_{BEP}, is

$$\varepsilon_{BEP} = \frac{1}{2}\sum_{p}\sum_{k}\left(t_{pk} - x_{pk}^{out}\right)^{2}, \qquad (7\text{-}5)$$

in which the indices p and k are relative to the p-th input training sample and the k-th output neuron, while the terms t_{pk} and x_{pk}^{out} are the desired output (or target values) and actual output of the k -th output neuron, respectively. A requirement of the BEP algorithm is that the nonlinear transfer function must be continuous (soft threshold). According to the results of the minimization of the error in Eq. 7-5 [Rumelhart *et al.*, 1986], the weight updates propagate backward and the updates of the l-1-th layer are function of the updates of the l - th layer. Particularly, when the neuron transfer function is the sigmoid of Eq. 7-3, the error signal of the generalized learning rule of Eq. 7-3 is

$$\delta_{pj}^{out} = \left(t_{pj} - x_{pj}^{out} \right) x_{pj}^{out} \left(1 - x_{pj}^{out} \right), \text{ for the output layer;} \qquad (7\text{-}6)$$

$$\delta_{pj}^{l} = \left(1 - x_{pj}^{l} \right) x_{pj}^{l} \sum_{m} \delta_{pm}^{l+1} w_{mj}^{l+1}, \text{ for the other (hidden) layers.} \qquad (7\text{-}7)$$

The subscript p indicates the p -th training sample, which is the input vector that generates the firing of the signal x_{pj}^{l} from the j-th neuron belonging to the l layer.

After introducing these definitions, in the next section we present a volume hologram based architecture able to implement artificial neural network operations including a learning algorithm such as the BEP.

7.3 The Architecture

Figure 7-2 schematically depicts a holographic/optoelectronics architecture dedicated to implement a two layer feed-forward artificial neural network. The network presents two input signals, $N_s = 8$ neurons on the first layer and one output neuron. In essence, the network of Fig. 7-2 is an optoelectronic version of the network of Fig. 7-1.

The interconnections of the first layer are implemented by angularly multiplexed volume holograms recorded in a photorefractive crystal (PRC). The PRC, which is a nonpermanent holographic material, can implement real time adaptive holographic interconnections. In practical problems, this first layer may implement a very large number of interconnections, and for this task a multiplexed volume hologram can be an ideal solution, due to the high storage

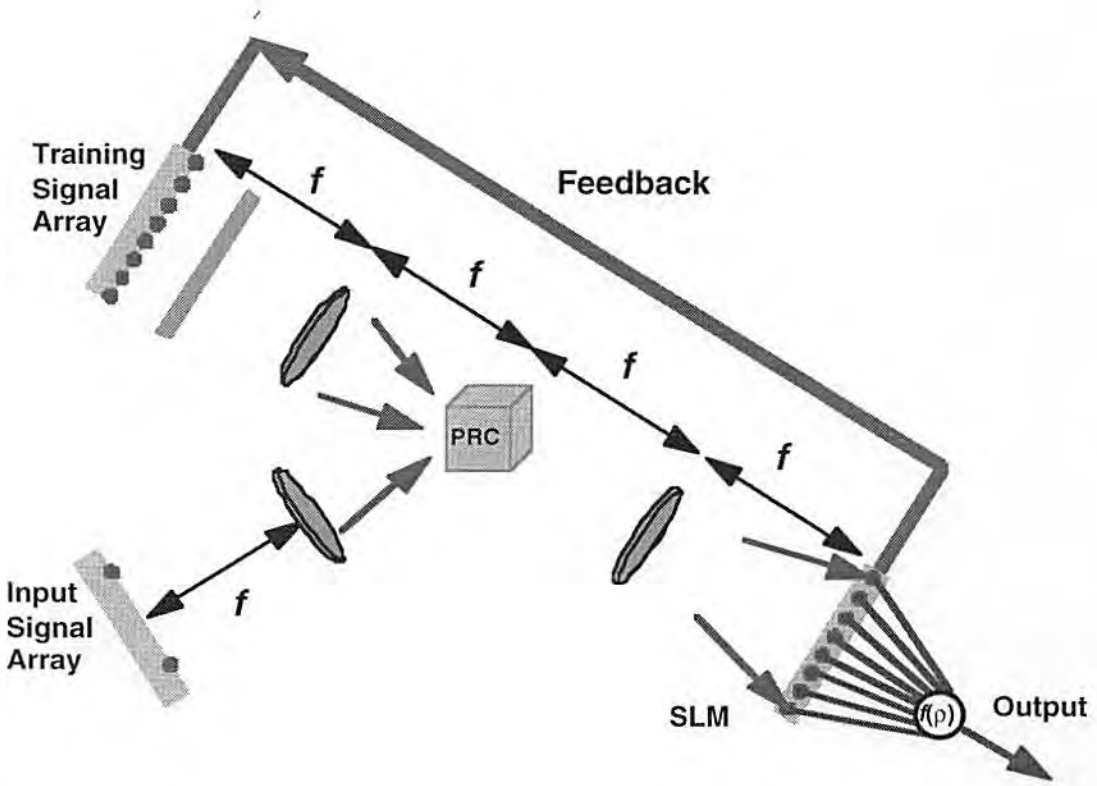

Figure 7-2. Optoelectronics equivalent of the two layer feed-forward artificial neural network of Fig. 7-1. The first layer weighted interconnections are implemented by angularly multiplexed volume holograms recorded in a photorefractive crystal (PRC). The holograms are recorded by the interference of the plane waves originated by the point sources of two arrays. The point sources are Fourier transformed into plane waves by lenses located a the focal distance from the arrays and the PRC. The output SLM consists of a detector array which collects the light diffracted by the PRC, and elaborates the output signal of the first layer via sigmoidal transfer functions. The output layer is electronically implemented. During training, the output SLM sends the signal error to the driver of the training signal array which modulates the intensity of the single point source.

capacity of the PRC [Psaltis *et al.*, 1988]. The angularly multiplexed holograms are recorded by interference of waves which are generated by the two source arrays. The source arrays can be composed by single emitting sources whose intensities are controlled by an electronic driver or by spatial light modulators (SML) [Karim *et al.*, 1994]. The input signal array encodes the network input signals (input patterns), while the training signal array is responsible for generating the signal errors during training, as in Eq. 7-7. Two fourier lenses transform the light emitted by the point sources into plane waves which interfere in the PRC. An array of N_s detectors, positioned at the focal distance from the output lens, collects the light diffracted by the volume hologram. Each single detector in the array constitutes a part of a single neuron of the first layer, and the intensity of the detected light signal is proportional to the input potential, which is locally elaborated by the related sigmoidal transfer functions.

The second layer weights are electronically implemented [Lee and Sheu, 1995]. The weighted signals of the output SLM feed electronically into the output neuron. In essence, the output SLM of Fig. 7-2 is implementing a detector array, the transfer function, and moreover it can elaborate the first layer error signals which drive the training signal array (as seen later in this chapter).

During learning, the network operates as follows. A training sample is at the input signal array, while the shutter facing the other array is closed. The output signal, generated from this training sample, is compared to the target signal and the related error signals are calculated. During weights update, the error signals are back propagating. The output SLM computes the first layer error

signals, and sends them, via an electronic feedback, to the driver of the training array. Each emitting source of this array changes its intensity to encode such error signals. The shutter is open and the interference among the training signals and the input signal writes the gratings, in a short exposure time, which update the holographic weights in the PRC. The weights of the second layer are electronically updated. The process of presentation and learning continues until the network converges to a solution.

The next two sections describe in detail how the volume holographic medium can implement the first layer interconnection weights, and what are the requirements for such implementation and for the optical representation of the neural signal.

7.4 Grating Multiplexing

The purpose of this section is to illustrate how a volume hologram may implement the function of weighted interconnections required by a feed-forward neural network. In order to do so, we present a diffraction analysis of angularly multiplexed volume holograms recorded in the PRC. The result indicates how this device may physically accommodate both the algebraic sum of Eq. 7-2 [Slinger, 1991 #1] and a weight update rule (shown in the next section).

In this example, we envision a pagewise sequential exposure of multiple gratings. In other terms, during recording, a single beam of the input array

interferes with all the plane waves coming from the training array, Fig. 7-3 (a). Inside the holographic medium, the waves originated by the training signal array propagate as

$$E_{ij}^{s} = s_{ij}\exp\left(-j\underline{\rho}_i \bullet \underline{r}\right), \tag{7-8}$$

in which s_{ij} is the (maybe complex) field amplitude, the $\underline{\rho}_i$ is the wavevector associated to the i-th source (with $i = 1,2,\ldots N_s$) on the training signal array, while the index j (with $j = 1,2,\ldots,N_r$) is related to the exposure sequence. Concurrently, the waves generated by the input signal array are here indicated as

$$E_{j}^{r} = r_j\exp\left(-j\underline{\sigma}_j \bullet \underline{r}\right) \tag{7-9}$$

in which r_j is the (meaybe complex) field amplitude, $\underline{\sigma}_j$ is the wavevector, while the index j (with $j = 1,2,\ldots,N_r$) specifies the source in the input array and (for now) the sequence of the exposure.

Here we assume the same time duration for each exposure. Grating decay (which is taken in to consideration later in this chapter) and self diffraction effects are omitted. According to these hypotheses, one can obtain the following expression of $\Delta n_{tot}(\underline{r})$, which is the overall grating modulation

$$\Delta n_{tot}(\underline{r}) \tag{7-10}$$
$$= \left(\sum_{i=1}^{N_s}\sum_{j=1}^{N_r}\Delta n_{ij}e^{-j\left(\underline{\rho}_i-\underline{\sigma}_j\right)\bullet\underline{r}} + cc\right) + \sum_{m=1}^{N_s}\sum_{n=1}^{N_s}\Delta n_{mn}^{cg}\left(e^{-j\left(\underline{\rho}_m-\underline{\rho}_n\right)\bullet\underline{r}} - \delta_{mn}\right)$$

where δ_{mn} is the Kronecker delta. The total grating modulation is the combination of N_rN_s main gratings and unwanted $N_s(N_s\text{-}1)/2$ gratings. The main grat-

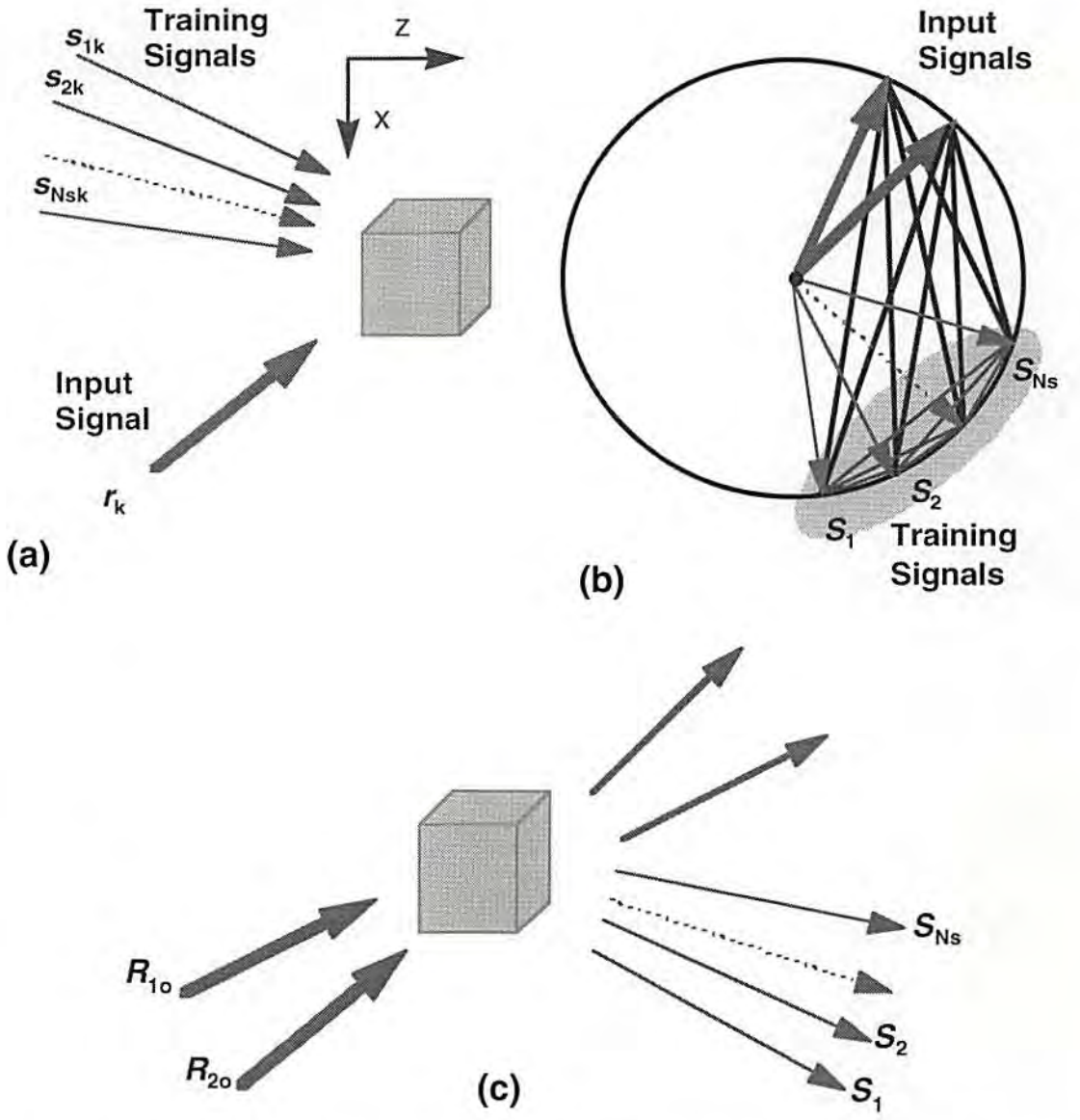

Figure 7-3. Grating multiplexing in an angularly multiplexed volume hologram. **(a)** In the recording phase, N_s plane waves generated by the training signal array interfere with the plane wave generated by the input signal array. **(b)** Geometrical relations between the Recording waves and grating wavevectors on the Ewald sphere. The main grating wavevectors link the input signal wavectors with the training signal wavevectors. The cross gratings (shaded area) link among themselves the training signal wavevectors. **(c)** Reconstruction from an anglularly multiplexed volume hologram. Plane waves from the input signal array are diffracted and they generate N_s output signals, which are supposed to feed the output SLM because they carry information proportional to the neuron input potentials of the first layer.

ings are originated by the interference of each wave from the input array, and the waves from the training array. The resulting grating amplitude is

$$\Delta n_{ij} = \xi_o s_{ij} r^*_j, \tag{7-11}$$

with ξ_o a constant depending on the physical properties of the PRC, the illuminating light, and the exposure duration (Chap. 6). Concurrently, the unwanted gratings, or cross gratings, are originated by the internal interference of the waves emitted by the training array, and they are related to the wave amplitudes as

$$\Delta n^{cg}_{mn} = \xi_o \sum_{j=1}^{N_r} s_{mj} s^*_n. \tag{7-12}$$

During hologram reconstruction, these cross gratings greatly affect the quality and the fidelity of the recalled information, because they link all the main gratings, as indicated in Fig. 7-3 (b), and they originate an undesired exchange of energy among the reconstructed beams. The presence of cross gratings may be seen as a source of recording noise that can affect the training neural network, and, eventually, the quality of copied multiplexed volume hologram, as it is carefully illustrated later in this chapter.

During hologram reconstruction or readout, the PRC is illuminated with reference plane waves originated by the input array. The amplitudes of these reference waves at beginning of the holographic region is R_{oj}, for $j = 1, \ldots, N_r$. The propagating waves within the holographic region are then

$$E^R_j = R_j(z) \exp(-j\underline{\sigma}_j \bullet \underline{r}) \text{ for } i = 1, \ldots, N_r, \text{ and} \tag{7-13}$$

$$E_i^S = S_i(z) \exp(-j\underline{\rho}_i \bullet \underline{r}) \text{ for } i = 1, . , N_s, \tag{7-14}$$

with the total field given by

$$E_T = \sum_{j=1}^{N_r} E_j^R + \sum_{i=1}^{N_s} E_i^S . \tag{7-15}$$

To determine the evolution of the propagating waves within the holographic region we have to solve the wave equation

$$(\nabla^2 + q^2) E_T = 0 , \tag{7-16}$$

with the propagation constant q, which is here defined (similarly to what earlier done in Chap. 4) as

$$q^2 = \beta^2 \left(n_o^2 + 2 n_o \Delta n_{tot}(\underline{r}) \right), \tag{7-17}$$

where, as usual, β is the wavenumber *in vacuo*, n_o is the refractive index of the PRC which we assume lossless.

By inserting the definition of total field as in Eq. 7-15 and of the grating modulation of Eq. 7-10 and solving the wave equation, approximating according to the SVA hypothesis (as also seen in Chap. 4), and matching the terms with the same harmonic dependence, according to what indicated by [Slinger, 1991 # 2] we the following coupled wave equations

$$\frac{dS_i}{dz} = -j \frac{\pi}{\lambda \cos(\theta_{\rho i})} \left(\sum_{j=0}^{N_r} \Delta n_{ij} R_j + \sum_{m=1}^{N_s} \Delta n_{im}^{cg} (1 - \delta_{im}) S_m \right), \tag{7-18}$$

$$\frac{dR_j}{dz} = -j\frac{\pi}{\lambda\cos(\theta_{\sigma j})}\sum_{i=0}^{N_s}\Delta n^*_{ji}S_i, \tag{7-19}$$

in which $\theta_{\rho i}$, and $\theta_{\sigma i}$ are the incidence angles (internally the PRC) of the training waves and input signal waves. The above equations can be better summarized with the state equation [Gaylord, 1985]

$$\frac{d}{dz}\begin{bmatrix}\underline{R}\\ \underline{S}\end{bmatrix} = -j\frac{\pi}{\lambda}\left[\frac{1}{\cos(\theta)}\right]\begin{bmatrix}[0] & [\Delta n_{ij}]\\ [\Delta n_{ij}]^* & \left[\Delta n^{cg}_{im}\right]\end{bmatrix}\begin{bmatrix}\underline{R}\\ \underline{S}\end{bmatrix}, \tag{7-20}$$

with the initial condition for propagating beam of $\begin{bmatrix}\underline{R}(0)\\ \underline{S}(0)\end{bmatrix} = \begin{bmatrix}\underline{R}_o\\ \underline{0}\end{bmatrix}$. The vectors $\underline{S}$ and $\underline{R}$ correspond to the training wave amplitudes and the input wave amplitudes, the matrix of the grating modulations is composed by a null sub-matrix, [0], of dimension $N_r \mathrm{X} N_r$, a sub-matrix $[\Delta n_{ij}]$ (and its transpose conjugate $[\Delta n_{ij}]^*$) whose elements are the amplitude modulations of the $N_r N_s$ main gratings, while the elements of the cross-talk matrix $\left[\Delta n^{cg}_{im}\right]$ (dimensionally $N_s \mathrm{X} N_s$) are the modulation amplitudes of the cross gratings as in Eq. 7-10. The matrix $\left[\frac{1}{\cos(\theta)}\right]$, is a diagonal matrix whose terms are the inverse of the cosines of the wave incidence angles as seen at the denominators of the coupled wave equations. Even if the solutions of the state equation, or their dual of Eq. 7-18 and 7-19, may far from resembling to the implementation of a layer of neural interconnections, however, this same implementation may be more visible after introducing the following approximations. When a large number of (main) gratings are angularly multiplexed in a volume medium, the correspondent values of the grating modulations are very low, and because of the low diffraction of the input signal waves we get

$$\frac{dR_j}{dz} \approx 0 . \tag{7-21}$$

During recording, if the intensities of input waves are much larger than those relative to the training array, we have that the modulations of the cross gratings much less that of the main gratings, with $\left|\Delta n_{mn}^{cg}\right| \ll \left|\Delta n_{ij}\right|$ (for any indices m,n,i, and j). Therefore we can drop the cross grating terms of Eq. 7-18, which can be solved as

$$S_i(T) = \sum_{j=0}^{N_r} \tilde{\eta}_{ij} R_{jo} . \tag{7-22}$$

The term $\tilde{\eta}_{ij}$ is the complex amplitude diffraction efficiency (Chap. 4, Sec. 4.2), which is related to the main gratings as

$$\tilde{\eta}_{ij} \approx -j \frac{\pi \Delta n_{ij} T}{\lambda \cos(\theta_{\rho i})} . \tag{7-23}$$

The analogy of the above with its neural equivalent is now immediate. If we compare Eq. 7-22 with Eq. 7-2, we can clearly determine the similarity between the diffracted amplitude of the wave $S_i(T)$ which impinges the j-th detector of the output SLM, and the input potential of a neuron, with the equivalent of the generic weight w_{ij} given by

$$w_{ij} \propto \tilde{\eta}_{ij}, \tag{7-24}$$

where the weights are encoded by the complex amplitude diffraction efficiency and the field amplitude encodes the neuron signal.

Unfortunately, a consequence of this holographic implementation is an

existing compromise between diffraction efficiency versus the fidelity and the noise of the interconnections themselves: the optimization of one of these factors automatically penalizes the other [Slinger, 1991 # 2]. Clearly, when the light is efficiently diffracted by the main gratings, the basic assumption of Eq. 7-21, leading to the fundamental result of Eq. 7-23, is not valid. Moreover, to achieve high diffraction efficiency from the multiplexed volume holograms it is necessary to record main gratings with large amplitude modulations. To do so, during holographic exposure, the intensities of the training waves and input waves must be comparable (if not equal), which favors the formation of larger cross grating amplitude modulations, with the consequence of a noisier reconstructions during holographic readout. Of course, a nosier readout may affect the successful convergence of the learning algorithm to a solution.

The study of the performance of a neural network affected by different level of cross gratings noise is an argument of great interest, which therefore it will be investigated in the continuation of this chapter. Before to proceed with this argument, however, few more definitions are necessary to create a perfect correspondence between the neural network of Fig.7-1, with its optoelectronics realization of Fig. 7-2.

7.5 Signal Representation

In this section we map the generic two layer feed-forward network of Fig. 7-1 on its optoelectronics implementation of Fig. 7-2. The crucial issue is here to relate the neural signal, synaptic weights, and their updates to the relative

field amplitudes impinging on the detector array, the hologram field diffraction efficiencies, and the grating updates during learning. Before describing in detail this neural mapping for the field encoding suggested by Eq. 7-23, we must point out that a number of other architectural solutions may be considered for the holographic implementation of neural networks, such as the fully coherent [Psaltis *et al.*, 1988] and the incoherent/coherent intensity encoding [Petrisor *et al.*, 1996]. Choice of the best suitable encoding is motivated by the particular architectural and technological system requirements as the minimization of the hardware complexity (fully coherent) or the reduction of the phase stability noise (incoherent/coherent). In our proposed architecture, the choice of field encoding represents a good compromise in keeping relatively simple the analogy between the neural architecture and its hardware implementation.

7.5.1 Signal encoding

For sake of simplification, we assume in our modelling and during our computer simulations that the plane waves incident the PRC have no phase component. Therefore, r_j and s_i are positive real numbers, and so are the amplitude of grating modulations appearing in Eq. 7-18 and Eq. 7-19.

The output signal from a neuron is unipolar, bounded in the range [0 1]. Concurrently, we can map the field amplitude, of the waves originated from input signal array and training signal array, with the neural signal output and the error signal as

$$x_j = \frac{r_j}{E_o}, \text{ for } j = 1,2,..,N_r; \text{ and } \alpha(n+1)\,\delta_{ij}(n+1) = \frac{s_{ij}}{E_o},$$

$$\text{for } i = 1,2,..,N; \tag{7-25}$$

in which E_o is the largest field amplitude of a plane wave generated by a single source in the arrays.

7.5.2 Weight Encoding

During readout, the signal of neural interconnection can map the field diffraction efficiencies according to the relation

$$w_{ij}x_j = G_o|\tilde{\eta}_{ij}|R_{jo}, \tag{7-26}$$

where G_o is a gain of the array detector, and the RHS absolute value is motivated by the action of the detector array during readout (we already have supposed a real field amplitude R_{jo}). In fact, avoiding phase detection of the readout signal, we assume that each detector of the array read out the field absolute value, which is proportional to the signal intensity square root as

$$|S_i(T)| = \left|\sum_{j=1}^{N_r} \tilde{\eta}_{ij}R_{jo}\right|. \tag{7-27}$$

The above detection technique is advantageous because it eliminates instability related to the phase detection, but it may impair the implementation of bipolar weights when their are needed. A way to circumvent this drawback is the use of dual rail weight encoding [Owechko, 1993]. In essence, in dual rail encoding the training signal array is doubled in size with $2N_s$ sources which

originates the related $2N_sN_r$ main gratings. Half of sources this array are dedicated to the implementation of the "positive weights" w_{ij}^{+} or the "positive field diffraction efficiencies" $\tilde{\eta}_{ij}^{+}$, by recording the interference of the corresponding training waves of amplitude s_{ij}^{+} with r_j. Similarly, the other half of the SLM sources originates the waves of amplitude s_{ij}^{-} which interfere with r_j to record the "negative weight" w_{ij}^{-} or the "negative complex amplitude diffraction efficiency" $\tilde{\eta}_{ij}^{-}$. During readout, the output SLM will detect and elaborate the input potential

$$\rho_j = G_o\left(\left|\sum_{j=0}^{N_r} \tilde{\eta}_{ij}^{+} R_{jo}\right| - \left|\sum_{j=0}^{N_r} \tilde{\eta}_{ij}^{-} R_{jo}\right|\right), \qquad (7\text{-}28)$$

with the above signal substraction electronically implemented by the output SLM. Dual rail encoding also influences the weight updated during learning as is exposed in the following section.

7.5.3 Grating Update

Even if a PRC can accommodate the function of grating update, and therefore of neural learning, its grating update mechanism is not totally consistent with the requirements of the neural learning rule of Eq. 7-4. In fact, during grating update, the very same exposure responsible of adjusting the modulation of the gratings induces a decay of the gratings themselves as [Goldstein *et al.*, 1995]

$$\left|\tilde{\eta}_{ij}^{+}(n+1)_{ij}\right| = \left|\tilde{\eta}_{ij}^{+}(n)\right| e^{\frac{-\Delta t}{\tau}} + \alpha(n+1)\, C_n s_{ij}^{+}(n+1)\, r_j(n+1)\left(1 - e^{\frac{-\Delta t}{\tau}}\right), \quad (7\text{-}29)$$

in which n is the index of the iteration, Δt is the exposure update duration, τ is the exposure time constant of the PRC, and C_n is a constant linked to the exposure characteristics, as in Eq. 7-11 and Eq. 7-23. For the moment, without lack of generalization, we are considering only positive weights and positive updates. For the condition $\Delta t << \tau$ (which allows to simplify $e^{\frac{-\Delta t}{\tau}} \cong 1 - \frac{\Delta t}{\tau}$), the above can be readjusted as

$$\left|\tilde{\eta}_{ij}^{+}(n+1)\right| = \frac{\left|\tilde{\eta}_{ij}^{+}(n)\right|}{G_d} + \alpha(n+1)\, C_n \frac{\Delta t}{\tau} s_{ij}^{+}(n+1)\, r_j(n+1) \quad , \quad (7\text{-}30)$$

where the term G_d is the inverse of the decay (1- $\Delta t/\tau$), which is experienced by the gratings during exposure update. It is then evident that the grating decay that PRC field diffraction efficiencies experience not only gradually decreases the grating strengths, but also impedes the implementation of learning rule as seen in Eq. 7-4. While the first problem is somehow unavoidable, electronically we can overcame the second. If we consider that each iteration has same the grating decay $1/G_d$, we can program the output SLM to compensate this grating decay by increasing its detection gain by a factor of G_d during the training iteration itself. Of course, the error signal and the training source array will accommodate the detector gain by the following relations

$$\frac{\alpha(n+1)\,\delta_{ij}^{+}(n+1)}{G_d^{n+1}} = \frac{s_{ij}^{+}(n+1)}{E_o}, \text{ and } \delta_{ij}^{-}(n+1) = 0 \, , \quad (7\text{-}31)$$

positive update; while for negative updated it will hold

$$\frac{\alpha\,(n+1)\,\delta_{ij}^{-}\,(n+1)}{G_d^{n+1}} = \frac{s_{ij}^{+}(n+1)}{E_o} \quad \text{, and } \delta_{ij}^{-}(n+1) = 0\,. \tag{7-32}$$

Therefore, we can write the reading of the detector array for the j-th neuron input potential after the n+1 training iterations as

$$\rho_j(n+1) = G_o G_d^{n+1}\left(\left|\sum_{j=0}^{N_r}\tilde{\eta}_{ij}^{+}(n+1)\,R_{jo}\right| - \left|\sum_{j=0}^{N_r}\tilde{\eta}_{ij}^{-}\,(n+1)\,R_{jo}\right|\right). \tag{7-33}$$

7.5.4 Signal Array and PRC Requirements

The average Bragg angle given by the a signal wave interfering with an input wave was selected to be 10°. The PRC was 5 mm thick, the recording wavelength of 514 nm, and refraction index $n_o = 2.5$. This data indicate that the Klein's thickness parameter (Chap. 4, Eq. 4-24) is $Q = 1.9\text{X}10^4$ for the main gratings. Such thickness parameter is well above the requirements ($Q = \pi^2$) for the volume diffraction regime. Similarly, we want the cross gratings to diffract in volume regime, as characterized by the state equation in Eq. 7-20. To guarantee this, each cross grating needs a minimum $Q = \pi^2$ to which corresponds a minimum angular distance of $8\text{X}10^{-3}$ rad between two jason signal waves. If we use fourier transform lenses with $f = 50$ mm, then each pixel on the signal training array must be separated by 400 μm, which for a dual rail encoding, gives minimum dimension of $400\text{X}(2N_s\text{-}1)$ μm for the training array.

7.5.5 Grating Update

The exposure time of an update, concurrently with the intensities of the sources on the training and input signal arrays, defines the maximum diffraction efficiency (or weight) updated. If we consider the beam intensity ratio between training and input wave, $BR_{ij} = |s_{ij}|^2 / |r_j|^2$, limited in the range $0 \le BR_{ij} \le B_o$ for any i and j indices, then we can write for the maximum grating increment

$$|\Delta\eta_{ij}| = \frac{2\pi\Delta n_M T\sqrt{B_o}}{1 + N_s B_o}\frac{\Delta t}{\tau}, \tag{7-34}$$

in which Δn_M is the largest refraction index modulation attainable in the PRC, having simplified the exponential in Eq. 7-24 as $e^{\frac{-\Delta t}{\tau}} \cong 1 - \frac{\Delta t}{\tau}$. The above limit update applies for any weights (negative or positive) of the dual rail encoding.

7.6 Network Learning: Simulation of the XOR

The operations of an artificial neural network can be tested recurring to a number of benchmark problems available and suggested in literature [Rumelhart and McClelland, 1987]. One of the most used and popular among these benchmark problem has been the simulation of an exclusive OR (XOR) or otherwise termed the two dimensional parity problem [Petrisor, 1996]. The XOR problem can be considered a classic problem of pattern classification not solvable via linear classifier, which requires a two layer feed-forward network to be handled [Pao, 1989]. In our case, we will use to simulate the XOR with the two

layer network of Fig. 7-1. Considering the optoelectronic implementations of the network as seen in Fig. 7-2, one can observe that the first layer has 8 neurons, and therefore it is required the recording of 32 holographic weights in the PRC, due to the dual rail encoding of the weights ($32 = 2N_s X N_r$). It was chosen $N_s = 8$ because it allows us to analyze a system with a relative large number of interconnections, even if to simulate the XOR can be sufficient a network with $N_s = 2$. The first layer of holographic weights are recorded in a PRC with the $\Delta n_M = 0.0001$. During each update, the decay of the amplitude of the grating modulation was 2%, which implies that a constant light intensity is illuminating the PRC during the grating update itself. An eventual grating decay caused by readout was omitted. Also the effects of self diffraction were not considered. An initial learning rate $\alpha(0) = 0.1$ was used, however to speed up the convergence of the problem [Vogl *et al.*, 1988] the learning rate was increased of 5% in every iteration in which the error ε_{BEP} decreased ($\varepsilon_{BEP}(n+1) < \varepsilon_{BEP}(n)$), and it was reduced of 3% after an iteration which caused an error increment ($\varepsilon_{BEP}(n+1) > \varepsilon_{BEP}(n)$) with a lower limit of $\alpha(n) = 0.05$. The learning halted when a targeted $\varepsilon_{BEP}(n) = 0.05$ was reached, while a maximum of 300 iterations were permitted to the algorithm. To calculate the amount of light collected by the detector array in the output SLM, we solved (in each readout) the state equation as in Eq. 7-20, which allows us to take into account (differently from the linearized solution of Eq. 7-33) the noise originated by the cross gratings.

To begin the learning process, we assigned a set of initial random weights to the ideal network of Fig. 7-1. Such initial set of weights were transformed in holographic weights by selecting the proper amplitudes of the plane waves s_{ij}

which are interfering with the input waves r_j. By such interference the initial matrix of grating modulation Eq. 7-20 was generated and then selected the initial gain G_o of detector array, according to Eq. 7-28.

To understand the consequence of the cross grating noise on the algorithm, for the same initial set of equivalent weights, we repeated the neural training in three different cases, where the recording of the initial matrix of the grating modulation was performed each time with a different value of the maximum beam intensity ratio as $B_o = \{0.01, 0.1, 0.5\}$. For each training a proper initial G_o was calculated. Moreover, the training of the ideal network (no holographic implementation of the first layer) as that described by Fig. 7-1, was also performed and compared with three holographic implementations.

Tables 5 and 6 indicate a short summary of the data from the first 10 converging XOR simulations. The data are respectively comparing the length of the algorithm (number n_f of iterations to solution) and the largest values of the amplitudes of the modulation gratings for the different initial maximum beam intensity ratios. Table 5 clearly indicates that generally (except for simulation # 4) for a larger B_o value the process is slower to converge. Essentially, we can point out that a larger cross-talk noise related to a higher B_o slows down the algorithm. At the same time, because of a larger initial B_o, the initial amplitude of the main gratings are larger, which leads to a more (diffraction) efficient first layer of holographic interconnections.

Table 5: Number of Iteration to Convergence: n_f

Simulation	# 1	# 2	# 3	# 4	# 5	# 6	# 7	# 8	# 9	# 10
Ideal	73	93	74	255	57	82	59	84	68	62
B_o=0.001	73	93	74	263	56	81	60	85	68	62
B_o=0.01	74	92	75	211	58	78	63	114	68	65
B_o=0.05	82	105	86	169	65	82	67	88	81	67

At lower values of initial B_o the system is less efficient in diffracting the light, but advantageously a lower system noise, due to smaller cross grating amplitudes, facilitates the algorithm to converge with the same number of iterations as in an ideal system (as in Fig. 7-1), as clearly seen for most the simulation results of Table 5, where the simulations with initial $B_o = 0.01$ converge with (almost) the same speed of the ideal network. It is interesting that this (usual) inherent relation between high B_o vs. slow convergence, and low B_o vs. faster convergence may lead to a trade off in term of final grating amplitude modulation. In fact, a higher B_o supposes an initial amplitude of the modulations of the main gratings higher respect to a lower initial B_o. At the same time, the grating decay may be more severe in a process with a large initial B_o, because it takes a larger n_f to converge respect to a network with lower initial B_o. Therefore, a process with low initial B_o can compensate the initial disadvantage of lower initial amplitude grating modulation because its faster convergence can limit the grating decay effect. This concept is better understood after looking at the data in Table 6. In essence, if we compare the case of

initial $B_o = 0.5$, and $B_o = 0.01$, the initial ratio between the amplitudes of their respective larger main gratings has to be $\sqrt{0.5/0.01} \approx 7$, instead after the algorithms converge this ratio is at most ≈ 4.

Table 6: Largest Modulation Grating X10^{-6}

Simulation	# 1	# 2	# 3	# 4	# 5	# 6	# 7	# 8	# 9	# 10
B_o=0.001	2.38	1.56	2.26	0.059	3.2	2.0	3.09	1.9	2.56	2.9
B_o=0.1	6.29	4.31	5.9	0.54	8.5	5.7	7.8	2.85	6.9	7.4
B_o=0.5	7.17	4.36	6.41	3.1	1.0	7.08	9.6	6.42	7.2	9.5

To better illustrate the behavior of the network during learning, we present in Fig. 7-4 the variation of the error $\varepsilon_{BEP}(n)$ and the learning rate $\alpha(n)$, during training of simulation # 1, for the three different cases of initial B_o's.

Interestingly, for $B_o = 0.5$ (dotted curves) has associated with it the largest initial error $\varepsilon_{BEP}(1) = 1.75$, and the training history indicates that the error is not monotonically decreasing, as in the other cases of initial $B_o = 0.01$ (solid curves) and 0.1 (dashed curves), but (probably) because of the presence of cross-talk noise, it increases after 20 iterations, and then converges to the target $\varepsilon_{BEP} = 0.05$. Even if the initial errors are different for the initial $B_o = 0.1$ and 0.01, the training of these networks follows the same trend, having identical variation of their learning rate curves.

Finally, Fig. 7-5 presents the final values, concerning this simulation #1, of the solving matrix of the grating modulations for the different initials maximum input beam intensity ratios.

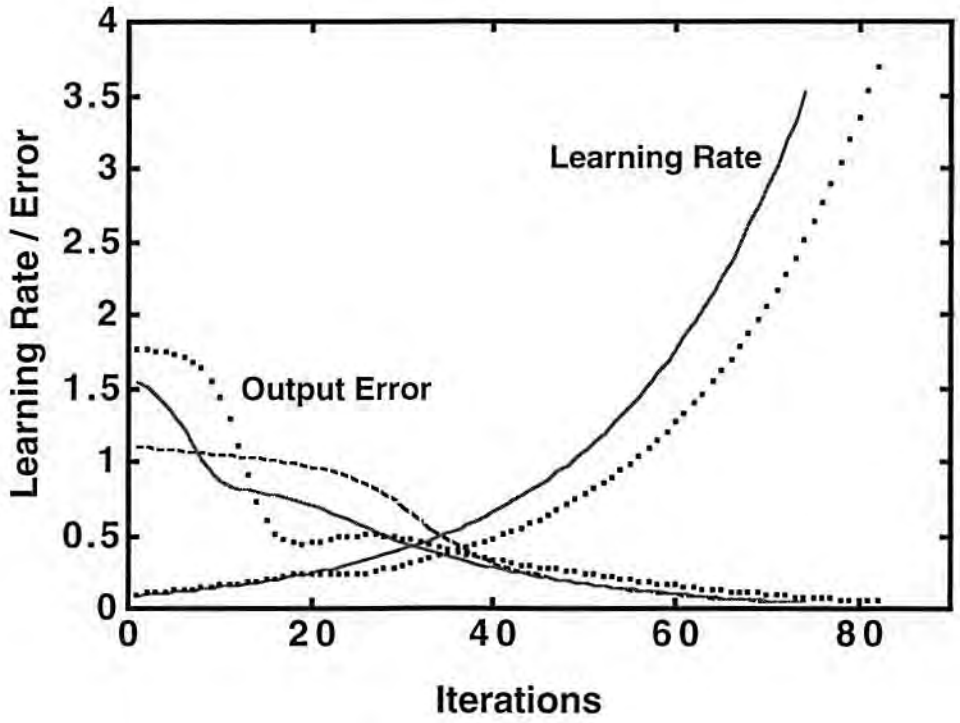

Figure 7-4. History of the network errors and learning rates during simulation #1, for the three initial maximum input intensity ratio 0.5 (dotted curves), 0.1 (dashed curves), 0.01 (solid curves). The case for $B_o = 0.5$ presents the largest initial error $\varepsilon_{BEP} = 1.75$, which decreases to the targeted value of $\varepsilon_{BEP} = 0.05$. The learning rates curve for $B_o = 0.01$, and 0.1 are almost identical, probably due to the limited cross-talk noise effective at this low level of initial input intensity ratio.

Of course, with increasing initial beam intensity ratios, the elements of the matrix corresponding to amplitude modulations of the cross gratings are more visible as witnessed by comparing Fig. 7-5 (a) and 7-5 (c). The matrix elements corresponding to the cross gratings have row and column indexes respectively as $3 \leq i \leq 18$, and $3 \leq j \leq 18$. The reader should remember that it was supposed to have incident waves recording on the PRC with zero phase values. Conse-

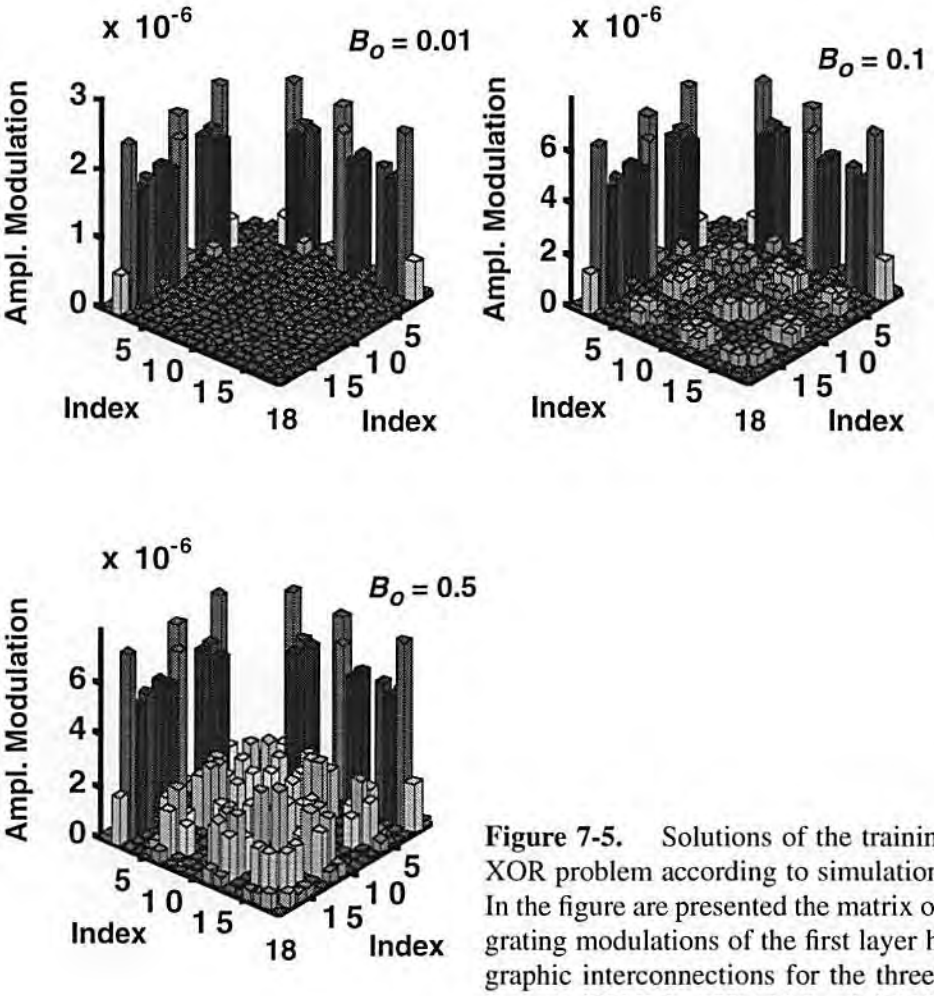

Figure 7-5. Solutions of the training of XOR problem according to simulation #1. In the figure are presented the matrix of the grating modulations of the first layer holographic interconnections for the three different initial B_o's. With higher initial input beam intensity ratios, the cross-talk gratings are more visible, and for $B_o = 0.5$ their are comparable with the main gratings. The cross-talk gratings correspond to the elements of the matrix with row and column with indices $3 \le i \le 18$ and $3 \le j \le 18$.

quently, the recorded gratings do not have phase value, and the elements belonging to the matrix of the grating modulations are positive numbers.

7.7 Network Copying: Simulation Results

Once that a neural network, such that in Fig. 7-2, is successfully trained, it can accomplish the required computational tasks. If one envisions to reproduce a large number of such neural networks, then it is convenient and more practical to duplicate holographic weights via blind copying instead of retraining new networks. Moreover, because of the neural training the actual values of the holographic weights embedded in the PRC are unknown, hence blind copying is the only effective paradigm (except for the training of new networks) to the duplication of the holographic weights themselves. Of course, once a copy is originated, one has to question about the quality of the copy, or better how an optical neural network using a copy of the holographic weights can accomplish the required computational tasks respect to the original network. This section is dedicated to give an answer to this specific question.

7.7.1 Preliminary Concepts

This section carries out a study of the performances of copied multiplexed holograms used in the XOR networks which where trained in previous section. To better compare a pool of homogeneous results, and holograms of comparable values of the amplitude modulation of the gratings, simulations #4 and #5

were excluded by this study, because they correspond to the extremes cases of solutions obtained with the largest and smallest n_f.

The study was carried out by comparing the network performances for the three different values of initial beam intensity ratios. It must be considered that, differently from what previously presented in Chapt. 6, we here mainly consider the field amplitude diffraction efficiencies Therefore the solution to blind copy will be

$$\frac{\left|E_r^c\right|}{\left|E_r^m\right|} = \frac{c_o}{G_{ad}N}\,, \tag{7-35}$$

in which is expressed the ratio between the field amplitudes of the copy and master reference beams as function of the complex amplitude diffraction efficiency gain, G_{ad}, the number of holograms N, with the constant c_o, Eq. 6-13, proportional to the secondary medium thickness and Δn_M. Note that, because of the linear nature of the problem (see Eq. 7-22 and 7-23), a gain G_{ad} of the amplitude diffraction efficiency should correspond to a gain G_{ad} of the copied amplitude modulation of the main gratings. Therefore in the next section this term gain can be applied without distinction (and confusion) for both these physical quantities.

The overall figure of merit that characterized the network performances, when using a copy of the master (angularly multiplexed) volume hologram, is the average network error, which we calculated as indicated in the following procedure:

(**1**) the master of the angularly multiplexed volume hologram (solution of

the XOR problem) of a network is copied according some specific requirements of the problem (*i.e.* diffraction efficiency gain, phase noise, secondary medium with higher Δn_M, etc.);

(2) blind copying is simulated to obtain the new matrix of the grating modulations: it is first calculated the intensity of the master reference beams, and of the copy reference beams; the recalled object beams then interfere with the copy reference beams in the secondary medium and write the main gratings along with the unwanted cross-talk gratings as well;

(3) the hologram copy properly substitutes the master hologram in the XOR neural network solution, and the error ε_{BEP} is calculated;

(4) steps **(1)**, **(2)**, and **(3)** are repeated for each of the eight networks having the initial B_o, the error is averaged.

In essence, the average network error, for a given gain G_{ad}, and for holograms having in common the same initial B_o, can be written as

$$< \varepsilon_{BEP}(G_{ad}, B_o) > \quad = \frac{1}{N_t} \sum_{l=1}^{N_t} \varepsilon_{BEPl}(G_{ad}, B_o) \ , \tag{7-36}$$

in which N_t is the number of networks considered for the average (here $N_t = 8$), and the generic $\varepsilon_{BEPl}(G_{ad},B_o)$ is the error of the copy of j-th network, with initial B_o, whose weights have been amplified G_{ad} times.

7.8 Diffraction Efficiency Gain Errors

Upon copying, magnification of the grating amplitude diffraction efficiencies (and of the amplitude modulation as well) of the master hologram is an application of great interest. In fact, in this way, we can relieve eventual power budget problems related to the low diffraction efficiencies of the master caused by the grating decay during training in a PRC.

Figure 7-6 (a) presents the variation of the average network error when diffraction efficiency magnification is incorporated with the copy of the master holograms. The secondary medium has the same holographic characteristics of the master. The plots are relative to the three different cases of initial beam intensity ratios. When such copies are used, all the other parameters of the neural networks (weights of the second layer, bias, etc.), which solve the XOR problem, are unchanged except for the output SLM gain, $G_o G_d^{nf}$ in Eq. 7-33, which is reduced by the gain of the field amplitude diffraction efficiencies, G_{ad}. The horizontal line in the figure corresponds to the targeted error $\varepsilon_{BEP} = 0.05$, and the gain of the (amplitude) diffraction efficiency is considered in the range $1 \leq G_{ad} \leq 10$. For $B_o = 0.01$, the are allowed error free copies with $G_{ad} = 3$, and after that gain the average error exceeds the targeted value.

Clearly, the figure indicates that for copies of masters associated with larger B_o's, the average error is the larger. Motivations of this larger average error are essentially explained by the fact that at higher B_o's, the copy can be more affected by lack of fidelity, and by larger cross-talk grating noise.

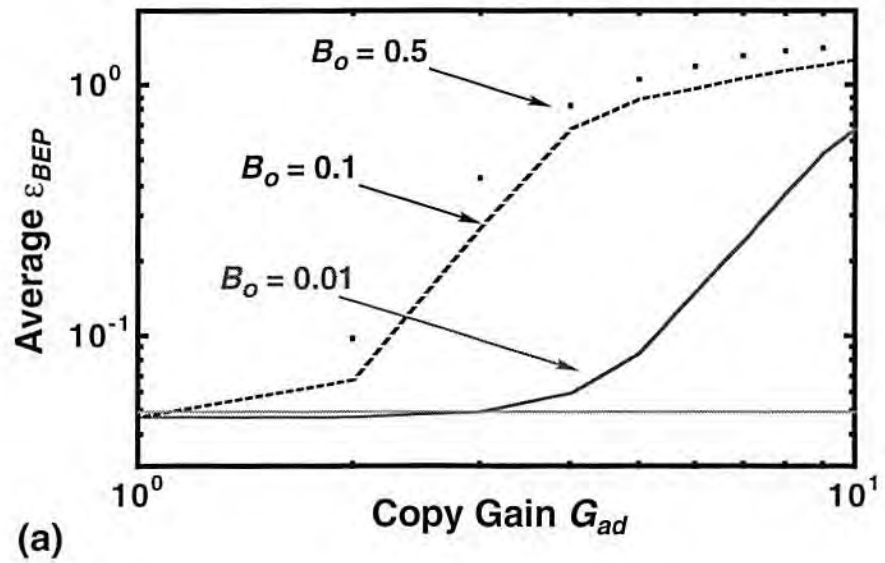

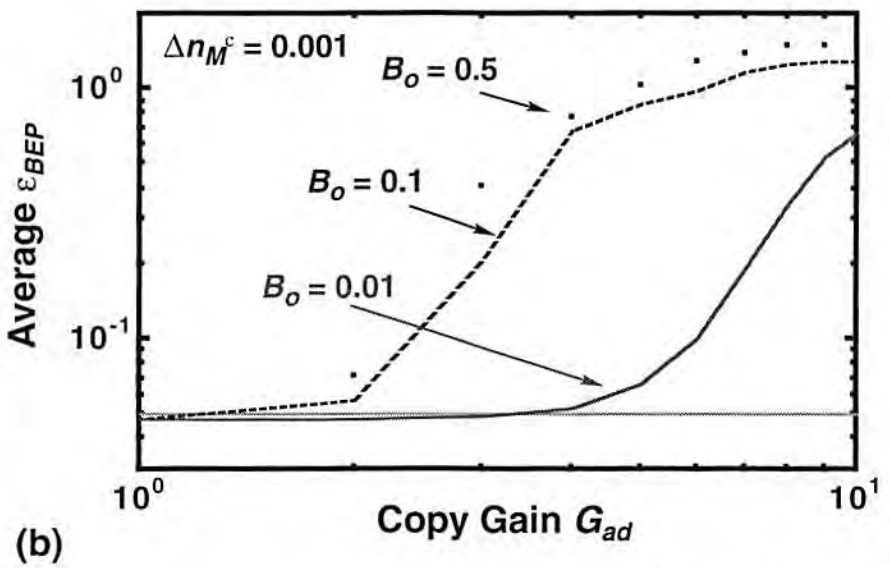

Figure 7-6. Average network error ε_{BEP} when are magnified the diffraction efficiencies of the holographic weights of the first layer of the XOR. The average ε_{BEP} is calculated over selected XOR simulations presented in the previous section. The master PRC is 5 mm thick, with $\Delta n_M = 0.0001$. The horizontal line indicates the targeted network error $\varepsilon_{BEP} = 0.05$ **(a)** Results when is performed copy and diffraction efficiency gain on secondary medium of the same nature of the master (same thickness and Δn_M) **(b)** Results when is performed copy with diffraction efficiency gain on a secondary medium of same thickness of the master PRC, but with Δn_M ten times larger.

The lack of fidelity is related to the fact that holographic masters recorded with a larger initial B_o's have larger amplitude modulations of their gratings. This factor can affect the copy according to these three following ways.

(1) Lack of linearity. During copying, and if gain is performed, the main gratings recorded on the secondary medium are magnified by a factor G_{ad}. Concurrently, if the copied main gratings are large enough, the diffraction efficiencies of the copied volume holograms may not increase proportionally to G_{ad}, because the diffraction regime may not be in the condition of linearity as seen in Eq. 7-22, and 7-23. As already pointed out, if the copy is more (diffraction) efficient, it must lack in fidelity, which explains the larger average error at larger G_{ad}'s.

(2) Lack of dynamics of the secondary medium. If the gain requested upon grating magnification is too large, the Δn_M of the secondary medium may not be large enough to allow the copied (main) gratings to be G_{ad} times larger of those of the master, which, of course, during readout of the copied gratings worsen the network performance.

(3) Proximity to the distortion zone. As understandable by the blind copying diagram of Fig. 6-7, a large average diffraction efficiency of the master induces a reduction of the gain and the fidelity region. Therefore, for a large gain the copying process can operate in the distortion zone, with the consequence that these distorted copies can lack of fidelity.

cross-talk grating noise behaves as any other kind of noise, and increases upon duplication and/or (diffraction efficiency) gain. As seen in Fig. 7-5, larger

cross-talk gratings are related to the recording with $B_o = 0.1$, or 0.5, and the noise generated by these cross-talk gratings can already affect copying with $G_{ad} = 2$ (for such low gain the contribution to the error by lack of fidelity is negligible), Fig. 7-6 (a). When a larger gain is requested, cross-talk noise increases. Essentially this is due to the fact that when copying with gain the intensity beam ratio at the secondary medium must increase, with the recording of cross-talk gratings of larger amplitude modulation. Moreover, due to cross-talk gratings, master readout beams do not have any more uniform phase when they interfere in the secondary medium. Therefore, the presence of cross-talk gratings in master leads to record (main and cross-talk) gratings of different phase content in the secondary medium. This is another source of noise that can affect the performance the average error of a copied network [Alferness, 1975].

Copying in a secondary medium with Δn_M larger than that of the master can alleviate problems caused both by the lack of fidelity and the cross-talk grating noise. Easily, one can see that a large Δn_M of the secondary medium can alleviate problems caused by of lack of fidelity as in **(2)** and **(3)**. Moreover, according to Eq. 7-35, recording on secondary medium with a larger Δn_M (respect to the master), it reduces the intensity beam ratio (during the recording of the copy), with the results that are recorded cross-talk gratings of lower modulation amplitude.

This concept is more practically illustrated with the help of Fig. 7-6 (b). Here the variation of the average network error is calculated for the secondary medium with $\Delta n_M = 0.001$ and same thickness of the master (it is beneficial to

remember that in the master $\Delta n_M = 0.0001$). In this case, an improvement in the performances of the copied holographic weights are noticeable. For $B_o = 0.01$, the system now allows a gain $G_{ad} \approx 4$, while for larger values of B_o's the error of curves are basically smaller that those of Fig. 7-6 (a). Counterintuitively, for larger gain value, the figure indicates that there is not sensitive improvement when this technique is used. Explanation to this circumstance is due the fact at such higher gain values the error caused by lack of fidelity are overwhelming.

Finally, in Fig. 7-7 the matrix of the grating modulations characterizing the copy of the holograms of results simulation # 1 is presented. Here the master and the secondary medium have same thickness and Δn_M, and a gain $G_{ad} = 5$ was performed upon duplication. It is useful to compare these data with those of the original master of Fig. 7-5. As a consequence of the gain, cross gratings are more visible in the copy, and are definitely comparable with the main gratings for larger values of B_o's. The change of the phase of the gratings is now visible, and it is even more evident for the case of master recorded with $B_o = 0.5$. Clearly, both the amplification of the cross gratings and the change of the grating phases in the copy constitute source of a network error, which for all the three different cases of B_o's is unacceptable with $\varepsilon_{BEP} > 0.05$. Particularly, for $B_o = 0.5$, Fig. 7-7 (e), the lack of dynamics of the modulation index induces an evident lack of fidelity of type **(2)**, because the amplitudes of the main gratings, differently from what requested by the copying process, are not five times larger than those of the master.

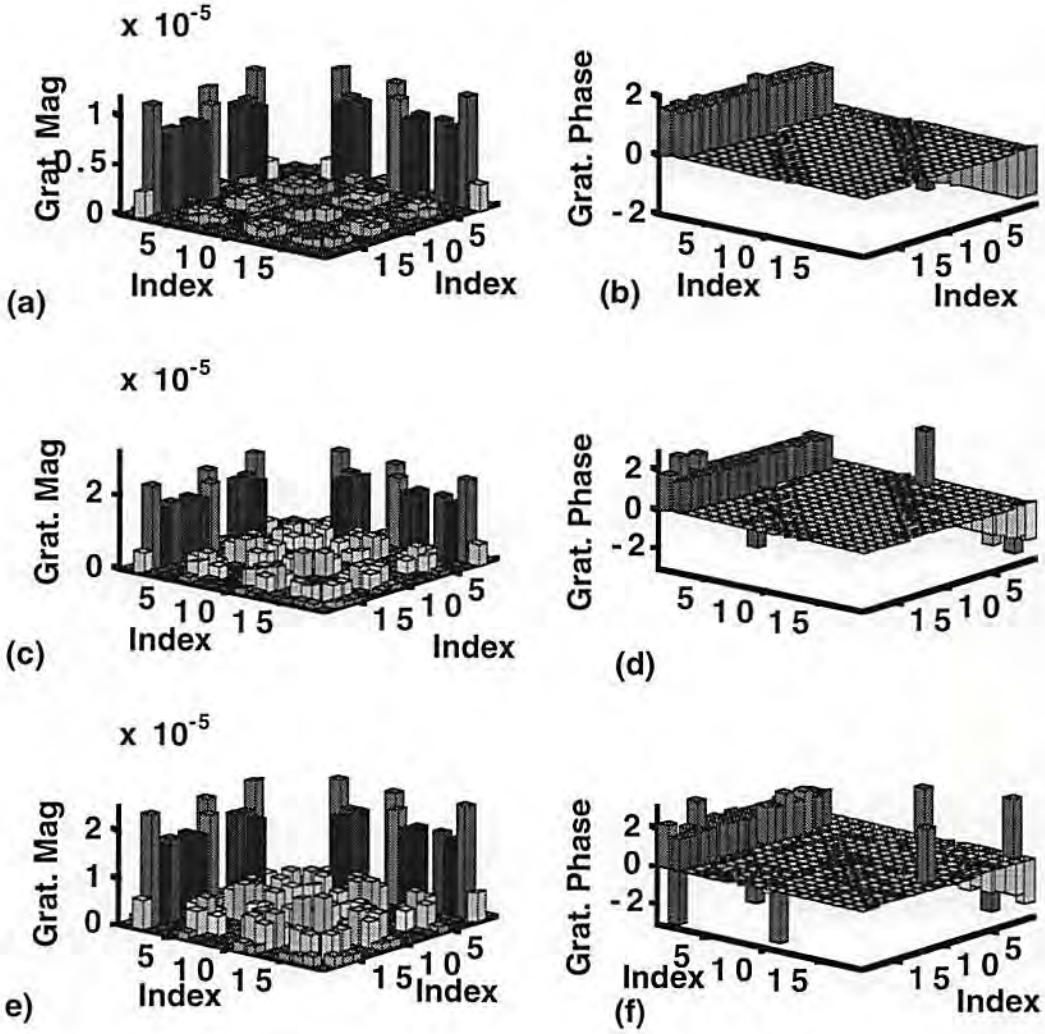

Figure 7-7. Magnitude and phase of the copied matrix of the grating modulations of simulation #1. A gain $G_{ad} = 5$ was performed. Note that the master gratings have zero phase. **(a)** Magnitude of the elements of the matrix of the grating modulations for $B_o = 0.01$. The cross-talk gratings are already visible. **(b)** Phase of the matrix of the grating modulations. **(c)** Magnitude of the elements of the matrix of the grating modulations for $B_o = 0.1$. Larger cross-talk gratings, respect to the master, are present. **(d)** Phase of the matrix of the grating modulations. **e)** Magnitude of the elements of the matrix of the grating modulations for $B_o = 0.5$. The material is close to saturation. **(f)** Phase of the matrix of the grating modulations.

7.8.1 Phase Noise During Copying

As seen in the last subsections, copying changes the phases of the (main and cross-talk) gratings in the secondary medium, and this change constitutes a source of network error. This change of phase is inherent with the copying process because of the presence of the master cross gratings and therefore it is unavoidable. In addition to this, other existing sources of noise can randomly affect the phase of the beams which are recording the secondary medium, with result that the recorded gratings can have random phases with detrimental consequences on the performances of the copied volume holograms. This type of phase noise can be originated by a number of sources. Among these, the easier ones to identify are related to the misalignment of the lenses and the holographic media along the $8f$ optical path of the copying architectures, and the always present mechanical vibrations of the optical set up and the air fluctuations.

To quantify the repercussions of the phase noise on the system we followed this procedure. The secondary medium was conceived with the same thickness and Δn_M of the master. During copying, it was supposed that each object beam impinging on the copying material had random phase noise, $\Delta\phi$, whose value was uniformly distributed in the range $0 \leq \Delta\phi \leq \pi/2$, and $0 \leq \Delta\phi \leq \pi$ in a subsequent simulations. Gain was performed, and we calculated the average network error for each of the three different initial B_o's using the following procedure. For each of the eight master holograms each belonging to one of the eight XOR network architectures so far characterized, the

copying was repeated ten times with different randomly generated values of phase of the object beams. In summary, for each G_{ad}, the average over 80 values of average error was calculated, which is

$$< \varepsilon_{BEP}(G_{ad}, B_o) > \quad = \frac{1}{10}\frac{1}{N_t}\sum_{l=1}^{N_t}\sum_{m=1}^{10} \varepsilon_{BEPlm}(G_{ad}, B_o) \tag{7-37}$$

in which $1 \leq m \leq 10$ is the index of the copy obtained by assigning random phase to the object beams during the copy of the master of the j-th network with gain G_{ad}, having initial maximum beam ratio B_o.

The average network error so calculated is plotted in Fig. 7-8. Surprisingly, for the first case of phase noise randomly generated as $0 \leq \Delta\phi \leq \pi/2$, the networks appear to be quite robust, Fig. 7-8 (a). Here the average error is similar of what seen in Fig. 7-6 (a), and no substantial difference can be detected between these two plots. Differently, when the phase noise is uniformly distributed as $0 \leq \Delta\phi \leq \pi$, the neural networks are not anymore error tolerant. As seen in the results of Fig. 7-8 (b), even for the most robust architecture with $B_o = 0.01$ and $G_{ad} = 1$, the average error is 0.1 exceeding the target of $\varepsilon_{BEP} = 0.05$, and, as expected, the average error is generally growing for larger G_{ad} and B_o 's. It is evident that phase noise can constitute a major drawback for the performance of copied optical holographic interconnections, and it must be accurately controlled and reduced by proper positioning the optical elements, by the accurate measurements of the optical paths of the beams, and by limiting mechanical vibrations and the air fluctuations upon recording. The reduction of these sources of phase noise can be a tedious and cumbersome project, how-

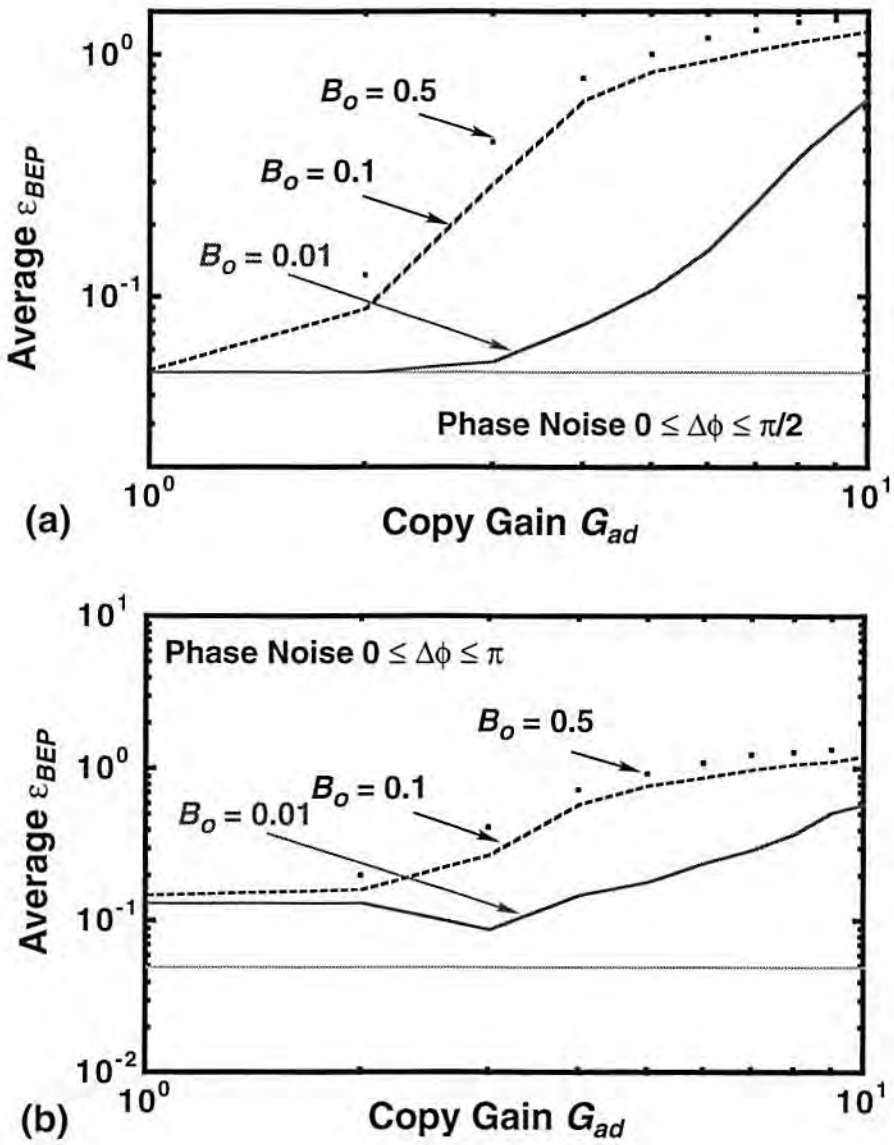

Figure 7-8. Average network error ε_{BEP} when are copied and magnified the holographic weights of the first layer of the XOR network in presence of phase noise. The average ε_{BEP} is calculated over selected XOR simulations presented in the previous section, and the error is averaged over ten of duplication of the same master for each simulation, *i.e.* for each G_{ad} average error is calculated over 80 values of ε_{BEP}. The secondary medium is 5 mm thick, with $\Delta n_M = 0.0001$. The horizontal line indicates the targeted network error $\varepsilon_{BEP} = 0.05$ **(a)** Average network error ε_{BEP} is performed copy and diffraction efficiency gain on secondary medium with object beam random phase noise as $0 \le \Delta\phi \le \pi/2$. **(b)** Average network error ε_{BEP} is performed copy and diffraction efficiency gain on secondary medium with object beam random phase noise as $0 \le \Delta\phi \le \pi$.

ever, it is only an one time effort, and after that initial extra care (during which all these noise sources are reduced) the hologram copying can be indefinitely repeated with constant results and reliability.

7.8.2 Subsequent Copies

If a large number of copies is required, a master hologram can deteriorate. PRC master gratings can decay, and so the information stored in master can be lost. A simple way to circumvent this drawback is to duplicate the master in a permanent material, and then to use the duplicate as a new master. As already seen in this chapter, the new master cannot be an exact copy of the original one, and therefore when the second generation of copies (*i.e* copies of the copy of the initial master) of the multiplexed volume holograms are used in the network, the network errors can be higher than the targeted value. To analyze this issue Fig. 7-9 presents the variation of the average ε_{BEP} when copying from master of different generation order, a concept that we explain as it follows. A copy of the first master belongs to the first generation order. Conversely, this copy can be a master for a second generation order, and so on. The error analysis is performed up to the tenth generation, while the average errors for the three different initial B_o's is considered. During this copying, master and secondary medium had same $\Delta n_M = 0.0001$, and thickness $T = 5$ mm. From the data in the figure, one can definitely deduce that the recordings relative to $B_o = 0.01$ are the ideal one. The average error is always well below the targeted value of 0.05, and therefore even the copy of the tenth generation master can be used without

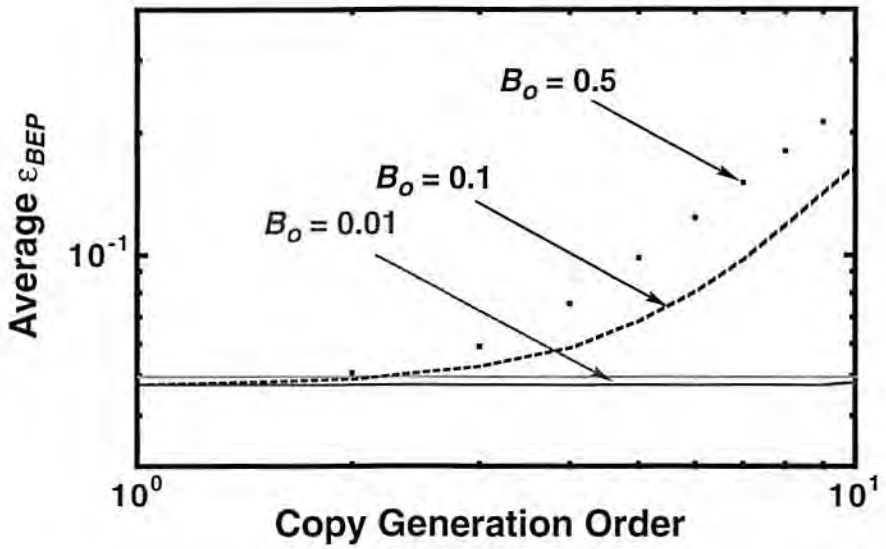

Figure 7-9. XOR system performance when hologram master and copy of different generation are used. A copy of first generation is the duplicate of the original master. A copy of second generation is the copy of the first generation copy, and so on. An unitary copy gain is envisioned upon copy. For $B_o = 0.01$, the average network error does not increase with the increase of the copy generation order. Differently, for $B_o = 0.1$, and $B_o = 0.5$ the system performances worsen with the increase of the generation order. Such difference of the performances is totally related to the action of the cross grating noise. The horizontal line indicates the targeted network error $\varepsilon_{BEP} = 0.05$

worsening the network performances. Differently, for higher initial B_o's, the maximum allowed generation number is the second, with higher errors for the curves related to $B_o = 0.5$. Intuitively, the difference between the three cases plotted here are solely to be associated with the larger cross grating noise related to larger B_o's. In fact, due to the unitary gain which is performed upon this copying process, the contribution to the average error caused by lack of fidelity ought to be excluded.

As already seen, master cross-talk noise affects the recording of the secondary medium in two different ways. First they amplitude modulation of the

recorded gratings can change during hologram copy. Next, cross-talk noise affects the phase of the copied gratings, which, according to the results of the previous subsection dedicated to the study of phase noise, may be a problem of major concern for the network performances. Of course, the effects of cross-talk noise worsen with the generation order. In fact as the generation order increases, the phase of the copied gratings changes in an almost random fashion, causing an increasing average ε_{BEP}. To explain better this last point, we can use the data in Fig. 7-10. Here are presented the matrices of the grating modulations of masters of generation orders 1, 5, and 10, relative to the XOR simulation # 1 with $B_o = 0.5$. Comparing these data with those of the original master of Fig. 7-5 (c), it easy to note that during copying, due to the intensity beam ratio at the secondary medium, the amplitude of the cross gratings is actually reduced. The influence of the initial (master of order zero) cross gratings, however, is demonstrated by the change of the phase of the main gratings, which is more evident at higher generation order. It must be reminded that it was supposed that the elements of the initial master (zero order) to have real value, and therefore zero phase.

7.9 Conclusion and Discussion

In this chapter we discussed and analyzed the implementation and the reproduction of the neural networks which are using multiplexed volume holograms to implement both synaptic weights and optical interconnections. We presented a neural architecture able to incorporate the first layer holographic

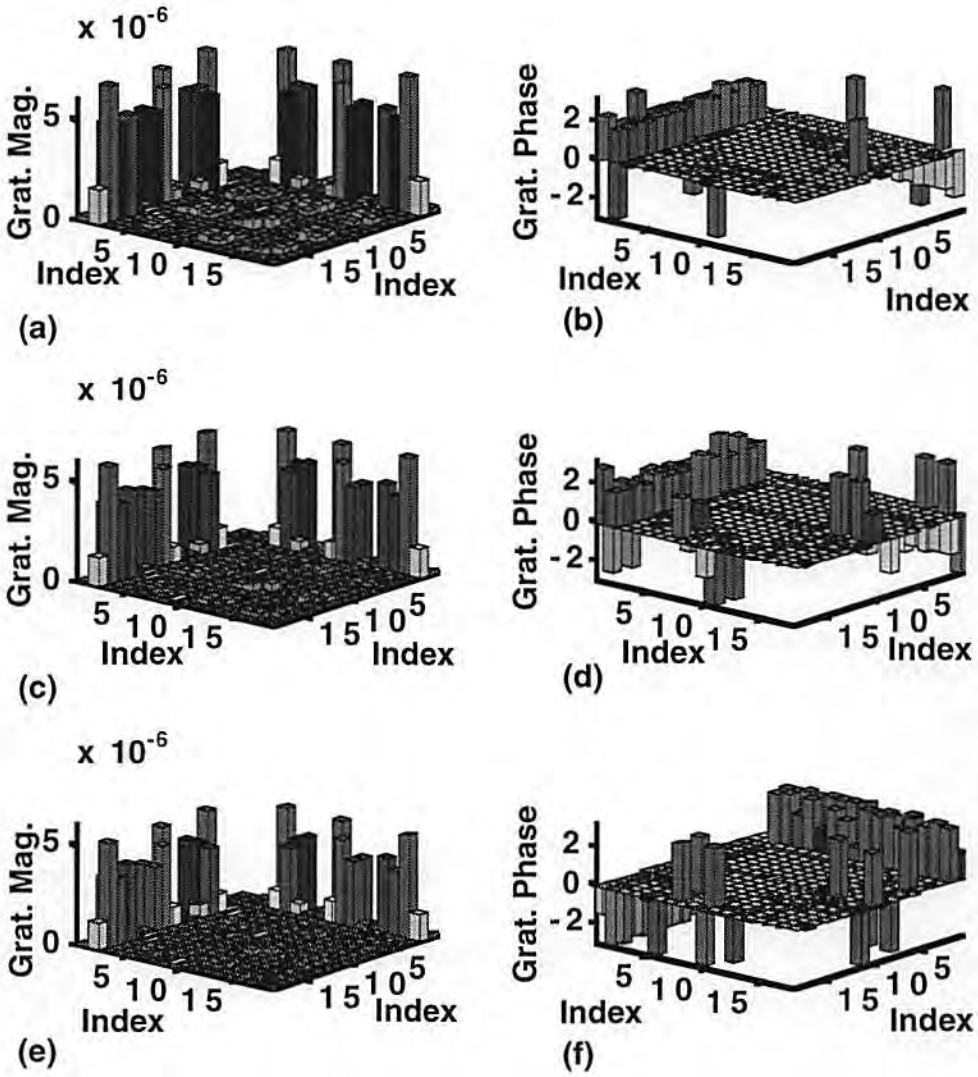

Figure 7-10. Masters of three different generation orders. The actual master of generation zero is relative to the XOR simulation #1, for $B_o = 0.5$ Importantly, it must be observed the change of the phase of the matrix of the grating modulations as the generation order increases. **(a)** Master of the first generation (copy of the master), magnitude of the matrix of the grating modulation. **(b)** Phase of the grating modulation. **(c)** Master of the fifth generation. Magnitude of the matrix of the grating modulation. **(d)** Phase of the grating modulation of the fifth generation. **(e)** Master of the tenth generation. Magnitude of the matrix of the grating modulation. **(f)** Phase of the matrix of the grating modulations belonging to the tenth generation.

weight via a trainable photorefractive crystal. Such network was trained to simulated the XOR problem using the back propagation algorithm, and then we considered the blind copying of the first holographic layer and the performances of such copied multiplexed holograms when used in the optoelectronic neural architecture. Essentially, we considered the degradation of the network performances due to recording of cross gratings, in term of diffraction efficiency gain, grating phase noise, and creation of master of different generation. A crucial parameter to consider during the recording and the training of angularly multiplex volume holograms is the beam intensity ratio among the recording beams. A larger beam intensity ratio can generate holographic interconnections more efficient, but the noise generated by the cross gratings, however, can hamper the training of the network and badly affect the performance of the copied holograms.

The results obtained in this chapter mostly apply to the specific signal representation, field coding, and to the specific problem solved. The methodology used, however, can be easily and advantageously extended to different applications, and to problems which are not solely confined to the holographic implementation of neural networks.

7.10 Bibliography

Alferness, R. and S. K. Case, "Coupling in Doubly Exposed Thick Holographic Grating," JOSA, **65**(9), 730-739, (1975).

Anderson, D. Z., ed. *Neural Information Processing Systems*, American Institute of Physics, (1988).

Gaylord, T. K. and M. G. Moharam, "Analysis and Application of Optical Diffraction by Gratings," Proc. of IEEE, 73(5), 894-936, (1985).

Goldstein, A., G. C. Petrisor, and B. K. Jenkins, "Gain and Exposure Scheduling to Compensate for Photorefractive Neural-Network Weight Decay," Opt. Lett., **20**(6), 611-613, (1995).

Goodman, J. W., "Fan-in Fan-out with Optical Interconnections," Optica Acta, **32**(12), 1489-1496, (1985).

Karim, Z., C. Kyriakakis, J. A. R. Tanguay, K. Hu, L. Chen, and A. Madhukar, "Externally Deposited Phase-Compensating Dielectric Mirrors for Asymmetric Fabry-Perot Cavity Tuning," Appl. Phys. Lett., **64**(22), (1994).

Lee, B. W., and B. J. Shue, *Hardware Annealing in Analog VLSI Neurocomputing*, Kluwer Academic Publisher, (1995).

Lee, H., X. Gu, and D. Psaltis, "Volume Holographic Interconnections with Maximal Capacity and Minimal Crosstalk," J. Appl. Phys., **65**(6), 2191-2194, (1989).

Lippman, R. P., "An Introduction to Computing with Neural Nets," IEEE ASSP Magazine, **4**, 14-22, (1987).

Owechko, Y., "Cascaded-Grating Holography for Artificial Neural Networks," Appl. Opt., **32**(8), (1993).

Pao, Y., *Adaptive Pattern Recognition and Neural Networks*, Addison-Wesley, (1989).

Petrisor, G. C., "Convergence of Backward-Error-Propagation Learning in Photorefractive Crystals," Ph.D. Thesis, University of Southern California, (1996).

Petrisor, G. C., A. Goldstein, and B. K. Jenkins, "Convergence of Backward-Error-Propagation Learning in Photorefractive Crystals," Appl. Opt., **35**(8), 1328-1343, (1996).

Psaltis, D., D. Brady, and K. Wagner, "Adaptive Optical Neural Networks Using Photorefractive Crystal," Appl. Opt., **27**(9), 1752-1759, (1988).

Rumelhart, D. E., G. E. Hinton, and R. J. Williams, "Learning Representations by Back-Propagation Errors," Nature, **323**(9), 533-536, (1986).

Rumelhart, D. E. and J. L. McClelland, *Parallel Distributed Processing*, MIT Press, (1987).

Slinger, C. W., "Analysis of the N-to-N Volume-holographic Neural Interconnect," JOSA-A, **8**(7), 1074-1081, (1991).

Slinger, C. W., "Weighted Volume Interconnects for Adaptive Networks," Optical Computing and Processing, **1**(3), 219-232, (1991).

Vogl, T. P., J. K. Mangis, A. K. Rigler, W. T. Zink, and D. L. Alkon, "Accelerating the Convergence of the Back-Propagation Method," Biol. Cybern., **59**, 257-263, (1988).

Chapter 8

Conclusion and Future Work

8.1 Introduction

In this dissertation we investigated the nature of the recording process in holographic photopolymers and a copying technique for angularly multiplexed volume holograms. The understanding of these two topics can be a key factor for the introduction in a consumer arena of holographic based optical storage devices, because holographic photopolymers are in essence reliable and economically advantageous real time holographic materials, while hologram copying is the solution to a large scale manufacturability of such devices. A summary of the results of our investigations on these two topics is presented in the following sections.

8.2 Holographic Photopolymers

In the first half of this dissertation we characterized the holographic properties of DuPont HRF-150-38 photopolymers. We introduced an initial model, termed as the HFMD model, which gives a simple closed form equation capable to describe the grating formation process when the average recording intensity

is sufficiently low, $I_o < 70$ mW/cm^2, such that we can assume that the diffusion of the free monomers is much faster than the grating formation. The HFMD combines results of the coupled wave theory with basic notions of photopolymerization and in essence it establishes that the saturation value of the grating modulation is proportional to the beam intensity modulation and that the grating formation time constant is related in nonlinear fashion to the inverse of the average recording intensity. The model was experimentally confirmed with data related to holographic exposures in which the recording beams had wavelength $\lambda = 514$ nm, and extraction of the figures of merit of the HFMD model helped the better understanding of the photopolymerization of process concerning the definition of the inhibition period, the determination of the photopolymerization function, and of the grating formation time constant. Importantly, we could extend the HFMD model to predict and control the recording of multiplexed holograms in photopolymers. Particularly, we emphasized on the studying of simultaneous incoherent/coherent recording of angularly multiplexed holograms in photopolymers. In this case, the model results indicated that during recording the temporal evolution of each single grating is in synchronization with each others, sharing among them common grating time constant, while the grating amplitudes of their different modulation indices at saturation are proportional to their beam intensity modulations. The HFMD model was validated experimentally with holographic exposures having recording beams with wavelength $\lambda = 514$ nm, however, all the figures of merit that we experimentally determined are valid for this recording wavelength. For the sake of a better characterization of the HRF-150-38, it is necessary to

carry out a validation of the model within the sensitivity spectrum of the material which is within the wavelength range of 450-550 nm. This characterization can represent an important future investigative effort.

Because holographic photopolymers are real time materials, self diffraction can or may occur during exposure. Using the HFMD model, we simulated and characterized the effects of self diffraction in photopolymers. Among these effects, we noticed that self diffraction can induce the change of the reconstructing Bragg angle and the recording of a nonuniform modulation of the grating index within the holographic region. We have successfully verified the prediction of our modelling of the self diffraction effects by comparing simulation results with measurements relevant to a number of experimental recordings. Particularly, we have investigated the effects of self diffraction in recordings in thicker holographic samples consisting in double layers of HRF-150-38. Interestingly, we proved that when recording with a nonunitary beam intensity modulation, each of the two layer experiences different phase and amplitude of the grating modulation. Because self diffraction effects can be extremely detrimental when holograms are recorded in very thick materials with large modulation index, we simulated the recording of holographic gratings in hypothetical 300 μm thick photopolymers having the same figures of merit (reaction order δ, and the constants γ and φ) of the photopolymerization process of the HRF-150-38. In these conditions, for a single grating recording, the simulation results show that it is very difficult to control the outcome of the recording in term of its saturation diffraction efficiency and its Bragg selectivity. Other computer simulations indicate, however, that such problems can vanish if a

number of holograms are angularly multiplexed using simultaneous recording with incoherent/coherent illuminations. In fact, in these recordings the effective modulation index that each single grating effectively sees is reduced by the number of gratings that are simultaneously multiplexed, and, because of this reduced modulation index, the effect of self diffraction are also minimized. Our investigation also indicated that when choosing a recording technique of multiplexed holograms, simultaneous incoherent/coherent recording is preferable to sequential recording.

At larger average recording intensities, $I_o > 70$ mW/cm^2, the HFMD model is not any more accurate in describing the grating formation process. In this case it is necessary to consider the presence of a limited diffusion of the free monomers during photopolymerization, to model more exactly the hologram formation. Experimentally, we observed that the diffusion of the free monomer diffusion varies during photopolymerization, from almost instantaneous at the beginning of the exposure, to very slow close to saturation, and therefore we credited this difference to the variation of material viscosity during the photopolymerization. As consequence of a limited free monomer diffusion, we assumed that the free monomer concentration is spatially modulated during recording, and that can be expressed as the combination of a DC term and of a sinusoidal term which is out of phase with the forming grating modulation. Therefore, to model more correctly the grating formation during this regime of limited diffusion of the free monomers, we combined the interaction among photopolymerization (as determined in the HFMD model), free monomer diffusion using Flick's diffusion laws, and basic results of the coupled wave

equation. To simplify the problem we averaged the diffusion coefficient during holographic exposure, which allowed us to obtain an analytical closed form describing the temporal variation of a grating during recording. This new diffusion model was able to predict both the saturation diffraction efficiency and the grating dynamics for varying beam intensity modulation and average recording intensity. Moreover, this diffusion model was able to predict even other experimental observations as the dark diffusion increment during recording. In essence, we noticed that when a holographic exposure is ceased before reaching saturation, the grating formation does not cease accordingly, but tends to increase asymptotically. According to our diffusion model, the dark diffusion transient must be associated with the migration of free monomers which continues even after the recording illumination is off, because of the disappearing of the sinusoidal concentration of the free monomers. In fact, we demonstrated that the increment of the diffraction efficiency due to dark diffusion transient is related to the amplitude of the sinusoidal free monomer concentration during recording, which is at the same time also depending on the recording intensity. Finally, we illustrated how the dark diffusion transient can be positively used to increase the recording diffraction efficiency, which is done by cyclically alternating an exposure period and dark (transient) period. In the diffusion model, we assumed a constant diffusion coefficient which originated a constant diffusion time constant $\tau_D = 0.9$ s for the specific case of grating recording with a Bragg angle of 20°. However, when we scale the values of the average diffusion time constant to predict the outcome of holographic exposures at different Bragg angles (specially at Bragg angle values as low as 10°) the diffusion

model may lack in accuracy. Therefore, we have suggested improvements to our diffusion model as a future research effort that includes a more efficient characterization of a time varying diffusion coefficient during hologram recording, and the study and the integration in the diffusion model of the effects of self diffraction at varying Bragg angles.

8.3 Generation and Copying of Angularly Multiplexed Volume Holograms

A limitation to the more widespread use of volume holographic elements has been their lack of manufacturability. To overcome this problem we have presented a new technique for the simultaneous copying of holograms which are angularly multiplexed in a master volume hologram. The copying technique uses an array of coherent but mutually incoherent coherent sources to retrieve the holograms in a master and an optical lens system that can image the optical information at the plane where is located the secondary holographic material for the copy. The function of the source array was to allow the incoherent/coherent recording of the copy with a reduced low cross-talk recording noise. As an experimental demonstration, we proved the feasibility of our copying technique multiplexing three complex holograms in a holographic photopolymer, and then copying in another photopolymer film. Furthermore, we presented an analysis of the copying technique which led to identify the conditions for the blind copying of angularly multiplexed volume holograms. For blind copying we intend a copying technique which allows the (hypothetical) exact duplication of master holograms without *a priori* knowledge about its dif-

fraction efficiencies or its grating modulations. We demonstrated that our copying architecture can perform blind copying with this two conditions on the recording intensities: (1) the set of master reference beams must be of equal intensity among them, and so the set of the copy reference beams; (2) the ratio copy/reference beam intensity must be related to some parameters of the copy material (modulation index and thickness) and proportional to the inverse of the square of the number of the multiplexed holograms. Because of the architectural flexibility of the presented technique, we extended its application to the use of different materials for copy and/or master. Particularly, we have investigated the compatibility between photorefractive crystals and holographic photopolymers, because of the attractive possibility of storing in a reliable, permanent, and economically advantageous material (photopolymers) the information generated in a trainable and therefore volatile material (photorefractive crystals). Among the several factors that can limit the performances of our copying technique we analyzed those related with the physical characteristics of the copying materials (thickness and modulation index) and the *f*-number of the optical system used to image the holograms retrieved from the master on the copy plane. We found that there is a precise relations among the number of holograms that can be duplicated on a secondary medium, their average diffraction efficiency, and the *f*-number of the imaging optical system. However, future characterization about the bounds that are provided by the aberrations of the lenses of the imaging systems and can complete this study about the limitation of the copying system.

As an example of application of optical computing and more specifically

of hologram copying we simulated the problem of the generation and the duplication of two layer feedforward optical neural networks in which the first layer weights are implemented by angularly multiplexed holograms in a photorefractive crystal. To study such application, we have demonstrated first how some basic operations of neural learning and signal processing can be replicated with holographic interconnections in photorefractive crystals, and then we simulated the learning of the XOR problem in a network which presented eight neurons on the first layer which corresponded to 32 angularly multiplexed holograms on the photorefractive crystals. To encode the neural signal we used a field amplitude representation with dual rail weights, while the simulation was able to take into account the grating decay originated during neural training and the noise generated by the cross-gratings. Interestingly, the simulation results of this problem hold significant indications about the convergency speed and the grating modulations. In fact, we found out that there is an inherent trade-off between high initial modulation of the gratings and the speed of convergency. To have high initial grating modulation it is necessary to record with a high beam intensity ratio, which surely enhances the amplitude of the main gratings, but unfortunately also causes the recording cross-gratings with large modulation which act as source of noise. The simulation results indicated that a network usually takes a larger number of iterations to learn the XOR problem when associated with larger initial cross-gratings. Of course, a larger number of iterations means a more severe gratings decay. Conversely, for initial recordings with low beam intensity ratio, the grating modulations are lower as so is the noise generated by cross-gratings, with the result of a generally faster convergency and less severe

decay of the modulation gratings. The action of the cross-gratings manifested itself in an even more severe fashion during copying of the holographic weights. In fact, we demonstrated that cross-gratings noise can hamper in different ways the quality and the fidelity of the copy. For instance, larger cross-grating noise can damage the magnification and reproduction of the hologram diffraction efficiencies during copying. This problem, however, can be limited by copying in a secondary medium with larger modulation index of the master. Moreover, a master with large amplitude modulation of the cross-gratings cannot allow generation of copies that can be used a masters for subsequent copying operations. Finally, we demonstrated that the phase noise which can affect the retrieved master hologram is one of the most damaging factor during copying. In the examples that we studied, a copy can still perform in the network when such phase noise is bounded as $0 \leq \Delta\phi \leq \pi/2$ (with uniform distribution), while, instead, a phase noise as $0 \leq \Delta\phi \leq \pi$ is totally detrimental.

This last part of our dissertation can be inspirational to a number of future investigations which can complete the work here presented. For instance, the performances of different implementation of holographic neural networks and their errors due to cross-grating noise can be studied. In fact, beside the field amplitude encoding that we considered, one can investigate different other encoding (*i.e* fully coherent intensity encoding, incoherent/coherent intensity encoding). Moreover, it will be essential to determine which encoding paradigm can hold the best performances during eventual generation of error tolerant copies, which is an essential topic in consideration of a future large use of holographic based memories.